UNIVERSITY OF OKLAHOMA

GRADUATE COLLEGE

STRUCTURAL AND FUNCTIONAL CHARACTERIZATION OF THE BINDING OF *C*-NITROSO COMPOUNDS TO MYOGLOBIN AND HEMOGLOBIN

A DISSERTATION

SUBMITTED TO THE GRADUATE FACULTY

in partial fulfillment of the requirements for the

Degree of

DOCTOR OF PHILOSOPHY

By

VIRIDIANA E. HERRERA
Norman, Oklahoma
2019

STRUCTURAL AND FUNCTIONAL CHARACTERIZATION OF THE BINDING OF *C*-NITROSO COMPOUNDS TO MYOGLOBIN AND HEMOGLOBIN

A DISSERTATION APPROVED FOR THE
DEPARTMENT OF CHEMISTRY AND BIOCHEMISTRY

BY THE COMMITTEE CONSISTING OF

Dr. George B. Richter-Addo, Chair

Dr. Ann H. West

Dr. Charles V. Rice

Dr. Daniel T. Glatzhofer

Dr. Elizabeth A. Karr

Dedication

Dedico este trabajo en parte a mi padre, Javier Herrera, quien sacrificó su tierra y lengua nativa en busca de un mejor futuro para sus hijos. Sin educación, pero con muchas ganas de avanzar, me enseñó con ejemplo que todo es posible. A mis hermanos, les dedico este logro, que es tanto mío como de ellos. Su apoyo incondicional y fe en mí fueron la energía que me impulsó a sobrepasar la montaña que fue este doctorado.

Acknowledgements

First and foremost, I would like to express my deep sense of gratitude to my Ph.D. advisor, Dr. George B. Richter-Addo. Without his invaluable guidance, timely advice and keen interest as a mentor, this work would not have been possible. Beyond the lab, his contagious positive outlook and constant civic engagement challenged the "isolated" way I viewed my role as a scientist. By example, he empowered me to accept opportunities and leadership roles in my community. I would also like to give a special thanks to Dr. West, for her generosity and support. Her input through numerous letters of reference helped me secure my postdoctoral fellowship and a few awards. I'd also like to thank the rest of my advisory committee, Dr. Elizabeth A. Karr, Dr. Charles V. Rice, and Dr. Daniel T. Glatzhofer, for their commitment and help thought out the years.

Next, I would like to thank everyone from the GBRA group, present and former members, for a pleasant and welcoming work environment. A big thanks to Drs. Bing Wang and Jun Yi (Eva) for teaching me their inside knowledge and special "tricks" as I learned to work with systems they had previously handled. I'd also like to express my sincere gratitude to Dr. Samantha Powell, for being an excellent mentor, an inspirational colleague and a dear friend. I will miss our informal one-on-one group meetings, where we bounced ideas off of each other to troubleshoot challenges in our projects. I have been blessed with a dedicated set of undergraduate colleagues, Kiana Prather, Nancy Nguyen, and Sara Crooks, who have helped in many aspects of my research. Along the way, they taught me to be a better mentor, and for that, I am grateful. A very big thanks to Dr. Erwin Abucayon and Jeremy Zink for all their help with NMR, and for teaching me the intricate principles of inorganic chemistry. A huge thanks to Jennifer Londoño Salazar for brightening my life with her presence and for being a beacon of happiness. I'd also like to express my gratitude to Dr. Leonard M. Thomas, for teaching me everything there is to know about X-ray crystallography,

and for helping me solve numerous structures. A special thanks to Drs. Smita Menon and Skyler Hebdon, for their help and guidance.

Finally, I am immensely indebted to my confidant Dr. Zahir Kouzbari, who has devoted innumerable hours listening to my struggles and providing direction. He has been a pillar of strength and hope for me throughout my years as a PhD student, and for that, I will be forever grateful.

Funding

I would like to thank the National Science Foundation (Grants CHE-1566509 and CHE-1900181to GBR-A) for funding for this work. The proteins used for the research presented in this dissertation were purified in part at the OU Protein Production Core (PPC) facility. All X-ray diffraction data collection was done at the OU Macromolecular Crystallography Laboratory (MCL). I am grateful to the National Institute of General Medical Sciences of the National Institutes of Health for providing funding for the PPC and MCL facilities through an Institutional Development Award (IDeA) under grant number P20GM103640. Furthermore, I would like to thank the Price Family Foundation for funding the anaerobic MBraun chambers used for anaerobic protein crystallization. The contents of this publication are solely the responsibility of the authors and do not represent the official views of the NSF or the NIH.

Table of Contents

List of Tables

List of Figures

Abstract

The formation and structural characterization of the interactions of the oxygen-carrier proteins myoglobin (Mb) and hemoglobin (Hb) with *C*-nitroso metabolites are described. The spectroscopic studies and X-ray crystal structures provide a direct correlation and explanation of the toxic side-effects associated with bioactivation of nitrogenous species into *C*-nitroso (RNO) metabolites *in vivo*.

Chapter 1 introduces the physiological pathways that give rise to *C*-nitroso compounds and provides specific examples of prescription drugs and other small molecules known to undergo such biotransformations. This chapter also provides a brief overview of the health-related problems linked to the binding of RNOs to hemeproteins, such as methemoglobinemia, hemolytic anemia, and liver enzyme damage. Overviews of the structures of Mb and Hb, and the active-site amino acid movements expected to mediate heme-ligand binding are also provided.

Chapter 2 describes the selection process and biological significance of a series of nitroalkanes (RNO_2; R = Me, Et, Pr, *i*Pr) used as RNO precursors for this systematic study. The same ligands were then used to form the Mb-RNO adducts (under reducing conditions) in order to determine the influence of RNO sterics on ligand binding to Mb and the stability of the complexes resulting from such binding. In that same chapter, I also determined the influence of the distal-pocket amino acid residue His64 on ligand access into the active site, as well as resultant Mb-RNO complex stability. The apparent rates of formation of each ferrous Mb^{II}-RNO adduct and seven distinct X-ray crystal structures are presented here. The resulting X-ray crystal structures show that these RNOs favor the N-binding mode when forming the ferrous Mb^{II}-RNO complexes in both wt and the H64A mutant. However, the geometric orientations of the ligands differ significantly between protein models. In some cases, these spatial discrepancies are due to ligand

sterics, and in others are due to the influence of distal pocket composition. These results reiterate the idea that protein-ligand interactions vary at the molecular level despite protein-ligand system similarities. Ultimately, these results depict how *C*-nitroso metabolites inhibit Mb from carrying out its role in O_2 storage by occupying the active site.

In Chapter 3, I continued to monitor the interactions of *C*-nitroso compounds, but this time with hemoglobin as the target protein. Numerous studies indicate that RNO binding to Hb induces protein degradation. Yet, the molecular mechanism for this process remained largely unknown. Using the same techniques as described in Chapter 2, I prepared crystals of the RNO (R= Me, Et, Pr) bound Hb-ligand complexes and solved their X-ray crystal structures. As observed with Mb, these nitroso metabolites favored an N-bound state in both the α and β subunits, forming ferrous Hb[α-Fe^{II}(RNO)][β-Fe^{II}(RNO)] complexes. To determine the structural consequences of RNO binding, I continued to harvest and collect data (every ~2 weeks) on crystals from the same crystallization vial as those used to solve the ligand-bound structures. As a result, I obtained 4 additional distinct X-ray crystal structures that reveal key intermediate steps in the overall molecular mechanism of Hb degradation. From the MeNO set, one structure revealed ligand displacement by a water molecule, and congruent Fe oxidation into the ferric Fe^{III} state. A different structure displayed hemichrome formation in the β subunit after EtNO binding. This was marked by bis-His coordination of the Fe center, which was accompanied by large unraveling of the βF-helix and βCys93 *S*-nitrosation. Another structure revealed that hemichrome formation is followed by simultaneous partial protein refolding and partial heme slippage. In this structure, Fe anomalous mapping revealed two positions for the metal: one in the original ligand-bound position and a second significantly displaced from the active site towards the solvent exterior of the protein (Fe-Fe measured distance of 5.2 Å). Finally, the PrNO related Hb structure was especially unique. In

this structure, the β subunit of Hb was observed in two distinct degradation stages. The βF-helix was modeled in both the ligand bound folded state and the hemichrome unraveled form. Furthermore, Fe anomalous mapping indicated two positions for the heme with equal occupancies as the βHis92 residue that serves to anchor the metal in place. Together, these structures provide crystallographic evidence for i) ligand binding, ii) Fe^{II} oxidation, iii) hemichrome formation, and iv) the heme slippage intermediate steps leading to Hb degradation. Each structure details the global changes and active site chemistry that occurs at the time of RNO binding to Hb, and as the structure morphs as a result of *C*-nitroso binding.

Chapter 4 explores the importance of metal identity and redox state of the macrocycle on Mb-RNO complex formation. Here, CoMb and ChlMb were prepared by removing heme from native Mb and substituting it with Cobalt PPIX and Chlorin, respectively. The reactions of the ensuing proteins were monitored with the same series of alkyl nitroalkanes as described in Chapter 2 for comparison. My results indicate that RNO binding to reduced Co^{II}Mb is unstable, evidenced by apparent oxidation of Co^{II}Mb into Co^{III}Mb upon addition of RNO_2 precursor. On the other hand, stable complex formation was observed with ChlMb. However, due to lack of X-ray crystallography results, the RNO binding mode (N vs O) remains unclear. Also discussed in this chapter are the interactions of native Mb with a series of nitrotoluenes (NTs) to probe the limits to which the active site of Mb can accommodate RNOs. Parallel studies were done with the H64A Mb mutant. In the wt species, binding of NT to ferrous Mb^{II} was unstable and resulted in spectral traits characteristic of the ferric wt Mb^{III}-H_2O species. Interestingly, the same reactions resulted in short-lived ferrous Mb^{II}-RNO complexes in the H64A analog. These results indicate that larger NTs can also bind Mb, but that the binding is transient.

Chapter 1. Introduction

The reactions between organic *C*-nitroso compounds (RNOs) and heme-containing proteins has been a topic of interest for well over a century. The earliest studies documented heme-nitroso chemistry resulting from the interactions of hemoglobin (Hb) with nitrobenzene. In the year 1878, Filehne W. reported that human blood actively reduced nitrobenzene ($PhNO_2$) to its active nitrosobenzene ((PhNO) form [1]. The reduced product of this redox reaction, PhNO, exhibited a strong affinity towards heme. In fact, early studies described this heme-nitroso chemistry in terms of "combining power," because PhNO and heme "combine" to form a single highly stable Hb-PhNO complex [1, 2]. Moreover, since PhNO occupied the heme active site of Hb upon complex formation, it rendered blood unable to bind and transport oxygen. This in turn was reported as the leading cause of some of the toxic side-effects associated with nitrobenzene poisoning, including methemoglobinemia [3-6]. While the prevalence of nitrobenzene poisoning during that time may have sparked an initial interest in the subject, heme-nitroso chemistry continues to be a highly relevant topic today. This is due in large part to the ubiquitous dispersal of heme proteins in nature and the swift bioactivation of nitrogenous species into reactive RNO metabolites.

Over the years, different types of spectroscopy, electrochemical techniques and biological assays, to name a few, have been used to investigate the interactions between *C*-nitroso compounds and various heme proteins. Synthetic heme models have been built to mimic biological systems in an attempt to facilitate the identification of intermediates formed from such reactions. More recently, X-ray crystallography, almost exclusively from our laboratory, has been employed to determine the three-dimensional structures of a handful of biologically-relevant protein models in the heme-nitroso binding state. These X-ray crystal structures have provided a great deal of insight

into the chemistry of these adducts [7-9]. However, several questions regarding the nature of binding and the effect(s) on active site structures remain unanswered.

In this work, I use X-ray crystallography and UV-vis spectroscopy as the main tools to interrogate the heme-nitroso chemistry resulting from the reactions of organic *C*-nitrosoalkanes with myoglobin (wild type and H64A mutant) and human hemoglobin.

1.1 *C*-nitroso compounds

Organic *C*-nitroso compounds (RNO) are valence isoelectronic with O_2, and this chemical characteristic makes RNOs biologically significant since it gives them the ability to compete for binding to the heme iron of various metalloproteins. While *C*-nitroso compounds are not regularly encountered in the environment in large quantities, they are common bioactivation products of drugs and other exogeneous compounds containing the amine (RNH_2) and/or nitro (RNO_2) functional groups [10-14]. Under normal or perturbed physiological conditions (e.g., during infection), nitrosoalkanes can form via two pathways, **i)** through the oxidative metabolism of amines and hydroxylamines (RNHOH) or **ii)** by the reduction of nitro-containing compounds (Figure 1.1) [14].

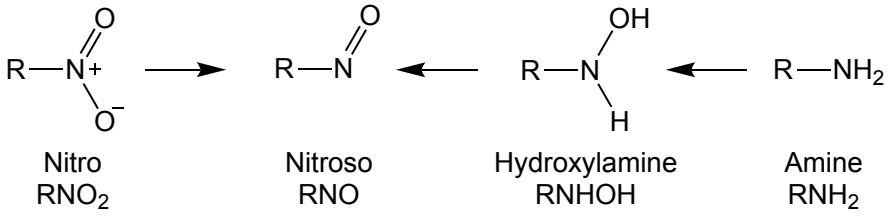

Figure 1.1 Left to right, reductive metabolism of nitro compound to nitroso products. Right to left, oxidative metabolism of amines and hydroxylamines to nitroso products.

Some examples of nitrogenous species known to undergo bioactivation through the oxidative pathway include dapsone (a dermatological drug containing an amine moiety), aniline

(an amine-containing compound, used for the manufacturing of industrial chemicals) and amphetamine (a prescription drug commonly used for the treatment of ADHD and obesity). Studies show that dapsone is bioactivated by cytochrome P450s to the hydroxylamine intermediate, which is then oxidized by hemoglobin in red blood cells to produce the nitroso product [15, 16]. It is also known that N-oxidation of amphetamine forms the N-hydroxyamphetamine metabolite, which can further [17, 18] react with cytochrome P450 [19, 20] and prostaglandin H synthase [21] to generate nitrosoamphetamine. In a similar manner, aniline has been reported to undergo metabolic activation in rats resulting in nitrosobenzene formation [22-24].

As mentioned before, blood itself is metabolically competent to reduce nitrobenzene into the nitroso derivative. Similarly, simple nitroalkanes can also undergo reductive metabolism resulting in the nitroso form [14]. Due to their widespread use (as solvents, chemical intermediates, and fuel for rockets and race cars) large amounts of nitroalkanes are released into the environment and can make their way into the human body [25]. Once inside, their interconversion is primarily catalyzed by cytochrome P450s [12]. Likewise, nitro-containing drugs such as chloramphenicol (a commonly prescribed antibiotic) and nitro-benzothiazinones (antitubercular agents) have also been reported to undergo reductive activation to form nitroso products [26]. Although these are only a few examples, biotransformations resulting in reactive *C*-nitroso compounds have been reported in detail [12, 23, 24, 27-30].

Our bodies metabolize nitrogenous species in an attempt to clear our system of foreign substances. However, the resulting *C*-nitroso products often impart severe damage to proteins, which can eventually cause health related problems [10-13]. For instance, the catalytic conversion of aniline to PhNO has been reported, in rats, to induce methemoglobinemia and hemolytic anemia

in the animal [22]. This is primarily caused by the initial binding of PhNO to red blood cells and consequential Fe release and accumulation in the spleen [3, 31]. Similarly, once formed, nitrosodapsone can also interact with red blood cells and cause methemoglobinemia. Furthermore, nitrosodapsone has been documented to bind cytochrome P450s and form Fe(II)-RNO inhibitory complexes, rendering the enzyme non-functional [15, 16, 32]. Unfortunately, many other nitro-containing drugs exhibit these serious side-effects upon reductive biotransformation [14, 21, 26, 28, 30, 33-36]. Chloramphenicol has even been named a suicide inhibitor of the very protein responsible for its detoxification [35].

Medicinal chemists have increased their efforts to turn away from the development of nitro-containing drugs due to their high toxicities and serious side-effects [28, 36]. Yet, deviating from such functional groups seems unlikely in the near future. As such, there is an increased need for the structural biology of the subsequent heme-nitroso complexes, which can provide a better understanding about the mode of binding of RNOs to heme protein, and the architectural consequences of such binding to protein structure and function.

1.2 Heme

Heme, also known as protoporphyrin IX, is an important redox-active biological cofactor. It is composed of an Fe atom tetra-coordinated to a macrocyclic compound (Figure 1.2). The Fe atom at its core in the reduced ferrous state gives heme its red color, and this color changes depending on the redox state of the metal. Heme is synthesized in organisms through a complex eight-step pathway involving multiple enzymes [37-39]. Due to its redox versatility, nature incorporates heme into several types of proteins essential for life on earth [40, 41]. In this work, we will only focus on two heme proteins, myoglobin (Mb) and hemoglobin (Hb).

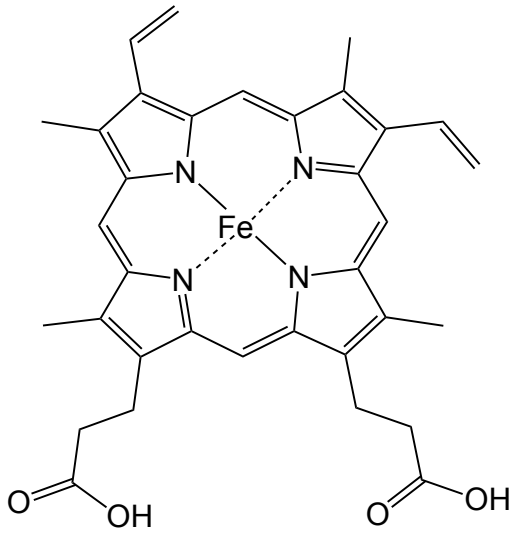

Figure 1.2 The prototypical heme: protoporphyrin IX.

1.3 Myoglobin

The heme protein, myoglobin (Mb), plays an important role in the physiological function of heart and skeletal muscle. This is predominantly due to Mb's ability to store and release dioxygen (O_2) as needed for cellular processes. Mb is a small monomeric protein of ~17 kDa. Mb composed of eight α-helices arranged in a globular 3D structure with a heme prosthetic group embedded within the protein near the surface (Figure 1.3A). As with most heme proteins, the central chemical function of Mb is dependent on the use of this heme cofactor.

The heme cofactor allows Mb to reversibly bind O_2 directly at the Fe center. In its ferric (i.e. "oxidized," Fe^{III}) state, Mb's heme Fe^{III} adopts a high-spin state with water bound at the sixth coordinating position; at the same time, a second bond connects heme to Mb through His93 coordination (Figure 1.3B) [42]. The area above the heme is termed the distal pocket, and it is made up mostly of hydrophobic amino acids, with the exception of His64 near the surface. Residue His64 is located at the entrance of the active site and it can participate in H-bonding with Fe-bound

ligands; in this example, His64 serves to stabilize the water molecule through H-bonding and acts as a gatekeeper limiting access into the active site (Figure 1.3B) [42].

In its ferrous form, the heme iron adopts a five-coordinate state, in which the sixth coordination position is available for binding. Thus, dioxygen can bind reversibly to the ferrous iron center of the heme cofactor for optimized O_2 storage and release [43].

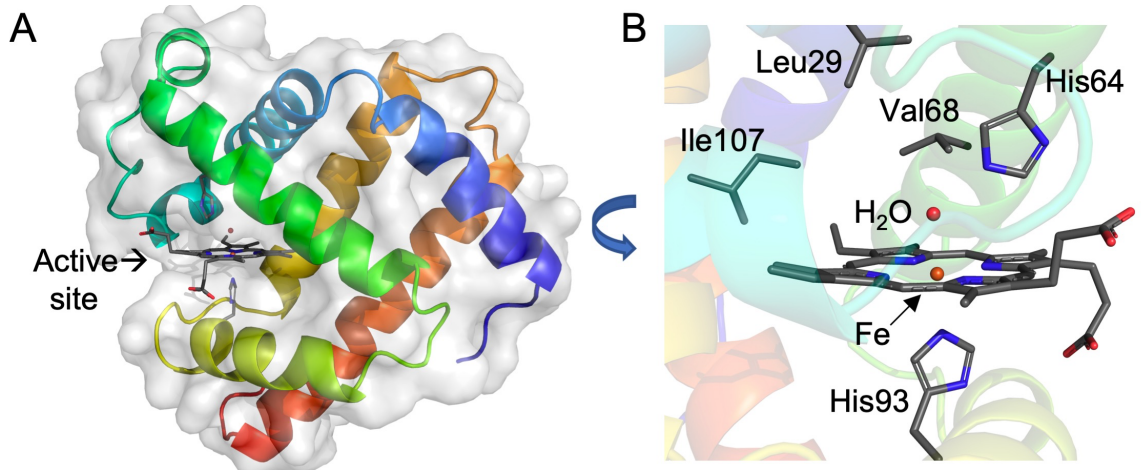

Figure 1.3. Structure of aquomet swMb (PDB ID 2MBW [42]). A) Globular 3D structure of Mb with the surface of the protein shown in light gray. An arrow points to the entrance of the active site. The 8 α-helices making up the 2° structure of Mb are shown in rainbow colors, with the N-terminal A α-helix shown in navy blue. B) Zoomed-in view of the active site rotated ~80° as compared to A. The area above the heme containing His64 and other labeled hydrophobic amino acids is referred to as the "distal pocket." Also shown is His93 that covalently links heme to Mb, and water bound at the sixth coordinating position which is the position for ligand binding.

1.4 Hemoglobin

Hemoglobin is a heme-containing protein found in the red blood cells of most vertebrates. The main purpose of Hb is to transport oxygen from the lungs to the muscle protein Mb. In humans, ~96% of circulating Hb is composed of two copies of an αβ dimer that combine to form a globular tetrameric structure of ~64 kDa (Figure 1.4). The individual α and β subunits share only 43% sequence identity, yet both subunits are composed of 8 α-helices folded in a similar manner (RMSD 0.861 Å). The active sites of both subunits of Hb are highly conserved and resemble that of Mb. The heme is anchored to the active site through an Fe-N bond with the proximal His residue (His87/92 in α and β respectively) similar to that seen in Mb. The distal His residue of Hb (His58/63 in α and β, respectively) plays an important role in dictating substrate access into the active site and by participating in H-bonding with certain ligands. Both sperm whale Mb and human Hb were used as the protein targets in this work.

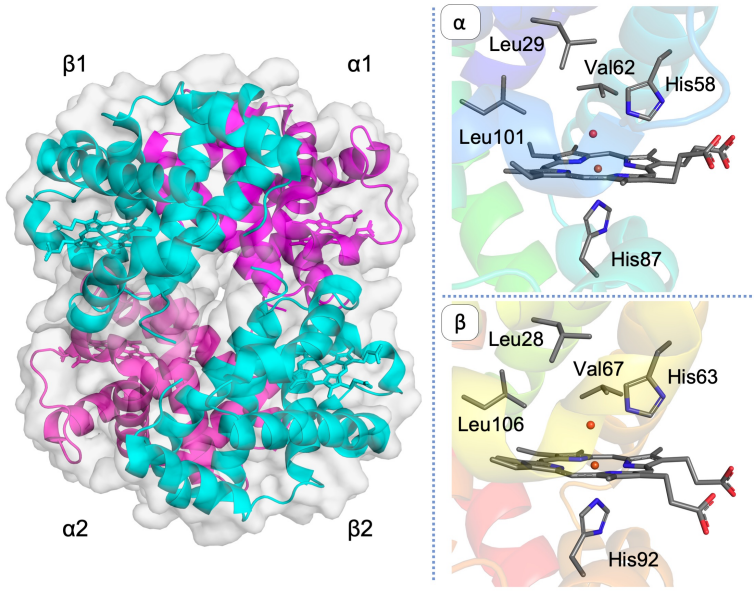

Figure 1.4 Structure of human Hb (PDB ID 305Q) Left: Tetrameric structure of Hb with the surface of the protein shown in light gray. Right: Active site models of the α and β subunits with relevant amino acids labeled.

1.5 Research Focus

The overarching goal of my research is to characterize the heme-nitroso chemistry resulting from the reactions of organic *C*-nitrosoalkanes (RNOs) with Mb and Hb. My work uses UV-vis spectroscopy to probe these reactions in solution, and it also harnesses the power of X-ray crystallography to develop a clear picture of the global and local structural changes that these proteins undergo as a result of RNO binding. To do so, I developed a series of systematic experiments designed to **i)** determine the influence of ligand sterics on RNO binding, and asses the stability of the resulting heme-nitroso complexes, **ii)** characterize the influence of distal pocket amino acid composition on ligand access into the active site and identify the amino acid residues involved in the coordination of these complexes and, **iii)** characterize the global architectural changes that these proteins undergo at the time of RNO binding, and after.

In Chapter 2, I describe my investigations into the interactions of Mb with nitrosoalkanes of increasing alkyl group sizes, in order to determine the effects of ligand sterics on RNO binding to Mb and the resulting stability of those complexes. I used UV-vis spectroscopy to monitor the formation of four distinct Mb-RNO (R = methyl, ethyl, propyl and isopropyl) derivatives and determined their apparent rates and extents of formation. To further characterize the products of these reactions, I used X-ray crystallography to solve the structures of these complexes. The resulting high-resolution models provide an in-depth view of the heme-nitroso chemistry occurring in the active site of Mb and also reveal the overall changes to the architecture of the protein.

Expanding on this line of research, I also studied the impact of distal-pocket site directed mutations on RNO ligand coordination and accessibility into the Mb active site. Residue His64, located at the entrance of the Mb active site, serves as a gatekeeper into the heme pocket and can participate in H-bonding with ligands. Using the H64A Mb mutant and same methodologies as

described above, I determined the extent to which His64 hinders RNO access to the heme. My research shows that by removing the distal pocket His64 residue, small RNOs (R = methyl, ethyl, propyl and isopropyl) enter the active site in an almost instantaneous manner and form stable Mb-RNO adducts. Furthermore, the H64A Mb-RNO crystal structures show significant differences in ligand orientation within the distal-pocket as compared to wt Mb, indicating the importance of His64 in ligand coordination.

In Chapter 3, I extended my research with the same small RNOs (R = methyl, ethyl, and isopropyl), but I turned to Hb as my heme protein model. Previous research by others had demonstrated that the interactions of certain nitroso compounds to human Hb induces heme loss, which can cause health related problems such as anemia. However, the structural mechanism by which RNO binding leads to Hb degradation was unknown. In Chapter 3, through several unique X-ray crystal structures, I successfully determined the step-by-step mechanism of heme loss caused by RNO binding that leads to Hb degradation. These structures depict in detail, the chemistry occurring at the active site at the time of complex formation, as well as the global structural-changes that the protein undergoes as it progresses through the different stages that lead to heme loss.

Lastly, in Chapter 4, I investigated the influence of metal identity, and the importance of redox state of the macrocycle on Mb-RNO complex formation and stability. To do so, I removed Mb's natural heme and reconstituted the apo-protein with either cobalt-protoporphyrin IX or with chlorin (an Fe-containing reduced macrocycle). The reactions of the resultant CoMb and ChlMb species were studied with the same series of nitroalkanes (R = methyl, ethyl, propyl and isopropyl) as those discussed in Chapter 2 for comparison. Furthermore, I monitored the reactions of Mb with a series of nitrotoluenes to determine the extent to which the protein's heme-pocket can

accommodate these RNOs. Finally, in that chapter, I also characterized the reactions of human Hb with arylhydrazines, a different class of ligands also known to lead to Hb degradation.

Altogether, my work illustrates explicitly how RNOs, which are naturally occurring metabolites, bind to Mb and Hb and disrupt their function either by inhibiting the protein or damaging its structure.

1.6 References

1. Murayama, M., *The combining power of normal human hemoglobin for nitrosobenzene.* J Biol Chem, 1960. **235**: pp 1024-8.
2. Albrecht, W. and H.G. Neumann, *Biomonitoring of aniline and nitrobenzene. Hemoglobin binding in rats and analysis of adducts.* Arch Toxicol, 1985. **57**(1): pp 1-5.
3. Lee, C.H., et al., *Two cases of methemoglobinemia induced by the exposure to nitrobenzene and aniline.* Ann Occup Environ Med, 2013. **25**(1): p 31.
4. Arakawa, S., et al., *Methemoglobinemia induced by 1,2-dichloro-4-nitrobenzene in mice with a disrupted glutathione S-transferase Mu 1 gene.* Drug Metab Dispos, 2010. **38**(9): pp 1545-52.
5. Martinez, M.A., et al., *Acute nitrobenzene poisoning with severe associated methemoglobinemia: identification in whole blood by GC-FID and GC-MS.* J Anal Toxicol, 2003. **27**(4): pp 221-5.
6. Schimelman, M.A., J.M. Soler, and H.A. Muller, *Methemoglobinemia: nitrobenzene ingestion.* JACEP, 1978. **7**(11): pp 406-8.
7. Yi, J., et al., *Degradation of human hemoglobin by organic C-nitroso compounds.* Chem Commun (Camb), 2013. **49**(95): pp 11179-81.
8. Wang, B., et al., *Nitrosoamphetamine binding to myoglobin and hemoglobin: Crystal structure of the H64A myoglobin-nitrosoamphetamine adduct.* Nitric Oxide, 2017. **67**: pp 26-29.
9. Copeland, D.M., A.H. West, and G.B. Richter-Addo, *Crystal structures of ferrous horse heart myoglobin complexed with nitric oxide and nitrosoethane.* Proteins, 2003. **53**(2): pp 182-92.
10. Liu, D., K. Thomson, and A.C. Anderson, *Identification of nitroso compounds from biotransformation of 2,4-dinitrotoluene.* Appl Environ Microbiol, 1984. **47**(6): pp 1295-8.
11. Takeda, Y. and H. Kanaya, *Formation of nitroso compounds and mutagens from tranquilizers by drug/nitrite interaction.* Cancer Lett, 1981. **12**(1-2): pp 81-6.
12. Durchschein, K., et al., *Reductive biotransformation of nitroalkenes via nitroso-intermediates to oxazetes catalyzed by xenobiotic reductase A (XenA).* Org Biomol Chem, 2011. **9**(9): pp 3364-9.
13. Kalgutkar, A.S., et al., *A comprehensive listing of bioactivation pathways of organic functional groups.* Curr Drug Metab, 2005. **6**(3): pp 161-225.
14. Lee, J., et al., *Interactions of organic nitroso compounds with metals.* Chem Rev, 2002. **102**(4): pp 1019-66.
15. Gill, H.J., M.D. Tingle, and B.K. Park, *N-Hydroxylation of dapsone by multiple enzymes of cytochrome P450: implications for inhibition of haemotoxicity.* Br J Clin Pharmacol, 1995. **40**(6): pp 531-8.
16. Mitra, A.K., et al., *Metabolism of dapsone to its hydroxylamine by CYP2E1 in vitro and in vivo.* Clin Pharmacol Ther, 1995. **58**(5): pp 556-66.
17. Wright, J., A.K. Cho, and J. Gal, *The metabolism of amphetamine in vitro by rabbit liver preparations: a comparison of R(-) and S(+) enantiomers.* Xenobiotica, 1977. **7**(5): pp 257-66.
18. Cashman, J.R., et al., *N-oxygenation of amphetamine and methamphetamine by the human flavin-containing monooxygenase (form 3): role in bioactivation and detoxication.* J Pharmacol Exp Ther, 1999. **288**(3): pp 1251-60.

19. Mansuy, D., et al., *The nature of the "455 nm absorbing complex" formed during the cytochrome P450 dependent oxidative metabolism of amphetamine.* Biochem Pharmacol, 1976. **25**(5): pp 609-12.
20. Franklin, M.R., *The formation of a 455 nm complex during cytochrome P-450-dependent N-hydroxyamphetamine metabolism.* Mol Pharmacol, 1974. **10**: pp 975-985.
21. Mahy, J.P. and D. Mansuy, *Formation of prostaglandin synthase-iron-nitrosoalkane inhibitory complexes upon in situ oxidation of N-substituted hydroxylamines.* Biochemistry, 1991. **30**(17): pp 4165-72.
22. Harrison, J.H., Jr. and D.J. Jollow, *Contribution of aniline metabolites to aniline-induced methemoglobinemia.* Mol Pharmacol, 1987. **32**(3): pp 423-31.
23. Miller, A.M. and A.A. Yunis, *Nitroso-chloramphenicol: cell cycle specificity of action.* Pharmacology, 1982. **24**(2): pp 61-6.
24. Yunis, A.A., et al., *Nitroso-chloramphenicol: possible mediator in chloramphenicol-induced aplastic anemia.* J Lab Clin Med, 1980. **96**(1): pp 36-46.
25. Smith, D.J. and R.C. Anderson, *Toxicity and metabolism of nitroalkanes and substituted nitroalkanes.* J Agric Food Chem, 2013. **61**(4): pp 763-79.
26. Nepali, K., H.Y. Lee, and J.P. Liou, *Nitro-Group-Containing Drugs.* J Med Chem, 2019. **62**(6): pp 2851-2893.
27. Hata, Y., et al., *Aziridine biotransformation by microsomes and lethality to hepatocytes isolated from rat.* Chem Biol Interact, 1987. **63**(2): pp 171-84.
28. Shu, Y.Z., B.M. Johnson, and T.J. Yang, *Role of biotransformation studies in minimizing metabolism-related liabilities in drug discovery.* AAPS J, 2008. **10**(1): pp 178-92.
29. Boutros, J. and M. Bayachou, *Myoglobin as an efficient electrocatalyst for nitromethane reduction.* Inorg Chem, 2004. **43**(13): pp 3847-53.
30. Taxak, N., et al., *Metabolic-intermediate complex formation with cytochrome P450: theoretical studies in elucidating the reaction pathway for the generation of reactive nitroso intermediate.* J Comput Chem, 2012. **33**(21): pp 1740-7.
31. Maples, K.R., P. Eyer, and R.P. Mason, *Aniline-, phenylhydroxylamine-, nitrosobenzene-, and nitrobenzene-induced hemoglobin thiyl free radical formation in vivo and in vitro.* Mol Pharmacol, 1990. **37**(2): pp 311-8.
32. Alston T.A, P.J.T.D., Bright H.J., *Enzyme Inhibition by Nitro and Nitroso Compounds* Acc. Chem. Res., 1983. **16**: pp 418-424.
33. Mansuy, D., *Formation of reactive intermediates and metabolites: effects of macrolide antibiotics on cytochrome P-450.* Pharmacol Ther, 1987. **33**(1): pp 41-5.
34. Hanson, K.L., et al., *Sequential metabolism of secondary alkyl amines to metabolic-intermediate complexes: opposing roles for the secondary hydroxylamine and primary amine metabolites of desipramine, (s)-fluoxetine, and N-desmethyldiltiazem.* Drug Metab Dispos, 2010. **38**(6): pp 963-72.
35. Hollenberg, P.F., U.M. Kent, and N.N. Bumpus, *Mechanism-based inactivation of human cytochromes p450s: experimental characterization, reactive intermediates, and clinical implications.* Chem Res Toxicol, 2008. **21**(1): pp 189-205.
36. Kebamo, S. and S. Tesema, *The Role of Biotransformation in Drug Discovery and Development.* Journal of Drug Metabolism & Toxicology, 2015. **06**(05).
37. Ryter, S.W. and R.M. Tyrrell, *The heme synthesis and degradation pathways: role in oxidant sensitivity. Heme oxygenase has both pro- and antioxidant properties.* Free Radic Biol Med, 2000. **28**(2): pp 289-309.

38. Ponka, P., *Tissue-specific regulation of iron metabolism and heme synthesis: distinct control mechanisms in erythroid cells.* Blood, 1997. **89**(1): pp 1-25.
39. Ajioka, R.S., J.D. Phillips, and J.P. Kushner, *Biosynthesis of heme in mammals.* Biochim Biophys Acta, 2006. **1763**(7): pp 723-36.
40. Baureder, M. and L. Hederstedt, *Heme proteins in lactic acid bacteria.* Adv Microb Physiol, 2013. **62**: pp 1-43.
41. Lin, Y.W. and J. Wang, *Structure and function of heme proteins in non-native states: a mini-review.* J Inorg Biochem, 2013. **129**: pp 162-71.
42. Brucker, E.A., et al., *High resolution crystal structures of the deoxy, oxy, and aquomet forms of cobalt myoglobin.* J Biol Chem, 1996. **271**(41): pp 25419-22.
43. Phillips, S.E., *Structure and refinement of oxymyoglobin at 1.6 A resolution.* J Mol Biol, 1980. **142**(4): pp 531-54.

Chapter 2. Coordination of alkyl nitroso compounds with myoglobin: effect of ligand sterics on RNO binding and complex stability

2.1 Introduction

Mb is a heme-containing protein found in the muscle cells of most vertebrates. Historically, Mb is known for its vital function in O_2 storage, which is essential for tissue health and O_2 metabolism. Recently, other functions of Mb involving simple nitrogen oxides (NO_x) have been identified. For example, Mb has been reported to play a crucial role in the homeostasis of the cardiovascular system by acting as a NO scavenger [1-4]. Research also shows that Mb is metabolically competent to bind and reduce nitrite (NO_2) to NO [4-7]. However, binding of certain NO_x derivatives, such as nitroso (RNO, R = alkyl or aryl) compounds, can be deleterious to the protein.

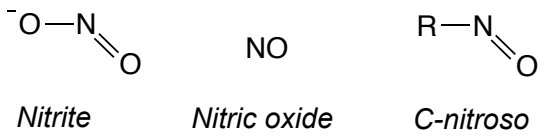

Figure 2.1 NO_x species known to interact with Mb.

C-Nitroso compounds are biologically relevant NO_x derivatives that are formed *in vivo* through the metabolic oxidation of amines (RNH_2) and hydroxylamines (RNHOH), or by the reduction of nitro-containing (RNO_2) compounds [8-12]. Once formed, RNO molecules have been reported to displace substrates from the heme pocket of certain metalloproteins and bind the iron center with a higher affinity than their natural ligands [13-15]. This Fe-RNO binding can often result in serious side-effects and health related problems [16-20]. For instance, decades of research show that binding of nitrosobenzene (PhNO) to hemoglobin (Hb) inhibits the protein, rendering it unable to transport oxygen [21, 22]. Ultimately, Hb-PhNO binding can lead to blood related

diseases such as methemoglobinemia and hemolytic anemia, which help explain some of the side-effects of associated with nitrobenzene poisoning [16, 23, 24]. Similarly, binding of certain RNOs to the heme-protein cytochrome P450 results in enzyme inhibition. The damaging effects of heme-nitroso interactions are well-documented, and a more detailed discussion was provided in Chapter 1.

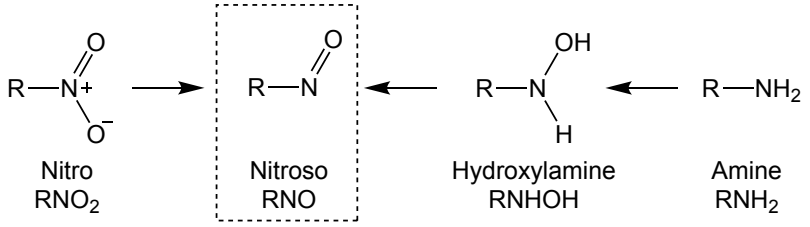

Figure 2.2 Left to right, reductive metabolism of nitro functional groups to nitroso products. Right to left, oxidative metabolism of amines and hydroxylamines to nitroso products.

Despite the negative physiological outcomes resulting from RNO binding to hemoproteins, only a few X-ray crystal structures have been published in the heme-nitroso binding state. In fact, to-date, only four Mb-RNO structures have been reported, all of which have been solved by the Richter-Addo research group. Both the N and O atoms of the RNO groups are basic sites that can, in principle, coordinate to metal centers. The N-binding mode is the most commonly observed mode of binding to date [25], although the O-binding mode has been reported in one case [26] (Figure 2.3). In 2003, Dr. Copeland obtained the structures of horse heart myoglobin (hhMb) in the ligand bound state with nitrosomethane (MeNO) and nitrosoethane (EtNO), then in 2007 the hhMb-PhNO structure was released [27, 28]. In all three instances, the ligand was N-bound to the Fe-atom with measured N-Fe distances of ~2.1 Å. Surprisingly, MeNO, EtNO, and PhNO had similar spatial conformations with respect to the heme-pocket regardless of size. In each case, the alkyl/aryl group was oriented towards the interior of the active site. Furthermore, larger RNOs were not expected to bind Mb due to its restricted active site volume. Then, in 2017, Drs. Wang

and Powell solved the structure of mutant H64A sperm whale myoglobin (swMb) liganded to nitrosoamphetamine (AmphNO) [13]. As observed with the hhMb analogues, AmphNO was also N-bound to the swMb heme with a measured N-Fe distance of 1.9 Å. Unlike the hhMb-RNO structures, however, H64A swMb-AmphNO revealed a distinct conformation in which the organic group was oriented towards the solvent region of the structure.

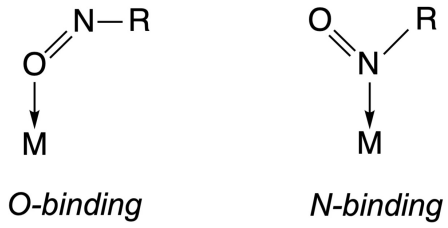

Figure 2.3 Possible Fe-RNO binding modes.

These X-ray crystal structures provided a great deal of information regarding the heme-nitroso chemistry resulting from RNO binding to Mb. However, they also raised some questions. First, while hhMb and swMb share ~88% sequence identity, it is unclear whether the organism from which Mb originated (hh or sw) influenced the RNO orientation. Alternatively, the observed differences in ligand coordination could have resulted from the H64A mutation. Therefore, the influence of ligand sterics on RNO binding remained unclear. The goal of the research presented in this chapter is to (i) determine the mode of RNO binding (O-bound *vs* N-bound), (ii) elucidate the importance of distal pocket amino acid composition on heme accessibility and ligand coordination, and (iii) determine the effects of ligand sterics on RNO binding and stability.

2.1.1 Protein models used in this study

To achieve my goals, I chose to work only with recombinant Mb proteins from sperm whale, this way I eliminated the organism variable. Mb is a small globular protein with a distal pocket composed mostly of hydrophobic residues, with two main exceptions (Figure 2.4A). First,

the proximal His93 located in the F-helix of the protein anchors the heme through an (His93)N^{ε}-Fe(heme) bond. The second exception is the distal His64 residue, which is located on the E-Helix and is situated directly at the entrance of the heme-pocket. His64 serves as a gatekeeper, in fact it is believed that the residue swings outward to grant ligands access to the heme [29-31]. Furthermore, His64 can also participate in H-bonding with Fe-bound substrates. To probe the importance of His64 on RNO entry into the active site and coordination within the heme pocket, I chose to monitor the reactions of wt and H64A swMb with a select group of nitroalkane precursors under reducing conditions. The H64A mutation is expected to remove the steric hindrance of His64 and allow Mb to accommodate larger RNOs as compared to the wt protein (Figure 2.4B). Furthermore, I expect the RNO molecules in the H64A mutant to have more dispersed spatial conformations with respect to the heme-pocket than in the wt swMb.

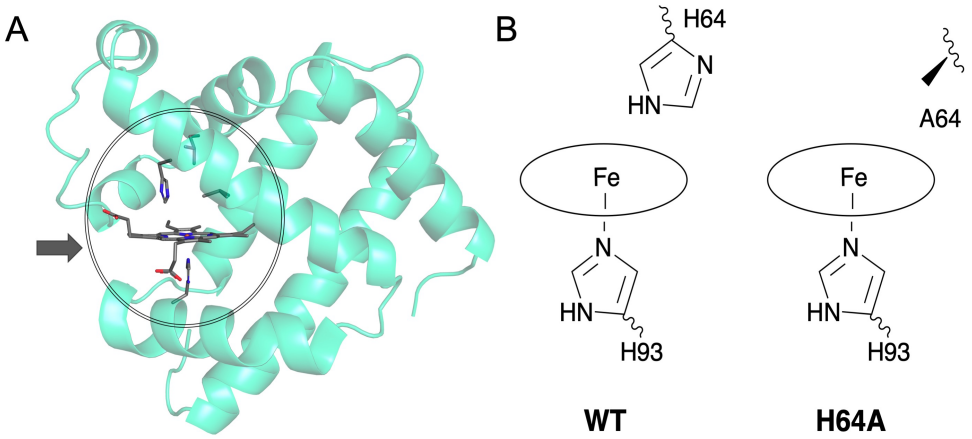

Figure 2.4. A) 3D structure of myoglobin with relevant heme-pocket residues shown. B) models of wt swMb and the H64A mutant.

2.1.2 Selection of RNO ligands

After choosing my protein models, careful consideration was taken in selecting RNO ligands for my systematic heme-nitroso studies. First, to remove the "metabolism" variable from my work, I chose to form all RNO ligands through the reductive pathway by utilizing nitro-

precursors as my starting material (Figure 2.5, left). Then, to gain insight into the effects of ligand sterics on RNO binding and complex stability, I chose nitroalkanes in which the alkyl group increased by a single methyl group at a time; i.e., R = Me, Et, and Pr. I also included the branched *i*PrNO$_2$ precursor into my study. Unlike the planar R group in the Mb-PhNO complex reported by Dr. Copeland, the *i*Pr group is expected to be less rigid. This means that *i*Pr can potentially bend/twist to fit within the active site, which can in turn alter heme-pocket amino acid residue conformation to facilitate binding. Therefore, this ligand would provide additional insight into the influence of ligands sterics on substrate binding and complex lifetime.

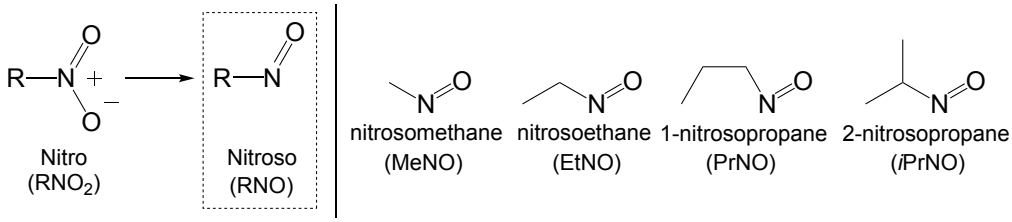

Figure 2.5 Reductive metabolism of nitro precursors (*left*) used to generate the RNO ligands for this study (*right*)

Finally, these small alkyl nitroalkane precursors were chosen in part for their biological relevance. Small nitroalkanes are toxic and have been classified as carcinogenic, neurotoxic and genotoxic. Due to their broad use, humans are frequently exposed to nitro-containing compounds [17, 32-34]. When nitroalkanes enter the blood stream, they can interact with different metalloproteins inside the body and can undergo bioactivation. For example, the 2-nitropropane ligand precursor from my series has been shown to undergo metabolic reduction in rats which ultimately results in liver damage [32, 35-37]. Likewise, from my series of RNOs, MeNO has been identified as an inhibitory ligand resulting from the catalytic conversion of aziridine based antitumor drugs [38]. Due to the increased health associated risks of the selected RNOs, it is crucial

to thoroughly characterize their reactions with Mb and to obtain three-dimensional models of the RNO-bound protein complexes.

My approach is relatively straight forward in concept, but not easy to achieve in practice. I used UV-vis spectroscopy to monitor the reactions of wt and H64A Mb with a series of nitroalkanes of increasing alkyl group size (R = Me, Et, Pr, *i*Pr). Then, I further characterized the products of those reactions using X-ray crystallography. The results of my reactivity studies uncovered several patterns in the extent of formation of the Mb-RNO derivatives and the lifetime of each protein-ligand complex. Furthermore, my structural biology efforts resulted in seven distinct high-resolution X-ray crystal structures of the Mb models in the heme-nitroso bound state.

2.2 Materials and Methods

2.2.1 Cloning of swMb mutants

The recombinant wild-type sperm whale myoglobin (wt swMb) plasmid (pET-28a-wt) was a generous gift by Dr. Mario Rivera from the University of Kansas. The wt swMb protein expressed from this plasmid has two differences in the peptide sequence as compared to native wt swMb; i) an additional Met residue at the N-terminus due to expression in *E. coli,* and ii) an unintended D122N mutation [39].

The H64A mutant used here was engineered in our lab by Dr. Bing Wang using the Quick-Change method by Stratagene. The resulting plasmid was transformed into *E. coli* DH5α competent cells, and the mutation was confirmed by DNA sequencing at the Oklahoma Medical Research Foundation (OMRF) sequencing facility.

2.2.2 Expression and purification of swMb proteins

Wild-type and H64A sperm whale myoglobins were expressed in *E. coli* BL21 (DE3) cells and purified as described by Springer and Sligar [40] with a few modifications as described by Wang [4]. Cell lysis and protein purification steps were performed at 4 °C. Briefly, cells were resuspended in lysis buffer (50 mM Tris-HCl, 1 mM EDTA, 1 mM PMSF, pH 7.4) and lysed using an Avestin C3 EmulsiFlex homogenizer. Then, the lysate was clarified by centrifugation followed by two rounds of ammonium sulfate (AS) precipitation. In the first round of precipitation, 60% AS was used to remove most of the unwanted proteins from the supernatant. Subsequently, 95% AS was used to precipitate the desired swMb. The isolated swMb was resuspended and dialyzed overnight in low salt buffer (100 mM potassium phosphate, 40 mM NaCl, pH 6.0) to remove excess ammonium sulfate.

After dialysis, the resulting protein sample was loaded into a CM-52 cellulose (Whatman) cation exchange column and the protein was eluted using a linear salt gradient from 40 mM to 1 M NaCl (in 100 mM potassium phosphate buffer, pH 6.0). Purification of swMb from *E. coli* cells often results in a mixture of apo and heme-bound protein. In order to ensure a homogeneous mixture, the fractions collected from the CM-52 column step, which contained the least amount of contaminating proteins (as determined by SDS-PAGE), were pooled together and reconstituted by adding excess heme (15 mM dissolved in 0.1 M NaOH) and stirred overnight.

As the final purification step, the reconstituted protein sample was centrifuged and applied to a G75 gel filtration column (Sigma; 20 mM Tris-HCl, 1 mM EDTA, pH 7.4). Fractions containing the desired protein with no visible contaminating proteins (as determined by SDS-PAGE) were pooled together and concentrated to either ~20 mg/mL (hanging drop) or ~60 mg/mL (batch method) for crystallization. The protein concentrations of both wt and H64A swMb were calculated using the extinction coefficient of ferric Mb^{III}-H_2O at the Soret peak (λ_{max} 408 nm; ε = 188 $mM^{-1}cm^{-1}$).

2.2.3 UV-vis spectroscopy studies of wt and H64A swMb adduct formation with nitrosoalkanes (MeNO, EtNO, PrNO and iPrNO)

UV-vis spectroscopy experiments were performed using a Hewlett Packard 8453 diode array spectrophotometer. The reactions were carried out in 3.5 mL quartz cuvettes equipped with screw caps (Starna Cells).

Formation of the $swMb^{II}$-RNO complexes were determined using similar reaction conditions as described by Mansuy [9] for the related horse heart Mb (hhMb) derivatives. First, 3 μM of either wt or H64A ferric $swMb^{III}$-H_2O (purified as described above) were added into a cuvette containing 3 mL of 0.1 M phosphate buffer at pH 7.4, and the spectrum for the ferric

protein was recorded. Sodium dithionite was added as a reducing agent to a final concentration of 20 mM, and the spectrum of the resulting ferrous sw deoxyMb^{II} was recorded. Once the protein was in its ferrous state, each ligand precursor ($MeNO_2$, $EtNO_2$, $PrNO_2$ or *i*$PrNO_2$; half diluted in MeOH) was added into the reaction mixture to a final concentration of 20 mM. At this point, the reactions were monitored at regular time intervals for 1 h.

2.2.3.1 Time-course and extent of formation

The extent of formation for each ferrous swMb^{II}-RNO (R= Me, Et, Pr, *i*Pr) complex as a function of time was determined by calculating the difference between the absorbance for the product complex (Soret λ_{max} ~424 nm) and the apparent isosbestic point (λ 460 nm; used as baseline reference). The resulting A_{424}-A_{460} value was then plotted as a function of time.

2.2.3.2 Ligand dissociation upon oxidation via ferricyanide

First, the ferrous swMb^{II}-RNO derivatives were formed as described above. Excess sodium dithionite was then removed by passing the reaction mixture through a 5 mL Sephadex G25 column. An aliquot of the resulting ligand-bound protein was then transferred into a 3.5 mL quartz cuvette containing 3 mL of 100 mM potassium phosphate buffer (pH 7.4 or 6.0), and the spectrum was recorded to confirm the formation of the ferrous swMb^{II}-RNO complex (λ_{max} ~424 nm). Ligand dissociation was achieved by the addition of 1-6 μL of 30 mg/mL potassium hexacyanoferrate (III) (a.k.a. ferricyanide) as determined by the reappearance of the Soret band corresponding to ferric swMb^{III}-H_2O (λ_{max} 408 nm). Oxidation and resultant ligand dissociation were observed for H64A ferrous swMb^{II}-RNO upon addition of ferricyanide at pH 7.4. On the other hand, only partial oxidation/dissociation (as indicated by peaks at both λ 408 and 424 nm)

were observed for ferrous wt swMb^{II}-RNO at pH 7.4. However, at pH 6.0, complete oxidations were observed for ferrous wt swMb^{II}-RNO upon ferricyanide addition.

2.2.4 Crystallization of ferric wt swMb^{III}-H$_2$O and preparation of crystals of the ferrous Mb^{II}-RNO (MeNO, EtNO and PrNO) derivatives

2.2.4.1 Crystallization of ferric wt swMb^{III}-H$_2$O

Ferric wt swMb^{III}-H$_2$O was crystallized using the hanging drop vapor diffusion method as described by Phillips [41] and Wang [4, 42] with slight modifications. Briefly, a droplet of 5 μL of wt swMb^{II}-H$_2$O at 20 mg/mL (as determined by absorbance at λ_{max} 408 nm) was placed on a cover slip and mixed with an equal volume of well solution containing 2.56-3.20 M AS, 100 mM Tris-HCl, 1 mm EDTA, at pH 7.4. The resulting mixture was allowed to equilibrate at 20 °C over the well buffer for approximately 8-10 h before seeding with crushed H64A swMb crystals. Brown hexagonal shaped crystals formed after approximately 5 d.

2.2.4.2 Preparation of crystals of the ferrous wt swMb^{II}-MeNO and -EtNO derivatives

Suitable sized hexagonal crystals of ferric wt swMb^{III}-H$_2$O were looped into a 100 μL drop of cryoprotectant solution (3.1 M AS, 100 mM Tris-HCl, 1 mm EDTA, 10% glycerol, pH 7.4) and covered with light mineral oil to prevent drying out. Then, 2.5 μL of the organic MeNO$_2$ or EtNO$_2$ precursors (half diluted in MeOH) were added into the droplet and allowed to soak for 1-2 h. Solid sodium dithionite was added into the droplet, grain by grain, until a color change from brown to pink was observed. At that point, the reaction was monitored every 30 min by dissolving one of the product crystals in a 2 μL drop of 100 mM potassium phosphate buffer at pH 7.4 and recording its UV-vis spectrum on a Take3 plate using a Synergy HTX multi-mode reader (BioTek®). The Soret peak at λ_{max} 408 nm fully shifted to λ_{max} 424 nm over a 1 h period, indicating that the ferrous

wt swMb^{II}-MeNO and -EtNO products had formed. At this point, the crystals remaining in the droplet were harvested and flash frozen in liquid nitrogen prior to X-ray diffraction data collection.

2.2.4.3 Co-crystallization of the ferrous wt swMb^{II}-PrNO derivative

The ferrous wt swMb^{II}-PrNO complex was formed anaerobically (in an MBraun anaerobic chamber) by incubating 100 μL of ferric wt swMb^{III}-H_2O at 20 mg/mL with 0.5 μL of $PrNO_2$ (half diluted in MeOH) for 1 h, followed by the addition of excess solid sodium dithionite (a few mg) for another hour. Once the reaction was complete, as judged by UV-vis spectroscopy, the complex was crystallized as described previously for ferric wt swMb^{III}-H_2O, with the exception that crystallization was done anaerobically. Suitable sized hexagonal crystals grew in approximately one week. Crystals were looped outside the anaerobic chamber in an argon bath to minimize exposure to air, cryoprotected and flash frozen in liquid nitrogen prior to X-ray diffraction data collection.

2.2.5 Co-crystallization of the ferrous H64A swMb^{II}-RNO (MeNO, EtNO, PrNO and iPrNO) adducts

The four ferrous H64A swMb^{II}-RNO complexes described here were prepared similarly; each complex was formed anaerobically in solution prior to anaerobic co-crystallization (in an MBraun anaerobic chamber). First, 85-100 μL of ~60-70 mg/mL ferric H64A swMb^{III}-H_2O in 20 mM Tris-HCl, 1 mm EDTA, pH 7.4 were mixed with 2-5 μL of the respective nitroalkane (half diluted in methanol) for 15-30 min. Then, solid sodium dithionite was slowly added until the solution changed color from brown to pink, at which point the reaction was allowed to proceed for another 30 min. The solution was deemed ready for crystallization, once the formation of the λ_{max} 424 nm peak, indicative of H64A swMb^{II}-RNO complex formation, was confirmed using UV-vis

spectroscopy. The batch method was used for co-crystallization, as described by Phillips [41] and Wang [43]. Briefly, 10 μL of the newly-formed ferrous H64A swMb^{II}-RNO solution was mixed with different amounts of crystallization buffer (3.20 M AS, 100 mM Tris-HCl, 1 mm EDTA, pH 7.4) to obtain a range of final concentrations between 2.3-2.6 M AS. Hexagonal or thin plate crystals grew after 2-3 d of anaerobic incubation. The sealed anaerobic vials containing the crystals were transferred to the main lab area and opened under argon, where the crystals were transferred into a 20 μL droplet of cryosolution (3.1 M AS, 100 mM Tris-HCl, 1 mM EDTA, 10% glycerol, pH 7.4) and covered with light mineral oil to minimize exposure to air. The ferrous H64A swMb^{II}-RNO crystals were then looped (also under argon), flash frozen in liquid nitrogen, and mounted directly onto the goniometer for X-ray diffraction data collection. Notably, the ferrous H64A swMb^{II}-RNO crystals that were exposed to air returned to the ferric state (indicated by reappearance of a peak at λ_{max} 408 nm) within 24 h, while crystals not exposed to air maintained their λ_{max} 424 nm peak for several weeks.

2.2.6 X-ray data collection

Diffraction data were collected in-house using a Rigaku MicroMax 007HF microfocus X-ray generator equipped with a set of VariMax HF X-ray optics coupled to a Dectris Pilatus 200K silicon pixel detector. The data were collected at 100 K with CuKα radiation (λ = 1.54178 Å) from the generator operated at 40 kV/30 mA.

2.2.7 Data processing, structure solution and refinement

The diffraction data collected were indexed, integrated and scaled using HKL3000R [44]. Then the computed *sca* files were converted into *mtz* files using scalepack2mtz (CCP4) [45]. Initial phases were calculated by molecular replacement via PHASER MR (CCP4). The model used for

molecular replacement was H64A swMb-tolyl (PDB accession code 5ILE, at a resolution of 1.77 Å) with the heme, waters and tolyl ligand removed from the structure. All structure refinements were performed using *Refmac5* (CCP4) [46] and the models were rebuilt using *COOT* [47]. The final structures were checked for unusual residue conformations and contacts using *MolProbity* [48].

Figures were created using *PyMOL* unless otherwise noted. The $2F_o$-F_c electron density maps were calculated by *Fast Fourier Transform* (*FFT*) in the CCP4 software package. The resulting *map* files were viewed in *PyMOL*. To generate the F_o-F_c electron density maps, the RNO ligands were first removed from the active site of the final *pdb* file and then processed though *Refmac5* (CCP4) to create a new F_c *mtz* file. Next, the output F_c *mtz* file was input into *FFT* to generate the F_o-F_c electron density *map* file which was in turn displayed in *PyMOL.*

2.2.7.1 Ferrous wt swMb^{II}-MeNO

Ten initial cycles of restrained refinement were run with *Refmac5*, and the R factor decreased from 0.4507 to 0.3171. Heme, MeNO, and waters were added to the model based on the F_o-F_c electron density map in the successive refinement cycles. Three sulfate ions, and two MeNO ligands were added using *COOT*. The MeNO bound to the Fe heme was modeled at 100% occupancy, while the MeNO ligand in the Xe-1 pocket was modeled at 50% occupancy. Residue Met0 was omitted from the structure due to lack of electron density. Two conformations were modeled with 50% occupancy each for the sidechains Val21 and Glu109. The final model was refined to a resolution of 1.76 Å, with an R factor of 0.1358 and R_{free} of 0.1719.

2.2.7.2 Ferrous wt swMb^{II}-EtNO

Ten initial cycles of restrained refinement were run with *Refmac5*, and the R factor decreased from 0.4471 to 0.3134. Heme, EtNO, and waters were added to the model based on the F_o-F_c electron density map in the successive refinement cycles. Five sulfate ions, one EtNO ligand, and a Cl^- ion were added using *COOT*. The EtNO ligand bound to the heme iron was modeled at 100% occupancy. Residue Met0 was omitted from the structure due to lack of electron density. Two conformations were modeled with 50% occupancy each for the sidechain Val21. The final model was refined to a resolution of 1.76 Å, with an R factor of 0.1599 and R_{free} of 0.1908.

2.2.7.3 Ferrous wt swMb^{II}-PrNO

Ten initial cycles of restrained refinement were run with *Refmac5*, and the R factor decreased from 0.3400 to 0.2855. Heme, PrNO, and waters were added to the model based on the F_o-F_c electron density map in the successive refinement cycles. Four sulfate ions, one PrNO ligand, and a Na^+ ion were added using *COOT*. The PrNO ligand bound to the heme iron was modeled at 100% occupancy. Residue Met0 was omitted from the structure due to lack of electron density. Two conformations were modeled with 50% occupancy each for the sidechain Lys133. The final model was refined to a resolution of 2.0 Å, with an R factor of 0.1734 and R_{free} of 0.2052.

2.2.7.4 Ferrous H64A swMb^{II}-MeNO

Ten initial cycles of restrained refinement were run with *Refmac5*, and the R factor decreased from 0.4595 to 0.3233. Heme, MeNO, and waters were added to the model based on the F_o-F_c electron density map in the successive refinement cycles. One sulfate ion, and one MeNO ligand were added using *COOT*. The MeNO bound to the Fe heme was modeled at 100% occupancy. Residues Met0, Gln152 and Gly153 were omitted from the structure due to lack of

electron density. Two conformations were modeled with 50% occupancy each for the sidechains of Ser35, Val68 and Tyr151. The final model was refined to a resolution of 1.75 Å, with an R factor of 0.1540 and R_{free} of 0.2002.

2.2.7.5 Ferrous H64A swMb^{II}-EtNO

During molecular replacement with PHASER MR (CCP4), two swMb molecules per asymmetric unit were identified. Ten initial cycles of restrained refinement were run with *Refmac5*, and the R factor decreased from 0.3809 to 0.2939. Heme, EtNO, and waters were added to the model based on the F_o-F_c electron density map in the successive refinement cycles. Four sulfate ions, and two EtNO ligands were added using *COOT*. The EtNO found in the active site of Chain A was modeled in at 100% occupancy, while the EtNO ligand in the active site of Chain B was modeled in at 60% occupancy with H_2O bound at the Fe center at 40% occupancy. No residues were omitted due to lack of electron density in either Chain A or B. Two conformations were modeled with 50% occupancy each for the Glu59 sidechain in Chain A. The final model was refined to a resolution of 1.8 Å, with an R factor of 0.1740 and R_{free} of 0.2240.

2.2.7.6 Ferrous H64A swMb^{II}-PrNO

Ten initial cycles of restrained refinement were run with *Refmac5*, and the R factor decreased from 0.2896 to 0.2726. Heme, PrNO, and waters were added to the model based on the F_o-F_c electron density map in the successive refinement cycles. Four sulfate ions and one PrNO ligand, were added using *COOT*. The PrNO ligand bound to the heme iron was modeled at 100% occupancy. Residue Met0 was omitted from the structure due to lack of electron density. The final model was refined to a resolution of 1.75 Å, with an R factor of 0.1602 and R_{free} of 0.1884.

2.2.7.7 Ferrous H64A swMb^{II}-iPrNO

Ten initial cycles of restrained refinement were run with *Refmac5*, and the R factor decreased from 0.3040 to 0.2847. Heme, *i*PrNO, and waters were added to the model based on the F_o-F_c electron density map in the successive refinement cycles. Three sulfate ions and one *i*PrNO ligand were added using *COOT*. The *i*PrNO ligand bound to the heme iron was modeled at 100% occupancy. Residue Met0 was omitted from the structure due to lack of electron density. The final model was refined to a resolution of 1.8 Å, with an R factor of 0.1967 and R_{free} of 0.2298.

2.3 Results

2.3.1 Expression and purification of swMb proteins

Both wt and H64A swMb were expressed in *E. coli* cells; typically, 4 L cell cultures were used to obtain sufficient protein yields. Protein purifications were performed using a three-step process which started with ammonium sulfate precipitation, followed by ion exchange chromatography and concluded with G75 gel filtration (see methods section *2.2.2*). The gel filtration eluent was collected in fractions which were then separated and analyzed by gel electrophoresis. On average, the final swMb proteins were visually determined to be ~99% pure (as determined by SDS-PAGE; Figure 2.6). Each round of purification resulted in ~1.5–2.0 mL of highly pure protein at a final concentration of ~20 mg/mL. Aliquots of the purified proteins were used for crystallization immediately, and the bulk quantities were stored at 4 °C for later use. Crystal trays set with freshly purified protein yielded better results, especially for wt swMb.

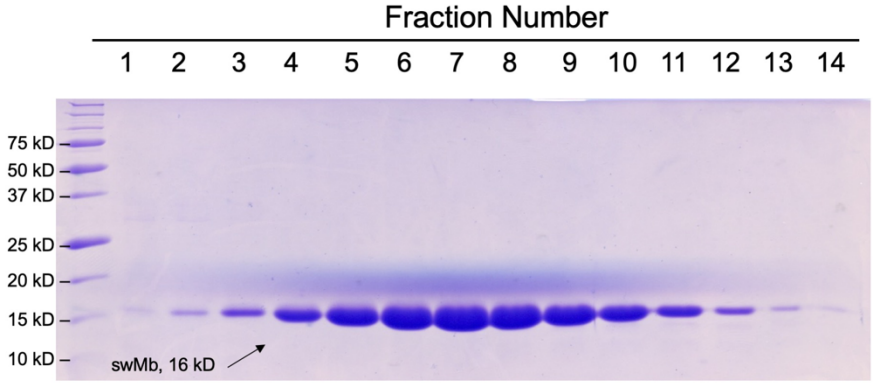

Figure 2.6. Representative wt swMb SDS-PAGE gel showing elution fractions from the last purification step, G75 gel filtration column chromatography. Similar protein purity was observed for swMb H64A.

2.3.2 UV-vis spectroscopy studies of wt and H64A swMb adduct formation with nitrosoalkanes (MeNO, EtNO, PrNO and iPrNO)

2.3.2.1 UV-vis characterization of wt swMb^{II}-RNO derivatives

The aerobic reactions of wt swMb with nitroalkanes, in a reducing environment, were performed using similar reaction conditions as that of Mansuy [9] and Yi [49] for the related horse heart (hh) myoglobin with nitroalkanes, and monitored by UV-vis spectroscopy. For the reaction between ferrous hh deoxyMb^{II} with RNOs (R = alkyl), Mansuy reported a peak shift in the Q-region of the UV-vis spectrum from λ 560 to 547 nm, and a shift in the Soret band from λ 435 to 425 nm. My reactions with dithionite-reduced Mb resulted in similar spectral shifts. For the reaction between ferrous wt sw deoxyMb^{II} and $MeNO_2$, I observed a spectral shift in the Q-region from λ 558 to 547 nm with a shoulder appearing at λ 580 nm upon ligand binding. Also in accord with Mansuy's results, the same reaction resulted in the disappearance of the λ_{max} 433 nm Soret band and appearance of a new peak at λ_{max} 424 nm, indicating the formation of the ferrous swMb^{II}-MeNO complex (Figure 2.7A). These trends were similar for the reactions of ferrous wt sw deoxyMb^{II} with all four ligands studied (MeNO, EtNO, PrNO, *i*PrNO) regardless of size and sterics (Figure 2.7A-D).

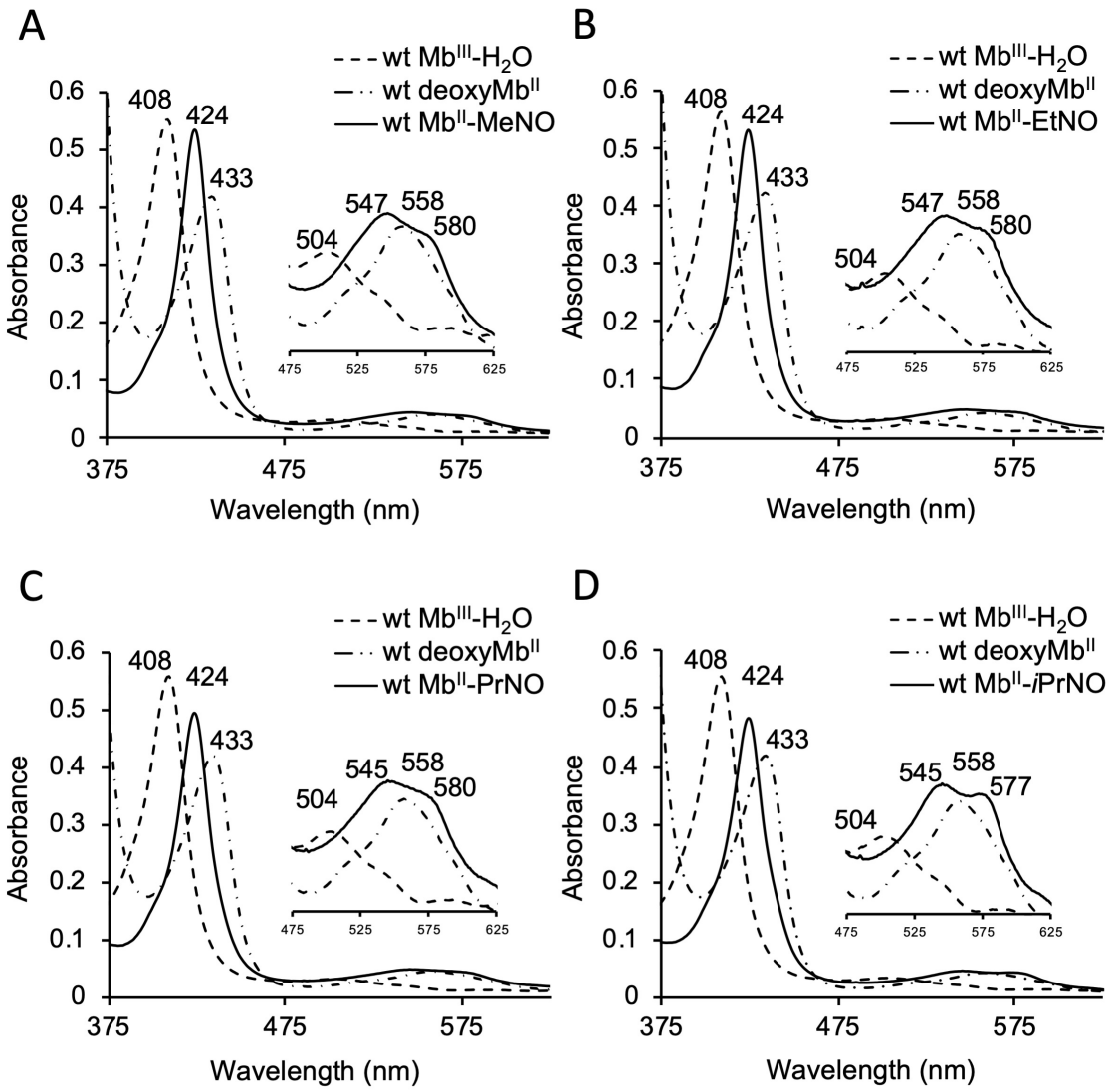

Figure 2.7. UV-vis spectral characterization of the reduction of ferric wt swMb^{III}-H$_2$O by dithionite, followed by the reaction of the resulting ferrous wt sw deoxyMb^{II} with the nitroalkane precursors to form the respective ferrous wt swMb^{II}-RNO adducts. A) wt swMb^{II}-MeNO, B) wt swMb^{II}-EtNO, C) wt swMb^{II}-PrNO, and D) wt swMb^{II}-*i*PrNO. Final reaction conditions: 3 μM wt swMb, 0.1 M phosphate buffer (pH 7.4), 20 mM dithionite, 20 mM RNO$_2$.

To further analyze the progress of each reaction, I recorded the absorbance at λ_{max} 424 nm, which corresponds to the Soret band of the ferrous wt swMb^{II}-RNO complex, and subtracted the absorbance corresponding to the apparent isosbestic point at λ 460 nm. I then plotted the A_{424}-A_{460} difference as a function of time. This difference plot allowed us to determine the trends in extent of formation (which is the maximum height of the trendline in the plot) and the apparent rate of formation (which I define as the time it takes for each reaction to reach the extent of formation plateau) for each ferrous wt swMb^{II}-RNO adduct. According to the data obtained, the smaller RNOs reached a higher extent of formation and at a much faster time, while lower extents of formation were observed for larger ligands with a slower apparent rate of formation (Figure 2.8). For example, ferrous wt swMb^{II}-MeNO reached an extent of formation of 0.51 in only 4 min. Following this trend, addition of one methyl group to the ligand decreased the extent of formation of ferrous wt swMb^{II}-EtNO to 0.49 and also decreased its rate of formation to 12 min. Interestingly, there was no difference in the apparent rate of formation between the ferrous wt swMb^{II}-EtNO and -PrNO derivatives. However, the extent of formation for the latter was observed to be slightly lower at only 0.46. Finally, wt swMb^{II}-*i*PrNO took 25 min to reach a maximum extent of formation of ~0.45. These results indicate that larger and bulkier ligands may have a difficulty entering the active site of wt swMb due to the increased steric hindrance provided by the distal His64 residue.

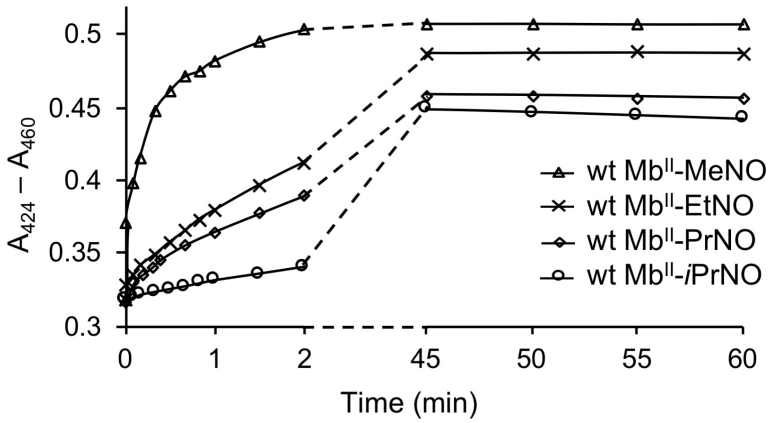

Figure 2.8. Extent of formation for each $swMb^{II}$-RNO complex determined by plotting the difference between the absorbances at λ_{max} 424 and λ 460 nm as a function of time. Absorbance at λ_{max} 424 nm is indicative of the $swMb^{II}$-RNO complex, and the absorbance at λ 460 nm corresponds to the apparent isosbestic point.

2.3.2.2 UV-vis characterization of ferrous H64A swMb^{II}-RNO derivatives

To properly assess the influence of the distal pocket His64 residue on ligand sterics and ferrous $swMb^{II}$-RNO complex stability, the aerobic reactions of mutant H64A swMb with alkyl-RNOs were performed using the same reaction conditions that were used for wt swMb (as described in methods, section *2.2.3*). The reactions of ferrous H64A sw deoxyMb^{II} with the RNO_2 precursors resulted in similar spectral shifts to those of wt swMb, but with minor differences. For example, the reaction between ferrous H64A sw deoxyMb^{II} with $MeNO_2$ resulted in the disappearance of the Soret λ_{max} 433 nm peak and the appearance of a new peak at λ_{max} 424 nm (Figure 2.9A), indicating the formation of ferrous H64A $swMb^{II}$-MeNO. Simultaneously, the major band in the Q-region shifted from λ 559 to 544 nm with a second (but broad) band appearing in the range of λ 504 -580 nm. Interestingly, while similar spectral shifts were observed in the Soret band for the larger ligands tested (EtNO, PrNO, *i*PrNO), their spectra revealed more defined peaks in the Q-region at λ ~542 and570 nm (Figure 2.9B-D).

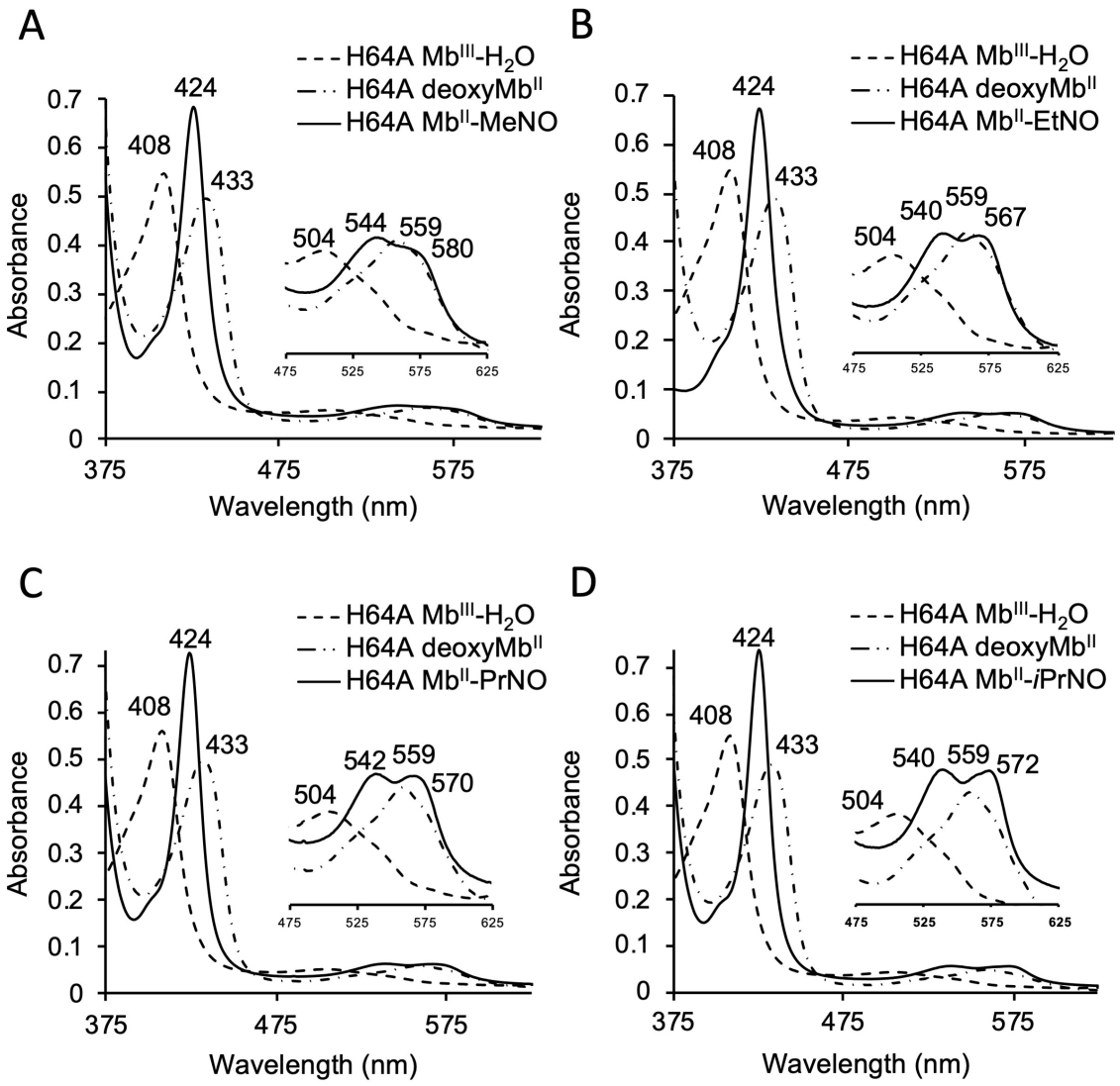

Figure 2.9. UV-vis spectral characterization of the reduction of ferric H64A swMb^{III}-H$_2$O by dithionite, followed by the reaction of ferrous H64A sw deoxyMb^{II} with the nitroalkane precursors to form the respective ferrous H64A swMb^{II}-RNO adducts. A) H64A swMb^{II}-MeNO, B) H64A swMb^{II}-EtNO, C) H64A swMb^{II}-PrNO, and D) H64A swMb^{II}-*i*PrNO. Final reaction conditions: 3 μM H64A swMb, 0.1 M phosphate buffer (pH 7.4), 20 mM dithionite, 20 mM RNO$_2$.

In contrast to the steadily increasing and "smooth curve" representing the reaction time-course for the formation of wt the swMb^{II}-RNOs (Figure 2.8), the reaction time-courses for the formation of the H64A adducts revealed that the reactions were quite rapid. The first major difference noted is that each of the four analogous H64A swMb^{II}-RNO (-MeNO, -EtNO, -PrNO and *i*-PrNO) derivatives reached a maximum extent of formation within the first absorption reading (< 5s; Figure 2.10). This suggests that the apparent rate of formation for all complexes is not affected by ligand sterics, since all formed in less than ~5 s after ligand addition. Equally important, these initial extents of formation were observed to plateau after ~15-20 min.

Although the apparent rate of formation was not observed to be influenced by ligand sterics, a relationship between size of ligand and extent of formation was observed. The bulker ligands reached a higher extent of formation than the smaller ones. For instance, the complex with my smallest ligand, ferrous H64A swMb^{II}-MeNO, had the lowest initial apparent extent of formation of only 0.61, which plateaued to 0.57 (Figure 2.10). The complex with a slightly bulkier ligand, ferrous swMb^{II}-EtNO, reached an initial extent of formation of 0.65 which leveled off to 0.60. Following in that trend, the H64A swMb^{II}-PrNO complex reached an initial extent of formation of only 0.66 and leveled off to 0.64. Finally, ferrous swMb^{II}-*i*PrNO reached an initial extent of formation of 0.67 which decreased and leveled off to 0.65. These results indicate that smaller ligands may have an easier time diffusing out of the active site, while larger more hydrophobic ligands may have a higher net affinity for the active site.

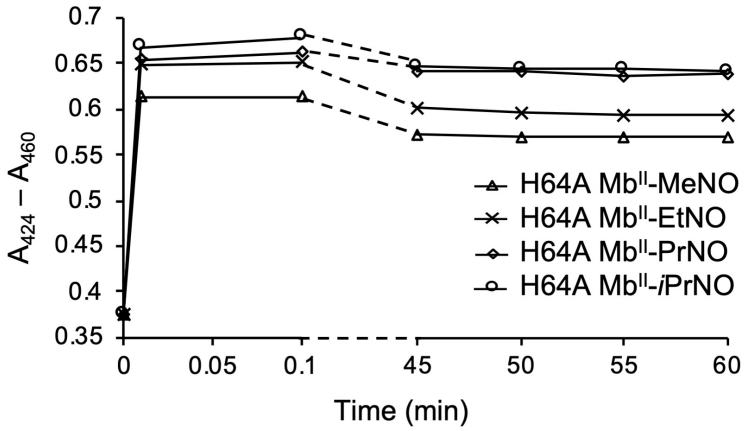

Figure 2.10. Extent of formation for each ferrous H64A swMb^{II}-RNO complex determined by plotting the difference between absorbance at λ_{max} 424 and λ 460 nm as a function of time. The absorbance at λ_{max} 424 nm is indicative of ferrous H64A swMb^{II}-RNO complex, and that at λ 460 nm corresponds to the apparent isosbestic point.

Table 2-1 summarizes the data from each reaction that reflects the importance of ligand sterics and the involvement of the distal pocket His64 residue on the extent and apparent relative rate of formation of each ferrous swMb^{II}-RNO product.

Table 2-1. Summary of the extent and time to reach maximum extent of formation for each wt and H64A ferrous swMb^{II}-RNO adducts

RNO	Ferrous wt swMb^{II}-RNOs		Ferrous H64A swMb^{II}-RNOs	
	Maximum extent of formation (A_{424}-A_{460})	Time to reach max extent of formation (min)	Maximum extent of formation (A_{424}-A_{460})	Time to reach max extent of formation (min)
-MeNO	0.51	4	0.61	< 0.1
-EtNO	0.49	12	0.65	< 0.1
-PrNO	0.46	12	0.66	< 0.1
-*i*PrNO	0.45	25	0.67	< 0.1

2.3.2.3 Ferrous wt swMb^{II}-RNO ligand dissociation upon oxidation by ferricyanide

Oxidation of each ferrous wt swMb^{II}-RNO complex using the oxidant potassium hexacyanoferrate (III) resulted in the generation of UV-vis spectral features corresponding to the formation of ferric swMb^{III}-H_2O (Figure 2.11A-D). This confirmed the oxidation state of iron in the Mb-RNO derivatives as Fe^{II}, which could be oxidized to Fe^{III} and result in the expulsion of the RNO ligand. It is important to note that the time it took for the products to convert back to their ferric form was dependent on ligand size. Larger ligands dissociated within a few minutes, while MeNO took a few hours to dissociate. Even then, in the case of wt swMb^{II}-MeNO, there remained a faint shoulder at λ_{max} 424 nm, indicating incomplete oxidation and dissociation of the ligand (Figure 2.11A).

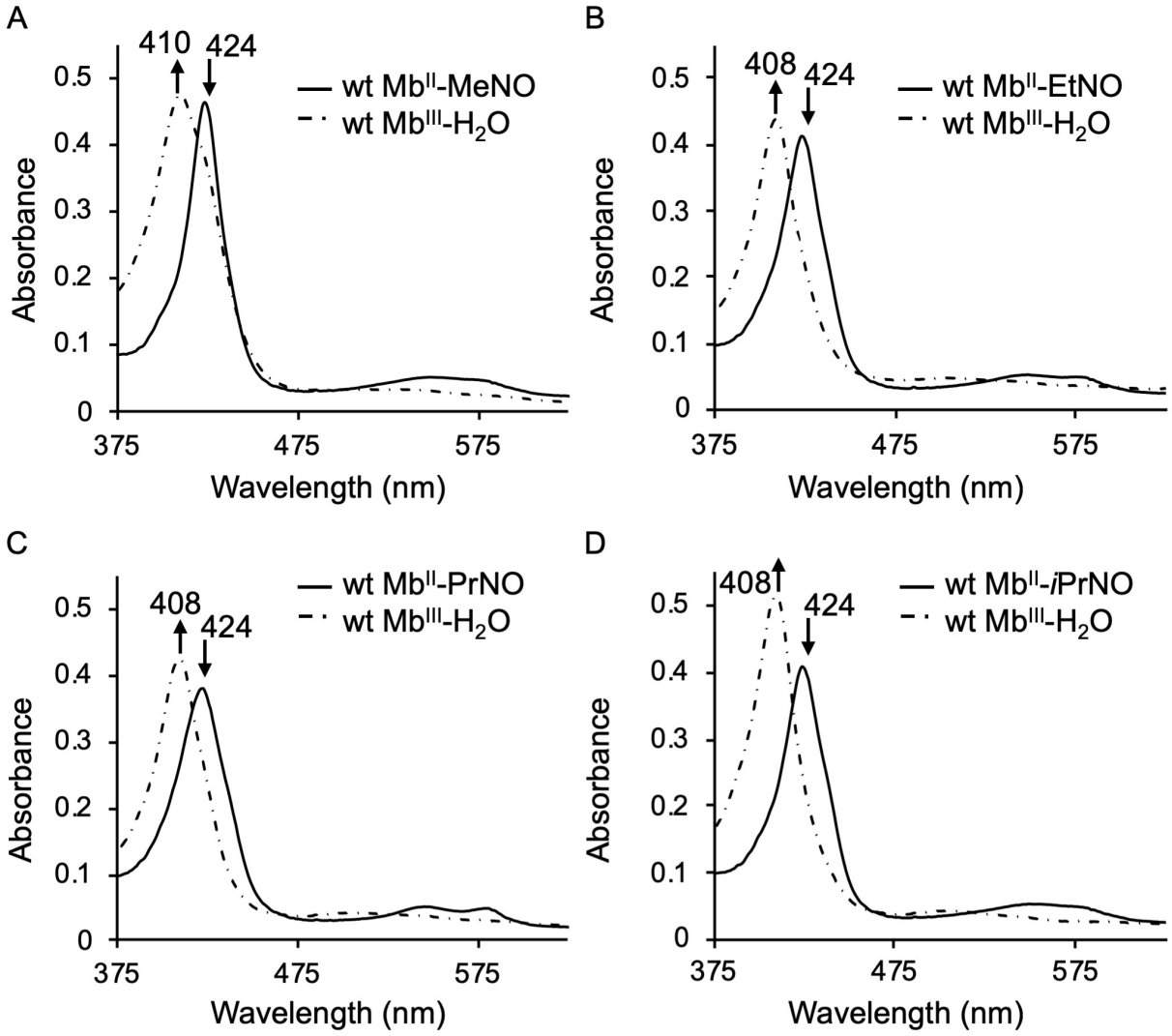

Figure 2.11. Ferrous wt swMb^{II}-RNO ligand dissociation upon oxidation by ferricyanide. The ferrous wt swMb^{II}-RNO derivatives were prepared as described section *2.2.3.2*, followed by the removal of excess dithionite using a desalting column. Afterwards, an aliquot of the sample was placed in a cuvette containing 3 mL of 0.1 M phosphate buffer (pH 6.0), followed by the addition of 3-6 μL of 30 mg/mL potassium hexacyanoferrate (III).

2.3.2.4 H64A swMb-RNO ligand dissociation upon oxidation by ferricyanide

Oxidation of each ferrous H64A swMb^{II}-RNO using potassium hexacyanoferrate (III) resulted in UV-vis spectral features corresponding to the formation of ferric H64A swMb^{III}-H_2O (Figure 2.12A-D). This confirmed the oxidation state of iron as Fe^{II}, and allowed me to conclude that binding between ferrous H64A sw deoxyMb^{II} and alkyl RNOs could be reversed upon changes in the oxidation state of Fe.

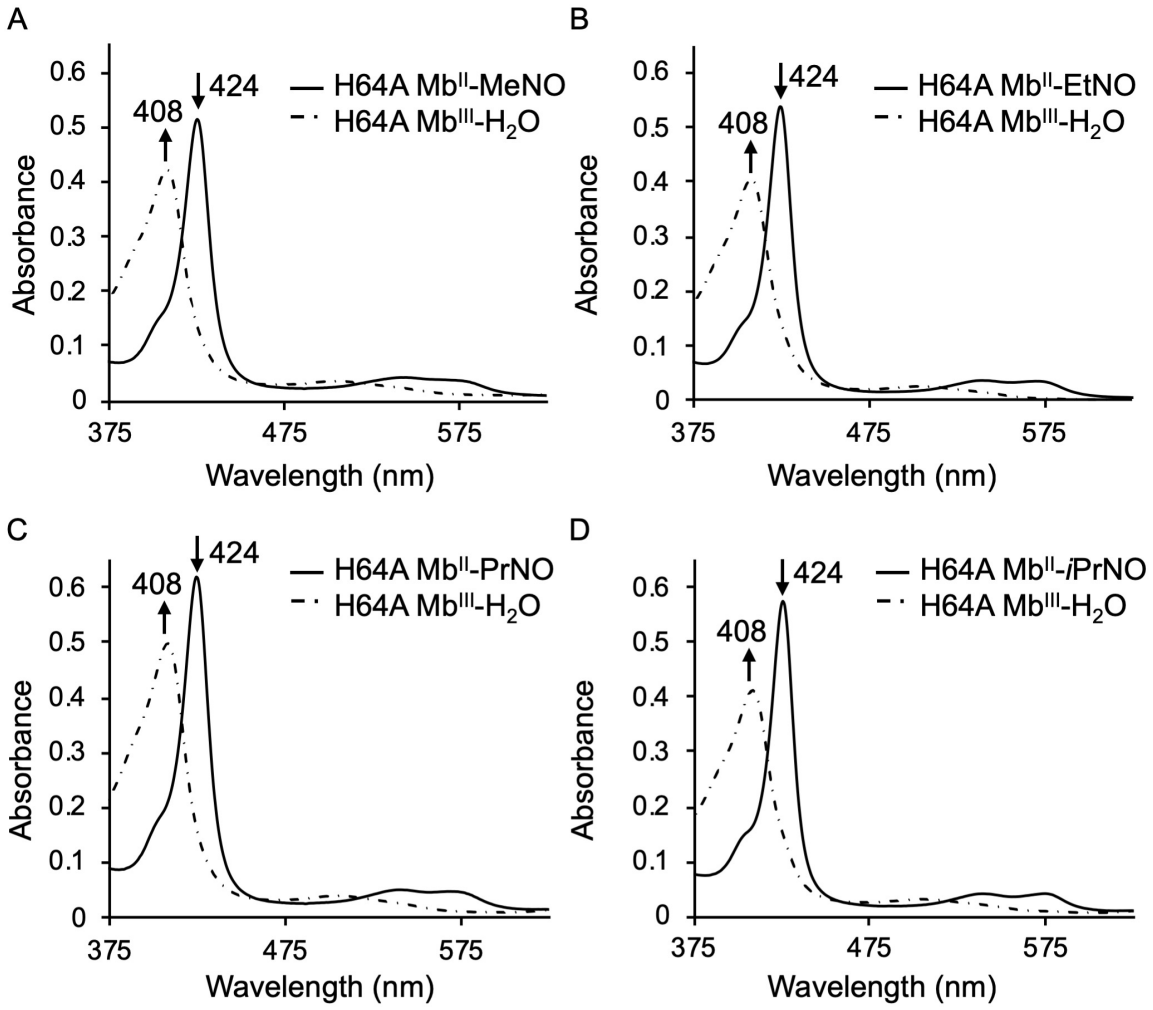

Figure 2.12. Ferrous H64A swMb^{II}-RNO ligand dissociation upon oxidation using ferricyanide. The ferrous H64A swMb^{II}-RNO derivatives were formed as described in section *2.2.3.2*, followed by the removal of excess dithionite using a desalting column. Afterwards, an aliquot of the sample was placed in a cuvette containing 3 mL of 0.1 M phosphate buffer (pH 7.4), followed by the addition of 1 μL of 30 mg/mL potassium hexacyanoferrate(III).

2.3.3 Properties of the wt and H64A swMb-RNO crystals

In this study, two different crystal shapes were obtained, each with a distinct space group. The ferrous wt swMb^{II}-MeNO and -EtNO derivatives were obtained by ligand soaking using hexagonal ferric swMb^{III}-H_2O crystals of distinct brown color which indexed with the *P*6 space group (Figure 2.13A). Soaking was carried out aerobically; the reaction was deemed complete once the crystals changed color from brown (e.g. Figure 2.13A) to violet-pink (e.g. Figure 2.13B). The ferrous wt swMb^{II}-PrNO complex was formed anaerobically in solution and then co-crystallized using the hanging drop vapor diffusion method; this approach also resulted in violet-pink hexagonal crystals belonging to the *P*6 space group (Figure 2.13B)

All the mutant H64A swMb^{II}-RNO derivatives were formed anaerobically in solution and then co-crystallized using the batch method. This protocol resulted in violet-pink hexagonal crystals (*P*6 space group) for the ferrous H64A swMb^{II}-PrNO and -*i*PrNO derivatives (Figure 2.13B), and in violet-pink thin plate crystals ($P12_11$ space group) for the ferrous H64A swMb^{II}-MeNO and -EtNO (Figure 2.13C) products.

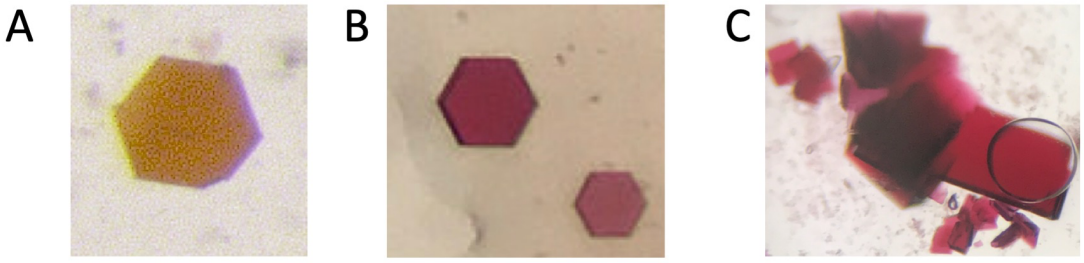

Figure 2.13. Shapes and colors of the crystals obtained in this study. A) Brown, ferric swMb^{III}-H_2O hexagonal shaped crystals indexed with the *P*6 space group. B) Violet-pink, ferrous swMb^{II}-RNO (-PrNO, -*i*PrNO) hexagonal shaped crystals indexed with the *P*6 space group. C) Violet-pink, ferrous swMb^{II}-RNO (-MeNO, -EtNO) thin plate crystals indexed with the $P12_11$ space group.

During crystal handling, I noticed that the violet-pink ferrous H64A swMb^{II}-EtNO crystals that were exposed to air appeared brown within a day, suggestive of oxidative degradation. In contrast, the crystals kept under anaerobic conditions remained violet-pink for several weeks (Figure 2.14B; note crystal color differences). This indicated to me that the ferrous H64A swMb^{II}-RNO complexes were stable anaerobically, but the presence of air destabilized each complex converting the protein back to its ferric state. To confirm my speculation, I dissolved a violet-pink crystal of H64A swMb^{II}-EtNO that had been kept anaerobically for several weeks (~3-4 weeks) and collected its UV-vis spectrum. Indeed, the spectrum corresponded to that of the ferrous H64A swMb^{II}-EtNO product (Figure 2.14B). Afterwards, I exposed the remaining crystals from the same vial to air for ~24 h, and in a similar manner collected the UV-vis spectrum of one of the air-exposed crystals. As anticipated by visual inspection, the resulting spectrum corresponded to ferric swMb^{III}-H_2O (Figure 2.14B). Similar trends in crystal color and spectral readings were observed for all ferrous H64A swMb^{II}-RNO crystals reported in this study (RNO = MeNO, EtNO, PrNO, *i*PrNO) and are listed in Figure 2.14A-D. Dr. Copeland, a previous member of the Richter-Addo lab, reported that the presence of ammonium sulfate in the crystallization buffer causes the ferrous hhMb^{II}-EtNO derivatives to decompose [27]. Therefore, I decided to test the lifetime of each H64A swMb^{II}-RNO complex over several days in the presence of air, but in the absence of ammonium sulfate (Figure 2.15). My results indicate that, in solution, the H64A swMb^{II}-RNO derivatives are unstable in the presence of air.

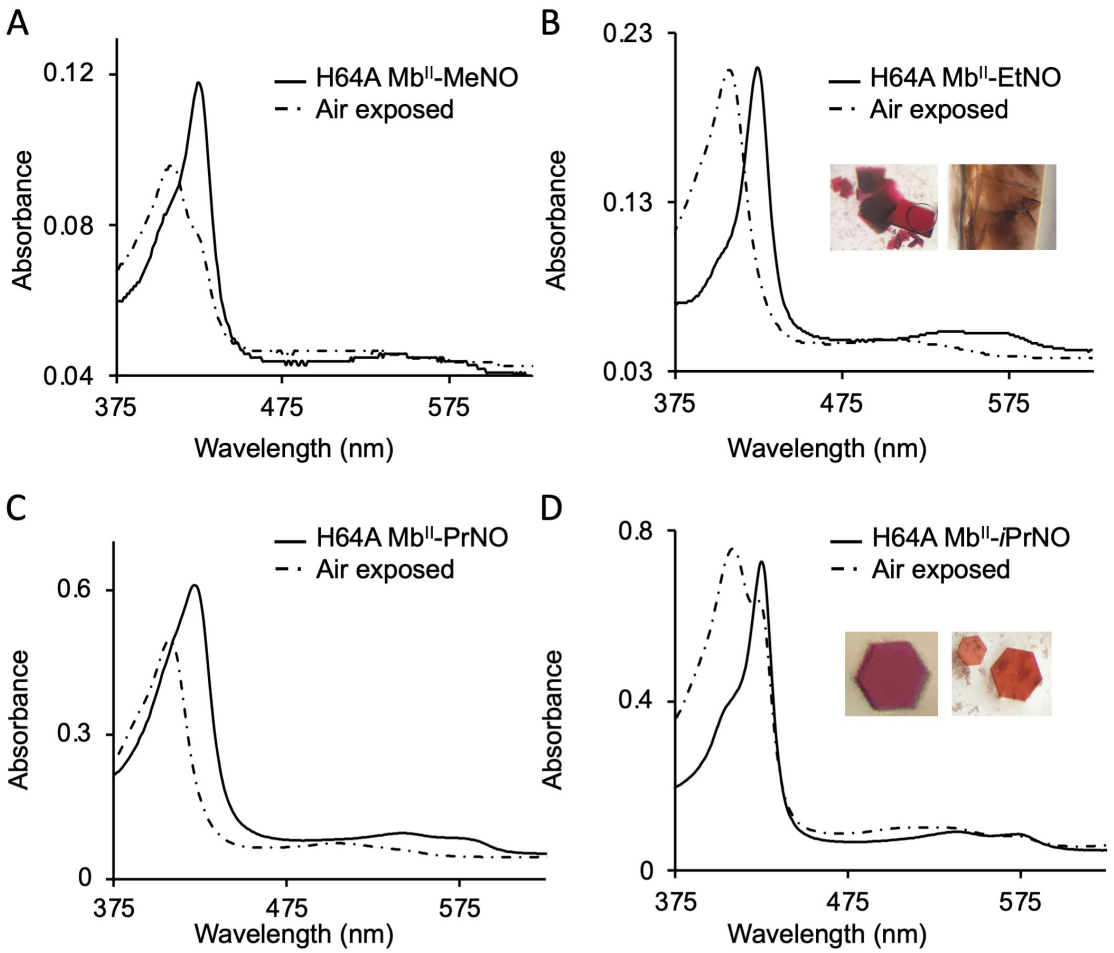

Figure 2.14. UV-vis spectra of the ferrous H64A Mb^{II}-RNO crystal adducts before and after exposure to air. A fresh vial of ferrous H64A Mb^{II}-RNO was opened to air 3-4 weeks after the batch method crystallization was set up anaerobically. A single crystal was dissolved in a 2 μL droplet of 0.1 M phosphate buffer (pH 7.4) and its spectrum was recorded immediately after opening the vial, then the spectrum of another crystal from the same vial was recorded after 24 h exposure to air. A) H64A Mb^{II}-MeNO, B) H64A Mb^{II}-EtNO, C) H64A Mb^{II}-PrNO, D) H64A Mb^{II}-*i*PrNO. Pictures show representative crystals immediately after air exposure, (*left*), and after 24 hrs, (*right*).

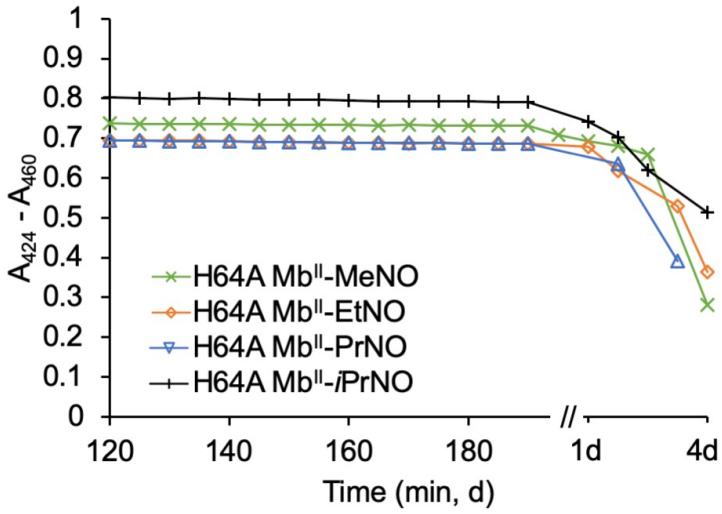

Figure 2.15 Lifetime of each ferrous H64A swMb^{II}-RNO complex over 4 d. Note: protein concentrations vary slightly between reactions, therefore maximum extents of formation here are not comparable. Reaction conditions are similar to those described previously (see section *2.2.3*).

2.3.4 Crystallographic results of the wt and H64A swMb^{II}-RNO derivatives

2.3.4.1 Select structural parameters defined

Before describing the final models of the wt and H64A swMb^{II}-RNO derivatives determined from the X-ray diffraction data, it is important to define a select group of structural parameters that will be discussed. First, in order to better understand the ligand orientation with respect to the heme, the angle *"θ"* is defined as the torsion angle hemeN^{22}-Fe-N^{RNO}-O^{RNO}. This angle provides a measurement of the extent to which the O-atom of the RNO is rotated towards the interior hydrophobic pocket or the solvent exterior (Figure 2.16B). The second angle of interest, *"φ,"* is defined as the axial N^{H93}-Fe-N^{RNO} angle (Figure 2.16C). Finally, *"ω"* is defined as the angle between the 4-N heme plane, and the RNO C^1-N-O plane. *"ω"* provides a measurement of the extent to which the RNO is tilted with respect to the heme plane (not shown). These parameters are referenced hereafter simply as *θ, φ,* or *ω*. Angles *θ, φ,* were calculated using *PyMOL* and *ω* was determined using *Mercury*.

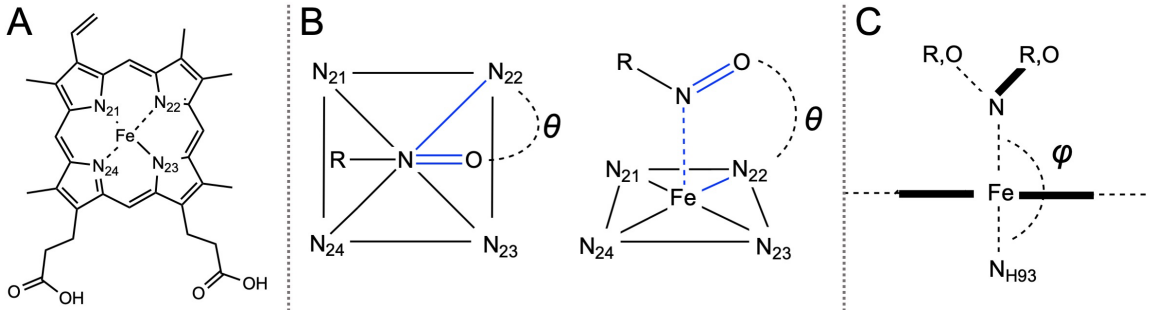

Figure 2.16. Select structural parameters. A) Heme structure with labeled nitrogens for reference. B) Torsion angle *"θ"* formed by the hemeN^{22}-Fe-N^{RNO}-O^{RNO} atoms (shown in blue); *left*: top view, *right*: side view. C) Axial angle *"φ"* formed by the N^{H93}-Fe-N^{RNO}. The tilt angle *"ω"* (not shown) formed by the intersecting heme 4-N plane and the RNO C^1-N-O plane.

2.3.4.2 Structural characterization of wt swMb^{II}-MeNO

The wt swMb^{II}-MeNO products were prepared by soaking the organic nitroalkane precursor $MeNO_2$ into ferric swMb^{III}-H_2O crystals followed by reduction with dithionite. The crystal structure of the product resulting from this procedure was solved to a 1.76 Å resolution, and the corresponding $2F_o–F_c$ electron density map and the $F_o–F_c$ electron density omit map are shown in Figure 2.17. The accompanying data collection and refinement statistics are listed in Table 2-3.

The electron density maps, and in particular the $F_o–F_c$ omit electron density map of the active site shows V-shaped density corresponding to MeNO at two distinct locations. The first MeNO density sits directly above the heme, with the ligand modeled in at 100% occupancy. This nitrosomethane molecule is N-bound to the Fe-atom (at a distance of 1.9 Å) and H-bonded to His64 in the distal pocket (at a distance between the MeNO(O)-atom and the His64(N^{ε}) atom of 2.3 Å). The methyl group is oriented towards the interior of the hydrophobic active site, with the closest neighboring residue atom Val68($C^{\gamma 2}$) at a distance of 3.6 Å from MeNO(C^1). From the top view, the C−N=O plane of MeNO is observed situated between adjacent porphyrin N(pyrrole) atoms, with a θ angle of -159° indicating an O-atom orientation towards the solvent. Furthermore, the axial φ angle was calculated as 173º, indicating that MeNO sits slightly off-center from the heme. Finally, the angle ω is 68º, indicating that the C−N=O plane has a slight tilt with respect to the 4-N heme plane.

The second MeNO molecule was modeled in at 50% occupancy. This MeNO is located below the heme, in what is known as the Xe-1 pocket. This region is speculated to be used by Mb for additional O_2 storage [50]. Alternatively, this density could correspond to the oxime CH_2N=OH, the tautomerization product of MeNO, which is more chemically stable [51-53].

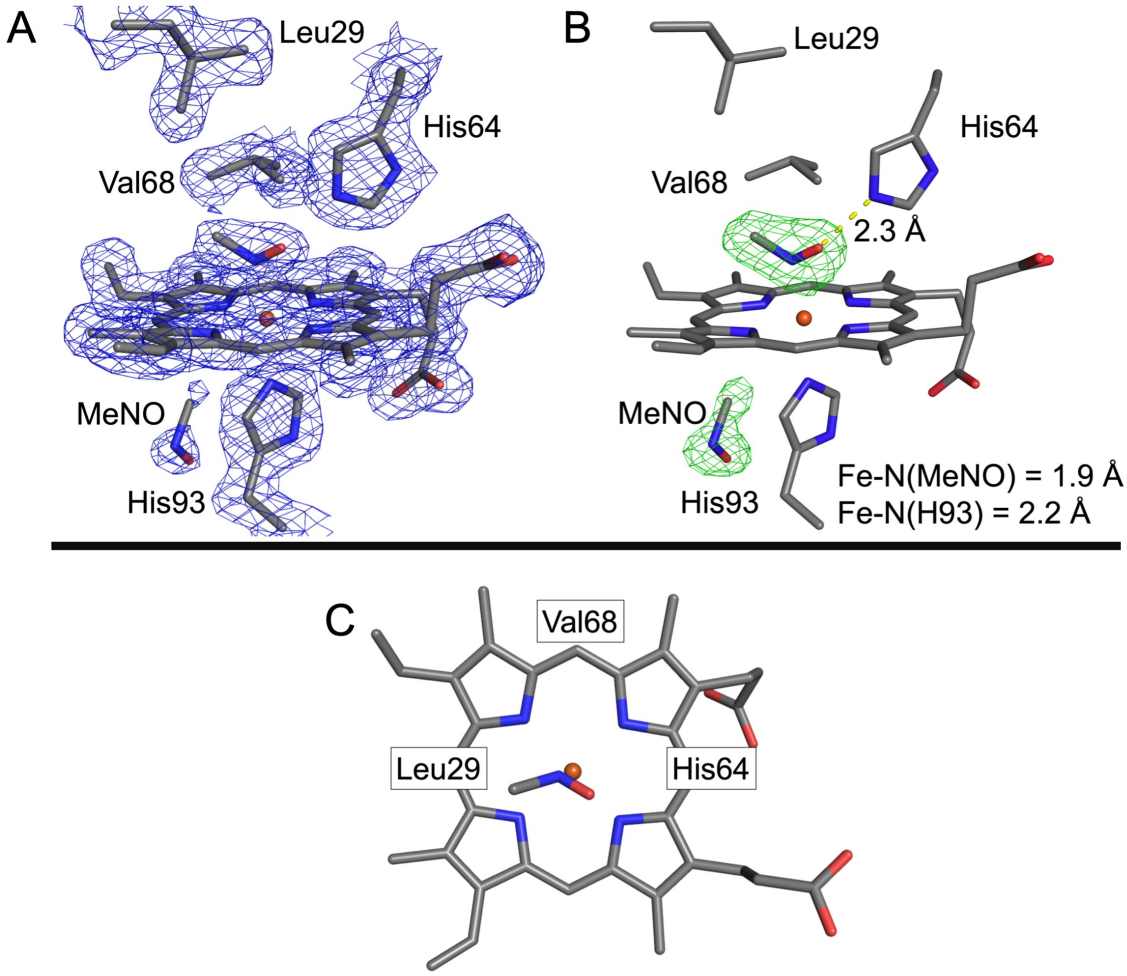

Figure 2.17. Final models of the active site of wt swMb^{II}-MeNO complex at a resolution of 1.76 Å. A) F_o–F_c omit electron density map (green mesh) contoured at 3σ, one MeNO is Fe bound and one is located in the Xe-1 pocket with 100% and 50% occupancy, respectively. B) $2F_o$–F_c electron density map (blue mesh) contoured at 1σ. C) Top view of the ligand orientation with respect to the heme plane.

2.3.4.3 Structural characterization of wt swMb^{II}-EtNO

The wt swMb^{II}-EtNO complex was similarly prepared by soaking organic $EtNO_2$ into ferric swMb^{III}-H_2O crystals followed by the addition of dithionite, and its crystal structure was solved to 1.76 Å resolution. The resultant $2F_o–F_c$ electron density map and the $F_o–F_c$ electron density omit map are shown in Figure 2.18, and the data collection and refinement statistics are listed in Table 2-3.

Electron density corresponding to nitrosoethane is evident in both calculated density maps directly above the heme, where EtNO was modeled in at 100% occupancy. Congruent with my UV-vis results, the ligand is N-bound to the heme Fe-atom (at a distance of 2.1 Å). A H-bond provides a direct interaction between the ligand's O-atom and His64(N^{ε}) at a distance of 2.1 Å. Consequently, the alkyl group is directed towards the interior of the hydrophobic active site with close hydrophobic residues Ile107 (at a distance of 3.0 Å from its C^2 atom) and Val68 (with distances to EtNO's C^1 and C^2 of 3.5 and 3.6 Å). The $C^2–C^1–N=O$ backbone of nitrosomethane is in the *trans* conformation and has a torsion angle of 152°.

The axial φ angle was calculated as 175º which corresponds to the slightly askew position of the ligand in regards to the Fe-atom. As observed from above the heme, the C−N=O moiety points directly towards the exterior of the protein resulting in a θ angle of -143°. Furthermore, the C−N=O plane bisects the 4-N heme plane with an ω angle of 62º, which relates to the slightly sideways binding of the ligand.

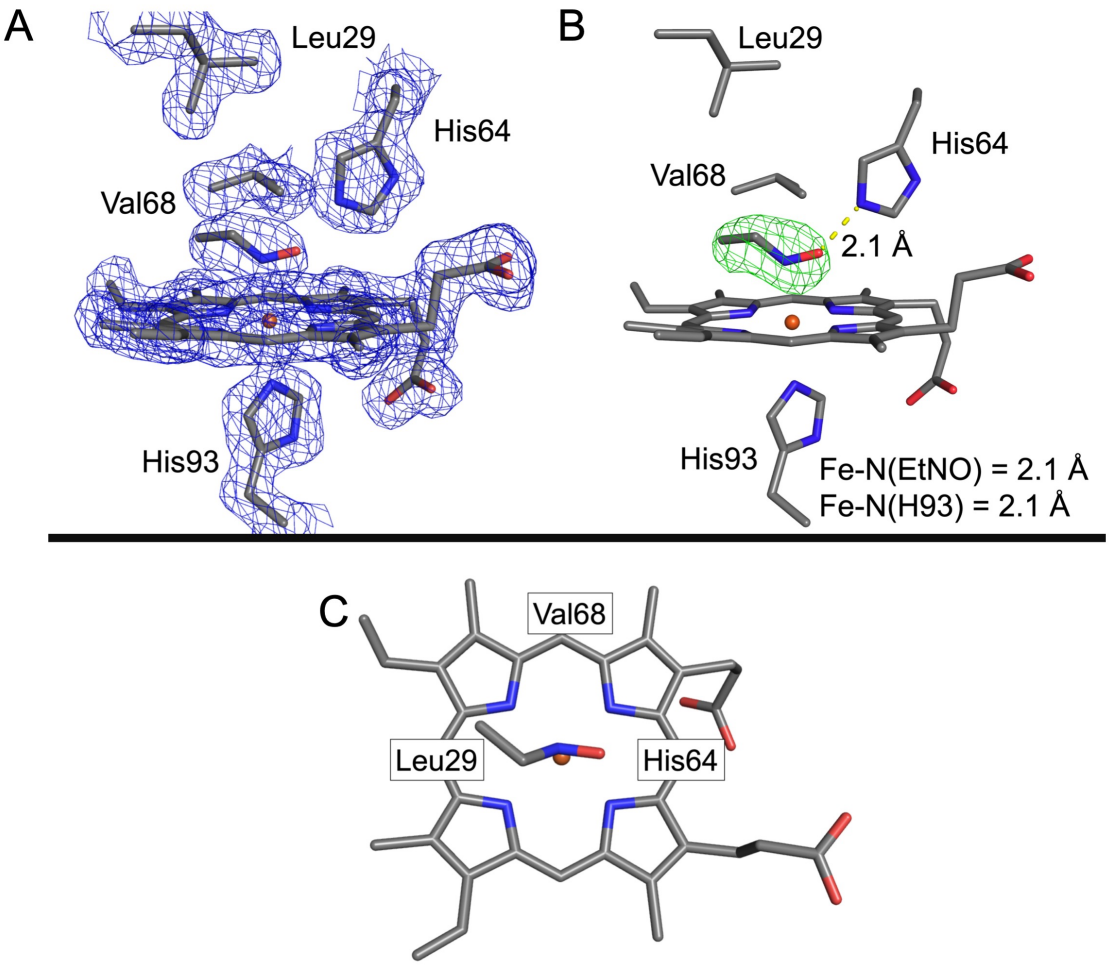

Figure 2.18. Final models of the active site of wt swMb^{II}-EtNO complex at a resolution of 1.76 Å. A) F_o–F_c omit electron density map (green mesh) contoured at 3σ, EtNO is Fe bound with 100% occupancy. B) 2F_o–F_c electron density map (blue mesh) contoured at 1σ. C) Top view of the ligand orientation with respect to the heme plane.

2.3.4.4 Structural characterization of wt swMb^{II}-PrNO

Co-crystallization of wt swMb^{II}-PrNO resulted in high quality crystals which were used to solve the structure of the complex to a resolution of 2.00 Å. The corresponding models of the active site can be found in Figure 2.19, as well as the accompanying electron density maps. Data collection and refinement statistics are located in Table 2-3.

Concrete electron density corresponding to PrNO is clearly noticeable above the heme in both the $2F_o–F_c$ electron density map and in the $F_o–F_c$ electron density omit map. PrNO was modeled into this location at 100% occupancy. The ligand is N-bound to the heme Fe at a distance of 1.8 Å. The O-atom is H-bonded to His64(N^{ε}) at a distance of 2.5 Å, which orients the propyl group towards the interior of the hydrophobic active site. Upon further inspection, multiple hydrophobic residues in the distal pocket were observed to closely surround PrNO. For instance, the PrNO(C^1) atom is closely neighbored by Val68's $C^{\delta 1}$ and $C^{\gamma 2}$ at 3.7 and 3.5 Å, respectively. The PrNO(C^2) atom is at a distance of 3.4 Å from Leu29($C^{\delta 2}$), and PrNO(C^3) atom is in close proximity to Ile107, Phe43, Leu32 and Leu29 at ~3.4-3.7 Å (from their nearest C-atoms). The backbone of PrNO has torsion angles of -23° for $C^2–C^1–N=O$, and -112° for $C^3–C^2–C^1–N$, which are best described as *cis* and *trans* respectively. Interestingly, I collected X-ray data diffraction and solved the structure of several different crystals of this product, and the PrNO torsion angles and orientation with respect to the heme remained consistent.

From the top view, the O-atom is observed to be oriented towards N^{24}, which corresponds to a θ angle of -1 58.7°. Additionally, the PrNO sits slightly off-center from Fe and has a φ angle of 174º. Finally, the C−N=O plane was determined to bisect the 4-N heme plane at ω 79º.

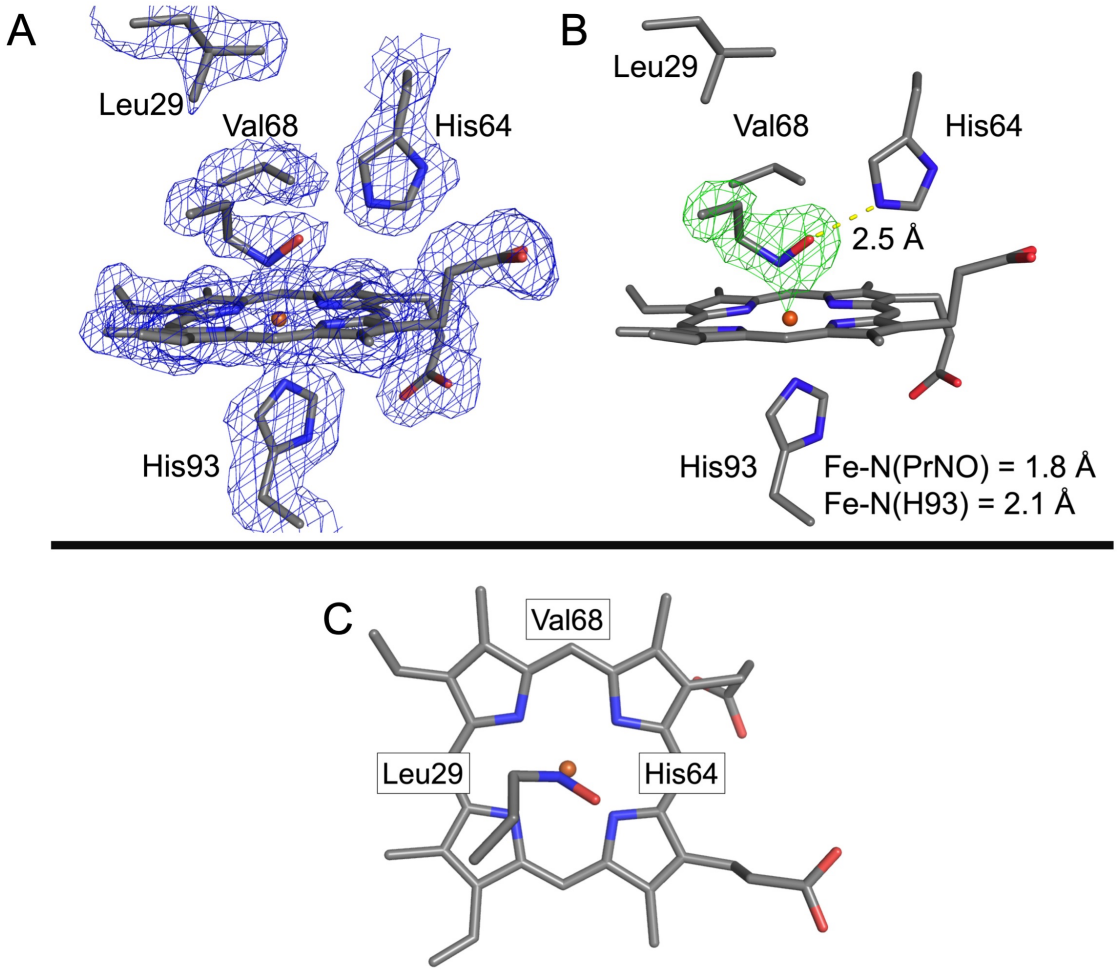

Figure 2.19. Final models of the active site of wt swMb^{II}-PrNO complex at a resolution of 2.00 Å. A) F_o–F_c omit electron density map (green mesh) contoured at 3σ, PrNO is Fe bound with 100% occupancy. B) 2F_o–F_c electron density map (blue mesh) contoured at 1σ. C) Top view of the ligand orientation with respect to the heme plane.

2.3.4.5 Structural characterization of H64A swMb^{II}-MeNO

Crystals of the H64A swMb^{II}-MeNO complex were formed through co-crystallization using batch method, and the structure was solved to a resolution of 1.75 Å. Table 2-4 summarizes the ensuing data collection and refinement statistics, the calculated $2F_o–F_c$ electron density map and the $F_o–F_c$ electron density omit map are shown in Figure 2.20.

The electron density maps show V-shaped density corresponding to MeNO above the heme, which was modeled in at 100 % occupancy. Similar to what I observed in wt swMb, MeNO is N-bound to the Fe-atom of the heme with its alkyl group pointing towards the interior of the hydrophobic pocket.

The nearest hydrophobic residue to the methyl C-atom is Val68 at a distance of 3.1 Å from Val68($C^{\gamma 2}$). Residues Phe43 and Leu29 are also closely surrounding the ligand with measured distances from MeNO(C) to Phe43(C^{ζ}) and Leu29($C^{\delta 2}$) of 3.8 and 4.0 Å, respectively. The H64A swMb^{II}-MeNO complex displays a chain of fixed waters for H-bonding with MeNO to replace the interaction observed in the wt derivative with the His64 residue. The O-atom of MeNO is H-bonded to the closest water at a distance of 2.5 Å. Three additional fixed water molecules make up the chain with distances between 2.7 – 2.8 Å from each other (Figure 2.20C).

The C−N=O plane sits midway between porphyrin N^{23} and N^{24} atoms with the O-atom directed towards the exterior of the protein, corresponding to a θ angle of -139°. The MeNO has an axial φ angle of 178º. Finally, the C−N=O plane bisects the 4-N heme plane at ω 75º.

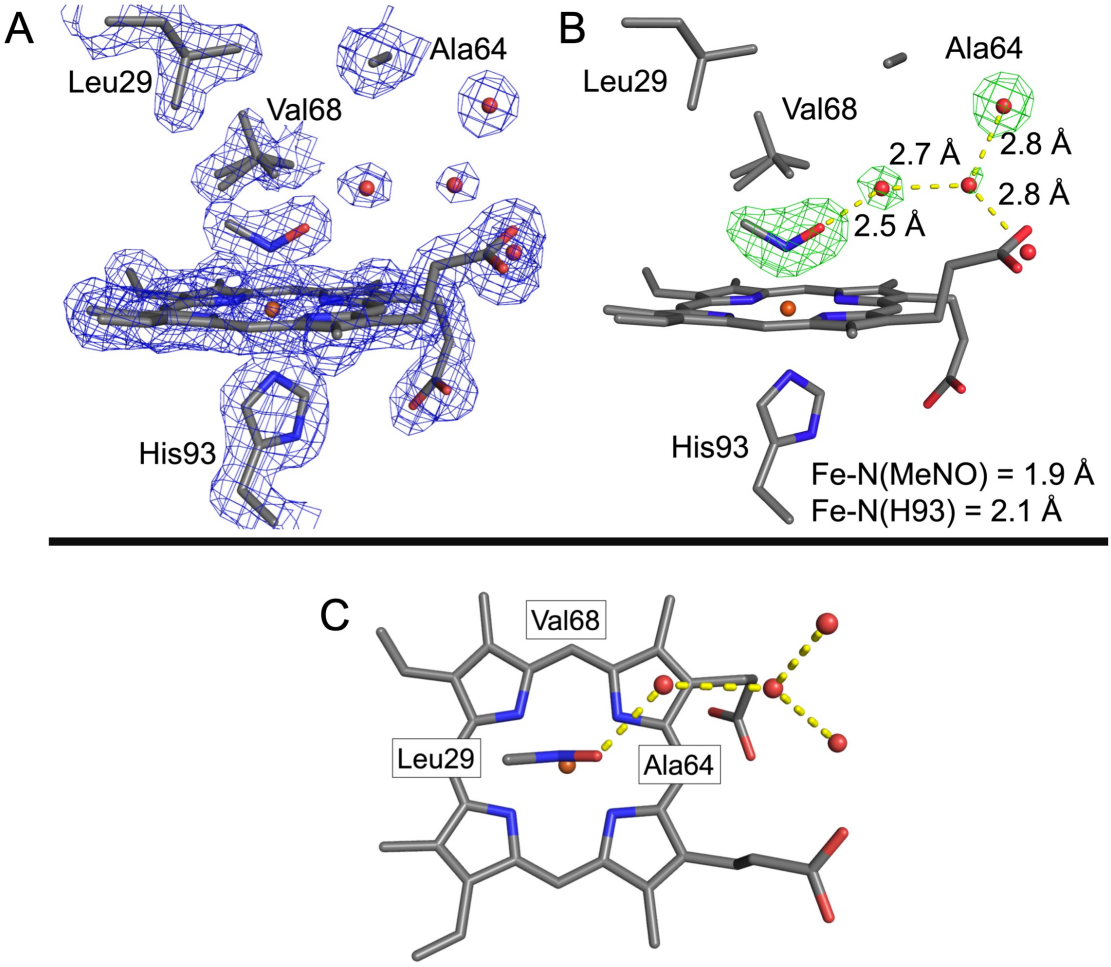

Figure 2.20. Final models of the active site of H64A swMb^{II}-MeNO complex at a resolution of 1.75 Å. A) F_o–F_c omit electron density map (green mesh) contoured at 3σ, MeNO is Fe bound with 100% occupancy. B) 2F_o–F_c electron density map (blue mesh) contoured at 1σ. C) Top view of the ligand orientation with respect to the heme plane.

2.3.4.6 Structural characterization of H64A swMb^{II}-EtNO (Chains A and B)

Co-crystallization using batch method allowed me to obtain and solve the structure of H64A swMb^{II}-EtNO to a resolution of 1.80 Å. Unlike any of my other Mb^{II}-RNO crystal structures, H64A swMb^{II}-EtNO had two asymmetric units per unit cell which I refer to as Chain A (Figure 2.21) and Chain B (Figure 2.22). Related data collection and refinement statistics are listed in Table 2-4.

In Chain A (Figure 2.21), the electron density maps, in particular the F_o–F_c electron density omit map, show prominent density corresponding to EtNO above the heme, which was modeled in at 100% occupancy. As observed with my other nitrosoalkanes, EtNO is N-bound to the Fe-atom of the heme with its ethyl group pointing towards the interior of the hydrophobic pocket. The torsion angle for C^2–C^1–N=O backbone is -68° which is best described as *trans* conformation. The closest hydrophobic point to the ethyl group is Leu29($C^{\delta 2}$) at a distance of 3.6 Å from EtNO(C^2), followed by Phe43(C^{ζ}) at a distance of 3.8 Å from EtNO(C^2). In this structure, Val68 is pointing away from the ligand with its methyl C-atoms at distances of 4.1 and 4.5 Å from EtNO(C^2) respectively.

From the top view, the C–N=O plane is rotated towards the interior of the active site with respect to the heme, as compared to the previously described swMb^{II}-RNO derivatives. In this complex, the O-atom is pointed towards porphyrin N^{23} and has a θ angle of -61° congruent with the rotation of the ligand towards the inside of the pocket. The axial φ angle was determined to be 177º. The C–N=O plane of the ligand was determined to bisect the 4-N heme plane at ω 47º, indicating that EtNO is more tilted towards the heme than in wt swMb. Finally, there is no fixed H-bonding to EtNO; in fact, the closest fixed water molecule is 7.0 Å away.

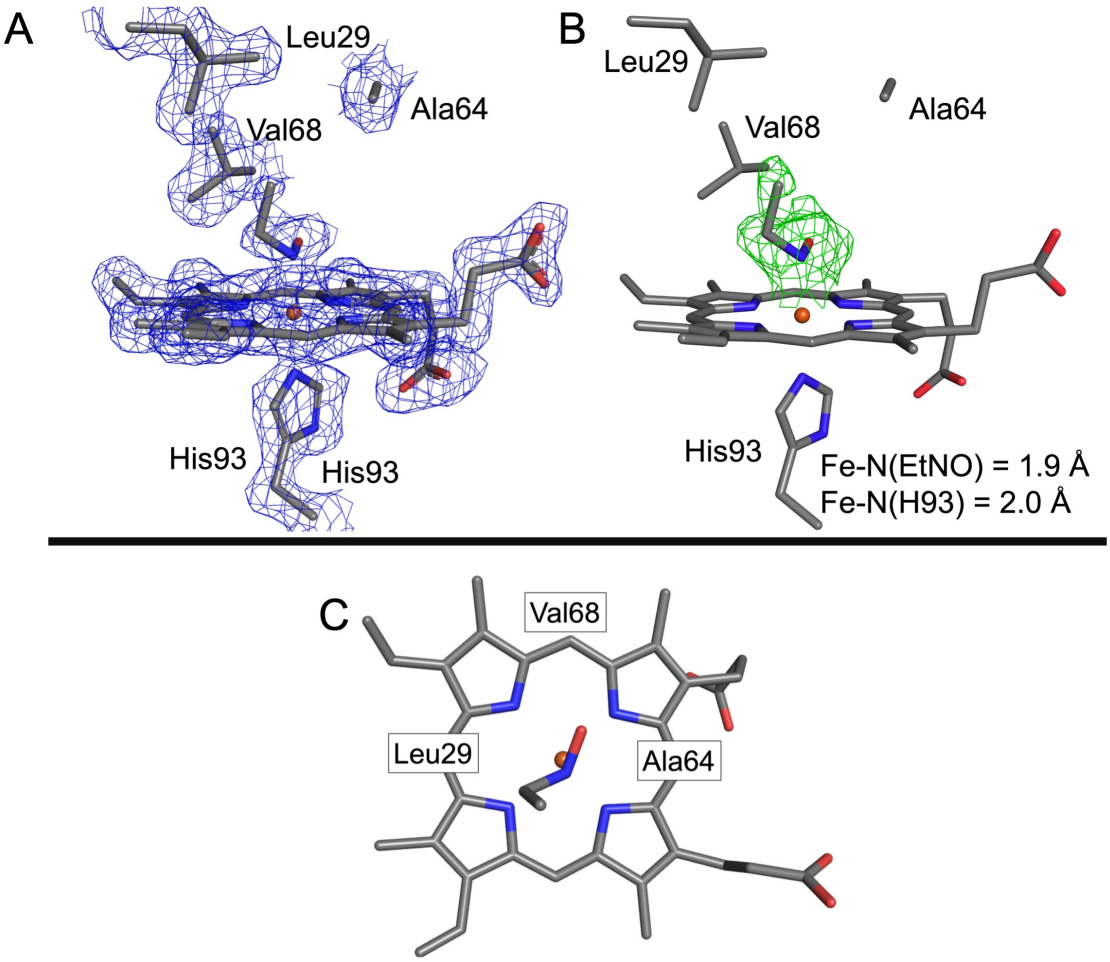

Figure 2.21. Final models of the active site of H64A swMb^{II}-EtNO complex, Chain A, at a resolution of 1.80 Å. A) F_o–F_c omit electron density map (green mesh) contoured at 3σ, EtNO is Fe bound with 100% occupancy. B) $2F_o$–F_c electron density map (blue mesh) contoured at 1σ. C) Top view of the ligand orientation with respect to the heme plane.

In Chain B of H64A swMb^{II}-EtNO, the F_o–F_c omit electron density map shows density corresponding to EtNO and a water molecule above the heme, these were modeled in at 60 and 40% occupancy respectively (Figure 2.22). The distance between Fe-N(EtNO) is 1.9 Å, and the distance between Fe-O(H_2O) is 2.5 Å. As observed with my other RNOs, EtNO is N-bound to the Fe-atom of the heme. However, unlike other RNOs in this study, the ethyl group is pointing towards the hydrophilic exterior. The torsion angle for the C^2–C^1–N=O backbone is 61°. The closest hydrophobic residue to the ethyl group is Ala64 at a distance of 3.6 Å from C^2. The next neighboring hydrophobic residue is Val68. However, its methyl groups are pointed away from EtNO, creating a distance from Val68's $C^{\gamma 2}$ and $C^{\delta 1}$ of 5.0 and 4.5 Å from EtNO(C^2), which is further away than that observed for other ligands. Perhaps it is this lack of hydrophobic interactions, along with its orientation towards the solvent, that makes EtNO unstable in the active site. As a result, EtNO is partially replaced by water in this structure.

Further analysis shows that the O-atom is angled towards porphyrin N^{21}atom, which is unlike any other ligand in this study; this orientation corresponds to an angle θ of 69°. Moreover, the axial φ angle is 168º, and ω is 79º. Finally, there is no observed H-bonding to the Fe bound water molecule nor to the EtNO ligand in the active site, which is likely due to nitrosoethane's O-atom orientation towards the interior.

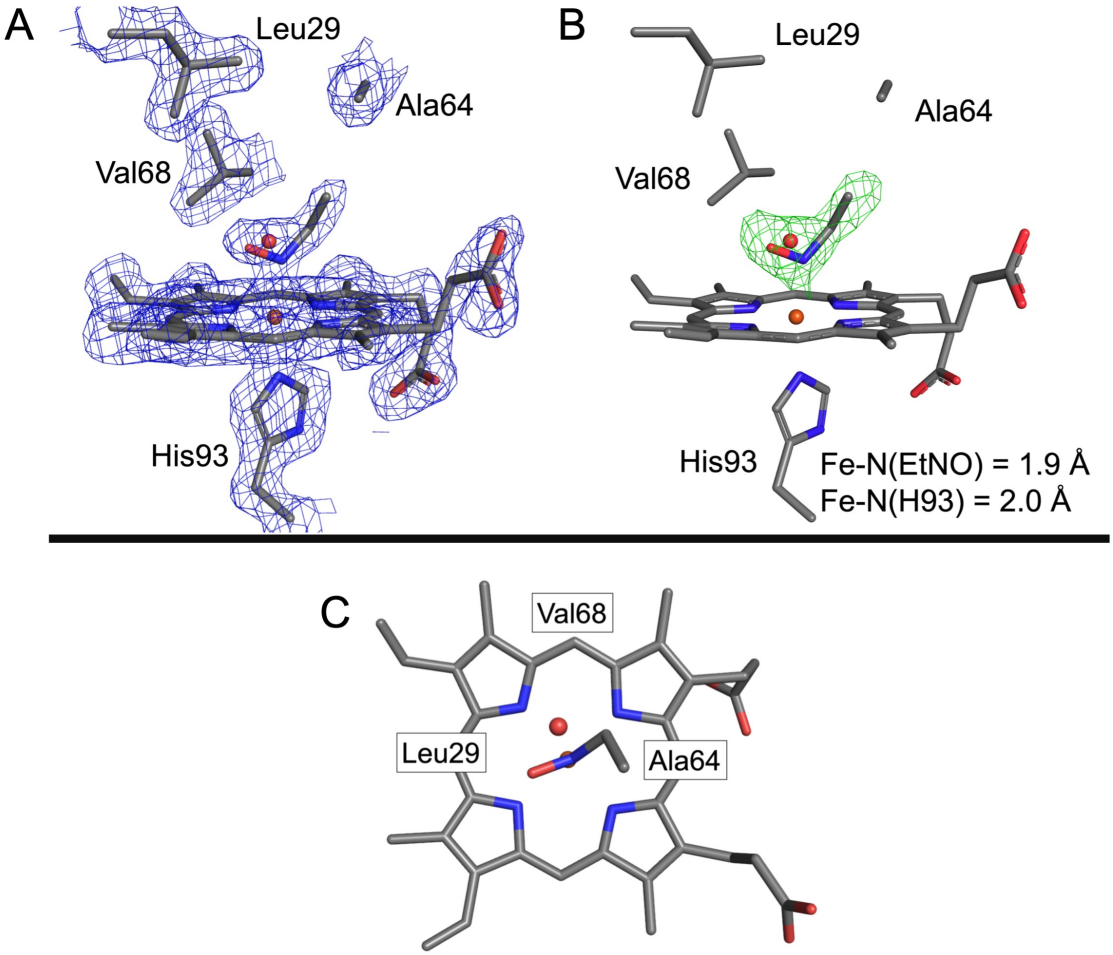

Figure 2.22. Final models of the active site of H64A swMb^{II}-EtNO complex, Chain B, at a resolution of 1.80 Å. A) F_o–F_c omit electron density map (green mesh) contoured at 3σ, EtNO is Fe bound with 60% occupancy, and water bound at 40% occupancy. B) $2F_o$–F_c electron density map (blue mesh) contoured at 1σ. C) top view of the ligand orientation with respect to the heme plane.

2.3.4.7 Structural characterization of H64A swMb^{II}-PrNO

The crystal structure of H64A swMb^{II}-PrNO was solved to a resolution of 1.75 Å from crystals formed by co-crystallization using the batch method. Models of the active site, along with the $2F_o–F_c$ electron density map and the $F_o–F_c$ electron density omit map are shown in Figure 2.23. Data collection and refinement statistics for the structure are listed in Table 2-4.

The calculated electron density maps have distinct density corresponding to PrNO directly above the heme, which was modeled in at 100 % occupancy. Similar to what was observed in wt swMb, PrNO is N-bound to the Fe-atom of the heme with its propyl group pointing towards the interior of the hydrophobic pocket. The $C^2–C^1–N=O$ and $C^3–C^2–C^1–N$ torsion angles are 69º and 66 respectively.

The nearest hydrophobic residues to the propyl group are Leu29 and Phe43, with measured distances from PrNO(C^3) to Leu29($C^{\delta 2}$) of 3.5 Å, and from Phe43(C^{ζ}) to PrNO(C^2) and PrNO(C^3) of 3.7 and 4.0 Å respectively. Also bordering the propyl group is Val68, with a calculated distance from Val68($C^{\gamma 2}$) to the PrNO(C^2) and PrNO(C^3) atoms of 4.1 and 4.4 Å respectively.

Analysis of the ligand orientation from above the heme reveals that the C−N=O group is significantly rotated towards the interior of the protein as compared to wt swMb^{II}-PrNO. This view shows that the O-atom rests halfway between porphyrin N^{22} and N^{23} atom, an orientation that corresponds to an angle θ of -65°. Furthermore, the propyl group lies directly above the N^{21} atom, similarly to that observed in wt swMb^{II}-PrNO. Additional analysis determined the φ angle to be 177º and the ω angle as 58º. Finally, the PrNO ligand in the H64A swMb^{II}-PrNO complex is H-bonded to fixed H_2O molecules that form a chain to the solvent exterior. The PrNO(O) atom is H-bonded to the closest water at a distance of 2.8 Å. Three additional fixed water molecules make up the chain with distances between ~2.7 – 2.8 Å away from each other.

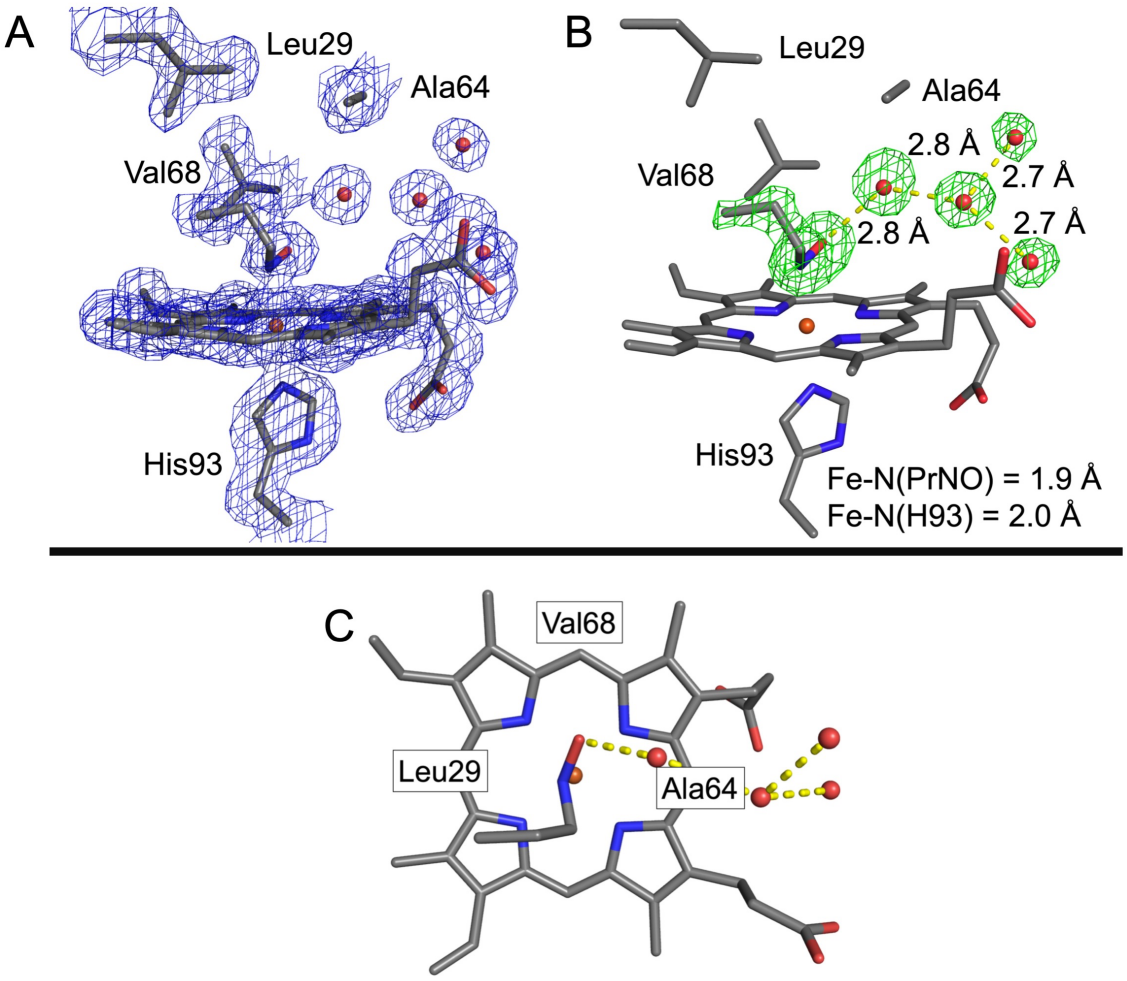

Figure 2.23. Final models of the active site of H64A swMb^{II}-PrNO complex, at a resolution of 1.75 Å. A) F_o–F_c omit electron density map (green mesh) contoured at 3σ, PrNO is Fe bound with 100% occupancy. B) 2F_o–F_c electron density map (blue mesh) contoured at 1σ. C) Top view of the ligand orientation with respect to the heme plane.

*2.3.4.8 Structural characterization of H64A swMb^{II}-i*PrNO

Suitable crystals of H64A swMb^{II}-*i*PrNO were obtained using the co-crystallization method, and the structure of the complex was solved to a resolution of 1.75 Å. Figure 2.24 illustrates the final models of the active site as well as the $2F_o–F_c$ electron density map and the $F_o–F_c$ electron density omit map. Data collection and refinement statistics for the structure are listed in Table 2-4.

The electron density maps show prominent density directly above the heme, where *i*PrNO was modeled in at 100% occupancy. The *i*PrNO ligand is N-bound to the Fe-atom of the heme with its isopropyl group pointing towards the interior of the hydrophobic pocket. The nearest hydrophobic residue to the isopropyl group is Phe43, with calculated distances from Phe43(C^{ζ}) and Phe43($C^{\varepsilon 1}$) to the *i*PrNO(C^2) atom of 3.4 and 3.0 Å. The next closest residues to the ligand are Val68 and Leu29 with their nearest carbon atoms at distances of 3.8 Å from *i*PrNO(C^2) each.

The top view of the active site shows that the C−N=O plane of the ligand is rotated towards the interior of the protein, this results in orientation of the O-atom midway between N^{22} and N^{23}, with θ = -56°. Upon further analysis the axial φ angle was calculated to be 173º. Moreover, the C−N=O plane of the ligand was determined to bisect the 4-N heme plane at a ω angle of 86º, indicating an almost perpendicular orientation to the heme plane.

Finally, the *i*PrNO ligand is H-bonded to a single fixed water at a distance of 2.6 Å. Unlike some of the other H64A swMb^{II}-RNO structures in this study, there are no additional fixed waters that form a chain. In fact, the nearest water to the fixed water molecule in the active site is 4.3 Å apart, which is too far away for direct H-bonding.

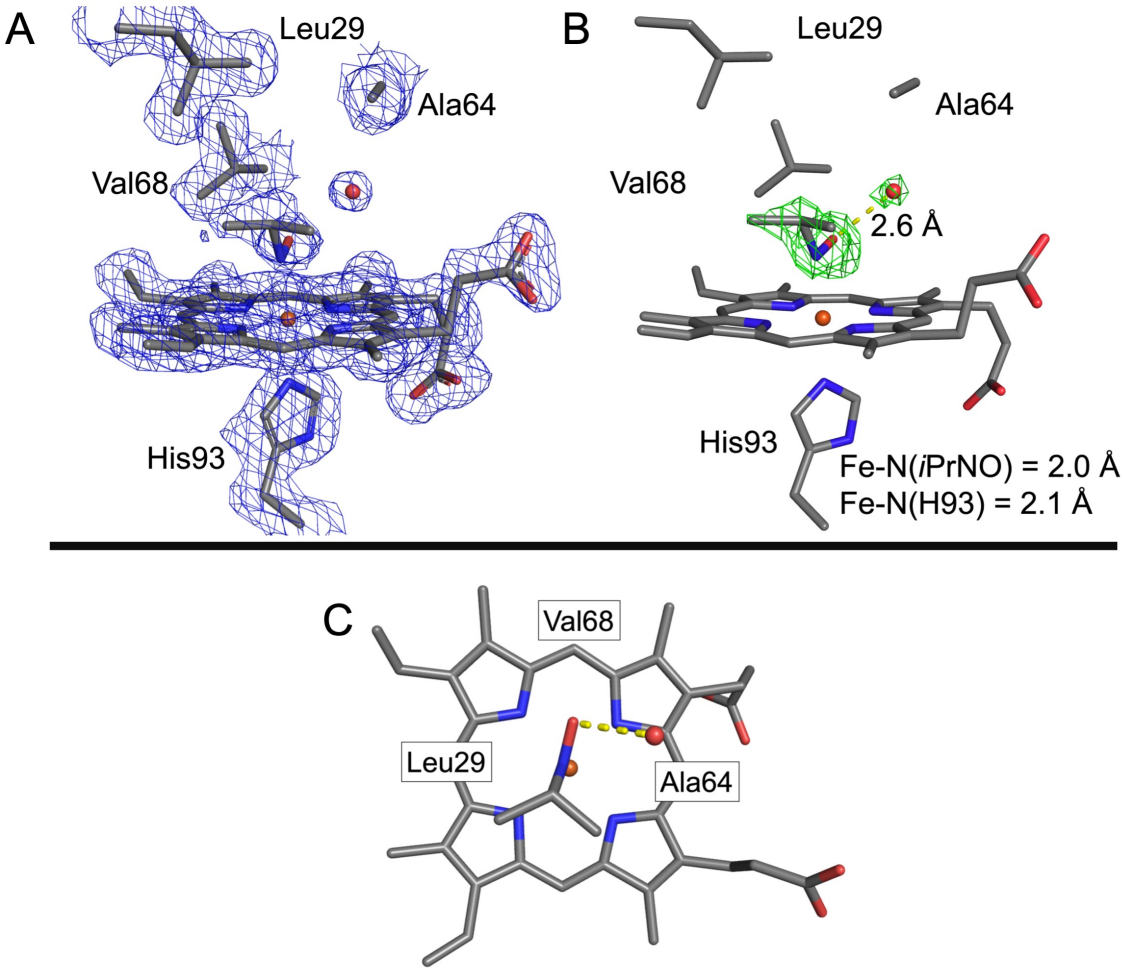

Figure 2.24. Final models of the active site of H64A swMb^{II}-*i*PrNO complex, at a resolution of 1.75 Å. A) F_o–F_c omit electron density map (green mesh) contoured at 3σ, EtNO is Fe bound with 100% occupancy. B) $2F_o$–F_c electron density map (blue mesh) contoured at 1σ. C) top view of the ligand orientation with respect to the heme plane.

Table 2-2. Summary of select structural parameters of each wt and H64A swMb^{II}-RNO complex.

Wt swMb^{II}-RNOs									
RNO	Fe-N(H93) (Å)	Fe-N(RNO) (Å)	θ^* (°)	φ^* (°)	ω^* (°)	∠C^1-N=O (RNO) (°)	∠C^2-C^1-N=O (RNO) (°)	∠C^3-C^2-C^1-N (RNO) (°)	Occupancy (%)
-MeNO	2.2	1.9	-159	173	68	104	NA	NA	100[a], 50[b]
-EtNO	2.1	2.1	-143	175	62	115	152	NA	100
-PrNO	2.1	1.8	-159	174	79	108	-23	-112	100
-*i*PrNO	NA	NA	NA	NA	NA	NA	NA	NA	NA
H64A swMb^{II}-RNOs									
RNO	Fe-N(H93) (Å)	Fe-N(RNO) (Å)	θ^* (°)	φ^* (°)	ω^* (°)	∠C^1-N=O (RNO) (°)	∠C^2-C^1-N=O (RNO) (°)	∠C^3-C^2-C^1-N (RNO) (°)	Occupancy (%)
-MeNO	2.1	1.9	-139	178	75	116	NA	NA	100
-EtNO (A)	2.0	1.9	-61	177	47	113	-68	NA	100
-EtNO (B)	2.0	1.9	69	168	79	117	61	NA	60[c]
-PrNO	2.0	1.9	-65	177	58	116	69	66	100
-*i*PrNO	2.1	2.0	-56	173	86	105	122, -115	NA	100

[a] corresponds to the MeNO bound to the heme. [b] corresponds to the MeNO in the Xe-1 pocket. [c] a water molecule is also bound to Fe at the active site with 40% occupancy.

[*] The θ, φ and ω angles are described in section *2.3.4.1* Select structural parameters defined.

Table 2-3. X-ray data collection and refinement statistics

	wt Mb^{II}-MeNO	**wt Mb^{II}-EtNO**	**wt Mb^{II}-PrNO**
Data collection[a]	MicroMax 007HF	MicroMax 007HF	MicroMax 007HF
Space Group	*P6*	*P6*	*P6*
Wavelength (Å)	1.54178	1.54178	1.54178
Cell dimensions (*a*, *b*, *c*) (α, β, γ)	90.35 90.35 45.33 90.0 90.0 120.0	90.27 90.27 45.31 90.0 90.0 120.0	90.47 90.47 45.34 90.0 90.0 120.0
Resolution range (Å)	45.33 – 1.76	45.14 – 1.76	45.34 – 2.00
Mean $I/\sigma(I)$	36.21 (7.48)	16.23 (1.70)	16.78 (3.96)
No. of reflections			
Observed	159168	143099	206470
Unique	21127 (2083)	20356 (1455)	14515 (1444)
Multiplicity	7.5 (4.3)	7.0 (1.7)	14.2 (13.6)
Completeness (%)	99.89 (99.10)	96.42 (69.33)	99.69 (100.00)
R_{merge}[b]	0.049 (0.174)	0.074 (0.247)	0.194 (0.622)
$CC_{1/2}$	0.969	0.902	0.925
Refinement statistics			
No. of protein atoms	1230	1224	1223
R factor (%)[c]	0.1358	0.1599	0.1734
R_{free} (%)[d]	0.1719	0.1908	0.2052
RMSD bond length (Å)	0.019	0.028	0.016
RMSD bond angles (°)	1.84	1.75	1.67
Overall Mean B factor	15.26	14.33	17.87
Ramachandran plot (%)[e]			
Most favored residues	98.01	98.01	98.01
Outliers	0.00	0.00	0.00

[a] Values in parentheses correspond to the highest resolution shells. [b] $R_{merge} = \Sigma|I - \langle I \rangle|/\Sigma(I)$, where I is the individual intensity observation and $\langle I \rangle$ is the mean of all measurements of I. [c] $R = \Sigma||F_o| - |F_c||/\Sigma|F_o|$, where F_o and F_c are the observed and calculated structural factors respectively. [d] R_{free} was calculated by using 5% of the randomly selected diffraction data which were excluded from the refinement. [e] As calculated using *MolProbity*.

Table 2-4. X-ray data collection and refinement statistics (continued)

	H64A Mb^{II}-MeNO	H64A Mb^{II}-EtNO	H64A Mb^{II}-PrNO	H64A Mb^{II}-*i*PrNO
Data collection[a]	MicroMax 007HF	MicroMax 007HF	MicroMax 007HF	MicroMax 007HF
Space Group	*P1 2₁ 1*	*P1 2₁ 1*	*P6*	*P6*
Wavelength (Å)	1.54178	1.54178	1.54178	1.54178
Cell dimensions (*a*, *b*, *c*) (α, β, γ)	34.86 29.03 64.26 90.0 105.9 90.0	41.83 76.77 50.53 90.0 103.8 90.0	90.59 90.59 45.40 90.0 90.0 120.0	90.58 90.58 45.40 90.0 90.0 120.0
Resolution range (Å)	33.57 – 1.75	41.35 – 1.80	39.28 – 1.75	39.3 – 1.75
Mean $I/\sigma(I)$	22.98 (6.87)	36.67 (3.85)	31.11 (6.27)	22.28 (3.14)
No. of reflections				
Observed	48328	218057	107327	120188
Unique	12692 (1225)	27896 (2496)	21383 (1974)	19658 (1877)
Multiplicity	3.8 (2.0)	7.8 (3.7)	5.0 (2.8)	6.1 (4.2)
Completeness (%)	99.45 (96.46)	96.80 (87.45)	98.80 (90.88)	97.87 (95.07)
R_{merge}[b]	0.046 (0.098)	0.074 (0.361)	0.052 (0.123)	0.133 (0.558)
$CC_{1/2}$	0.965	0.905	0.977	0.670
Refinement statistics				
No. of protein atoms	1198	2449	1212	1212
R factor (%)[c]	0.1540	0.1740	0.1602	0.1967
R_{free} (%)[d]	0.2002	0.2240	0.1884	0.2298
RMSD bond length (Å)	0.020	0.019	0.024	0.024
RMSD bond angles (°)	2.04	1.82	2.16	2.03
Overall Mean B factor	18.13	18.70	14.73	16.06
Ramachandran plot (%)[e]				
Most favored residues	99.33	97.37	98.68	97.35
Outliers	0.00	0.00	0.00	0.00

[a] Values in parentheses correspond to the highest resolution shells. [b] $R_{merge} = \Sigma|I - \langle I \rangle|/\Sigma(I)$, where I is the individual intensity observation and $\langle I \rangle$ is the mean of all measurements of I. [c] $R = \Sigma||F_o| - |F_c||/\Sigma|F_o|$, where F_o and F_c are the observed and calculated structural factors respectively. [d] R_{free} was calculated by using 5% of the randomly selected diffraction data which were excluded from the refinement. [e] As calculated using *MolProbity*

2.4 Discussion

2.4.1 Formation of wt and H64A Mb^{II}-RNO complexes as monitored by UV-vis spectroscopy

My UV-vis spectroscopy studies were designed to determine the relationship between ligand sterics and the extent of $swMb^{II}$-RNO complex formation, and to establish the degree to which the distal His64 residue limits RNO access into the active site. In the wt swMb protein complexes, I expected to see an inverse relationship between RNO (R = Me, Et, Pr, *i*Pr) sterics and extent of wt $swMb^{II}$-RNO formation as reported by Mansuy [9] and Yi [54] for the related hhMb protein. I also hypothesized that smaller substrates would reach maximum extents of formation faster than their larger counterparts. My reactivity studies supported both hypotheses for the wt swMb protein. However, the analogous reactions with the H64A mutant reveled an opposite trend for the extent of H64A $swMb^{II}$-RNO complex formation. In other words, the extent of formation increased gradually by addition of each CH_2 group or branching made to the RNO. Furthermore, for the H64A swMb system, I expected to see faster complex formation times due to the absence of the "gatekeeper" His64 residue in the distal pocket, yet I anticipated RNO sterics to remain a factor. To my surprise, the H64A mutation appeared to remove RNO sterics as a factor in heme-nitroso binding. This was evidenced by the rapid (~5 sec) H64A $swMb^{II}$-RNO complex formations for all RNOs regardless of size, as compared to the R-size dependent rates of formation for the equivalent wt reactions. Previous reports for the bulky nitrosoamphetamine (AmphNO) substrate showed the formation of H64A $swMb^{II}$-AmphNO to be relatively slow (~24 h) despite the protein not having the His residue at the entrance of the active site [13]. The H64A $swMb^{II}$-AmphNO results suggest that RNO sterics alone are important in dictating reaction times. However, the set of RNOs selected in my study are much smaller than the AmphNO ligand, and sterics do not appear to play a significant role in product formation time.

2.4.2 Comparison of the hh and swMb^{II}-MeNO and -EtNO structures

Prior to this work, there were only two X-ray crystal structures of Mb in complex with alkyl-RNOs, and these were reported by a former group member, Dr. Copeland [27, 28]. Those structures were obtained using Mb purified from horse heart. I utilized recombinant swMb in my study. In both hh and sw Mb, the MeNO and EtNO ligands are N-bound to the Fe-atom of the heme (Figure 2.25). Comparison of the hh and swMb^{II}-MeNO structures show negligible differences in ligand coordination within the active site. In the distal pocket, the side chain of His64 in hhMb swings outwards as compared to swMb. The distance between the hh and sw His64(N$^{\varepsilon}$) atoms was measured as 1.1 Å. This shift in the location of the residue affects the H-bonding interactions between His64 and the ligand. The MeNO(O)-(N$^{\varepsilon}$)His64 bond distances were measured as 2.3 and 2.7 Å in hh and swMb respectively. Small positional shifts were also observed for Phe43 in the active site. Global alignment of the hh and swMb^{II}-MeNO models exposed small structural differences (RMSD value of 0.599). The back-bone of the GH-loops assume different folds between the proteins (not shown).

Similar comparisons were made between the swMb^{II}-EtNO structure from this work, and the previously published hhMb analogue. Likewise, the locations of the distal pocket His64 residue were slightly different between the hh and swMb structures (Figure 2.25B). In the swMb derivative the His64 residue is closer to the EtNO ligand, but is slightly shifted outwards in the hhMb derivative. The distance between His64(N$^{\varepsilon}$) atoms in the two derivatives was calculated to be 0.7 Å. These positional differences result in H-bonding distances of 2.1 and 2.7 Å (measured between EtNO(O) and His64(N$^{\varepsilon}$)) for the sw and hhMb models, respectively. The torsion angles for the C^2–C^1–N=O ligand backbone in swMb and hhMb were calculated as 152° and -41.0° respectively, which denote distinct ligand conformations between species. Interestingly, the arrangement of

EtNO in hhMb more closely resembles the H64A swMb counterpart than the wt model, see section *2.4.3.3* for further discussion.

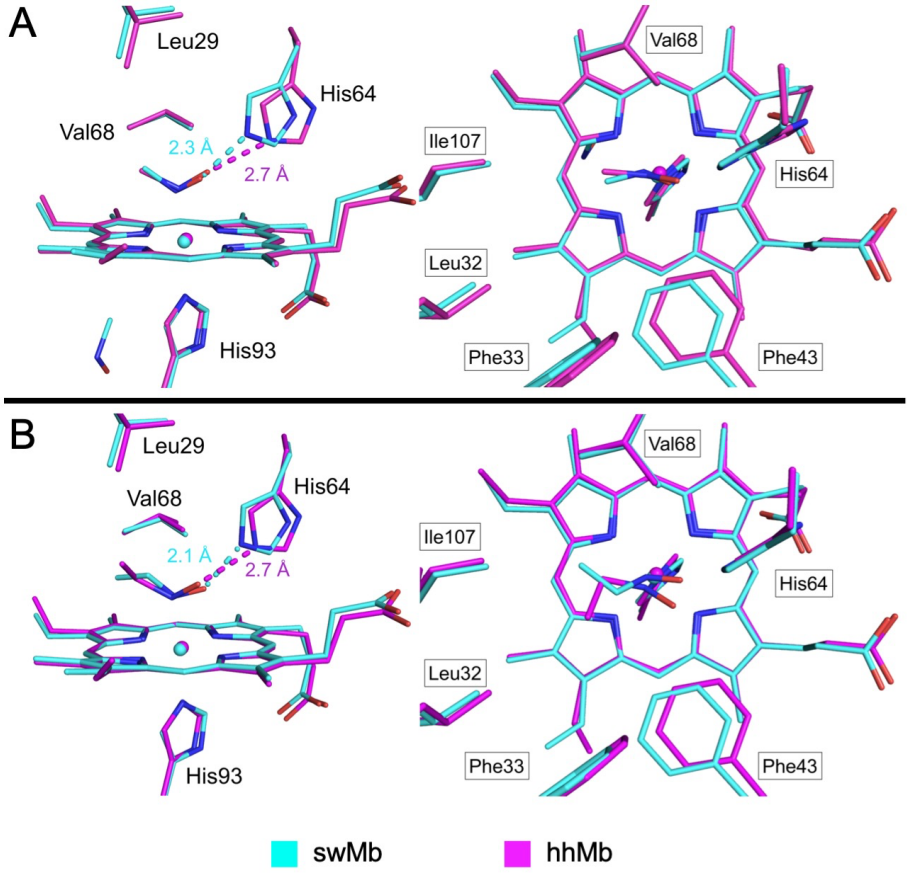

Figure 2.25. Superimposed models comparing RNO binding in the active sites of wt swMb and wt hhMb; *left*: side view and *right*: top view of the active sites of Mb. (A) Structure of wt swMb^{II}-MeNO (cyan) and wt hhMb^{II}-MeNO (magenta, PDB ID 2NSR) aligned by superpositioning along the C$_{\alpha}$ chain, RMSD = 0.599. (B) Structure of swMb^{II}-EtNO (cyan) and hhMb^{II}-EtNO (magenta, PDB ID 1NPG) aligned by superpositioning along the C$_{\alpha}$ chain, RMSD = 0.597.

2.4.3 Analysis of the influence of the distal His64 residue on RNO ligand orientation inside the heme-pocket of Mb

2.4.3.1 Overall comparison of RNO binding in wt and H64A swMb

In this work, I set out to investigate the relationship between RNO sterics and ligand orientation within the heme-pocket. A heme active site comparison of the wt and H64A swMb^{II}-

RNO structures (done by superpositioning along the C_{α} chain) obtained in this study is shown in Figure 2.26. This superpositioning indicates that amino acid composition of the distal pocket has a more significant role in ligand orientation than RNO sterics, at least for the ligands tested here. In wt swMb, the organic groups Me, Et and Pr have similar geometric positions within the active site. Furthermore, the C−N=O moieties of all three ligands are aligned similarly. On the other hand, the RNOs in the H64A mutant have vastly varied conformations as compared to the wt analogues. These results suggest that the presence of the His64 residue plays a more pronounced role in dictating the spatial arrangement of the RNO than ligand sterics.

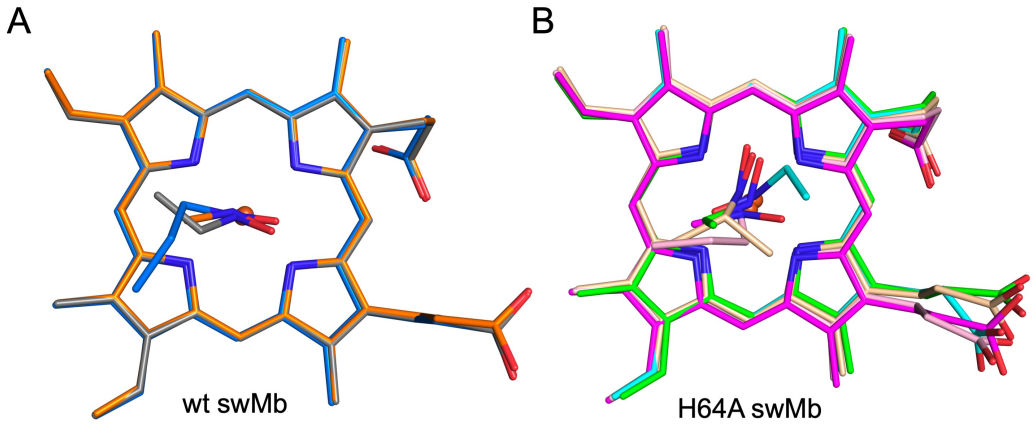

Figure 2.26 Comparison of the active sites of wt and H64A swMb^{II}-RNO structures obtained in this work. A) Overlaid wt swMb^{II}-RNO structures: orange -MeNO, gray -EtNO, marine -PrNO. B) Overlaid H64A swMb^{II}-RNO structures: magenta -MeNO, green -EtNO Chain A, cyan -EtNO Chain B, pink -PrNO, wheat -*i*PrNO.

2.4.3.2 Comparison of wt and H64A swMb^{II}-MeNO structures

Analysis of the active sites of wt and H64A swMb^{II}-MeNO structures reveal similar conformations for the MeNO molecule (Figure 2.27A), with an RMSD value of only 0.143 Å between the two ligands. Residue Val68, which is located above the MeNO molecule, has a different arrangement in each structure. In the wt protein the methyl groups of the side chain are

pointed towards the ligand, while the opposite holds true in the H64A structure. However, both MeNO molecules are equidistant from the closes C-atoms of Val68.

The overall alignment of the swMb-MeNO structures along the C_{α} chain resulted in an RMSD value of 0.467 Å. The major structural differences at the tertiary level are located in the GH-loop area (Figure 2.27B), indicating that RNO binding did not affect the structural integrity of the protein. A notable difference between the structures is the presence of a second MeNO ligand in the wt model. This MeNO molecule is located in the Xe-1 pocket, which has been speculated by others to be a site for O_2 storage [50]. The wt and H64A swMb^{II}-RNO derivatives were prepared using different protocols, ligand soaking and co-crystallization respectively, which is likely the source of this distinction. Nevertheless, it is interesting to see that MeNO can occupy both the Fe center of the heme and the Xe-1 pocket, which are both thought to be needed by the protein for O_2 storage.

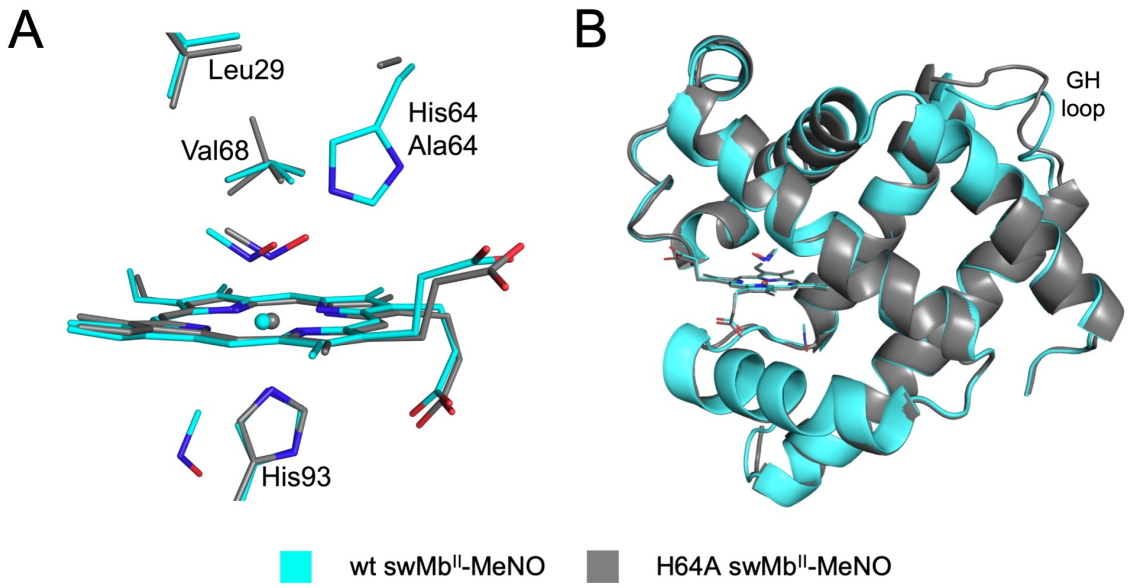

Figure 2.27. Overlaid models comparing MeNO binding in wt and H64A swMb. The structures were aligned by superpositioning along the C_{α} chain, RMSD = 0.467. A) side view of the active sites, B) overall protein fold comparison of wt and H64A swMb^{II}-MeNO.

2.4.3.3 Comparison of wt and H64A -swMb^{II}-EtNO structures

Superpositioning of the wt and H64A swMb^{II}-EtNO structures along the C_α chain reveled significant differences in the mode of binding of the RNO ligand between the two structures. Active site comparisons of the wt and H64A Chain A models are shown in Figure 2.28. In the wt structure, the EtNO(O) atom is fixed through H-bonding to His64(N^ε) resulting in alignment of the C−N=O atoms in a similar spatial arrangement as observed for the MeNO (Figure 2.27). The lack of residue His64 in the active site of the H64A swMb heme-pocket allowed the EtNO ligand to adopt alternate conformations. In Chain A of the H64A swMb^{II}-EtNO structure, the N=O region of the ligand is oriented inward towards the N^{22}-atom of the heme. This rotation necessitates the ethyl group of the RNO to adopt a different conformation than observed in the wt derivative.

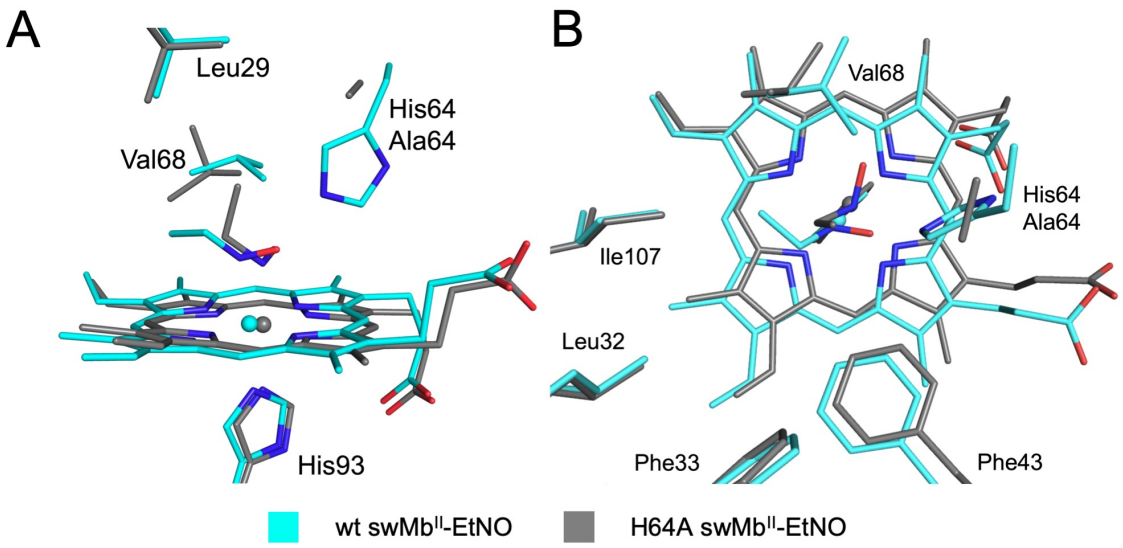

Figure 2.28. Superimposed models comparing EtNO binding in wt and H64A swMb^{II}-EtNO Chain A. A) side view and B) top view of the active sites of swMb.

Val68 has different orientations in the distal pockets of both proteins. In the wt protein, the methyl groups of Val68 point down towards the ligand. In the H64A model, they are oriented away from the RNO. Furthermore, in the wt structure, the ethyl group of EtNO is held in place by a small groove created by residues Val68 and Ile107 (Figure 2.29). In contrast, the ethyl group in

the H64A structure points away from Val68 towards a small tunnel located by Phe43, and this observation is also evident in the top view of the heme-pocket (Figure 2.28B). Interestingly, the RNO ligand of the hhMb^{II}-EtNO adduct (Figure 2.25B) has a geometric orientation more closely resembling the H64A swMb^{II}-EtNO (ChainA) structure than the wt swMb^{II}-EtNO derivative, suggesting that this is a more favorable arrangement for the EtNO molecule.

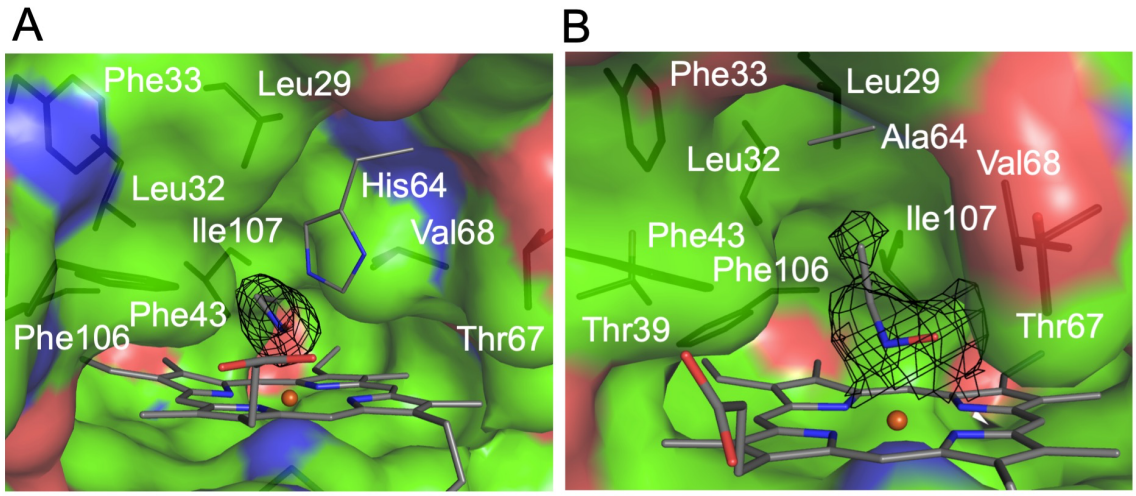

Figure 2.29 Surface of swMb pockets where EtNO is located. (A) wt Mb^{II}-EtNO and (B) H64A Mb^{II}-EtNO Chain A. The surface of His/Ala64 and Arg45 were omitted for clarity. Figures A and B are slightly rotated to highlight the different cavities occupied by the ethyl groups. The black mesh represents the F_o–F_c omit electron density maps contoured at 3σ.

The most distinctive features in EtNO binding are observed in Chain B of the H64A swMb^{II}-EtNO product (Figure 2.30). In this model, the N=O region of the ligand is situated in the hydrophobic interior of the protein, and the ethyl group is oriented towards the solvent exterior. This does not seem to be a favorable conformation for the ligand, as implied by its low occupancy (60%), and partial replacement by water (40%) in the structure. I note that it is highly unusual for a hydrophobic moiety in a Mb ligand to orient itself towards the hydrophobic exterior of the active site.

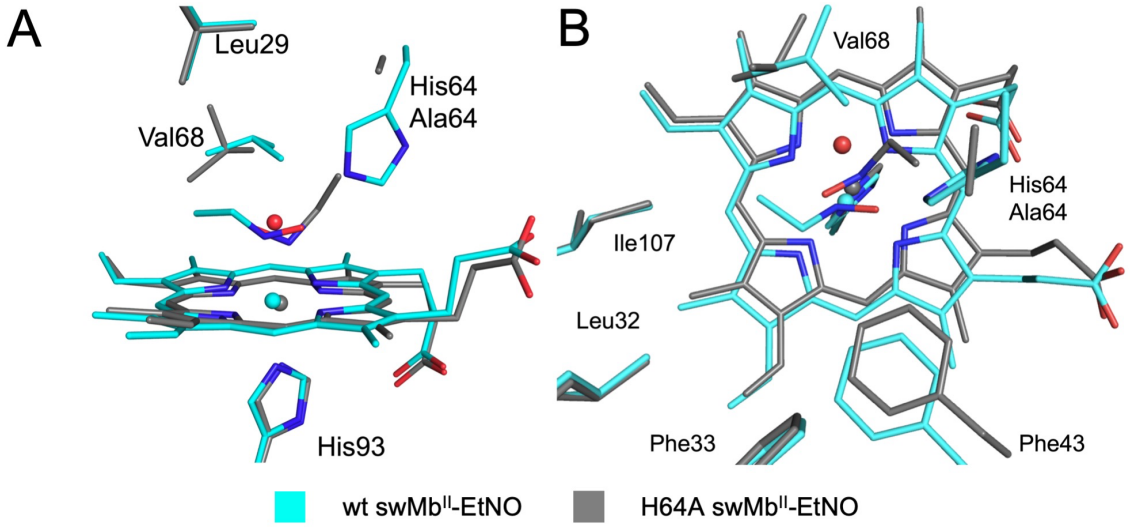

Figure 2.30. Superimposed models comparing EtNO binding in wt and H64A swMb^{II}-EtNO Chain B. A) side view and B) top view of the active sites of swMb.

Finally, alignment of the wt and both H64A swMb^{II}-EtNO chains revealed minor differences between the structures located in the CD- and GH-loops (Figure 2.31). This suggest that RNO binding serves to inhibit the protein by occupying the active site, but it does not harm its overall architecture.

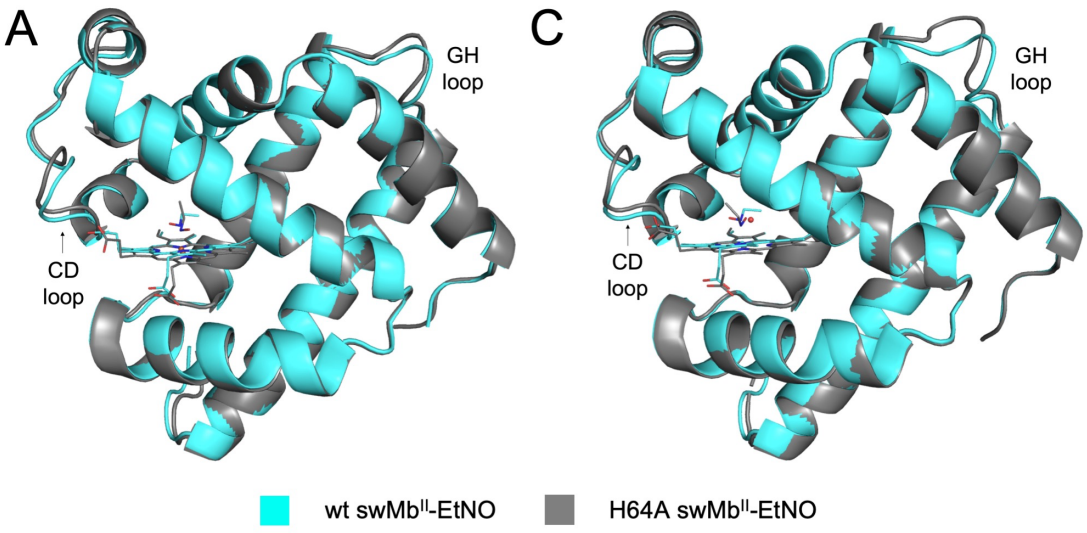

Figure 2.31 Overall protein fold comparison of wt and H64A swMb^{II}-EtNO structures The structures were aligned by superpositioning along the C$_{\alpha}$ chain, A) Chain A, RMSD = 0.380, B) Chain B, RMSD = 0.372.

2.4.3.4 Comparison of wt and H64A -swMb^{II}-PrNO structures

Comparisons of the wt and H64A swMb^{II}-PrNO models show different ligand conformations. In the wt proteins, the PrNO(O) atom is H-bonded to His64(N$^{\varepsilon}$), which imposes geometric arrangements for the C−N=O moiety similar to those observed for the MeNO and EtNO ligands in the wt proteins (Figures 2.27 and 2.28). Without the His64 residue (in the H64A mutant) to anchor the O-atom, PrNO is free to rotate towards the inside of the heme-pocket. Furthermore, alignment of the wt and H64A swMb^{II}-PrNO models show that their global structures are nearly identical (Figure 2.32). Only slight differences were noted in the CD-loop region of the proteins, with an RMSD value of 0.186.

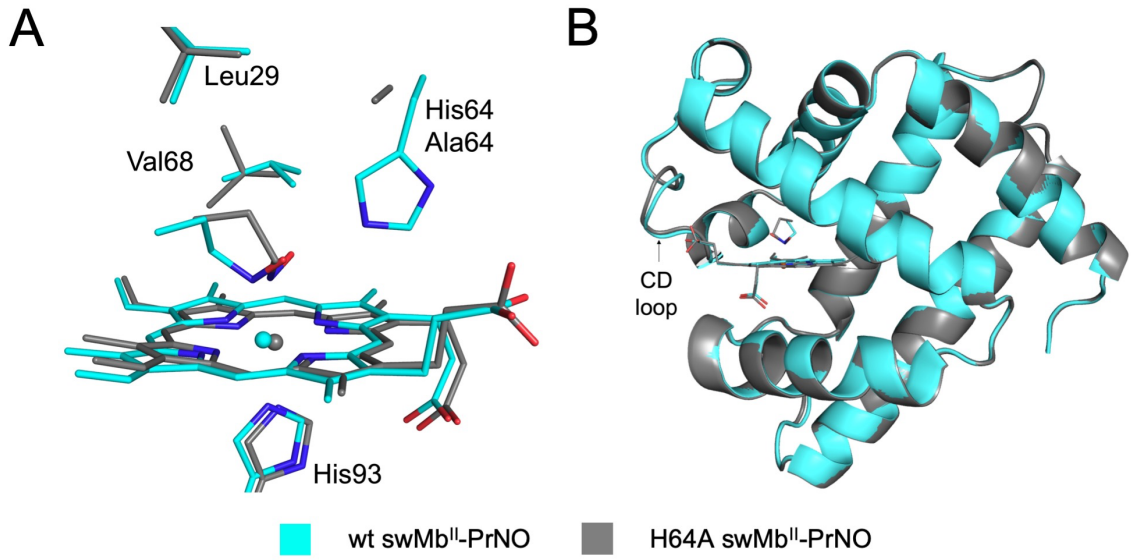

Figure 2.32. Superimposed models comparing PrNO binding in wt and H64A swMb. The structures were aligned by superpositioning along the C$_{\alpha}$ chain, RMSD = 0.186. A) side view of the active sites, B) overall protein fold comparison of wt and H64A swMb^{II}-PrNO.

I solved the H64A swMb^{II}-PrNO structure from three independent data sets using distinct crystals. Unlike my H64A swMb^{II}-EtNO product which had two conformations for the RNO ligand, the PrNO adopted the same conformation each time. This prompted me to ask why EtNO is able to rotate, whereas PrNO's conformation is relatively fixed within the active site of H64A

swMb. Analysis of the protein surface showed that the propyl group is buried inside a small hydrophobic channel located in the back of the active site (Figure 2.33A), whereas the ethyl group is too short to be trapped in this tunnel (Figure 2.29B). Furthermore, the propyl group in the wt structure occupies the same tunnel as the H64A analogous structure, despite having different geometric arrangements for the RNO itself (Figure 2.33B). These results suggest that in the case of the PrNO molecule, ligand sterics (instead of the His64 residue) dominate substrate orientation.

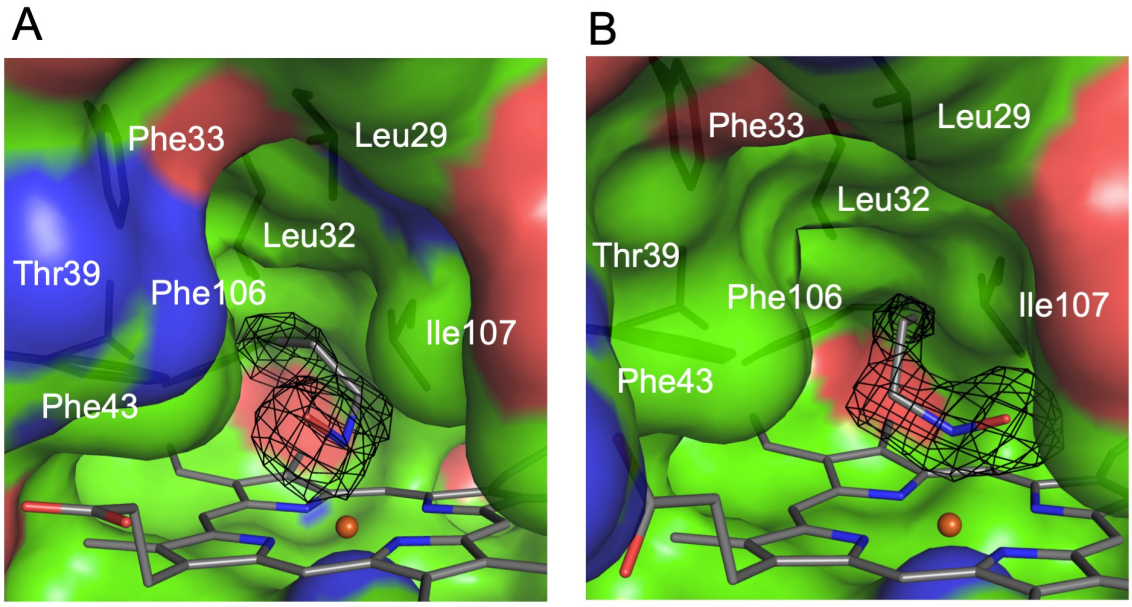

Figure 2.33 The interior surface of swMb pockets where PrNO is located. (A) wt Mb^{II}-PrNO and (B) H64A Mb^{II}-PrNO. The surface of His/Ala64 and Arg45 were omitted for clarity of view. The black mesh represents the F_o–F_c omit electron density maps contoured at 3σ.

2.4.3.5 H64A -swMb^{II}-iPrNO structure and predicted wt models

I successfully solved the crystal structure of the H64A swMb^{II}-*i*PrNO derivative (Figure 2.24). However, neither my co-crystallization nor ligand soaking attempts yielded positive crystallization results for the wt analog. To probe why crystals of the wt swMb^{II}-*i*PrNO complex were unable to form readily, I docked the ligand into the ferric wt swMb^{III}-H_2O protein (PDB ID 2MBW). In the hypothetical structure, I modeled the C−N=O moiety in a similar spatial

arrangement as previously described in the swMb^{II}-RNO structures (Figure 2.26). I also took into account the restrictive movement imposed by H-bonding with the distal His64 residue. In this predicted structure, the methyl groups of *i*PrNO clash with Val68 and Phe43 (Figure 2.34A). The distance between atoms Phe43(C^{ζ}) and PrNO(C^{2}) was measured as 2.5 Å, and the distance from Val68($C^{\gamma 1}$) to PrNO(C^{2}) was calculated as 2.8 Å. These calculated distances between the ligand and distal pocket residues are closer than measured for any other structure in this study. Comparison to the H64A derivative shows that the ligand was able to overcome this problem due to lack of H-bonding to His64 (Figure 2.34B). In the H64A swMb^{II}-*i*PrNO structure, the N=O moiety of the ligand is rotated into the active site. In such a way that one of the CH_3 groups of the ligand is consequently angled towards the hydrophobic tunnel located by residue Phe43 (described in Figures 2.29 and 2.33). The other CH_3 group is directed towards the solvent exterior of the protein to accommodate nitroso binding.

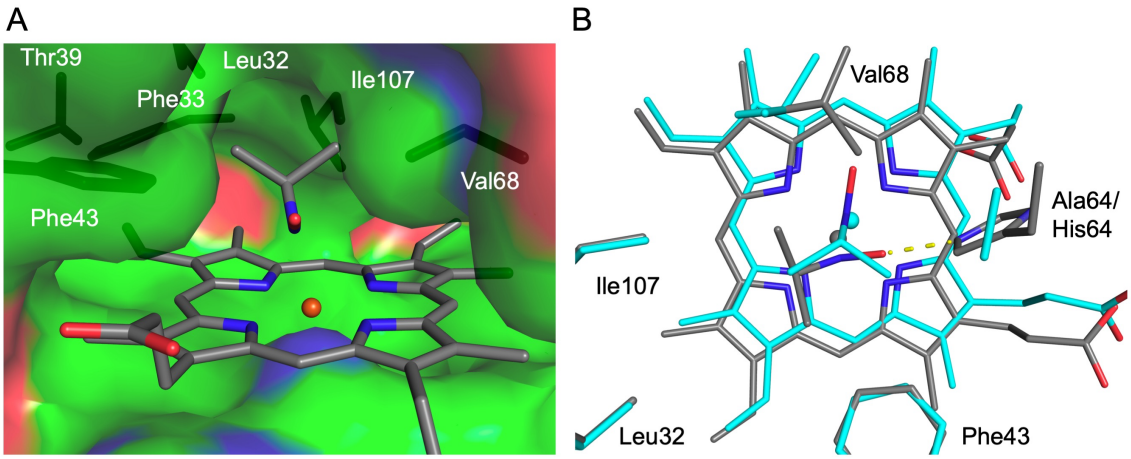

Figure 2.34 A) Docking model predicting the binding mode of *i*PrNO in wt swMb (PDB ID 2MBW). B) Superpositioning of the H64A swMb^{II}-*i*PrNO structure and the hypothetical wt swMb^{II}-*i*PrNO model.

To the best of my knowledge, my H64A swMb^{II}-*i*PrNO structure is the first heme-protein structure reported in complex with *i*PrNO. However, synthetic models containing *i*PrNO in the Fe^{II}-binding state have been previously described [55] and an unpublished analog from our lab is show in Figure 2.35. In the synthetic models, *i*PrNO assumes a similar configuration along the heme as observed in the H64A swMb heme-pocket. With and without the active site residues, these complexes adopt an RNO orientation in which the C−N=O nitroso planes bisect the porphyrin nitrogen atoms. Furthermore, the angles at which the C−N=O plane crosses the 4-N heme plane were calculated for the H64A swMb^{II}-*i*PrNO protein structure and the synthetic (PPDME)Fe(*i*-PrNO)(1-MeIm) model as 89° and 86° respectively. These results indicate that *i*PrNO binds the Fe center of the porphyrin in an almost perpendicular manner, perhaps due to the steric symmetry of the ligand.

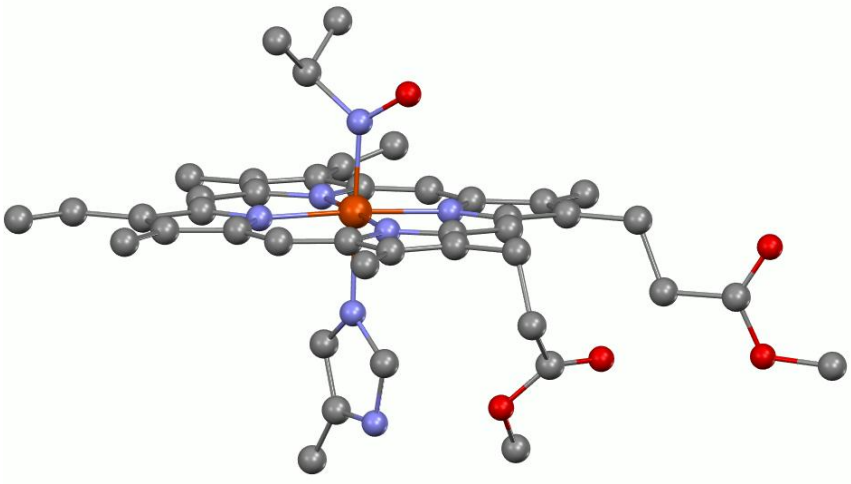

Figure 2.35 The small molecule X-ray crystal structure of (PPDME)Fe(*i*-PrNO)(1-MeIm).

2.5 Conclusion

Heme-nitroso binding has been implicated in enzyme inhibition and protein degradation which may lead to health problems, making it a relevant topic of study. The four previously

reported X-ray crystal structures of Mb-RNO complexes hinted at a possible correlation between RNO sterics and ligand orientation within the active site, where small R groups are oriented toward the hydrophobic pocket (for hhMb) [27] and larger organic-R groups are forcibly exposed to the solvent exterior (for swMb) [13]. These discrepancies in ligand coordination could have alternatively been described as resulting from differences in distal pocket composition between the proteins (hh *vs* sw) used to prepare those structures. My work was designed to (i) determine the mode of binding (O-bound *vs* N-bound), (ii) determine the importance of distal pocket composition on complex formation and ligand orientation, and (iii) determine the effects of ligand sterics on RNO binding and stability.

My preliminary goal was to characterize the reactions of wt swMb and its H64A mutant with a series of nitroalkanes under reducing conditions. By using RNO_2 precursors of increasing alkyl group size (R = Et, Me, Pr, *i*Pr) for my UV-vis spectroscopy studies, I determined an inverse relationship between size of ligand and extent of formation of the wt $swMb^{II}$-RNO complexes. Furthermore, the time it took each wt $swMb^{II}$-RNO complex to reach maximum extent of formation increased with addition of each $-CH_2$ group or branching of the ligand. However, the analogous H64A reactions showed a direct correlation between ligand sterics and extent of formation. Furthermore, lack of His64 allowed the H64A $swMb^{II}$-RNO complexes to form almost instantaneously. These results allowed me to conclude that ligand sterics only influence complex formation when His64 is present to restrict access into the active site.

After confirming complex formation in solution, I used X-ray crystallography to solve the structures of the wt and H64A $swMb^{II}$-RNO products. I was able to determine that H-bonding to His64 in the distal pocket influenced the geometric arrangement of the ligand within the active site to a greater extent than differences in R-group sterics. In the presence of His64, the N=O moieties

of the ligands point directly towards the solvent exterior of the protein, causing the R-groups to be oriented towards the hydrophobic interior of the protein; in the H64A mutant, the RNOs are free to rotate within the active site. However, it would be incorrect to say that RNO sterics had absolutely no influence in their own orientation. For the small MeNO adducts, no significant differences were observed between the protein models. I also noted that the Et group in wt swMb^{II}-EtNO was small enough to situate itself in-between the side-chains of Val68 and Ile107. The Et group was also short enough to rotate freely inside the active site and occupy two conformations in the H64A swMb^{II}-EtNO structure. Interestingly, the propyl groups in wt swMb^{II}-PrNO were too big to fit between Val68 and Ile107. They were also too long, and as a result, the Pr group was sequestered inside a small tunnel behind the active site in both the wt and H64A swMb^{II}-PrNO structures. Furthermore, the sterics of *i*PrNO in wt swMb^{II}-*i*PrNO (hypothetical) clashed with side-chains inside the heme-pocket, which made the wt swMb^{II}-*i*PrNO short lived and unable to crystalize in the heme-nitroso bound state.

Together, these results provide a detailed description of the heme-nitroso chemistry occurring at the active site of Mb emanating from the reductive metabolism of nitro-compounds. Furthermore, my results allow me to conclude that nitroso binding to Mb renders the protein unable to bind O_2 and perform its normal functions.

2.6 References

1. Moller, J.K. and L.H. Skibsted, *Nitric oxide and myoglobins.* Chem Rev, 2002. **102**(4): pp 1167-78.
2. Dejam, A., et al., *Emerging role of nitrite in human biology.* Blood Cells Mol Dis, 2004. **32**(3): pp 423-9.
3. Gladwin, M.T., R. Grubina, and M.P. Doyle, *The new chemical biology of nitrite reactions with hemoglobin: R-state catalysis, oxidative denitrosylation, and nitrite reductase/anhydrase.* Acc Chem Res, 2009. **42**(1): pp 157-67.
4. Wang, B., et al., *Nitrosyl Myoglobins and Their Nitrite Precursors: Crystal Structural and Quantum Mechanics and Molecular Mechanics Theoretical Investigations of Preferred Fe -NO Ligand Orientations in Myoglobin Distal Pockets.* Biochemistry, 2018. **57**(32): pp 4788-4802.
5. Feelisch, M., et al., *Long-lasting blood pressure lowering effects of nitrite are NO-independent and mediated by hydrogen peroxide, persulfides and oxidation of protein kinase G 1alpha redox signaling.* Cardiovasc Res, 2019. *Ahead of Print*
6. Helms, C.C., X. Liu, and D.B. Kim-Shapiro, *Recent insights into nitrite signaling processes in blood.* Biol Chem, 2017. **398**(3): pp 319-329.
7. Heinecke, J.L., et al., *Nitrite reduction by Co(II) and Mn(II) substituted myoglobins: towards understanding necessary components of Mb nitrite reductase activity.* J Inorg Biochem, 2012. **107**(1): pp 47-53.
8. Gowenlock, B.G. and G.B. Richter-Addo, *Preparations of C-nitroso compounds.* Chem Rev, 2004. **104**(7): pp 3315-40.
9. Mansuy, D., J.C. Chottard, and G. Chottard, *Nitrosoalkanes as Fe(II) Ligands in Hemoglobin and Myoglobin Complexes Formed from Nitroalkanes in Reducing Conditions.* European Journal of Biochemistry, 1977. **76**(2): pp 617-623.
10. Takeda, Y. and H. Kanaya, *Formation of nitroso compounds and mutagens from tranquilizers by drug/nitrite interaction.* Cancer Lett, 1981. **12**(1-2): pp 81-6.
11. Liu, D., K. Thomson, and A.C. Anderson, *Identification of nitroso compounds from biotransformation of 2,4-dinitrotoluene.* Appl Environ Microbiol, 1984. **47**(6): pp 1295-8.
12. Lee, J., et al., *Interactions of organic nitroso compounds with metals.* Chem Rev, 2002. **102**(4): pp 1019-66.
13. Wang, B., et al., *Nitrosoamphetamine binding to myoglobin and hemoglobin: Crystal structure of the H64A myoglobin-nitrosoamphetamine adduct.* Nitric Oxide, 2017. **67**: pp 26-29.
14. Taxak, N., et al., *Metabolic-intermediate complex formation with cytochrome P450: theoretical studies in elucidating the reaction pathway for the generation of reactive nitroso intermediate.* J Comput Chem, 2012. **33**(21): pp 1740-7.
15. Durchschein, K., et al., *Reductive biotransformation of nitroalkenes via nitroso-intermediates to oxazetes catalyzed by xenobiotic reductase A (XenA).* Org Biomol Chem, 2011. **9**(9): pp 3364-9.
16. Martinez, M.A., et al., *Acute nitrobenzene poisoning with severe associated methemoglobinemia: identification in whole blood by GC-FID and GC-MS.* J Anal Toxicol, 2003. **27**(4): pp 221-5.
17. Lee, C.H., et al., *Two cases of methemoglobinemia induced by the exposure to nitrobenzene and aniline.* Ann Occup Environ Med, 2013. **25**(1): pp 31.

18. Alston T.A, P.J.T.D., Bright H.J., *Enzyme Inhibition by Nitro and Nitroso Compounds* Acc. Chem. Res., 1983. **16**: pp 418-424.
19. Yamada, H., et al., *Tissue-specific expression, induction, and inhibition through metabolic intermediate-complex formation of guinea pig cytochrome P450 belonging to the CYP2B subfamily.* Arch Biochem Biophys, 1992. **299**(2): pp 248-54.
20. Yi, J., et al., *Degradation of human hemoglobin by organic C-nitroso compounds.* Chem Commun (Camb), 2013. **49**(95): pp 11179-81.
21. Maples, K.R., P. Eyer, and R.P. Mason, *Aniline-, phenylhydroxylamine-, nitrosobenzene-, and nitrobenzene-induced hemoglobin thiyl free radical formation in vivo and in vitro.* Mol Pharmacol, 1990. **37**(2): pp 311-8.
22. Murayama, M., *The combining power of normal human hemoglobin for nitrosobenzene.* J Biol Chem, 1960. **235**: pp 1024-8.
23. Schimelman, M.A., J.M. Soler, and H.A. Muller, *Methemoglobinemia: nitrobenzene ingestion.* JACEP, 1978. **7**(11): pp 406-8.
24. Lareng, L., et al., *[Acute, toxic methemoglobinemia from accidental ingestion of nitrobenzene].* Eur J Toxicol Environ Hyg, 1974. **7**(1): pp 12-6.
25. Yi, J., A.S. Soares, and G.B. Richter-Addo, *Crystallographic characterization of the nitric oxide derivative of R-state human hemoglobin.* Nitric Oxide, 2014. **39**: pp 46-50.
26. Wang, L.S., et al., *The first structural studies of nitrosoarene binding to iron-(II) and -(III) porphyrins.* Chemical Communications, 1996(3): pp 323-324.
27. Copeland, D.M., A.H. West, and G.B. Richter-Addo, *Crystal structures of ferrous horse heart myoglobin complexed with nitric oxide and nitrosoethane.* Proteins, 2003. **53**(2): pp 182-92.
28. Copeland, D.M., *A Study of the Interactions of Nitric Oxide and Nitric Oxide Containing Molecules with Heme Proteins*, in *Chemistry and Biochemistry* 2006, University of Oklahoma Norman, Oklahoma. Dissertation
29. Ruscio, J.Z., et al., *Atomic level computational identification of ligand migration pathways between solvent and binding site in myoglobin.* Proc Natl Acad Sci U S A, 2008. **105**(27): pp 9204-9.
30. Johnson, K.A., J.S. Olson, and G.N. Phillips, Jr., *Structure of myoglobin-ethyl isocyanide. Histidine as a swinging door for ligand entry.* J Mol Biol, 1989. **207**(2): pp 459-63.
31. Scott, E.E., Q.H. Gibson, and J.S. Olson, *Mapping the pathways for O_2 entry into and exit from myoglobin.* J Biol Chem, 2001. **276**(7): pp 5177-88.
32. Smith, D.J. and R.C. Anderson, *Toxicity and metabolism of nitroalkanes and substituted nitroalkanes.* J Agric Food Chem, 2013. **61**(4): pp 763-79.
33. Shu, Y.Z., B.M. Johnson, and T.J. Yang, *Role of biotransformation studies in minimizing metabolism-related liabilities in drug discovery.* AAPS J, 2008. **10**(1): pp 178-92.
34. Piska, K., et al., *Cunninghamella Biotransformation--Similarities to Human Drug Metabolism and Its Relevance for the Drug Discovery Process.* Curr Drug Metab, 2016. **17**(2): pp 107-17.
35. Dayal, R., et al., *Oxidative denitrification of 2-nitropropane and propane-2-nitronate by mouse liver microsomes: lack of correlation with hepatocytotoxic potential.* Chem Biol Interact, 1991. **79**(1): pp 103-14.
36. Conaway, C.C., et al., *Comparison of oxidative damage to rat liver DNA and RNA by primary nitroalkanes, secondary nitroalkanes, cyclopentanone oxime, and related compounds.* Cancer Res, 1991. **51**(12): pp 3143-7.

37. Hussain, N.S., et al., *Oxidative DNA and RNA damage in rat liver due to acetoxime: similarity to effects of 2-nitropropane.* Carcinogenesis, 1990. **11**(6): pp 1013-6.
38. Hata, Y., et al., *Aziridine biotransformation by microsomes and lethality to hepatocytes isolated from rat.* Chem Biol Interact, 1987. **63**(2): pp 171-84.
39. Quillin, M.L., et al., *High-resolution crystal structures of distal histidine mutants of sperm whale myoglobin.* J Mol Biol, 1993. **234**(1): pp 140-55.
40. Springer, B.A. and S.G. Sligar, *High-level expression of sperm whale myoglobin in Escherichia coli.* Proc Natl Acad Sci U S A, 1987. **84**(24): pp 8961-5.
41. Phillips, G.N., Jr., et al., *Crystal structure of myoglobin from a synthetic gene.* Proteins, 1990. **7**(4): pp 358-65.
42. Wang, B., L.M. Thomas, and G.B. Richter-Addo, *Organometallic myoglobins: Formation of Fe-carbon bonds and distal pocket effects on aryl ligand conformations.* J Inorg Biochem, 2016. **164**: pp 1-4.
43. Wang, B., *X-Ray Crystal Structures and Characterization of the Products from the Interactions of Myoglobin with Nitrogen Oxides and Arylhydrazines, and Nitroreductase Interactions with Organic Nitro Compounds* in *Department of Chemistry and Biochemistry* 2016, University of Oklahoma Norman, OK pp. 176.
44. Otwinowski, Z. and W. Minor, *Processing of X-ray diffraction data collected in oscillation mode.* Methods Enzymol, 1997. **276**: pp 307-26.
45. Winn, M.D., et al., *Overview of the CCP4 suite and current developments.* Acta Crystallographica Section D-Biological Crystallography, 2011. **67**: pp 235-242.
46. Murshudov, G.N., A.A. Vagin, and E.J. Dodson, *Refinement of macromolecular structures by the maximum-likelihood method.* Acta Crystallographica Section D-Structural Biology, 1997. **53**: pp 240-255.
47. Emsley, P. and K. Cowtan, *Coot: model-building tools for molecular graphics.* Acta Crystallographica Section D-Biological Crystallography, 2004. **60**: pp 2126-2132.
48. Chen, V.B., et al., *MolProbity: all-atom structure validation for macromolecular crystallography.* Acta Crystallographica Section D-Structural Biology, 2010. **66**: pp 12-21.
49. Yi, J., *Biologically relevant NOx adducts of cystein, myoglobin, and hemoglobin*, in *Department of Chemistry and Biochemistry* 2008, University of Oklahoma Norman, Oklahoma. Dissertation
50. Abraini, J.H., et al., *Crystallographic studies with xenon and nitrous oxide provide evidence for protein-dependent processes in the mechanisms of general anesthesia.* Anesthesiology, 2014. **121**(5): pp 1018-27.
51. Raczyńska, E.D., et al., *Tautomeric equilibria, H-bonding and π-electron delocalization ino-nitrosophenol. A B3LYP/6-311 + G(2df,2p) study.* Journal of Physical Organic Chemistry, 2005. **18**(8): pp 892-897.
52. Beaudoin, D. and J.D. Wuest, *Dimerization of Aromatic C-Nitroso Compounds.* Chem Rev, 2016. **116**(1): pp 258-86.
53. Long, J.A., N.J. Harris, and K. Lammertsma, *Formaldehyde oxime <--> nitrosomethane tautomerism.* J Org Chem, 2001. **66**(20): pp 6762-7.
54. Yi, J., *Biologically relevant NOx adducts of cysteine, myoglobin, and hemoglobin*, in *Department of Chemistry and Biochemistry*. 2008, University of Oklahoma: OKShare. Dissertation

55. Sohl, C.D., et al., *Synthesis and solid-state molecular structures of nitrosoalkane complexes of iron porphyrins containing methanol, pyridine, and 1-methylimidazole ligands.* J Inorg Biochem, 2004. **98**(7): pp 1238-46.

Chapter 3. Crystallographic characterization of the stepwise degradation of human hemoglobin induced by *C*-nitroso binding

3.1 Introduction

Hemoglobin (Hb) is a small globular protein found in the red blood cells (RBCs) of most vertebrates. In humans, ~96% of Hb is in its tetrameric form consisting of two α and two β subunits. Embedded in each subunit is a heme cofactor, which the protein uses to bind and transport oxygen throughout the body. Nitroalkanes (RNOs) are valance isoelectronic with O_2 and can also bind the Fe center of heme. However, the resultant heme-nitroso interaction is detrimental to human health.

As detailed in Chapter 1, nitrosoalkanes are bioactivation metabolites of certain nitrogenous species including nitroalkanes (RNO_2) (Figure 3.1) [1]. Once formed, binding of RNOs to hemeproteins can be deleterious. In the case of cytochrome P450 enzymes, RNOs can bind heme to form Fe^{II}-RNO inhibitory complexes [2, 3]. In humans, exposure to nitroalkanes occurs mainly through the respiratory tract. This is particularly problematic because blood is metabolically competent to activate nitroalkanes to the reactive nitroso form [4]. Consequently, Hb regularly encounters RNOs, and interaction of the two has been implicated as a cause leading to protein degradation [5]. Ultimately, this heme-nitroso interaction can result in anemia [6-9] and subsequent accumulation of Fe in the spleen [10].

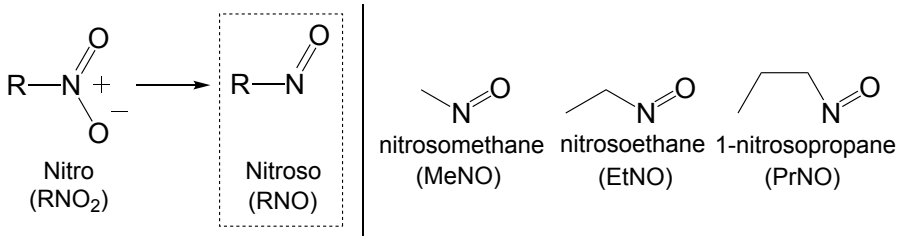

Figure 3.1 Reductive metabolism of nitroalkanes, and RNO metabolites used to track the degradation of Hb.

However, Hb degradation and its associated health implications are not limited to RNO binding. Great strives have been made to determine the mechanism of drug-induced hemolytic anemia in general. As the current model stands, the first step in the mechanism is oxidation of Hb by nucleophilic displacement of O_2 (or superoxide) from Hb^{II}-O_2, either by a water or a OH^- molecule [11, 12]. This results in ferric Hb with water bound at the 6th coordinating position. Afterwards, the protein is predicted to transition into a hemichrome state, a process which is reported to be reversible [13, 14]. Over time, high concentrations of hemichromes in RBCs provide enough "sticking points" for denatured Hb to accumulate and form Heinz bodies [15]. Ultimately, RBCs containing Heinz bodies undergo degradation causing hemolytic anemia and Fe accumulation in the spleen [15-17]. The proposed mechanism of Hb degradation is summarized below (Figure 3.2).

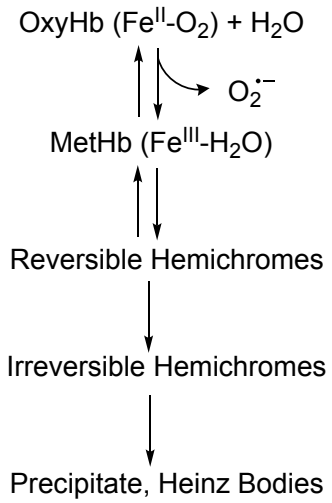

Figure 3.2 Currently proposed mechanism leading to Hb degradation [11, 12, 15].

Despite the health risks associated with Hb degradation, there is a lack of structural information showing the conformational changes that the protein undergoes as it progresses through each step. However, the Richter-Addo lab has taken initiative to determine the structural consequences resulting from *C*-nitroso binding to Hb. In 2013 Dr. Yi (from our lab) published two

X-ray crystal structures resulting from the interactions of Hb with RNOs [18]. Her crystals were prepared through the reductive metabolism of nitroalkanes (Figure 3.1). In the MeNO-related Hb derivative, the ligand was N-bound in both the α and β subunits. In her second structure, EtNO was observed N-bound to the Fe atom in the α subunit, but the heme active site of the β subunit was deformed [18]. Fe anomalous signals revealed two positions for the metal, one in its natural location and the other significantly displaced from the active site (Figure 3.3). Her work provided the first structural insight of such RNO induced protein damage by capturing heme-slippage. This contributed an additional step to the overall mechanism previously proposed by others.

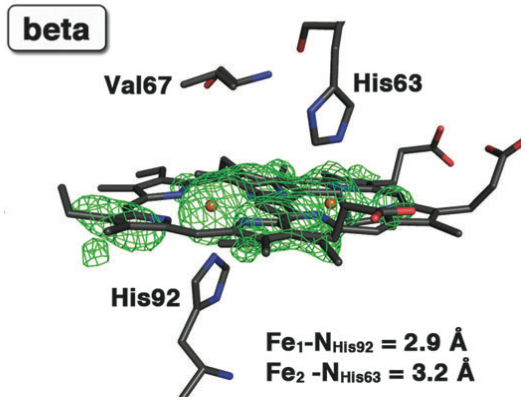

Figure 3.3 2 F_o–F_c omit electron density map for the beta subunit of the structure resulting from the reaction of dithionite reduced Hb^{II} and $EtNO_2$ (PDB ID 4M4B).

The goal of my research is to provide structural evidence of each step leading to Hb degradation. The structural differences observed between MeNO and EtNO binding in Dr. Yi's work prompted some questions: i) can we monitor EtNO induced degradation of Hb at different stages? and ii) will MeNO and PrNO, despite their steric differences, yield similar binding and degradation given enough time? Here, I present seven distinct X-ray crystal structures that show the chronological molecular changes that Hb undergoes as a result of RNO binding. Altogether, these structures provide a step-by-step mechanism of RNO induced Hb degradation.

3.2 Materials and Methods

3.2.1 Preparation of human hemoglobin

3.2.1.1 Isolation and purification of oxyHb (ferrous Hb^{II}-O_2) from red blood cells

Human hemoglobin (Hb) was isolated from packed red blood cells (RBC) according to previously established protocols by Antonini [19] and Safo [20] with a few modifications described hereafter. One unit of packed RBCs (300 mL) was obtained from the local Blood Bank at the University of Oklahoma Health Sciences Center (OUHSC). To protect the proteins from ice damage, the bag containing RBCs was carefully wrapped before being placed on ice until the Hb was isolated. Furthermore, all purification and temporary storage practices were performed at 4°C unless otherwise stated. All glassware, plasticware and buffers used for protein extraction and purification were autoclaved and chilled to 4°C prior to use.

Protein extraction began by washing 75 mL of packed RBCs with an equal volume of 0.9% NaCl. Then, the RBCs were separated by centrifugation (Beckman Coulter Avanti, JLA-16.250, 3.0 krpm, 20 min) and the supernatant was discarded. The RBC pellet was resuspended and washed again with 75 mL of 0.9% NaCl followed by centrifugation; this step was repeated for a total of three washes. After the third centrifugation, the RBC pellet was resuspended in 70 mL of lysis buffer (50 mM Tris, 4 g/L EDTA, pH 8.6 at 4 °C) and placed on ice for 40 min. The RBCs were then sonicated (Branson Sonifier 250) to break up the cells and to release oxyHb (ferrous Hb^{II}-O_2).

After lysis, the cell debris was removed by centrifugation (Beckman Coulter Avanti, JLA-16.250, 9.5 krpm, 2 h) and the supernatant containing the red ferrous Hb^{II}-O_2 was carefully transferred into a chilled beaker. Solid NaCl was added to the protein solution to a final concentration of 50 mg/mL and stirred for 1 h. Another round of centrifugation was performed to remove additional cell debris. Afterwards, the supernatant was pooled and dialyzed once in lysis

buffer (~6 h), and then twice (~8 h each time) in storage buffer (10 mM sodium phosphate buffer, 4 g/L EDTA, pH 7.0). Purification of ferrous Hb^{II}-O_2 concluded with a last round of centrifugation. The final concentration of the isolated ferrous Hb^{II}-O_2 was determined by UV-vis spectroscopy using its extinction coefficient at λ 541 nm (ε = 13.8 mM^{-1} cm^{-1}) and at λ 577 nm (ε = 14.6 mM^{-1} cm^{-1}) in 100 mM potassium phosphate buffer, pH 7.4 [19, 21]. The isolated protein was aliquoted into 15 mL Falcon™ tubes, flash frozen in liquid nitrogen and stored at -80 °C until needed.

3.2.1.2 Preparation of metHb (ferric Hb^{III}-H_2O)

Most experiments in this work required the oxidized metHb (ferric Hb^{III}-H_2O) as the starting material, which was obtained by oxidizing ferrous Hb^{II}-O_2. To do so, ferricyanide ($K_3[Fe(CN)_6]$) was added as an oxidizing agent in ~1.5 molar excess to the thawed ferrous Hb^{II}-O_2. The reaction was deemed complete upon observing a color change from red (characteristic of ferrous Hb^{II}-O_2) to brown (characteristic of ferric Hb^{III}-H_2O). Afterwards, the sample was loaded onto a G25 gel filtration column (equilibrated in 30 mM potassium phosphate buffer, pH 6.7) to remove excess ferricyanide. The brown-colored fractions corresponding to ferric Hb^{III}-H_2O were pooled together and concentrated to 30 mg/mL using a Millipore Amicon ultra filter with a cutoff of 10 kDa. The final concentration was determined by UV-vis spectroscopy using the extinction coefficient of the ferric Hb^{III}-H_2O protein at λ_{max} 406 nm (ε = 179 mM^{-1} cm^{-1}) in 100 mM potassium phosphate buffer, pH 7.4 [19, 21].

3.2.2 UV-vis spectral studies of the reactions of Hb with nitroalkanes ($MeNO_2$, $EtNO_2$ and $PrNO_2$)

UV-vis spectroscopy was used to monitor the reactions of dithionite reduced deoxyHb (ferrous Hb^{II}) with nitroalkanes (RNO_2, R= Me, Et and Pr) using similar conditions as described

in Chapter 2 and by Mansuy [22]. The reactions were carried out in 3.5 mL quartz cuvettes equipped with screw caps (Starna Cells). Each measurement was taken using a Hewlett Packard 8453 diode array spectrophotometer unless otherwise noted. The experiments were performed both aerobically and anaerobically to compare the stability of the ferrous Hb^{II}-RNO products in the presence of air.

3.2.2.1 Aerobic UV-vis spectroscopy

An initial reading of the starting ferric Hb^{III}-H_2O protein at a concentration of ~3 μM in 3 mL of 0.1 M phosphate buffer at pH 7.4, was taken. Sodium dithionite (DT; 1 M) was then added to a final concentration of 20 mM to reduce the protein. The spectrum corresponding to the ferrous deoxyHb^{II} was recorded, and each RNO precursor ($MeNO_2$, $EtNO_2$ or $PrNO_2$ half diluted in MeOH) was added into the cuvette to a final concentration of 20 mM. Spectrum readings were collected at regular time intervals to monitor the reaction over several days. Each day, the cuvettes were briefly opened and exposed to air to maintain aerobic conditions.

3.2.2.2 Anaerobic UV-vis spectroscopy

Prior to all anaerobic experiments, buffers were degassed by bubbling nitrogen through them for ~20-40 min, depending on their volume. Solid DT was weighed out and aliquoted into Eppendorf tubes aerobically. Then, solid DT and all liquids were transferred into an anaerobic MBraun chamber at least ~1 d prior to use and allowed to equilibrate. Dithionite was dissolved in buffer only after being degassed immediately prior to use. Ferric Hb^{III}-H_2O was degassed in small volumes (~100 μL) by simply degassing the vial headspace and allowing the protein to equilibrate inside the chamber for a few hours (bubbling nitrogen gas through the protein resulted in Hb aggregation).

The anaerobic reactions of ferrous Hb^{II} with nitroalkanes were performed using the same reactants and concentrations as described in section *3.2.2.1.* Each reactant was added anaerobically to a quartz cuvette and sealed to avoid exposure to O_2 upon being transported to the main lab area for data collection. To prevent the RNO_2 from reacting with ferrous Hb^{II} inside the anaerobic chamber, the ligand precursor was carefully pipetted directly onto the inside cover of the cuvette lid. The lid was then gently flipped over the cuvette and sealed. Afterwards, the cuvette was carefully transferred out of the chamber to the spectrophotometer for data collection, making sure not to mix the RNO_2 and Hb reagents. To confirm that the hanging drop of RNO_2 did not drip into the reaction mixture, a new spectrum was taken and compared to that of the previously recorded dithionite reduced ferrous Hb^{II} spectrum. If no difference in the spectrum was observed, the sealed cuvette was inverted to mix the reagents and start the reaction and the rest of the experiment was carried out as described for the aerobic reactions, but without breaking the seal to sustain anaerobic conditions.

3.2.2.3 Time-course and extent of formation for the ferrous Hb^{II}-RNO derivatives

To determine the reaction time-course of each ferrous Hb^{II}-RNO (R= Me, Et or Pr) derivative, the absorbance difference between λ_{max} ~421 and λ ~458 nm was first calculated. Absorbance at the apparent isosbestic point (at λ 458 nm) served as a baseline reference and was subtracted from the absorbance corresponding to the ferrous Hb^{II}-RNO complex (at λ_{max} ~421 nm). The resulting A_{421}-A_{458} absorbance difference was plotted as a function of time.

3.2.2.4 Ligand dissociation upon oxidation via ferricyanide

The ferrous Hb^{II}-RNO derivatives were formed in solution by mixing 30 µL ferric Hb^{III}-H_2O (30 mg/mL) with 2 µL RNO_2 precursor, followed by the addition of ~3 mg solid sodium

dithionite. Once each ferrous Hb^{II}-RNO complex was confirmed by UV-vis spectroscopy, 3 μL of the ligand-bound protein reaction mixture were transferred into a 3.5 mL quartz cuvette containing 3 mL of 100 mM potassium phosphate buffer (pH 6.0). A new spectrum was then recorded, and 2-5 μL of 30 mg/mL ferricyanide ($(K_3[Fe(CN)_6]$) were added as an oxidizing agent. Reappearance of the Soret band corresponding to ferric Hb^{III}-H_2O (λ_{max} 406 nm) in subsequent spectrum measurements confirmed ligand dissociation.

3.2.3 Crystallization of the products resulting from the reactions between ferrous Hb^{II} and $MeNO_2$, $EtNO_2$ or $PrNO_2$

As human Hb is made up of α and β subunits, their structures are described hereafter as Hb[α-Fe(ligand)][β-Fe(ligand)], to differentiate the Fe oxidation state, Fe-bound ligand, and other modifications between each monomer.

3.2.3.1 Crystals resulting from the reaction of Hb^{II} with $MeNO_2$

Co-crystallization was used to obtain the X-ray crystal structures of the ligand bound Hb[α-Fe^{II}(MeNO)][β-Fe^{II}(MeNO)] complex, and the Hb[α-Fe^{II}(MeNO)][β-Fe^{III}(H_2O)] derivative. Prior to crystallization, 3.5 mL of ferric Hb^{III}-H_2O (30 mg/mL) were placed in a small beaker and stirred with 25 μL of $MeNO_2$ for ~1 h. Then, 85 mg of solid sodium dithionite were added to the solution mixture and allowed to react for ~20 min, until the Soret peak at λ_{max} ~421 nm stabilized. Once the Hb^{II}-MeNO complex was formed in solution, crystals were grown aerobically using batch method as described by Safo [20] and Yi [18]. Briefly, 150 μL of the protein-ligand complex were placed in 10.25x64 mm Monoject blood collection tubes (COVIDIEN) containing varying volumes (0.33-0.51 mL, in 0.03 mL increments) of 3.2 M sodium potassium phosphate buffer pH 6.12, and 5 μL toluene. Violet-pink diamond shaped crystals grew within ~3 d. Suitable sized

crystals were transferred into a small droplet of cryosolution (made from the crystallization well solution plus 10% glycerol) covered with mineral oil. After soaking for ~5 min, the crystals were looped and immediately mounted on the goniometer for X-ray data collection the same day.

Crystallographic data of the Hb[α-Fe^{II}(MeNO)][β-Fe^{II}(MeNO)] complex and the Hb[α-Fe^{II}(MeNO)][β-Fe^{III}(H_2O)] derivative were obtained from crystals grown in the same co-crystallization vial, but with crystals harvested several weeks apart.

3.2.3.2 Crystals resulting from the reaction of Hb^{II} with $EtNO_2$

The same reaction conditions and crystallization buffers as described in section *3.2.3.1* were used to obtain the X-ray crystal structures of the ligand bound Hb[α-Fe^{II}(EtNO)][β-Fe^{II}(EtNO)] complex, the hemichrome Hb[α-Fe^{II}(EtNO)][β-Fe$(His)_2$-SNO] derivative and the degradation Hb[α-Fe^{II}(EtNO)][β-Fe(2 positions)] product. The only difference was that the precursor nitroethane was used in the reaction.

To determine whether the different crystal products appeared randomly or chronologically, X-ray diffraction data of several crystals from the same crystallization vial were collected over a period of time. Within the first ~3-4 weeks, complete data sets were collected, from more than a dozen crystals, and only structures corresponding to the ligand bound Hb[α-Fe^{II}(EtNO)][β-Fe^{II}(EtNO)] complex were obtained. Over the following weeks (weeks ~5-9), about another dozen X-ray diffraction data sets were collected, and all the structures corresponded to the hemichrome Hb[α-Fe^{II}(EtNO)][β-Fe$(His)_2$-SNO] derivative. Finally, the degradation Hb[α-Fe^{II}(EtNO)][β-Fe(2 positions)] product appeared chronologically towards the end of our screening (~3 months later). This indicated that indeed the derivatives observed in this study appeared chronologically and not at the same time.

3.2.3.3 Crystals resulting from the reaction of Hb^{II} with $PrNO_2$

The X-ray crystal structures of the ligand bound Hb[α-Fe^{II}(PrNO)][β-Fe^{II}(PrNO)] complex and the degradation Hb[α-Fe^{II}(PrNO)][β-Fe(2 positions)] product were obtained using co-crystallization via the batch method. The same reaction conditions and crystallization buffers as described in section *3.2.3.1* were used. The only difference being that these crystals were prepared anaerobically in an MBraun chamber using anaerobic buffers prepared as described in section *3.2.2.2*, and that the ligand precursor used for complex formation was $PrNO_2$.

The headspace of the vial containing ferric Hb^{III}-H_2O was deaerated prior to transfer into the MBraun chamber, and the protein (~ 3 mL) was allowed to equilibrate inside the chamber overnight. Once the buffers and reagents equilibrated, crystal trays were set as described previously. Diamond shaped crystals grew over a ~3 d period, after which the vials were transferred to the main lab area and exposed to air on a semi daily basis. Several data sets of different crystals from the same crystallization vial were collected over a period of time. The crystals were looped, cryoprotected and mounted on the goniometer for X-ray data collection the same day. Only structures corresponding to the ligand bound Hb[α-Fe^{II}(PrNO)][β-Fe^{II}(PrNO)] complex appeared initially, followed by the appearance of the degradation Hb[α-Fe^{II}(PrNO)][β-Fe(2 positions)] product after several weeks (~4-6 wks).

3.2.4 X-ray data collection

The diffraction data for all X-ray crystal structures were collected at the OU Macromolecular Crystallography Laboratory, using a home source Rigaku MicroMax 007HF microfocus X-ray generator equipped with a set of VariMax HF X-ray optics coupled to a Dectris Pilatus 200K silicon pixel detector. Data were collected at 100 K with CuKα radiation (λ = 1.54178 Å) from the generator operated at 40 kV/30 mA.

3.2.5 Data processing, structure solution and refinement

The X-ray diffraction data for each structure were processed indexed, integrated and scaled using *HKL3000R* [23]. Scalepack2mtz (CCP4 program suite) was used to convert the resulting *sca* files into *mtz* files [24]. Prior to molecular replacement (MR), *Mathews –cell content analysis* (CCP4) was used to determine the number of molecules per asymmetric unit. Unless otherwise noted, the Hb structures in this study were solved as dimers of a single α and β subunit pair. PHASER MR (CCP4) was used for molecular replacement (MR) using ferric Hb^{III}-H_2O (PDB ID 3P5Q; 2.0 Å resolution), with the heme, water molecules, toluenes and ligands removed, as the model for all the Hb structures. All refinements were performed using *Refmac5* (CCP4) [25] and the models were rebuilt using *COOT* [26]. The final structures were analyzed with the *MolProbity* server [27] for unusual residue conformations and contacts. The details of each structure are described below.

Unless otherwise noted, structure figures were created using *PyMOL*. The $2F_o$-F_c electron density maps were calculated by *Fast Fourier Transform* (*FFT*) in the CCP4 software package and the resulting *map* files were viewed in *PyMOL*. To generate the F_o-F_c electron density maps, the RNO ligands were first removed from the active site of the final *pdb* file and then processed though *Refmac5* (CCP4) to create a new F_c *mtz* file. The output F_c *mtz* file was then used as the input document in *FFT* to generate the F_o-F_c electron density *map* file. The final *map* file was displayed in *PyMOL.*

3.2.5.1 Ligand bound Hb[α-Fe^{II}(MeNO)][β-Fe^{II}(MeNO)]

Ten initial cycles of restrained refinement were run with *Refmac5*, and the R factor decreased from 0.3346 to 0.2677. Two hemes, MeNO, and waters were added to the model based on the F_o-F_c electron density maps in the subsequent refinement cycles. Three MeNO ligands were

added using *COOT*. An Fe-bound MeNO molecule was modeled above each heme in both the α and β subunit at 100% occupancy. A third MeNO molecule was modeled in at the B- and E-helix interphase at 100% occupancy. The final model was refined to a resolution of 2.09 Å, with an R factor of 0.2029 and R_{free} of 0.2635.

3.2.5.2 Ligand bound Hb[α-Fe^{II}(MeNO)][β-Fe^{III}(H_2O)]

Ten initial cycles of restrained refinement were run with *Refmac5*, and the R factor decreased from 0.3043 to 0.2508. Ligands, waters and other molecules were added to the model based on the F_o-F_c electron density maps in the subsequent refinement cycles. Two hemes, one toluene, one MeNO ligand, and waters were added using *COOT*. MeNO was modeled bound to the Fe heme (α subunit) at 100% occupancy. Residues Arg141 (α subunit) and Val1 (β subunit) were omitted from the structure due to lack of electron density. Two conformations were modeled with 50% occupancy each for the Arg40 side chain (β subunit). The final model was refined to a resolution of 2.29 Å, with an R factor of 0.2029 and R_{free} of 0.2635.

3.2.5.3 Ligand bound Hb[α-Fe^{II}(EtNO)][β-Fe^{II}(EtNO)]

Ten initial cycles of restrained refinement were run with *Refmac5*, and the R factor decreased from 0.3188 to 0.2590. Ligands, cofactors and waters were added to the model based on the F_o-F_c electron density maps in the subsequent refinement cycles. Two hemes, two EtNO ligands, waters and two toluenes were added using *COOT*. An EtNO molecule was modeled bound to Fe above each heme at 100% occupancy. Residue Val1 (β subunit) was omitted from the structure due to lack of electron density. The final model was refined to a resolution of 1.97 Å, with an R factor of 0.1922 and R_{free} of 0.2228.

3.2.5.4 Hemichrome Hb[α-Fe^{II}(EtNO)][β-Fe(His)$_2$-SNO]

Ten initial cycles of restrained refinement were run with *Refmac5*, and the R factor decreased from 0.3451 to 0.2858. Ligands, hemes, waters and other molecules were added to the model based on the F_o-F_c electron density maps in the subsequent refinement cycles. Two hemes, three EtNO molecules, one toluene and one Fe atom (β subunit) were added using *COOT*. In the α subunit, EtNO was modeled Fe bound to the heme at 100% occupancy. In the β subunit, anomalous mapping using *SFall* (CCP4) reveled two positions for Fe, and based on the maps, heme was modeled at 90% occupancy in the hemichrome position. An Fe atom was modeled in at 10% occupancy at the second position (there was no clear electron density for the porphyrin in this minor location in the β subunit). Also in the β subunit, one EtNO molecule was modeled behind the heme and a second EtNO was modeled at the B- and E-helix interphase, both at 100% occupancy. Residue βCys93 was changed (using the mutate function of *COOT*) to the *S*-nitrosocysteine derivative (ligand ID SNC), and split into two conformations at 50% each, to accommodate substantial electron density around the -SH group. Residues Arg141 from the α subunit, and Lys144, Tyr145 and His146 from the β subunit, were omitted from the structure due to lack of electron density. The final model was refined to a resolution of 1.89 Å, with an R factor of 0.1900 and R_{free} of 0.2536.

3.2.5.5 Degradation Hb[α-Fe^{II}(EtNO)][β-Fe(2 positions)] product

Ten initial cycles of restrained refinement were run with *Refmac5*, and the R factor decreased from 0.3288 to 0.2797. Ligands, cofactors and waters were added to the model based on the F_o-F_c electron density maps in the subsequent refinement cycles. One EtNO, one toluene, and three hemes were added using *COOT*. The EtNO molecule was modeled in the α subunit above the heme at 100% occupancy. In the β subunit, anomalous mapping using *SFall* (CCP4) reveled

two positions for Fe. Based on these results, the heme was modeled in two positions according to the anomalous scattering peak ratios (56% and 44% occupancy); the two hemes were modeled in at the two Fe positions. Poor electron density was observed for the porphyrin macrocycles in the β subunit. Two conformations were modeled for the sidechains of Arg40 (β subunit, 52% and 48% occupancy each) and Asp99 (β subunit, 50% occupancy each). Residues Tyr140 and Arg141 from the α subunit, and Tyr145 and His146 from the β subunit, were omitted from the structure due to lack of electron density. The final model was refined to a resolution of 1.90 Å, with an R factor of 0.2328 and R_{free} of 0.3228.

3.2.5.6 Ligand bound Hb[α-Fe^{II}(PrNO)][β-Fe^{II}(PrNO)]

Ten initial cycles of restrained refinement were run with *Refmac5*, and the R factor decreased from 0.3302 to 0.2652. Ligands, cofactors and waters were added to the model based on the F_o-F_c electron density maps in the subsequent refinement cycles. Two hemes, two PrNO molecules, and one toluene were added using *COOT*. PrNO was modeled Fe bound above each heme at 100% occupancy. Two conformations were modeled for the sidechains of Leu29 (α subunit, 39 and 61% occupancy each) and Arg40 (β subunit, 49 and 51% occupancy each). The final model was refined to a resolution of 1.90 Å, with an R factor of 0.2098 and R_{free} of 0.2551.

3.2.5.7 Degradation Hb[α-Fe^{II}(PrNO)][β-Fe(2 positions)] product

Ten initial cycles of restrained refinement were run with *Refmac5*, and the R factor decreased from 0.3190 to 0.2799. Ligands, waters and other molecules were added to the model based on the F_o-F_c electron density maps in the subsequent refinement cycles. Three hemes, one PrNO and one toluene were added using *COOT*. PrNO was modeled in the α subunit above the heme at 100% occupancy. Two conformations were modeled for the sidechains of Lys127 in the

α subunit. Anomalous mapping (*SFall,* CCP4) reveled two positions for Fe in the β subunit at 46 and 54% occupancy. Two hemes were thus modeled according to the anomalous scattering peak ratios to coincide with the two Fe positions. Poor density was observed for the porphyrin macrocycles in the β subunit. Residues Ala86 to Asp99 of the F-helix in the β subunit displayed disorder, and two conformations for this F-helix segment were modeled in (46 and 54% occupancy). Residues Tyr140 and Arg141 from the α subunit, and His146 from the β subunit, were omitted from the structure due to lack of electron density. The final model was refined to a resolution of 1.90 Å, with an R factor of 0.2350 and R_{free} of 0.3038.

3.4.5.8 Data collection and refinement statistics

Data collection and refinement statistics are listed in Table 3-1.

Table 3-1 X-ray data collection and refinement statistics

	Hb[α-Fe^{II}(MeNO)] [β-Fe^{II}(MeNO)]	**Hb[α-Fe^{II}(MeNO)] [β-$Fe^{III}(H_2O)$]**	**Hb[α-Fe^{II}(EtNO)] [β-Fe^{II}(EtNO)]**	**Hb[α-Fe^{II}(EtNO)] [β-$Fe(His)_2$-SNO]**
Data collection[a]	MicroMax 007HF	MicroMax 007HF	MicroMax 007HF	MicroMax 007HF
Space Group	*P 4₁ 2₁ 2*	*P 4₁ 2₁ 2*	*P 4₁ 2₁ 2*	*P 4₁ 2₁ 2*
Wavelength (Å)	1.54178	1.54178	1.54178	1.54178
Cell dimensions (*a*, *b*, *c*) (α, β, γ)	53.35 53.35 197.23 90.0 90.0 90.0	53.68 53.68 192.94 90.0 90.0 90.0	53.48 53.48 193.21 90.0 90.0 90.0	53.34 53.34 195.30 90.0 90.0 90.0
Resolution range (Å)	35.23 – 2.09	41.21 – 2.29	35.85 – 1.97	41.26 – 1.89
Mean $I/\sigma(I)$	30.56 (12.96)	14.37 (1.36)	26.37 (4.21)	59.78 (4.32)
No. of reflections				
Observed	153078	100108	198390	185932
Unique	17244 (1255)	11961 (247)	20732 (1965)	23238 (2186)
Multiplicity	8.8 (6.2)	7.8 (1.3)	9.5 (4.8)	8.0 (5.0)
Completeness (%)	97.41 (73.65)	94.6 (49.2)	99.52 (96.85)	99.00 (96.43)
R_{merge}[b]	0.071 (0.095)	0.095 (0.314)	0.081 (0.236)	0.056 (0.297)
$CC_{1/2}$	0.992	0.754	0.939	0.922
Refinement statistics				
No. of protein atoms	2207	2172	2193	2197
R factor (%)[c]	0.2029	0.1999	0.1922	0.1900
R_{free} (%)[d]	0.2635	0.2830	0.2228	0.2536
RMSD bond length (Å)	0.017	0.017	0.015	0.015
RMSD bond angles (°)	1.89	1.99	1.74	1.78
Overall Mean B factor	27.41	35.35	26.42	23.90
Ramachandran plot (%)[e]				
Most favored residues	98.23	94.64	97.87	98.91
Outliers	0.00	0.36	0.00	0.00

[a] Values in parentheses correspond to the highest resolution shells. [b] $R_{merge} = \Sigma|I - \langle I \rangle|/\Sigma(I)$, where I is the individual intensity observation and $\langle I \rangle$ is the mean of all measurements of I. [c] $R = \Sigma||F_o| - |F_c||/\Sigma|F_o|$, where F_o and F_c are the observed and calculated structural factors respectively. [d] R_{free} was calculated by using 5% of the randomly selected diffraction data which were excluded from the refinement. [e] As calculated using *MolProbity*

Table 3-1 X-ray data collection and refinement statistics (continued)

	Hb[α-Fe^{II}(EtNO)] [β-Fe(2 positions)]	**Hb[α-Fe^{II}(PrNO)] [β-Fe^{II}(PrNO)]**	**Hb[α-Fe^{II}(PrNO)] [β-Fe(2 positions)]**
Data collection[a]	MicroMax 007HF	MicroMax 007HF	MicroMax 007HF
Space Group	*P 4$_1$ 2$_1$ 2*	*P 4$_1$ 2$_1$ 2*	*P 4$_1$ 2$_1$ 2*
Wavelength (Å)	1.54178	1.54178	1.54178
Cell dimensions (*a*, *b*, *c*) (α, β, γ)	53.48 53.48 194.89 90.0 90.0 90.0	53.73 53.73 192.71 90.0 90.0 90.0	53.46 53.46 195.20 90.0 90.0 90.0
Resolution range (Å)	41.29 – 1.90	48.18 – 1.90	46.89 – 1.90
Mean $I/\sigma(I)$	21.73 (1.29)	22.16 (1.95)	23.5 (1.14)
No. of reflections			
Observed	184654	219199	196493
Unique	23287 (2238)	22230 (1704)	22189 (1345)
Multiplicity	4.4 (2.4)	9.5 (6.0)	8.4 (4.1)
Completeness (%)	99.85 (99.07)	95.55 (75.67)	95.56 (59.59)
R_{merge}[b]	0.060 (0.487)	0.089 (0.580)	0.089 (1.055)
$CC_{1/2}$	0.406	0.677	0.408
Refinement statistics			
No. of protein atoms	2173	2219	2258
R factor (%)[c]	0.2328	0.2098	0.2350
R_{free} (%)[d]	0.3228	0.2551	0.3038
RMSD bond length (Å)	0.018	0.016	0.020
RMSD bond angles (°)	1.99	1.80	1.83
Overall Mean B factor	45.59	21.82	26.22
Ramachandran plot (%)[e]			
Most favored residues	92.83	97.53	96.77
Outliers	1.08	0.35	0.00

[a] Values in parentheses correspond to the highest resolution shells. [b] $R_{merge} = \Sigma|I - \langle I \rangle|/\Sigma(I)$, where I is the individual intensity observation and $\langle I \rangle$ is the mean of all measurements of I. [c] $R = \Sigma||F_o| - |F_c||/\Sigma|F_o|$, where F_o and F_c are the observed and calculated structural factors respectively. [d] R_{free} was calculated by using 5% of the randomly selected diffraction data which were excluded from the refinement. [e] As calculated using *MolProbity*

3.2.6 Aggregation studies of the Hb^{II}-MeNO, -EtNO and -PrNO products

The Hb^{II}-RNO derivatives were formed aerobically using the same protein and reagent concentrations as described in section *3.2.3*, but with smaller sample volumes. In summary, 8 μL of RNO_2 were added to an Eppendorf tube containing 1 mL of ferric Hb^{III}-H_2O (30 mg/mL). Then, ~24 mg of solid sodium dithionite were added to the solution mixture and allowed to react overnight. As controls, one reaction contained ~24 mg of dithionite but no ligand. A second control contained no dithionite nor ligand, but it did contain an equivalent volume of MeOH (which we typically use as solvent for RNO_2). The following day, the solutions were centrifuged for 5 min at 15 rpm (Eppendorf centrifuge 5424). The supernatant was removed, and the precipitate was photographed using a cellphone for visualization.

3.3 Results

3.3.1 UV-vis spectral studies of the reactions of Hb with nitroalkanes ($MeNO_2$, $EtNO_2$ and $PrNO_2$)

3.3.1.1 UV-vis characterization of ferrous Hb^{II}-RNO derivatives

The reactions of ferrous Hb^{II} with nitroalkanes were monitored by UV-vis spectroscopy using similar conditions as those described in Chapter 2. First, ferric Hb^{III}-H_2O was reduced to the ferrous Hb^{II} derivative by the addition of dithionite. This resulted in absorption changes in the UV-vis spectrum most notably in the Soret band, which moved from λ_{max} 406 to 430 nm. Simultaneously, the λ 500 nm peak in the Q-region of the spectrum shifted to 555 nm. After obtaining the ferrous unliganded Hb^{II}, the ligand precursor RNO_2 was added into the reaction mixture and the reaction was monitored over a period of time. For the reaction between ferrous Hb^{II} and $MeNO_2$, we observed the disappearance of the λ_{max} 430 nm Soret band and appearance of a new peak at λ_{max} 421 nm upon ligand binding. The same reaction resulted in spectral changes in the Q-region (where the single broad band at λ 555 nm was replaced by bands at λ 543 and 565 nm) indicating the formation of the ferrous Hb^{II}-MeNO complex (Figure 3.4A). These shifts in the UV-vis spectrum were similar for the reactions of ferrous Hb^{II} with the other ligands in this study (MeNO, EtNO, PrNO) regardless of size and sterics (Figure 3.4A-C).

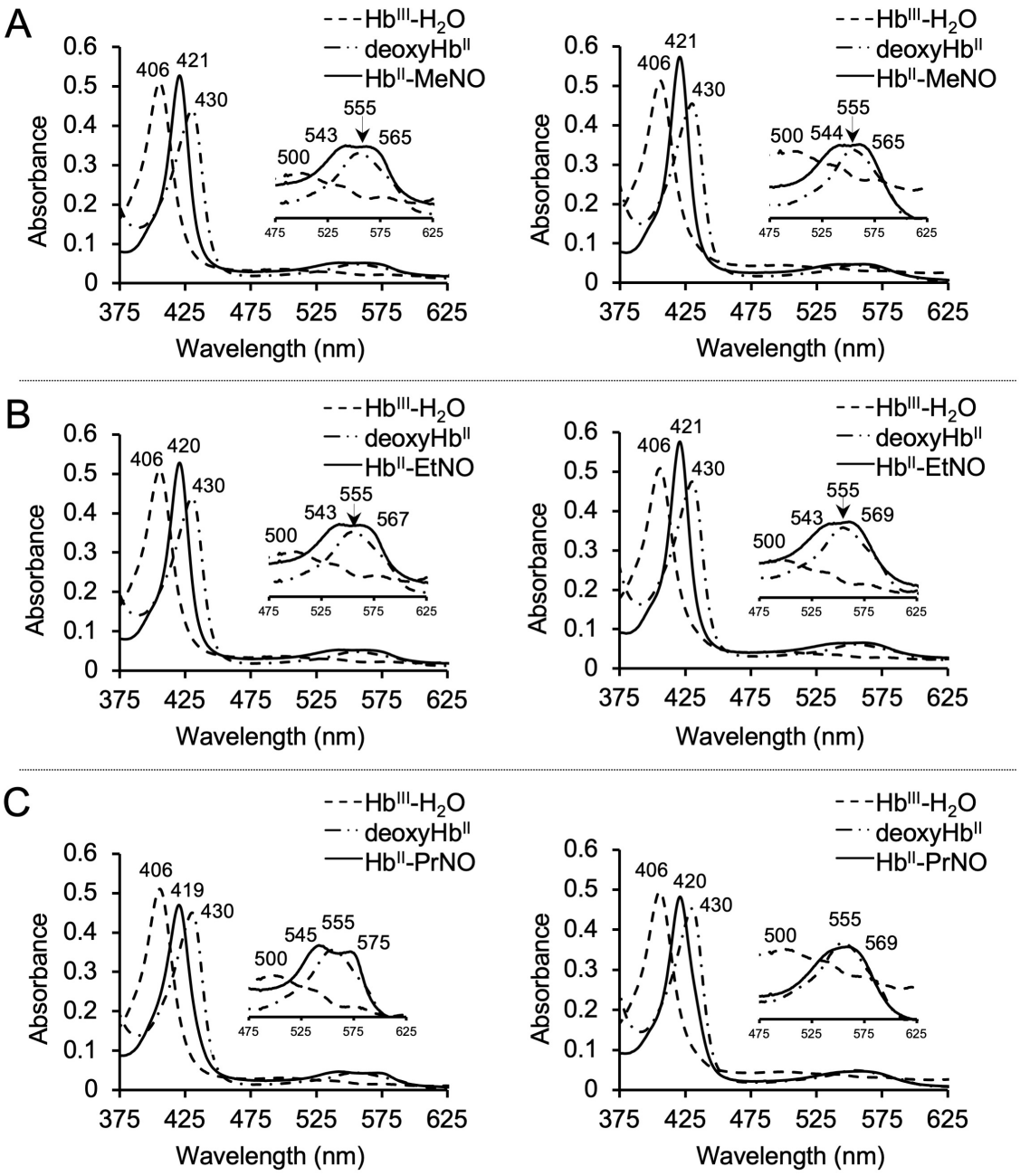

Figure 3.4 UV-vis spectral characterization of the reduction of ferric Hb^{III}-H_2O by dithionite, followed by the reaction of the resulting ferrous Hb^{II} with the nitroalkanes to form the respective ferrous Hb^{II}-RNO adducts. A) Hb^{II}-MeNO, B) Hb^{II}-EtNO, C) Hb^{II}-PrNO; *left*: aerobic and *right*: anaerobic environment. Final reaction conditions: ~3 µM Hb, 0.1 M phosphate buffer (pH 7.4), 20 mM dithionite, 20 mM RNO_2.

The reactions were monitored over time to analyze the progress of each reaction and to determine the stability of each Hb^{II}-RNO complex. Comparisons were generated by calculating the difference between the absorbance at λ_{max} 421 nm, which is characteristic of the ferrous ligand bound Hb^{II}-RNO derivative, and λ 458 nm, which corresponds to the apparent isosbestic point in this reaction. The resulting A_{421}-A_{458} differences were then plotted as a function of time (Figure 3.5). The maximum height of the trendline represents the extent of formation for each reaction. Under both aerobic and anaerobic conditions, an inverse relationship between size of ligand and extent of formation was observed. For instance, under aerobic conditions, ferrous Hb^{II}-MeNO reached a maximum extent of formation of 0.53 while the ferrous Hb^{II}-EtNO reached a maximum extent of formation of 0.51. Continuing with that trend, ferrous Hb^{II}-PrNO reached a maximum extent of formation of 0.45 under aerobic conditions. Similar trends were observed for the anaerobic reactions.

A notable difference between the aerobic and anaerobic reactions was the lifetime of each ferrous Hb^{II}-RNO complex. The presence of air, appeared to enhance instability, leading to slow oxidation of the ferrous products back to their ferric precursors with attendant ligand dissociation (Figure 3.5). For example, within a day, the extent of formation of Hb^{II}-MeNO decreased from 0.53 to 0.51 in the presence of air, and from 0.54 to 0.53 in the absence of air. In a clearer example, the extent of formation of Hb^{II}-PrNO decreased from 0.45 to 0.37 in the presence of air, and from 0.46 to 0.42 in the absence of air after one day.

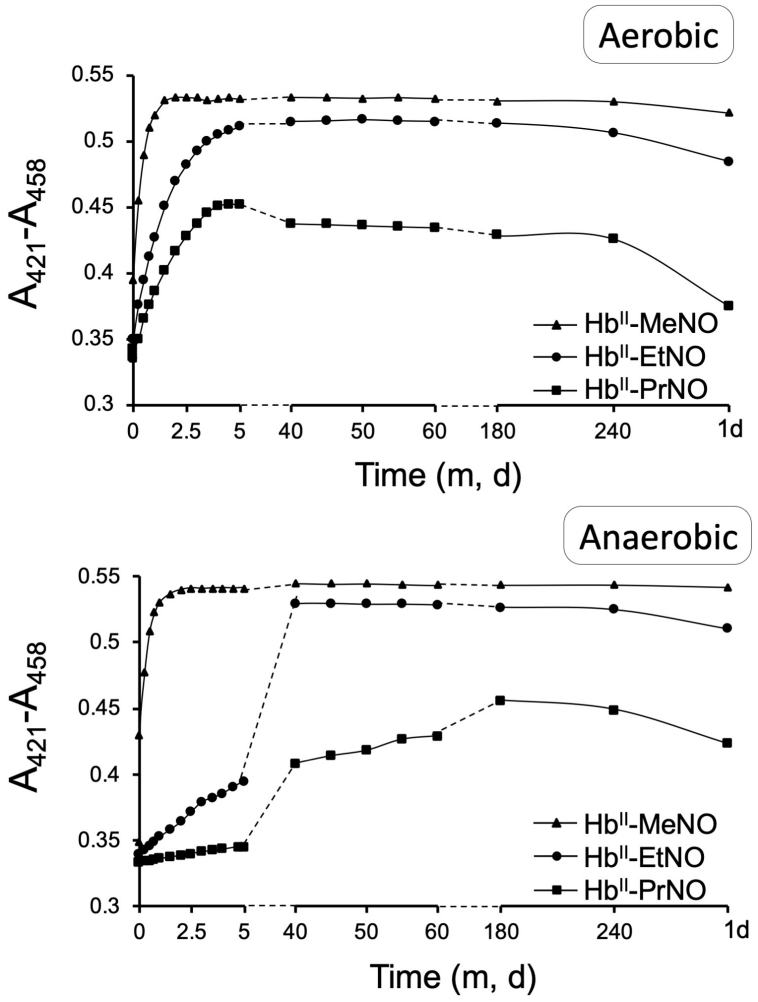

Figure 3.5 Extent of formation for each ferrous Hb^{II}-RNO complex determined by plotting the difference between the absorbance at λ_{max} 421 and 458 nm as a function of time. Absorbance at λ_{max} 421 nm is indicative of the ferrous Hb^{II}-RNO complex, and the absorbance at λ 458 nm corresponds to the apparent isosbestic point.

Table 3-2 provides a summary of the results from each ferrous Hb^{II}-RNO reaction that reflects the qualitative inverse relationship between ligand sterics and extent of formation. This table also indicates the time it took for each complex to reach the maximum extent of formation. Notably, the presence or absence of air made no significant difference in the time the reactions with the small ligands (MeNO and EtNO) reached maximum extent of formation. In contrast, air had a significant impact on the reaction with the largest ligand (PrNO). The Hb^{II}-PrNO complex

formed within 4 min in the presence of air, but the reaction slowed down significantly in the absence of air (120 min). Furthermore, not only was formation of the Hb^{II}-PrNO complex slower anaerobically, the ligand protein complex was longer lived. This observation correlates to our crystallization attempts, and helps explain why we were only able to form crystals of the Hb[α-Fe^{II}(PrNO)][β-Fe^{II}(PrNO)] complex under anaerobic conditions.

Table 3-2 Summary of the extent of formation and time required for each ferrous Hb^{II}-RNO complex to reach max extent of formation.

RNO	Aerobic ferrous Hb^{II}-RNOs		Anaerobic ferrous Hb^{II}-RNOs	
	Maximum extent of formation (A_{421}-A_{458})	Time to reach max extent of formation (min)	Maximum extent of formation (A_{421}-A_{458})	Time to reach max extent of formation (min)
MeNO	0.53	2	0.54	2
EtNO	0.51	6	0.53	4
PrNO	0.45	4	0.46	120

3.3.1.2 Ferrous Hb^{II}-RNO ligand dissociation upon oxidation with ferricyanide

The oxidation state of each ferrous Hb^{II}-RNO derivative was further verified by oxidizing the complexes with potassium hexacyanoferrate (III). Addition of the oxidant to ferrous Hb^{II}-RNO in buffer (100 mM potassium phosphate buffer, pH 6.0) generated spectral features corresponding to the formation of ferric Hb^{III}-H_2O (Figure 3.6). This confirmed the oxidation state of iron in the Hb^{II}-RNO derivative as Fe^{II}. Oxidation to Fe^{III} resulted in consequential expulsion of the RNO ligand.

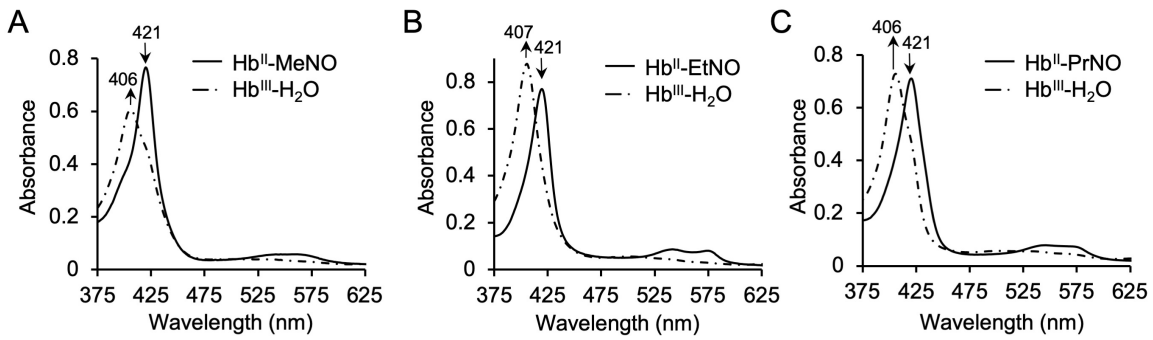

Figure 3.6 Ferrous Hb^{II}-RNO ligand dissociation upon oxidation by ferricyanide. The ferrous Hb^{II}-RNO derivatives were formed as described in section *3.2.2.4*, followed by the addition of ~2-5 µL of 30 mg/mL potassium hexacyanoferrate (III) as an oxidizing agent.

3.3.2 Properties of the Hb^{II}-RNO (MeNO, EtNO, PrNO) crystals

Crystals of the products resulting from the reactions of ferrous Hb^{II} with $MeNO_2$ and $EtNO_2$ were grown aerobically in 3.2 M sodium potassium phosphate buffer (pH 6.12) using the batch method. Crystals resulting from the reaction of ferrous Hb^{II} with $PrNO_2$ were formed using the same procedure, but under anaerobic conditions. In this study, only diamond-shaped, violet-pink crystals, as those shown in Figure 3.7, were used for X-ray diffraction and data collection. All crystals reported here are in the $P4_12_12$ space group.

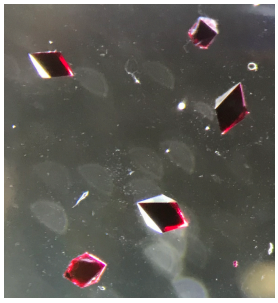

Figure 3.7 Characteristic diamond-shaped, violet-pink crystals of the Hb products formed in this study, indexed with the $P4_12_12$ space group.

3.3.2 X-ray crystal structures of the products from the reactions of Hb with RNOs

3.3.2.1 MeNO bound Hb[α-Fe^{II}(MeNO)][β-Fe^{II}(MeNO)]

Crystals of the ligand bound Hb[α-Fe^{II}(MeNO)][β-Fe^{II}(MeNO)] complex were obtained aerobically by co-crystallization using the batch method. The structure was solved as an α1β1 dimer to a 2.09 Å resolution.

The $2F_o–F_c$ electron density maps and the $F_o–F_c$ omit electron density maps of the α and β active sites show clear density corresponding to MeNO in both subunits (Figure 3.8). In both cases, the MeNO density sits directly above the heme with the ligand modeled in at 100% occupancy. The MeNO molecule is N-bound to the Fe atom (at a distance of 1.9 Å) and H-bonded to the distal His residue (at a distance between the MeNO O-atom and the His58/63 N^{ε} atom of 2.7 Å). Consequently, the methyl group is oriented towards the interior of the hydrophobic active site. In the α subunit, the closet neighboring residue is Leu101 at a distance of 3.5 Å from its $C^{\delta 2}$ atom to MeNO's C-atom. In the β subunit, similar hydrophobic contacts are observed between Leu106 ($C^{\delta 2}$) and the ligand's C-atom with a distance of 3.6 Å.

Perhaps the most notable difference between the α and β active sites is the orientation of the propionate groups of the heme. In the α subunit, the propionate groups point in opposite directions, with the propionate($O^{\delta 2}$) atom forming close contacts His45($N^{\varepsilon 2}$) at 2.8 Å. The propionate groups of the heme in the β active site are both oriented down and have no direct contacts with fixed waters nor protein residues.

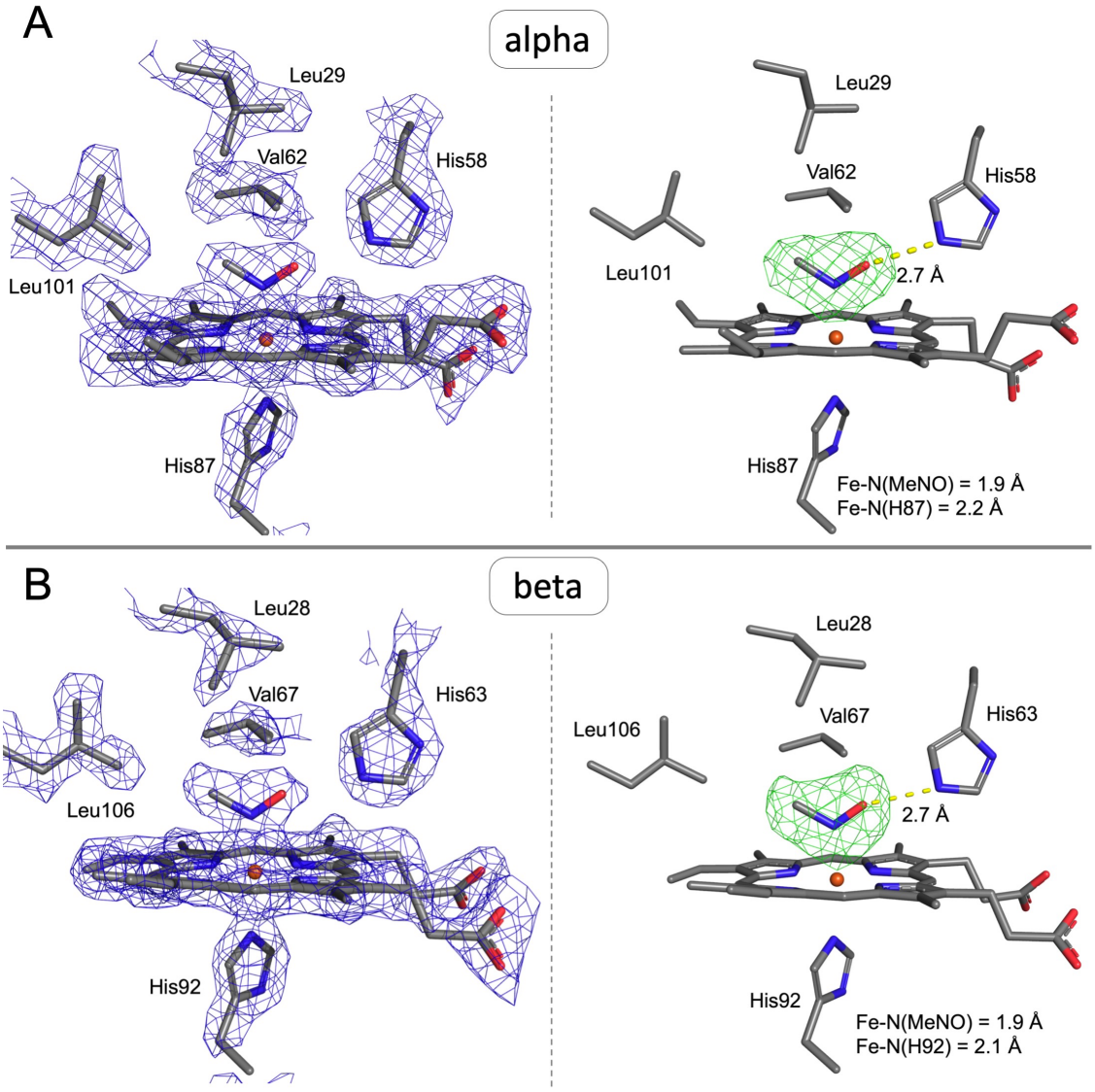

Figure 3.8 Models of the heme active site of the (A) α and (B) β subunits of the Hb[α-Fe^{II}(MeNO)][β-Fe^{II}(MeNO)] complex at a resolution of 2.09 Å. *Left*: $2F_o–F_c$ electron density map (blue mesh, contoured at 1σ). *Right:* $F_o–F_c$ omit electron density maps (green mesh, contoured at 3σ). In both subunits the Fe-bound MeNO ligands were modeled at 100% occupancy.

The overall tetrameric structure of Hb[α-Fe^{II}(MeNO)][β-Fe^{II}(MeNO)] was generated to determine the quaternary state of the complex (Figure 3.9A). In this figure, the global structure of the dimer is represented by the α1 and β1 subunits, while the α2 and β2 subunits are *PyMol* generated symmetry mates. The tetrameric structure was then aligned with representative Hb structures and a comparison of the β2 FG corner and α1 C-helix was made (Figure 3.9B). The β2His97 residue sits halfway between the α1Thr38 and α1Thr41 residues and is oriented towards the α1C-helix. Based on this signature "switch" region, the Hb[α-Fe^{II}(MeNO)][β-Fe^{II}(MeNO)] structure (cyan) most closely resembles the R-state Hb (green) model.

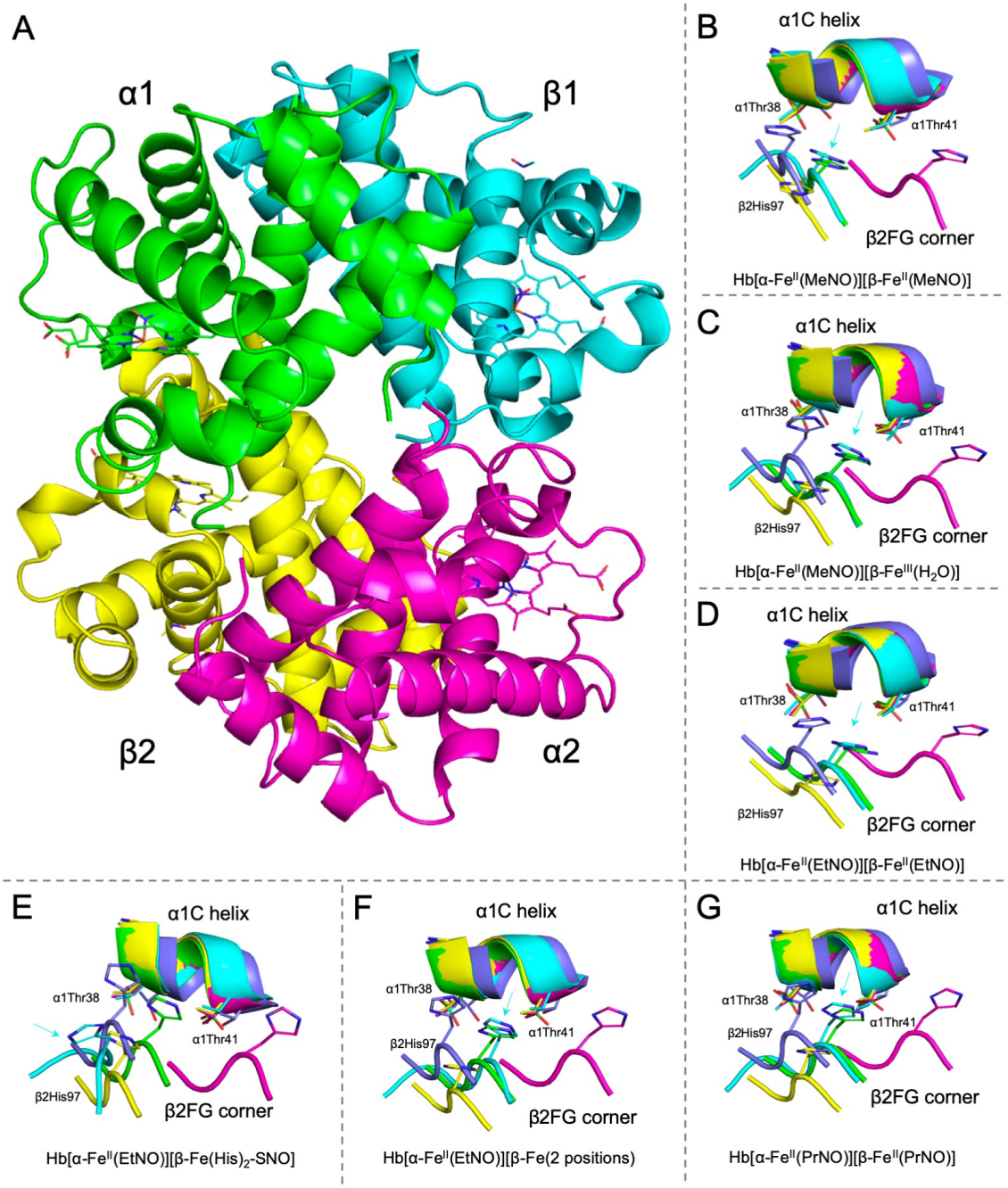

Figure 3.9 (A) Representative Hb^{II}-RNO tetrameric structure. The α2 and β2 subunits are *PyMol* generated symmetry mates. (B-G) comparisons of the α1β2 interface of each Hb[α-Fe(ligand)][β-Fe(ligand)] derivative with characteristic Hb models. Magenta: T-state deoxyHb (PDB ID 1B86), Green: R-state Hb(CO) (PDB ID 1AJ9), Yellow: R2-state Hb(CO) (PDB ID 1BBB), Slate: R3-state Hb(CO) (PDB ID 1YZI). Cyan: this work, arrow indicates position of β2His97 residue.

The oxidation state of Fe in the Hb[α-Fe^{II}(MeNO)][β-Fe^{II}(MeNO)] structure was further verified by collecting the UV-vis spectrum of the crystal after X-ray diffraction data collection. This was achieved by dissolving the crystal in 0.1 M phosphate buffer (pH 7.4) after X-ray data collection. One high-intensity peak was observed in the Soret region, at λ_{max} ~420 nm, and two low-intensity peaks were observed in the Q-region of the spectrum, at λ ~540 and 565 nm (Figure 3.10). These results are consistent with the spectrum obtained in our solution studies (Figure 3.4A) corresponding to the ferrous Hb^{II}-MeNO complex, thus confirming the redox state of iron remained as Fe^{II} in the crystal.

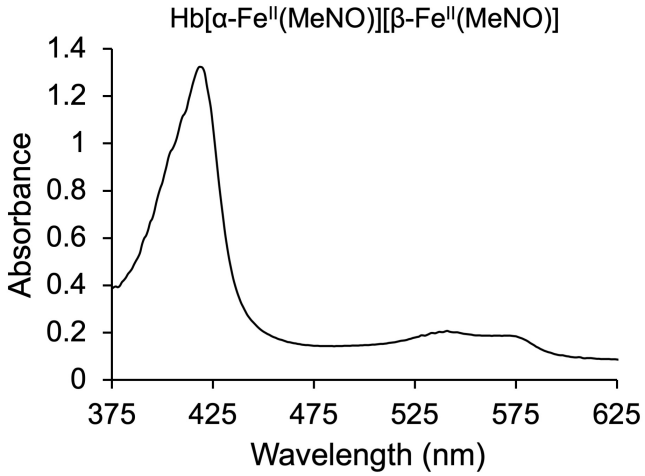

Figure 3.10 UV-vis spectrum of the Hb[Fe^{II}(MeNO)][β-Fe^{II}(MeNO)] crystal dissolved in 0.1 M phosphate buffer (pH 7.4) after X-ray diffraction data collection.

3.3.2.2 Ligand bound Hb[α-Fe^{II}(MeNO)][β-Fe^{III}(H_2O)]

Crystals of the Hb[α-Fe^{II}(MeNO)][β-Fe^{III}(H_2O)] complex were collected from the same vial that contained the Hb[α-Fe^{II}(MeNO)][β-Fe^{II}(MeNO)] derivative, but they were harvested several weeks later. The crystal structure of the Hb[α-Fe^{II}(MeNO)][β-Fe^{III}(H_2O)] product was solved as an α1β1 dimer to 2.29 Å resolution.

The $2F_o–F_c$ electron density map and the $F_o–F_c$ omit electron density map of the active site of the α subunit show clear density corresponding to the MeNO ligand (Figure 3.11A) above the heme. The ligand was modeled in to this location at 100% occupancy, N-bound to the Fe-atom at a distance of 1.9 Å. The MeNO ligand is engaged in H-bonding to the distal His58 N^{ε} atom 2.6 Å apart. This bonding restricts the orientation of the MeNO ligand, as such the methyl group orients towards the interior of the hydrophobic active site. The closet neighboring residue to MeNO is Leu101, with a distance from its $C^{\delta 2}$ atom to the ligand's C-atom of 3.6 Å. In contrast, the electron density maps of the β subunit lack density for a bound MeNO ligand (Figure 3.11B). Instead, an H_2O molecule was modeled Fe-bound above the heme (100% occupancy) with an Fe-OH_2 distance of 2.4 Å.

The orientation of the propionate groups resembles those observed in the Hb[α-Fe^{II}(MeNO)][β-Fe^{II}(MeNO)] structure. In the α subunit, the propionate groups point in opposite directions. This results in close contacts between propionate($O^{\delta 2}$) and His45($N^{\varepsilon 2}$) at 2.8 Å, and between propionate($O^{\alpha 1}$) and Lys61(N^{ζ}) at 3.4 Å. In the β active site, both propionate groups are oriented down and have no direct contact with neighboring residues or fixed waters.

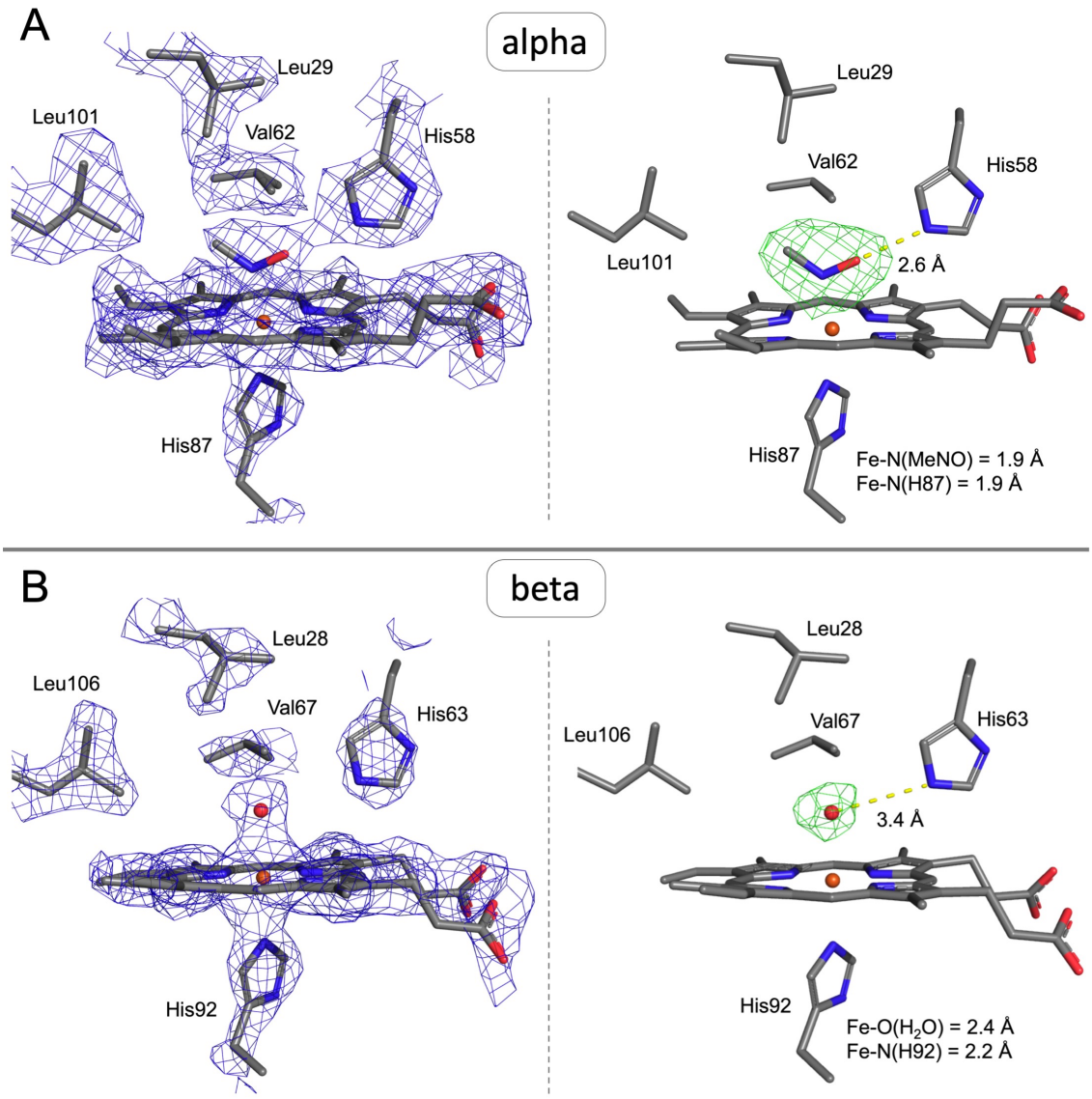

Figure 3.11 Models of the heme active site of the (A) α and (B) β subunits of the [α-Fe^{II}(MeNO)][β-Fe^{III}(H_2O)] structure solved to a resolution of 2.29 Å. *Left:* $2F_o–F_c$ electron density map (blue mesh, contoured at 1σ). *Right*: $F_o–F_c$ omit electron density maps (green mesh) with MeNO modeled at 100% occupancy (contoured at 3σ) and H_2O also modeled at 100% occupancy (contoured at 4σ).

To investigate the conformational state (e.g. T-state, R-state) of the Hb[α-Fe^{II}(MeNO)][β-Fe^{III}(H_2O)] dimer, its tetrameric structure was generated in *PyMol*. Comparison of the α1β2 switch region to Hb structures of known conformation show that the Hb[α-Fe^{II}(MeNO)][β-Fe^{III}(H_2O)] structure (cyan) is in the R-state conformation (Figure 3.9C). This is indicated by the position of the β2His97 residue midway between the α1Thr38 and α1Thr41 residues, and its tilt towards the α1C-helix, similar to that of the R-state Hb (green) model.

3.3.2.3 Ligand bound Hb[α-Fe^{II}(EtNO)][β-Fe^{II}(EtNO)]

Crystals of the ligand bound Hb[α-Fe^{II}(EtNO)][β-Fe^{II}(EtNO)] derivative were obtained aerobically by co-crystallization. The X-ray crystal structure of this complex was solved as an α1β1 dimer to 1.97 Å resolution.

The $2F_o–F_c$ electron density maps, and particularly the $F_o–F_c$ omit electron density maps of the α and β active sites show clear density corresponding to EtNO directly above the heme (Figure 3.12). The EtNO molecules were modeled at 100% occupancy. In both subunits, EtNO is Fe-bound with an Fe-N(EtNO) distance of 1.9 Å. In the α subunit, EtNO is H-bonded through its O-atom to His58($N^{\varepsilon 2}$) at 2.7 Å. Consequentially, the ethyl group is directed towards the interior of the active site, making multiple hydrophobic contacts with distal pocket residues. The calculated distances between the EtNO(C^2)-atom and neighboring Leu101($C^{\delta 2}$), Met32(C^{ε}) and Leu29($C^{\delta 2}$) atoms are 3.8, 4.0 and 3.4 Å, respectively. Similarly, the calculated distances between the EtNO(C^1) and neighboring Leu29($C^{\delta 2}$) and Val62($C^{\gamma 2}$) are 3.9 and 3.8 Å, respectively. The $C^2–C^1–N=O$ backbone of the EtNO ligand in the α subunit is best modeled in the *trans* conformation with a -54.9° torsion angle. Furthermore, the propionate groups point in opposite directions with the propionate($O^{1\delta}$) atom in close contact with His45($N^{\varepsilon 2}$) at 2.8 Å.

In the β subunit, H-bonding connects EtNO(O) to His63($N^{\varepsilon 2}$) at 2.8 Å, which directs the ethyl group towards the interior of the active site. The $C^2–C^1–N=O$ backbone has multiple hydrophobic interactions; the distances from EtNO(C^1) to Val67($C^{\gamma 2}$) and Leu106($C^{\delta 2}$) were calculated as 3.6 and 3.5 Å, respectively. Similarly, the distances from EtNO(C2) to Leu31($C^{\delta 2}$), Leu106($C^{\delta 2}$), Leu28($C^{\delta 1}$) and Phe42(C^{ζ}) were measured as 4.0, 4.0, 3.4, and 3.6Å, respectively. The EtNO ligand in this subunit is also modeled in the *trans* conformation with a torsion angle of

-60.0°. The propionate groups of the heme in the β active site are both oriented down and H-bond to a water molecule siting between the two propionates at 2.6-2.7Å.

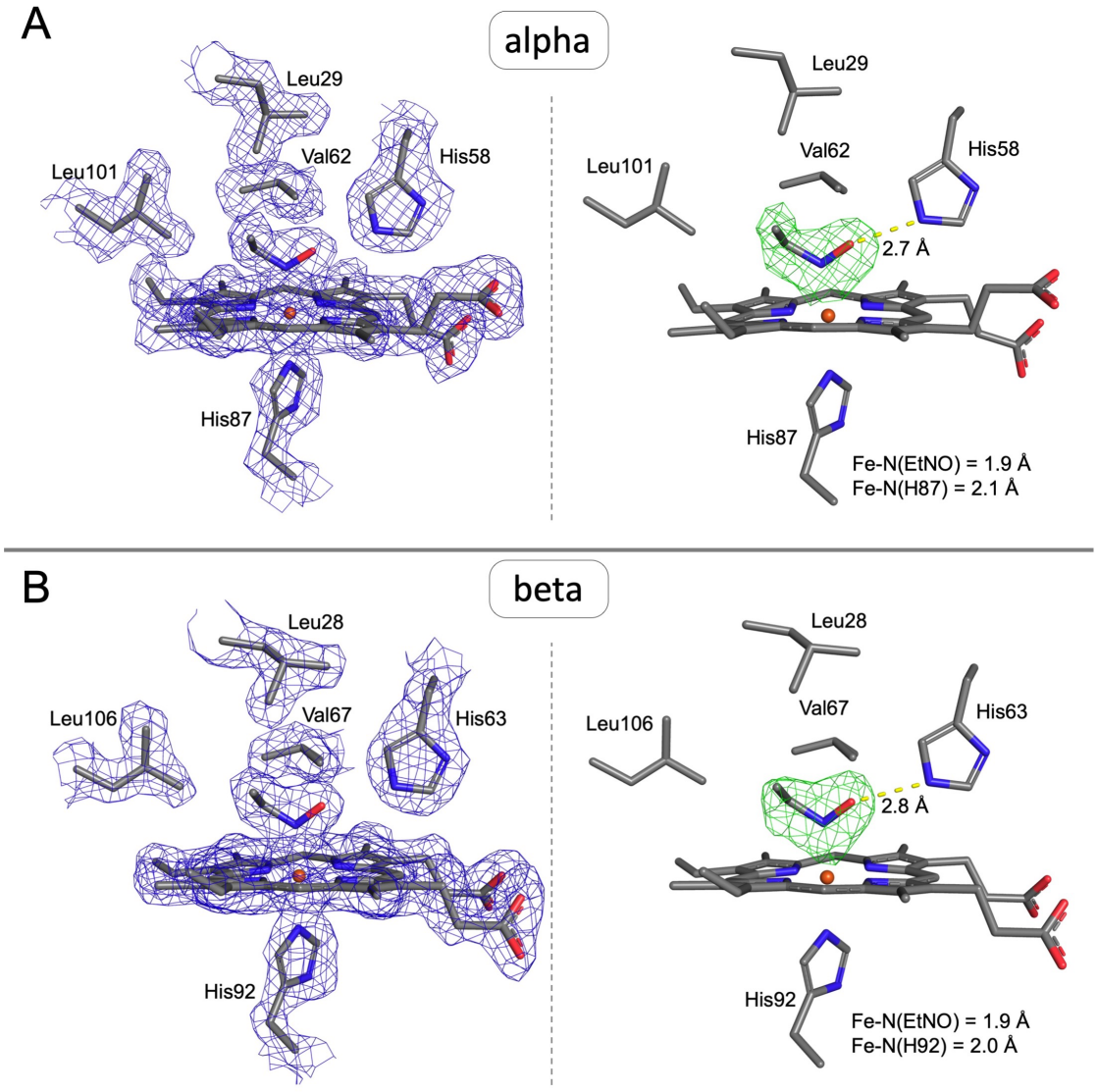

Figure 3.12 Models of the heme active site of the (A) α and (B) β subunits of the Hb[α-Fe^{II}(EtNO)][β-Fe^{II}(EtNO)] complex at 1.97 Å resolution. *Left:* $2F_o–F_c$ electron density map (blue mesh, contoured at 1σ). *Right*: $F_o–F_c$ omit electron density maps (green mesh, contoured at 3σ). In both subunits, the Fe-bound EtNO ligands were modeled at 100% occupancy.

The symmetry mate of Hb[α-Fe^{II}(EtNO)][β-Fe^{II}(EtNO)] was generated in *PyMol* to create the global tetrameric structure of the complex. This model was then used to compare the α1β2 interphase with structures of known conformation (Figure 3.9D). The resulting signature "switch" model shows the β2His97 situated between the α1Thr38 and α1Thr41 residues (cyan) similar to that of the R-state Hb (green) model. Further analysis of the α1β2 interphase corroborates the finding that the Hb[α-Fe^{II}(EtNO)][β-Fe^{II}(EtNO)] structure is in the R-state conformation.

After X-ray diffraction data collection, the Hb[α-Fe^{II}(EtNO)][β-Fe^{II}(EtNO)] crystal was dissolved in 0.1 M phosphate buffer (pH 7.4) to collect its UV-vis spectrum. In the Soret region of the spectrum, one peak was observed at λ_{max} ~420 nm, and in the Q-region of the spectrum two peaks were observed at λ ~540 and ~565 nm (Figure 3.13). These results are analogous to those observed for the solution reaction of dithionite-reduced Hb with nitroethane (see Figure 3.4); this confirms the notion that iron is in the ferrous state in the Hb[α-Fe^{II}(EtNO)][β-Fe^{II}(EtNO)] structure.

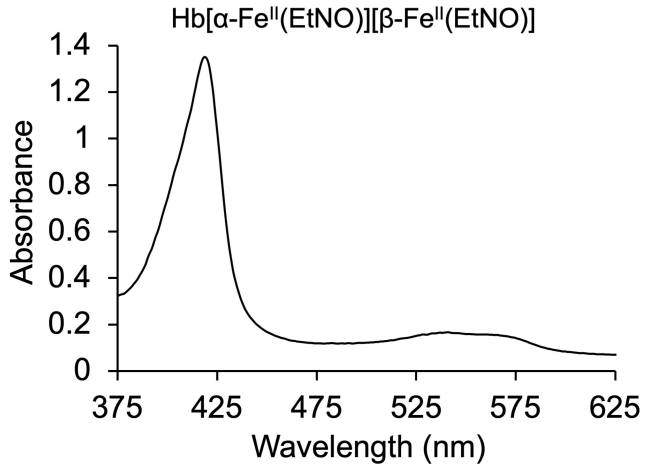

Figure 3.13 UV-vis spectrum of the Hb[α-Fe^{II}(EtNO)][β-Fe^{II}(EtNO)**]** crystal dissolved in 0.1 M phosphate buffer (pH 7.4) after X-ray diffraction data collection.

3.3.2.4 Hemichrome Hb[α-Fe^{II}(EtNO)][β-Fe(His)$_2$-SNO] derivative

Crystals of the Hb[α-Fe^{II}(EtNO)][β-Fe(His)$_2$-SNO] hemichrome were collected from the same vial from which the Hb[α-Fe^{II}(EtNO)][β-Fe^{II}(EtNO)] crystals were harvested, but they were collected several weeks later to track the process of Hb degradation. The X-ray crystal structure of this complex was solved as an α1β1 dimer to 1.89 Å.

The electron density maps ($2F_o–F_c$ and $F_o–F_c$) and models of the α subunit of Hb[α-Fe^{II}(EtNO)][β-Fe(His)$_2$-SNO] (Figure 3.14) closely resemble those of the α subunit in the Hb[α-Fe^{II}(EtNO)][β-Fe^{II}(EtNO)] structure. In fact, careful analysis of the active site revealed only minor differences in ligand orientation, H-bonding, and hydrophobic interactions. In this structure, EtNO was also modeled at 100% occupancy with a $C^2–C^1–N=O$ torsion angle of -67.0°. Furthermore, the ligand is similarly N-bound to the heme Fe (at 1.8 Å) and participates in H-bonding with His58($N^{\varepsilon 2}$) (at 2.4 Å) through the O-atom. The ethyl group of the ligand is closely surrounded by hydrophobic residues. For instance, the calculated distances from EtNO(C^1) to Leu29($C^{\delta 2}$), Val62($C^{\gamma 2}$) and Leu101($C^{\delta 2}$) are 3.9, 3.6 and 3.6 Å, respectively. Similarly, EtNO(C^2) interacts with neighboring residues, with distances to Leu29($C^{\delta 2}$), Met32(C^{ε}) Phe43(C^{ζ}) and Leu101($C^{\delta 2}$) calculated as 3.9, 4.0, 4.0 and 3.9 Å respectively.

In the exterior of the heme pocket, the propionate groups are oriented in opposite directions with the propionate ($O^{1\delta}$) atom H-bonded to His45($N^{\varepsilon 2}$) at 2.9 Å. The other O-atoms of the propionates form close contacts with fixed water molecules, ranging from 2.6 – 3.5 Å in distance.

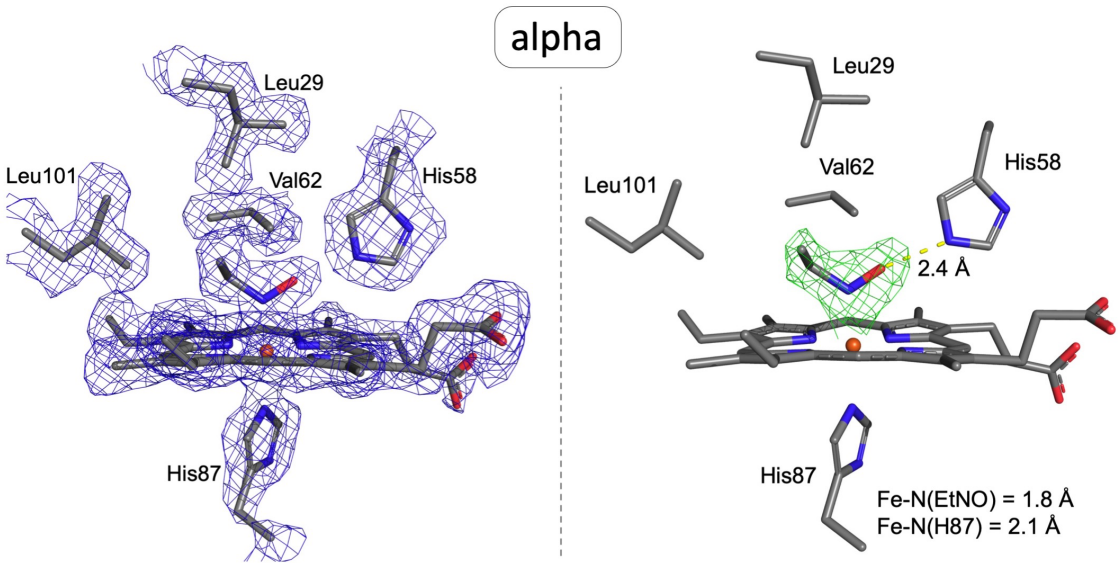

Figure 3.14 Models of the active site of the α subunit of the Hb[α-Fe^{II}(EtNO)][β-Fe(His)$_2$-SNO] hemichrome at 1.89 Å resolution. *Left:* $2F_o–F_c$ electron density map (blue mesh, contoured at 1σ). *Right*: $F_o–F_c$ omit electron density map (green mesh, contoured at 3σ) with EtNO modeled at 100% occupancy.

In contrast to the α subunit, the β subunit of the Hb[α-Fe^{II}(EtNO)][β-Fe(His)$_2$-SNO] derivative has undergone large backbone movements at the secondary and tertiary structure level, as well as significant localized active site structural differences to facilitate hemichrome formation. The $2F_o–F_c$ electron density map of the β subunit and the corresponding model of the heme pocket are shown in Figure 3.15A. In this structure, the heme is shifted towards the solvent exterior of the protein which results in bis-coordination by the distal His63 and the proximal His92. Furthermore, the propionate groups of the heme appear to be highly disordered, as indicated by poor density in the $2F_o–F_c$ map (contoured at 1σ) around these groups.

Unlike any of the previous structures in this study, the EtNO ligand was modeled in this β subunit behind the heme (100% occupancy), in the interior of the heme pocket (Figure 3.15B). Alternatively, this density could correspond to the isomeric CH^3–CH^2–N=OH oxime, which is the tautomerization product of EtNO and is more chemically stable [28-30]. Assuming that the density

in fact corresponds to EtNO, the closest calculated distances to the ligand from nearby hydrophobic residues were from EtNO(C^2) to Phe41($C^{\delta 2}$) and Phe42($C^{\delta 2}$) at 3.8 and 3.6 Å. On the other hand, the only possible polar interaction observed was between EtNO(O) with Asn102($N^{\delta 2}$) at 3.6 Å.

Upon further analysis of the β subunit, Fe anomalous scattering mapping revealed two positions for iron, namely Fe^1 and Fe^2 (Figure 3.15C). Based on these results and the electron density maps, heme was modeled at 90% occupancy at the hemichrome position (Fe^2). At position Fe^1, due to lack of electron density for a macrocycle, a lone Fe atom was modeled at 10% occupancy. It bears repeating that the Hb[α-Fe^{II}(EtNO)][β-Fe$(His)_2$-SNO] structure appeared chronologically after ligand binding. Taking this into consideration, it is possible that the 10% of the heme represented by the lone Fe atom at Fe^1 lingers in the original "ligand bound" position that was observed in the Hb[α-Fe^{II}(EtNO)][β-Fe^{II}(EtNO)] structure.

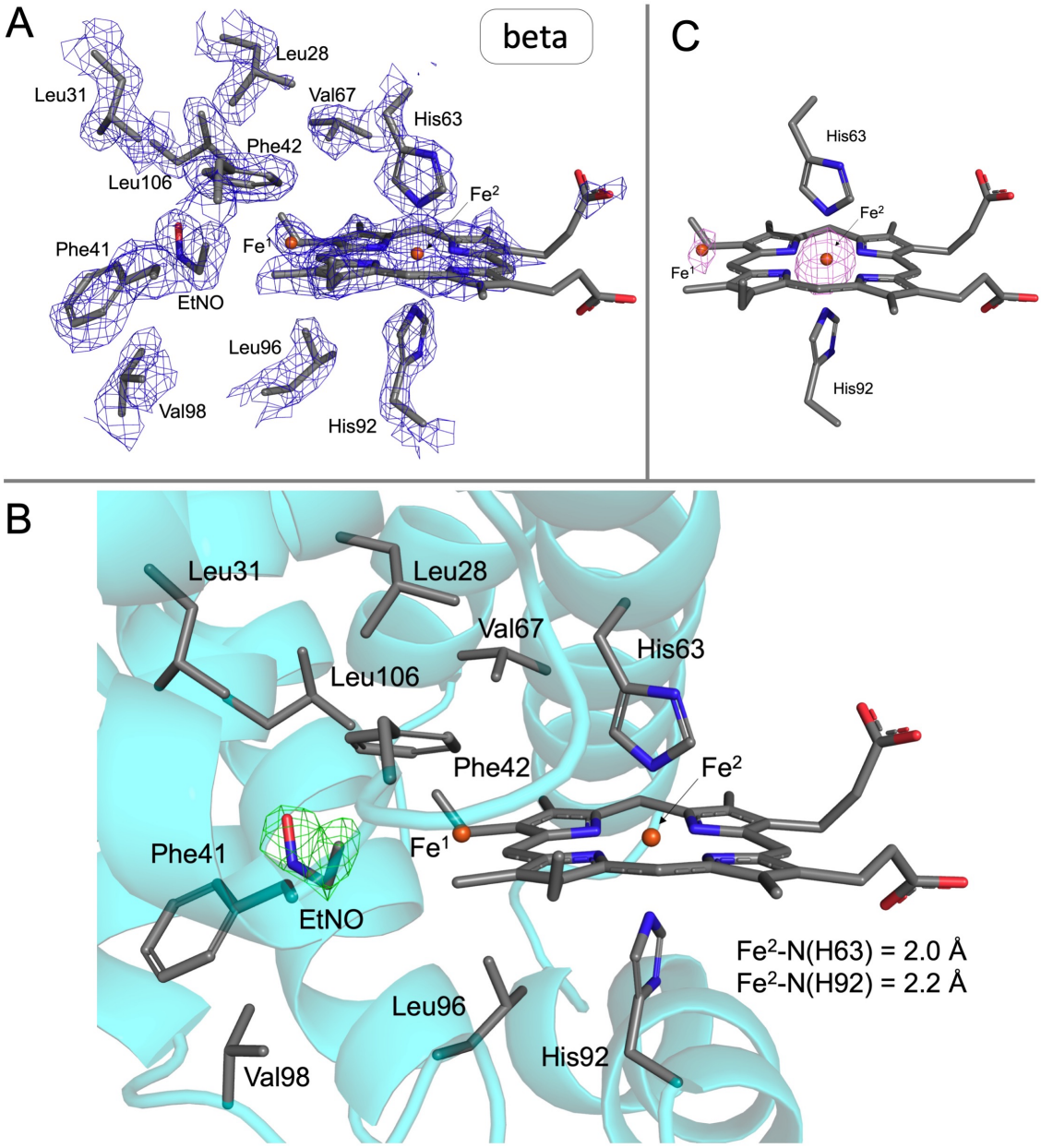

Figure 3.15 Models of the β subunit of the Hb[α-Fe^{II}(EtNO)][β-Fe$(His)_2$-SNO] hemichrome. (A) $2F_o–F_c$ electron density map (blue mesh, contoured at 1σ). (B) $F_o–F_c$ omit electron density map (green mesh, contoured at 3σ) with EtNO modeled at 100% occupancy behind the heme in the hydrophobic interior of the protein. (C) Fe anomalous map (violet mesh, contoured at 3σ) indicating two positions for Fe. A lone iron atom (Fe^1) was modeled in at 10% occupancy behind the heme illustrated, however not enough density was observed to model in the porphyrin ring. The heme (at position Fe^2) corresponds to the hemichrome position, which was modeled in at 90% occupancy.

Another unexpected feature of this structure is the nitrosation of βCys93, which resulted in the formation of the *S*-nitrosothiol (SNO) derivative (Figure 3.16). The βCys93 residue is located in the FG loop exposed to the solvent regions of the structure, which makes it easily accessible to diffusing molecules. Based on the F_o–F_c omit electron density maps, SNO was modeled in place of the -SH group in two different conformations (50% occupancy each). Each SNO conformation is stabilized through H-bonding interactions with fixed waters linked to nearby βGlu90 (β subunit) in the F-helix and αThr8 (α subunit) in the A-helix (Figure 3.16C).

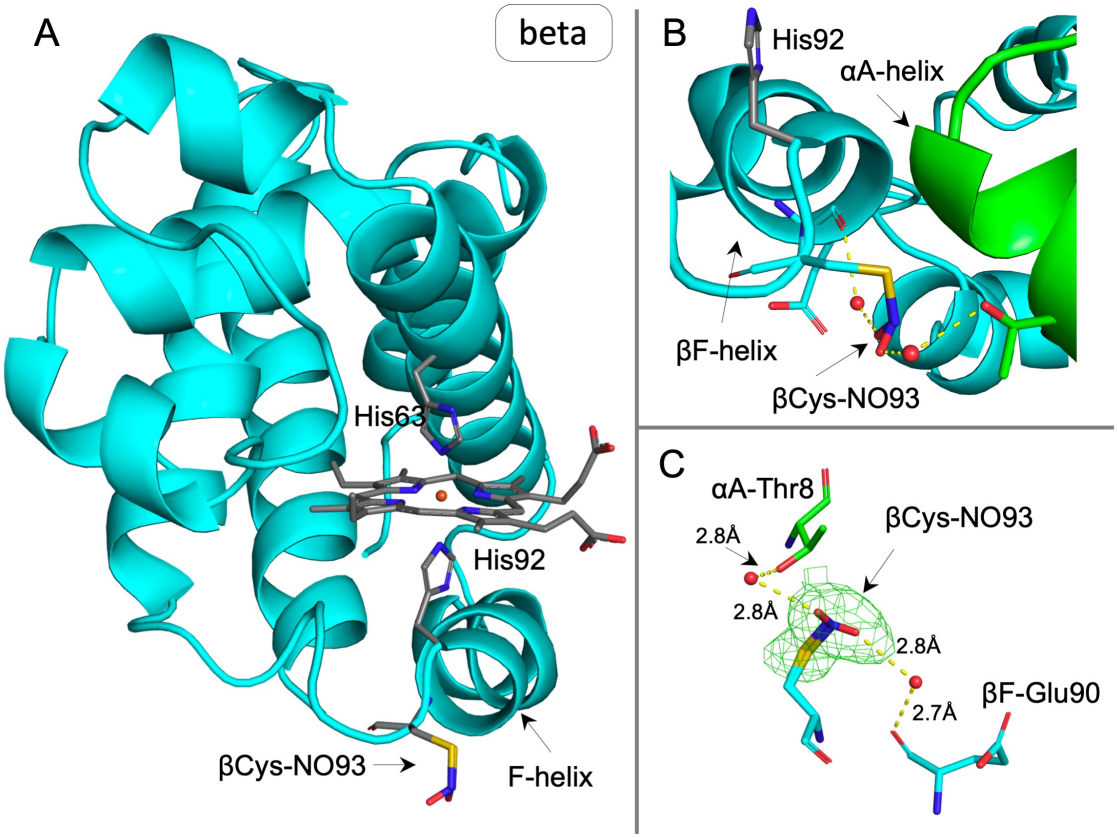

Figure 3.16 (A) Overall view of the Hb[α-Fe^{II}(EtNO)][β-Fe(His)$_2$-SNO] hemichrome β subunit. (B) Model of the overall environment surrounding the βCys-NO93 residue. (C) H-bonding interactions of the βCys-NO93 residue with the C=O backbone of neighboring Glu90 (βF-Helix) and Thr8 (αA-Helix) of a generated symmetry mate through fixed water molecules. Also shown, F_o–F_c omit electron density map (green mesh, contoured at 1.5σ) showing both conformations of βCys-NO93, each modeled at 50% occupancy.

Analysis of the α1β2 "switch" region (Figure 3.9E) revealed a distinct quaternary state conformation from any of the canonical (e.g., T and R-state) structures. The β2His97 and the β2FG corner deviate significantly from the location of the T-state structure (magenta). While the backbone β2FG corner and β2His97 are closer to the vicinity of the R-state models, these two regions have notably different spatial arrangements from any of the R(1, 2 or 3)-state (green, yellow, slate) structures. Thus, the conformation of the Hb[α-Fe^{II}(EtNO)][β-$Fe(His)_2$-SNO] hemichrome is best described as an altered R-state.

3.3.2.5 Degradation Hb[α-Fe^{II}(EtNO)][β-Fe(2 positions)] product

Crystals of the degradation Hb[α-Fe^{II}(EtNO)][β-Fe(2 positions)] product were harvested from the same vial from which crystals of Hb[α-Fe^{II}(EtNO)][β-Fe^{II}(EtNO)] (Figure 3.12) and Hb[α-Fe^{II}(EtNO)][β-Fe(His)$_2$-SNO] (Figure 3.14 and Figure 3.15) were collected, but they were harvested at later time points. The X-ray crystal structure of this complex was solved as an α1β1 dimer to a 1.90 Å resolution.

The α subunit of the Hb[α-Fe^{II}(EtNO)][β-Fe(2 positions)] degradation product remains highly conserved, in the sense that the $2F_o–F_c$ electron density map and the $F_o–F_c$ omit electron density map of the α subunit (Figure 3.17) closely resemble the two previously discussed Hb-EtNO related structures: (Hb[α-Fe^{II}(EtNO)][β-Fe^{II}(EtNO)] and Hb[α-Fe^{II}(EtNO)][β-Fe(His)$_2$-SNO]).

In the α subunit of the Hb[α-Fe^{II}(EtNO)][β-Fe(2 positions)] structure, the EtNO molecule was modeled at 100% occupancy N-bound to the heme Fe at a distance of 1.9 Å, with a torsion angle of -57.8°. Hydrogen bonding from the ligand's O-atom to His58(N$^{\varepsilon 2}$) at 2.6 Å restricts its conformation inside the heme pocket, orienting the ethyl group towards the interior of the active site where it is enclosed by multiple hydrophobic residues. The distances from EtNO(C^1) to Leu29(C$^{\delta 2}$), Val62(C$^{\gamma 2}$) and Leu101(C$^{\delta 2}$) were measured as 3.7, 3.8 and 3.6 Å, respectively. Similarly, the distances from EtNO(C^2) atom to neighboring Leu29(C$^{\delta 2}$), Met32(C$^{\varepsilon}$), Phe43(C$^{\zeta}$) and Leu101(C$^{\delta 2}$) were calculated as 3.2, 3.8, 3.7 and 4.1 Å, respectively. Outside of the hydrophobic pocket, the propionate groups are oriented in opposite directions, with the propionate (O$^{\delta 2}$) atom H-bonded to His45(N$^{\varepsilon 2}$) at 2.7 Å.

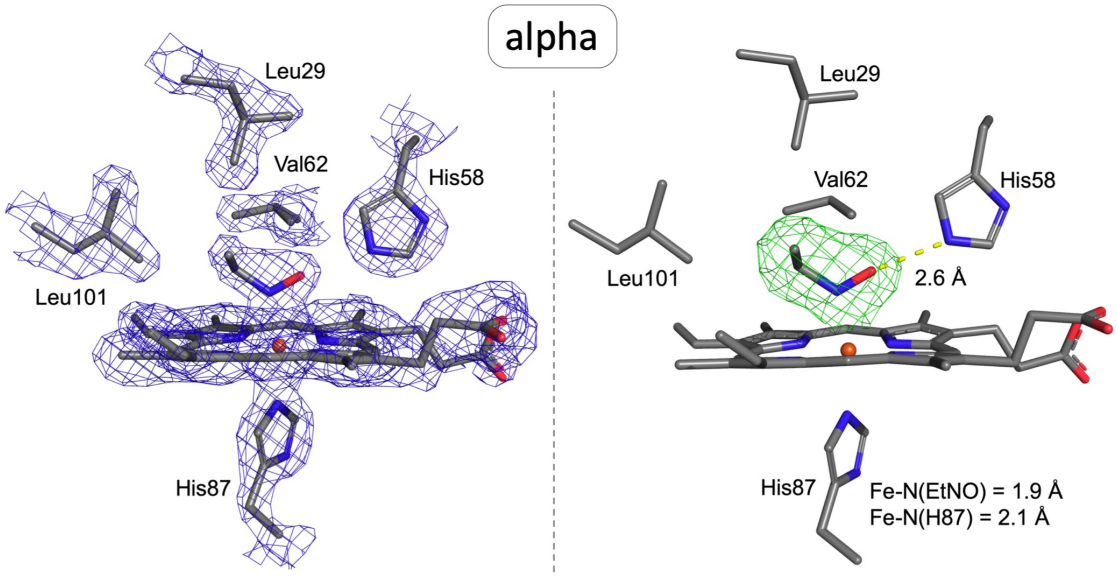

Figure 3.17 Active site models of the α subunit of the degradation Hb[α-Fe^{II}(EtNO)][β-Fe(2 positions)] product at 1.90 Å resolution. *Left:* $2F_o–F_c$ electron density map (blue mesh, contoured at 1σ). *Right*: $F_o–F_c$ omit electron density map (green mesh, contoured at 3σ) with EtNO modeled at 100% occupancy.

The $2F_o–F_c$ electron density map, and in particular the $F_o–F_c$ omit electron density map of the β subunit of Hb[α-Fe^{II}(EtNO)][β-Fe(2 positions)] reveled disordered and insufficient density for heme (Figure 3.18A-B). This prompted us to analyze the structure further with Fe anomalous scattering mapping. The results revealed two positions for Fe, at which we modeled two lone Fe atoms, Fe^1 and Fe^2 (Figure 3.18C). Fe^1 was modeled directly above His92 (56% occupancy) similar to canonical Hb structures, coordinated to His92($N^{\varepsilon 2}$) at a distance of 2.3 Å. On the other hand, Fe^2 was modeled (44% occupancy) below the distal His63($N^{\varepsilon 2}$) at a 3.3 Å distance. Overall, Fe^2 exhibits significant displacement towards the exterior of the protein (5.2 Å outward movement) as would be expected in the progression of heme loss from the active site.

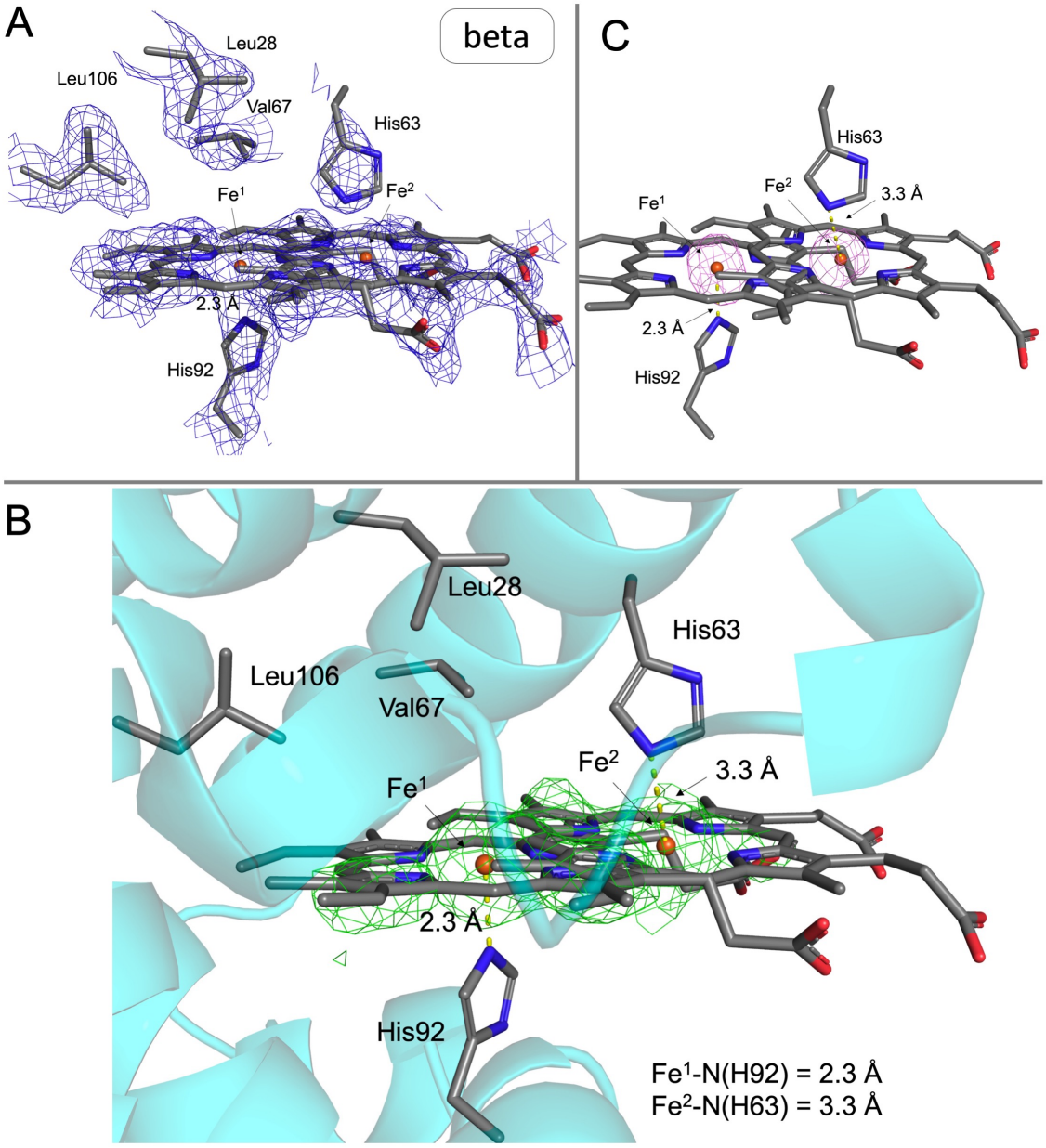

Figure 3.18 Models of the β subunit of the Hb[α-Fe^{II}(EtNO)][β-Fe(2 positions)] degradation product. (A) $2F_o–F_c$ electron density map (blue mesh, contoured at 0.75σ). (B) $F_o–F_c$ omit electron density map (green mesh, contoured at 3σ) showing disordered density for a single heme. (C) Fe anomalous map (violet mesh, contoured at 3σ) indicating two positions for Fe. The Fe_1 and Fe_2 atoms were modeled in at 56 and 44% occupancy respectively, as determined by anomalous scattering ratios.

Comparison of the α1β2 interphase of the tetrameric structure of Hb[α-Fe^{II}(EtNO)][β-Fe(2 positions)] with archetypical Hb structures suggest that the quaternary structure of Hb[α-Fe^{II}(EtNO)][β-Fe(2 positions)] (cyan) is in the R-state conformation (Figure 3.9F). This is indicated by the position of β2His97 between the α1Thr38 and α1Thr41, and by the overall alignment of the β2FG backbone, which most closely overlaps the spatial arrangement of R-state Hb(CO) (green).

3.3.2.6 Ligand bound Hb[α-Fe^{II}(PrNO)][β-Fe^{II}(PrNO)]

Crystals of the ligand bound Hb[α-Fe^{II}(PrNO)][β-Fe^{II}(PrNO)] complex were grown anaerobically through co-crystallization using the batch method. The crystal structure of this complex was solved as an α1β1 dimer to a 1.90 Å resolution.

The electron density maps ($2F_o$–F_c and F_o–F_c) of the active sites show conspicuous density corresponding to PrNO in both the α and β subunits (Figure 3.19). In both models, the PrNO density is situated directly above the heme with the ligand modeled in at 100% occupancy. In accord with our UV-vis studies, the PrNO ligand is N-bound to the Fe-atom at distances of 1.7 and 1.9 Å in the α and the β subunits, respectively. Moreover, the O-atom of PrNO interacts with distal His58/63($N^{\varepsilon 2}$) at distances of 2.7 (α) and 2.8 (β) Å respectively. This H-bonding anchors the ligand, causing the propyl group to orient towards the interior of the heme pocket where it participates in several hydrophobic interactions.

In the α subunit, the calculated distance between PrNO(C^1) and Leu101($C^{\delta 2}$) is 3.6 Å. Neighboring PrNO(C^2) are Phe43($C^{\varepsilon 1}$) and Phe43(C^{ζ}) at distances of 3.8 and 3.5 Å, respectively. Finally, the C^3 atom of PrNO is buried inside a small hydrophobic tunnel with distances from PrNO(C^3) to Leu29($C^{\delta 2}$), Met32(C^{ε}) and Phe43($C^{\varepsilon 1}$) of 3.4, 3.3 and 3.4 Å respectively. In the β subunit, similar hydrophobic contacts are observed. The distances from PrNO(C^1) to Val67($C^{\gamma 2}$) and Leu106($C^{\delta 2}$) were measured as 3.6 Å each. Likewise, the distances from PrNO(C^2) to Leu28($C^{\delta 1}$) and Phe42(C^{ζ}) were calculated as 3.5 Å each. Finally, the atoms Leu28($C^{\delta 1}$) and Leu31($C^{\delta 2}$) border PrNO(C^3) with measured distances of 3.4 and 3.0 Å respectively.

The propionate groups in the α subunit are angled in opposite directions. Furthermore, the heme($O^{\delta 2}$) atom forms a hydrogen-bond interaction with His45($N^{\varepsilon 2}$) at 2.8 Å. The propionate

groups in the β active site align towards the same side of the heme and form no direct interactions with protein residues or fixed solvent molecules.

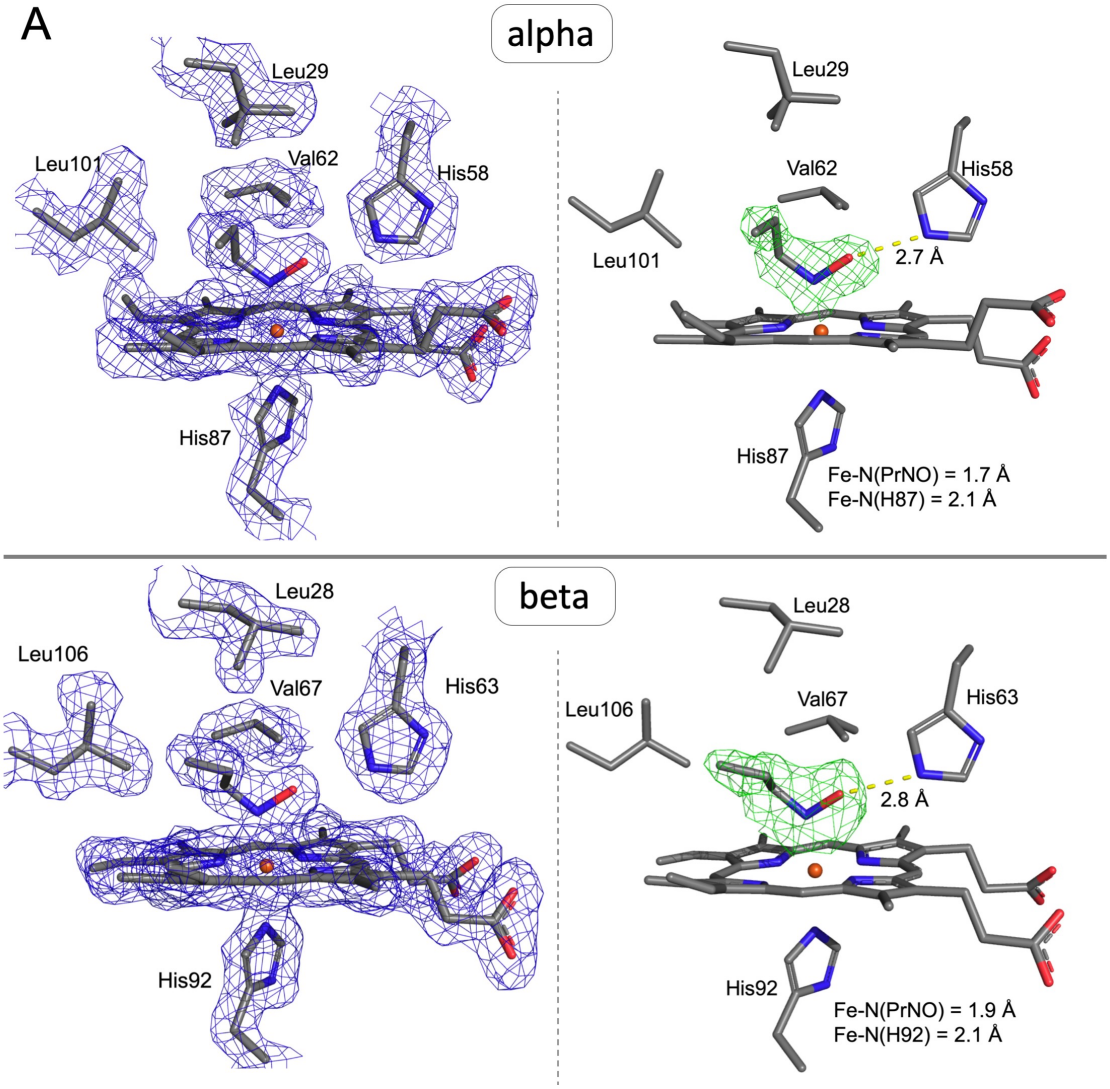

Figure 3.19 Active site models of (A) α and (B) β subunits of the ligand bound Hb[α-Fe^{II}(PrNO)][β-Fe^{II}(PrNO)])] complex at a resolution of 1.90 Å. *Left:* $2F_o–F_c$ electron density map (blue mesh, contoured at 1σ). *Right*: $F_o–F_c$ omit electron density maps (green mesh, contoured at 3σ and 2σ in the α and β subunits respectively). In both subunits, the Fe-bound PrNO ligands were modeled at 100% occupancy.

The Hb[α-Fe^{II}(PrNO)][β-Fe^{II}(PrNO)] structure was determined to be in the R-state conformation, where the residue β2His97 and the β2FG corner of Hb[α-Fe^{II}(PrNO)][β-Fe^{II}(PrNO)] (cyan) best mimic the spatial arrangement of the R-state (green) Hb(CO) structure (Figure 3.9G).

The oxidation state of Fe in the Hb[α-Fe^{II}(PrNO)][β-Fe^{II}(PrNO)] structure was determined by recording its absorption spectrum. This became particularly important because our UV-vis studies of the Hb^{II}-PrNO complex showed that the ferrous product is short-lived in solution, yet the crystals took several days to grow. Therefore, after X-ray diffraction data collection, the crystal was dissolved in 0.1 M phosphate buffer (pH 7.4) and the UV-vis spectrum was collected. The results show a peak at λ_{max} ~420 nm in the Soret band and two peaks at λ ~540 and 565 in the Q-region of the spectrum (Figure 3.20). These results are in agreement with data obtained from our spectral studies of the reactions between dithionite-reduced Hb^{II} and $PrNO_2$ in solution (see *3.3.1*), thus confirming the redox state of iron as Fe^{II}.

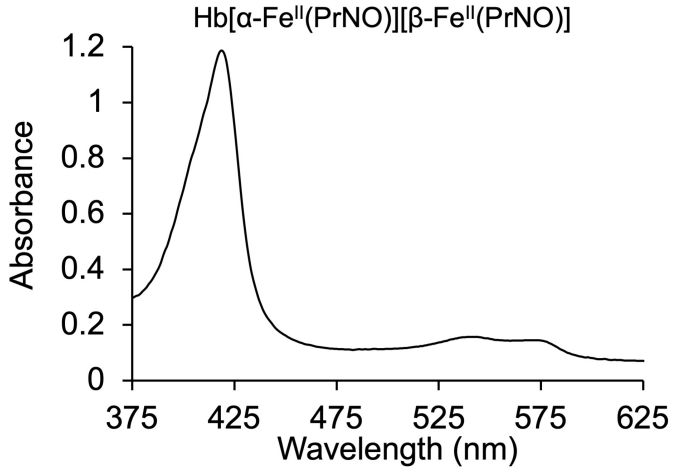

Figure 3.20 UV-vis spectrum of the Hb[α-Fe^{II}(PrNO)][β-Fe^{II}(PrNO)] crystal dissolved in 0.1 M phosphate buffer (pH 7.4) after X-ray diffraction data collection.

3.3.2.7 Degradation Hb[α-Fe^{II}(PrNO)][β-Fe(2 positions)] product

Crystals of the degradation Hb[α-Fe^{II}(PrNO)][β-Fe(2 positions)] product were harvested from the same vial where Hb[α-Fe^{II}(PrNO)][β-Fe^{II}(PrNO)] crystals grew, but the crystals were looped several weeks later.

The active site models of the α subunit of the Hb[α-Fe^{II}(PrNO)][β-Fe(2 positions)] degradation product at 1.90 Å resolution (Figure 3.21) are almost indistinguishable from those of the α subunit of Hb[α-Fe^{II}(PrNO)][β-Fe^{II}(PrNO)] (Figure 3.19). Based on the resultant electron density maps, PrNO was modeled at 100% occupancy N-bound to Fe (1.8 Å distance). A hydrogen bond between PrNO(O) and His58($N^{\varepsilon 2}$) creates a docking point that restricts ligand rotation inside the active site. Consequently, the propyl group is buried in the hydrophobic interior of the heme pocket, with calculated distances from PrNO(C^1) to Leu101($C^{\delta 2}$) and Val62($C^{\gamma 2}$) at 3.5 and 3.6 Å. Similarly, the distances from PrNO(C^2) to Leu29($C^{\delta 2}$), Phe($C^{\varepsilon 1}$) and Phe(C^{ζ}) were measured at 3.0, 4.0 and 4.0 Å respectively. Finally, the PrNO(C^3) atom has measured distances to Leu29($C^{\delta 2}$), Met32(C^{ε}) and Phe43($C^{\varepsilon 1}$) of 3.7, 3.2 and 3.9 Å, respectively.

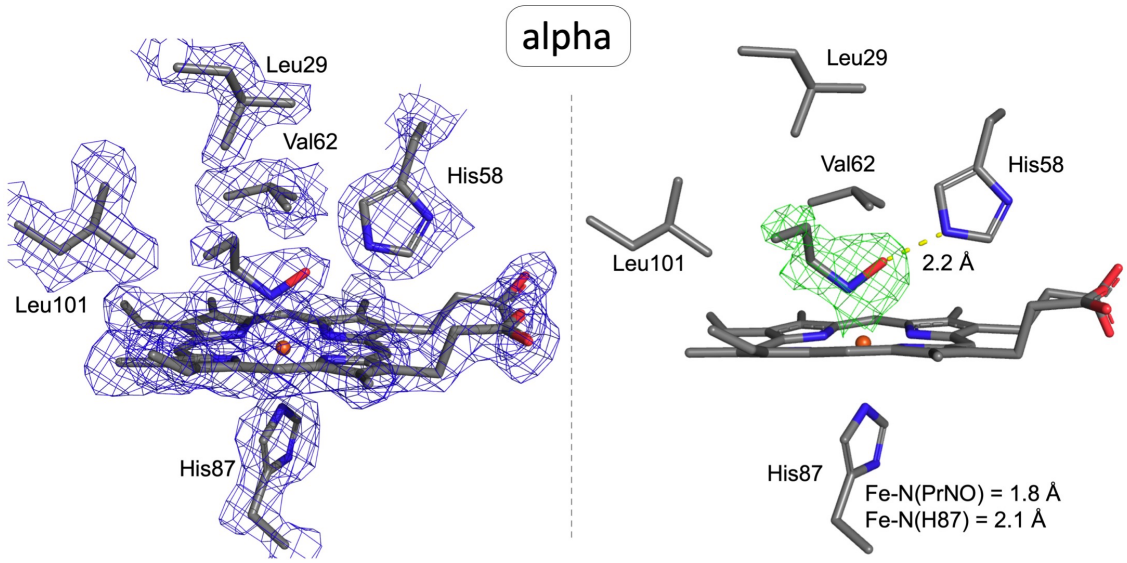

Figure 3.21 Active site models of the β subunit of Hb[α-Fe^{II}(PrNO)][β-Fe(2 positions)] degradation product at 1.90 Å resolution. *Left:* $2F_o–F_c$ electron density map (blue mesh, contoured at 1σ). *Right*: $F_o–F_c$ omit electron density map (green mesh, contoured at 3σ) with PrNO modeled at 100% occupancy.

Upon inspection of the $2F_o–F_c$ electron density map of the β subunit (Figure 3.22A), we observed sparse density surrounding the heme. Similar results were noted in the $F_o–F_c$ omit electron density map (Figure 3.22B). Based on these observations, we interrogated the structure further. Similarly to Hb[α-Fe^{II}(EtNO)][β-Fe(2 positions)], Fe anomalous scattering mapping exposed two locations for Fe. Two lone iron atoms, Fe^1 and Fe^2, were modeled at these positions with 46 and 54% occupancy each. Unlike any of our previous structures, the βF-helix of Hb[α-Fe^{II}(PrNO)][β-Fe(2 positions)] was modeled in two conformations, giving βHis92 two conformations as well. Consequently, each Fe atom is anchored to the heme pocket by binding to βHis92 (2.3 and 2.1 Å). Interestingly, Fe^2 is simultaneously bound to His63 and His92, and this bis-coordination strongly resembles hemichrome formation observed in our Hb[α-Fe^{II}(EtNO)][β-$Fe(His)_2$-SNO] structure (Figure 3.15).

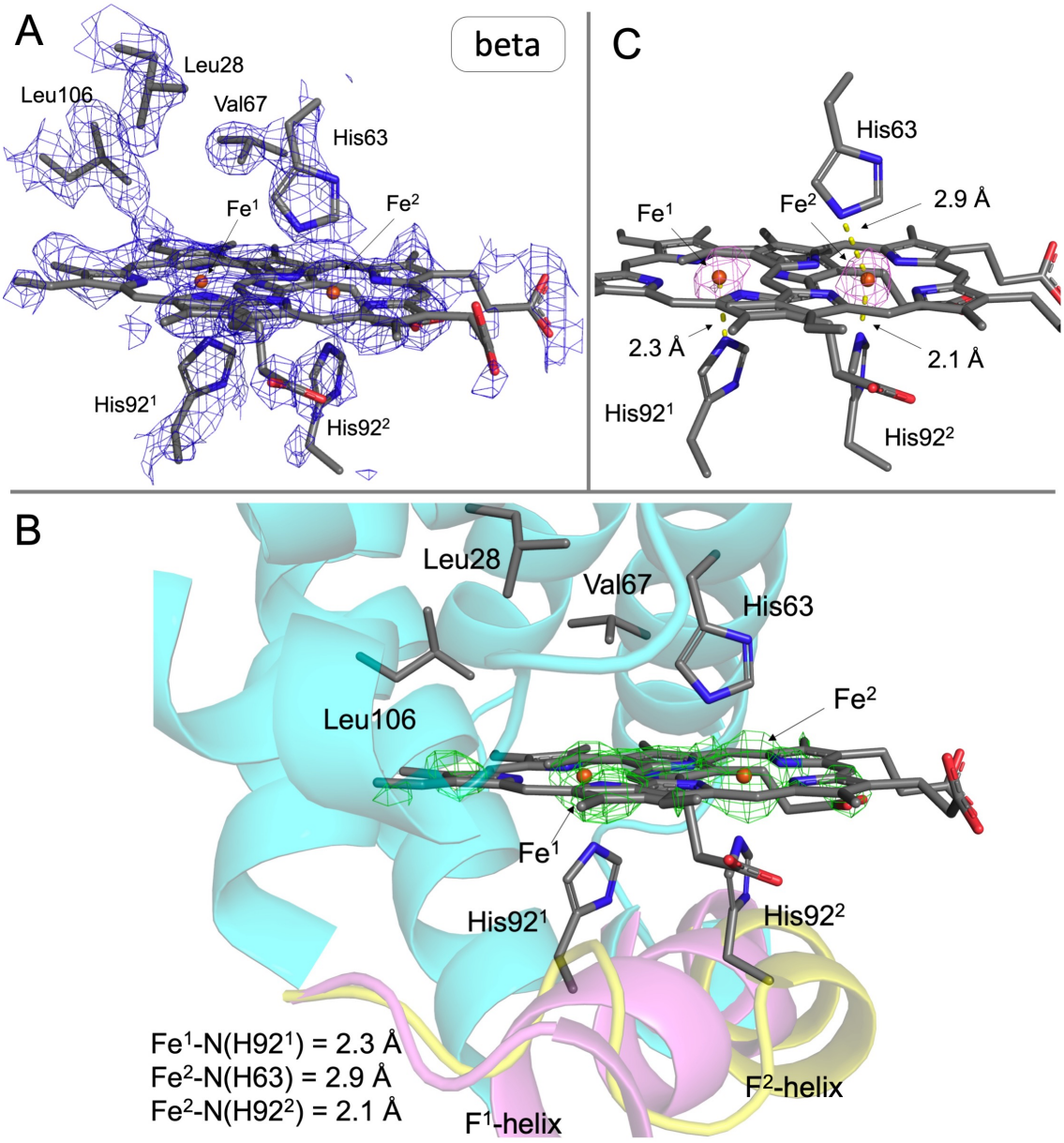

Figure 3.22 Active site models of the β subunit of the Hb[α-Fe^{II}(PrNO)][β-Fe(2 positions)] degradation structure. (A) $2F_o–F_c$ electron density map (blue mesh, contoured at 0.75σ). (B) $F_o–F_c$ omit electron density map (green mesh, contoured at 3σ) showing disordered density for a single heme. Two conformations were modeled for the F-helix (shown in pink and yellow). (C) Fe anomalous map (violet mesh, contoured at 3σ) indicating two positions for Fe. The hemes at Fe^1 and Fe^2 were modeled in at 46 and 54% occupancy respectively, as determined by anomalous scattering ratios.

Figure 3.23 shows the $2F_o–F_c$ electron density map (gray mesh) corresponding to the different conformations of the βF-helix. The structure was built by splitting residues Ala86 – Asp99 (which are: 86A-TLSELHCDKLHV-99D). The ensuing F^1 and F^2 helices were modeled with 46 and 54% occupancy respectively, which are the same ratios used to model the lone Fe atoms. Note that electron density for the backbones of both helices are clearly present, and that only a few side chains lack electron density.

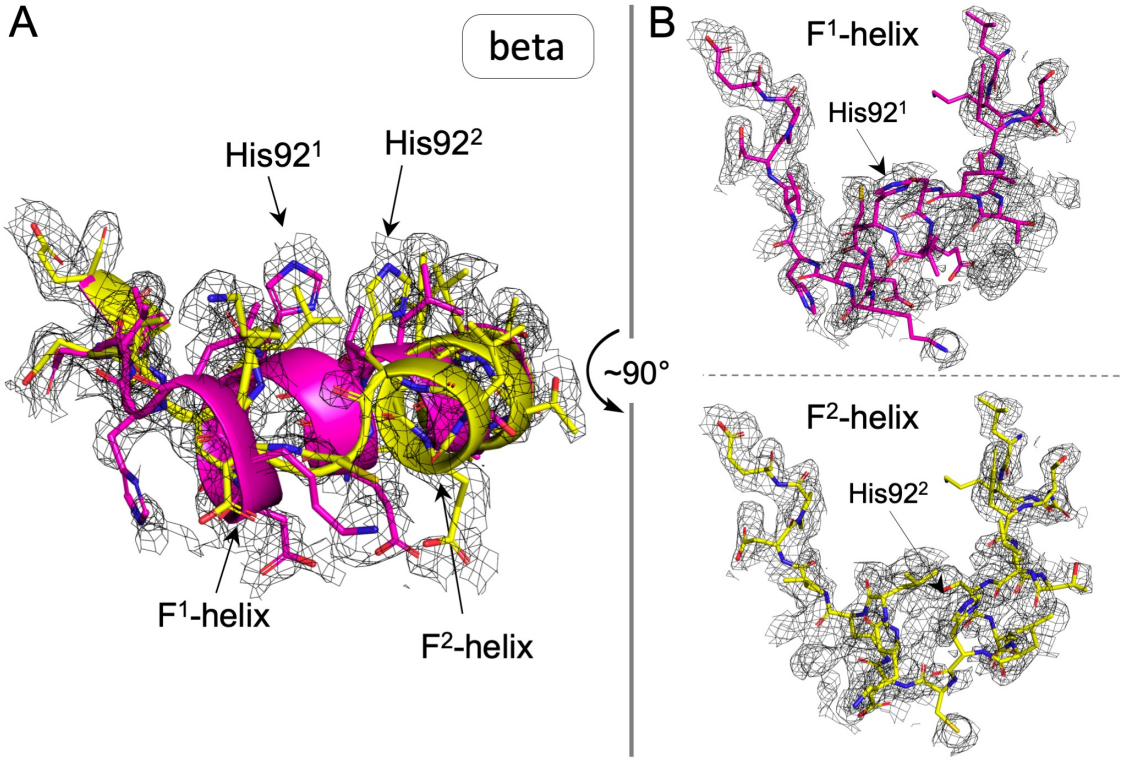

Figure 3.23 (A) Models of the two distinct conformations of the F-helix in the β subunit of the Hb[α-Fe^{II}(PrNO)][β-Fe(2 positions)] degradation product and $2F_o–F_c$ electron density map (gray mesh, contoured at 0.5σ) (B) top view (~90° counter clockwise vertical rotation) indicating individual F-helix conformations

Determining the quaternary state of the Hb[α-Fe^{II}(PrNO)][β-Fe(2 positions)] degradation product proved challenging. Unlike any of our previous structures, portions of the β2FG corner are modeled in two positions, giving rise to two β2His97 residues (Figure 3.24, cyan). The β2His97 corresponding to the F^1-helix (orange arrow), closely resembles the R-state conformation of Hb(CO) (green). On the other hand, the β2His97 of the F^2-helix (pink arrow) and the overall alignment of the β2FG backbone in this conformation, do not resemble any of the canonical Hb structures.

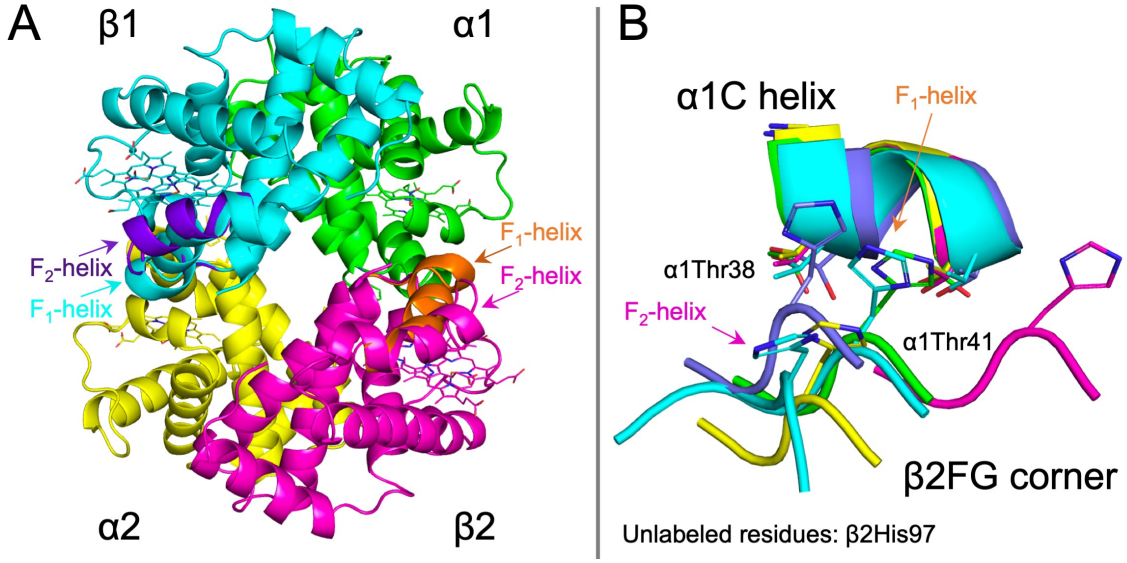

Figure 3.24 (A) X-ray crystal structure of the Hb[α-Fe^{II}(PrNO)][β-Fe^{II}(2 positions)] dimer represented in the tetrameric form by the α1 and β1 subunits. The α2 and β2 subunits are *PyMol* generated symmetry mates. The different conformations of the βF-helix are indicated by arrows and represented in distinct colors. (B) Comparison of the α1β2 interface with characteristic Hb structures. Magenta: T-state deoxyHb (PDB ID 1B86), Green: R-state Hb(CO) (PDB ID 1AJ9). Yellow: R2-state Hb(CO) (PDB ID 1BBB), Slate: R3-state Hb(CO) (PDB ID 1YZI). Cyan: Hb[α-Fe^{II}(PrNO)][β-Fe^{II}(2 positions)] from this work. The β2His97 indicated by the orange arrow corresponds to the βF^1-helix in an R-state. The β2His97 indicated by the pink arrow in the βF^2-helix is best represented as a modified R-state conformation.

3.3.3. Degradation studies of the Hb^{II}-MeNO, -EtNO and -PrNO products

While many pieces of crystallographic evidence presented here suggest that RNO (MeNO, EtNO, PrNO) ligand binding leads to Hb degradation, none of the X-ray crystal structures show complete heme loss and subsequent protein degradation. However, this may be due to the packing environment of the crystals, which obstruct heme from diffusing out of the active site. Therefore, we reproduced the reactions that were used to form the Hb^{II}-RNO derivatives for co-crystallization (see section *3.2.6*) and monitored their stability in solution. After one day, we separated any aggregation products from solution by centrifugation and found that all ligand-containing reactions resulted in precipitation (Figure 3.24). Interestingly, we noted that damage to Hb increased with increasing size of the RNO alkyl group. The control experiment containing sodium dithionite but no ligand also resulted in protein aggregation, but to a lesser extent. Finally, the control containing no ligand and no sodium dithionite resulted in no precipitation. These results along with our crystallographic evidence, suggest that RNO binding leads to Hb degradation.

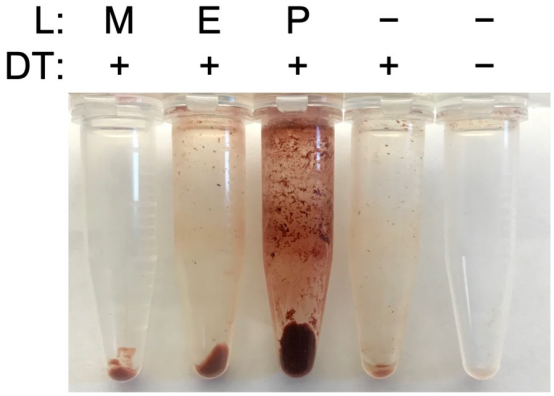

Figure 3.25 Hb degradation studies. Reaction mixture: 1 mL Hb^{III}-H_2O (30 mg/mL) + 8 µL of RNO_2 + ~24 mg sodium dithionite. L: ligand, DT: sodium dithionite, M: MeNO, E: EtNO, P: PrNO, + : added to the reaction, – : not added to the reaction.

Table 3-3 Configuration state of the Hb[α-Fe(ligand)][β-Fe(ligand)] structures

Structure	Configuration state
ferric Hb^{III}-H_2O	R-state
Hb[α-Fe^{II}(MeNO)][β-Fe^{II}(MeNO)]	R-state
Hb[α-Fe^{II}(MeNO)][β-Fe^{III}(H_2O)]	R-state
Hb[α-Fe^{II}(EtNO)][β-Fe^{II}(EtNO)]	R-state
Hb[α-Fe^{II}(EtNO)][β-Fe$(His)_2$-SNO]	Altered R-state
Hb[α-Fe^{II}(EtNO)][β-Fe(2 positions)]	R-state
Hb[α-Fe^{II}(PrNO)][β-Fe^{II}(PrNO)]	R-state
Hb[α-Fe^{II}(PrNO)][β-Fe(2 positions)]	R-, and altered R-state

Table 3-4 Selected structural parameters

Alpha-subunit							
Structure	Fe-N(H87) (Å)	Fe-N(RNO) (Å)	∠C_1-N=O (RNO) (°)	∠C_2-C_1-N=O (RNO) (°)	∠C_3-C_2-C_1-N (RNO) (°)	Ligand occupancy (%)	Propionate orientation
Hb[α-Fe^{II}(MeNO)][β-Fe^{II}(MeNO)]	2.2	1.9	115	NA	NA	100	Oposite
Hb[α-Fe^{II}(MeNO)][β-Fe^{III}(H_2O)]	1.9	1.9	115	NA	NA	100	Oposite
Hb[α-Fe^{II}(EtNO)][β-Fe^{II}(EtNO)]	2.1	1.9	114	55	NA	100	Oposite
Hb[α-Fe^{II}(EtNO)][β-Fe$(His)_2$-SNO]	2.1	1.8	112	67	NA	100	Oposite
Hb[α-Fe^{II}(EtNO)][β-Fe(2 positions)]	2.1	1.9	113	58	NA	100	Oposite
Hb[α-Fe^{II}(PrNO)][β-Fe^{II}(PrNO)]	2.1	1.8	108	48	142	100	Oposite
Hb[α-Fe^{II}(PrNO)][β-Fe(2 positions)]	2.1	1.8	106	45	97	100	Oposite
Beta-subunit							
Structure	Fe-N(H92) (Å)	Fe-N(RNO) (Å)	∠C_1-N=O (RNO) (°)	∠C_2-C_1-N=O (RNO) (°)	∠C_3-C_2-C_1-N (RNO) (°)	Occupancy (%)	Propionate orientation
Hb[α-Fe^{II}(MeNO)][β-Fe^{II}(MeNO)]	2.1	1.9	114	NA	NA	100	Down
Hb[α-Fe^{II}(MeNO)][β-Fe^{III}(H_2O)]	2.2	NA[C]	NA	NA	NA	100	Down
Hb[α-Fe^{II}(EtNO)][β-Fe^{II}(EtNO)]	2.0	1.9	109	60	NA	100	Down
Hb[α-Fe^{II}(EtNO)][β-Fe$(His)_2$-SNO]	2.2	NA[D]	NA	NA	NA	NA	??
Hb[α-Fe^{II}(EtNO)][β-Fe(2 positions)]	2.3	NA[E]	NA	NA	NA	NA	??
Hb[α-Fe^{II}(PrNO)][β-Fe^{II}(PrNO)]	2.1	1.9	106	62	155	100	Down
Hb[α-Fe^{II}(PrNO)][β-Fe(2 positions)]	2.3[A], 2.1[B]	NA[F]	NA	NA	NA	NA	??

[A] bond to Fe^1, [B] bond to Fe^2, [C] Fe binds H_2O instead at 2.4 Å, [D] Fe is bis-coordinated binding to His63 at 2.0 Å instead of an RNO, [E] Fe^1 only binds His92 while Fe^2 is coordinated to His63 at 3.3 Å, [F] Fe^2 is bis-coordinated to His63 at 2.9 Å instead of an RNO.

3.4 Discussion

3.4.1 Analysis of the reactions of Hb with nitroalkanes ($MeNO_2$, $EtNO_2$ and $PrNO_2$) under reducing conditions as determined by UV-vis spectroscopy

UV-vis spectroscopy was used to monitor the reactions of Hb^{II} with nitroalkanes. My goal was to determine how ligand sterics impact the extent of Hb^{II}-RNO complex formation, and to elucidate the stability of the resultant complexes in the presence and absence of air. Given the similarities in heme-pocket architecture between Mb and Hb, I expected to see an inverse relationship between ligand sterics and extent of formation of each complex, as discussed in Chapter 2 for the analogous Mb reactions. Additionally, I expected to gain information regarding the stability of these complexes to help guide my crystallization attempts of the Hb^{II}-RNO derivatives. For the aerobic reaction between ferrous Hb^{II} with nitromethane under reducing conditions, Mansuy reported a shift in the Soret band from λ_{max} 430 to 421 nm, and simultaneous spectral changes in the Q-region from λ 555 to 562 nm with a shoulder appearing at λ ~545 nm [22]. Our aerobic and anaerobic reactions between dithionite reduced Hb^{II} and nitroalkanes resulted in similar spectral shifts (Figure 3.4). As expected, temporal tracking of these reactions uncovered an apparent inverse relationship between extent of formation and ligand sterics (Figure 3.5). Specifically, the smallest RNO, MeNO, resulted in the highest extent of formation (0.53, aerobically) and EtNO followed at a slightly lower extent of formation (0.51, aerobically), while formation of the Hb^{II}-PrNO complex was significantly lower (0.43, aerobically). Also, a direct relationship between complex stability and ligand sterics was noted. Interestingly, the Hb^{II}-MeNO and -EtNO complexes with these small MeNO and EtNO groups were relatively more stable and longer lived than Hb^{II}-PrNO, which began to dissociate its PrNO ligand at earlier timepoints. Furthermore, stability of the complexes was higher in the absence of air. These results provided

crucial information used to guide my crystallization conditions. The Hb^{II}-MeNO and -EtNO crystals were prepared aerobically, yet the same conditions resulted in Hb^{II}-O_2 crystals during attempted crystallization of Hb^{II}-PrNO. However, crystallization of intact Hb^{II}-PrNO was successful under anaerobic conditions.

After the UV-vis spectroscopy studies, I collected X-ray diffraction data on each of the Hb^{II}-RNO (R = Me, Et and Pr) crystals had been prepared and maintained in crystalline form over a period of time. Based on the trends in stability observed for the Hb^{II}-RNO complexes in solution (Figure 3.5), I expected each complex to reveal different stages in the structural fluctuations leading to RNO-induced Hb degradation.

3.4.2 Heme oxidation resulting from Hb-MeNO binding

Monitoring of the Hb^{II}-MeNO crystals resulted in two distinct structures that revealed the initial steps in the overall mechanism leading to Hb degradation.

3.4.2.1 Step 1, MeNO binding: Hb[α-Fe^{II}(MeNO)][β-Fe^{II}(MeNO)]

The X-ray crystal structure of Hb in complex with MeNO was previously published by a former lab member, Dr. Yi [18]. Her structure was obtained through the reaction of ferric Hb^{III}-H_2O with nitromethane in the presence of dithionite as a reducing agent. Although her structure was available, I decided to obtain my own Hb[α-Fe^{II}(MeNO)][β-Fe^{II}(MeNO)] structure and use it as a baseline reference to monitor structural changes after ligand binding. Comparison of these two structures revealed faithful MeNO binding mode (Figure 3.26). In both cases, the ligand was N-bound to the heme, and no significant differences were noted in bonding distances, ligand orientation, or spatial arrangement of the amino acids in the distal pocket. Additionally, the global folds of the α1β1 dimer are essentially the same, with an overall RMSD calculated as 0.270 Å.

This comparison indicates that the structures obtained likely correspond to the most favorable configuration of the complex.

The Hb[α-Fe^{II}(MeNO)][β-Fe^{II}(MeNO)] structure was further compared to ferric Hb^{III}-H_2O. As observed in Figure 3.27, ligand binding resulted in minor geometrical fluctuations in the arrangement of the amino acids within the active site. The major differences are noted on the distal His58/92 residues. In both subunits, the His58/92 residues swing out, towards the solvent exterior to accommodate MeNO binding. Swinging distances of 1.3 and 1.1 Å were calculated (as measured between His58/92 N^{ε} atoms) in the α and β subunits respectively. Finally, MeNO binding did not affect the global structure of the protein nor its R-state configuration (Table 3-3, Figure 3.9).

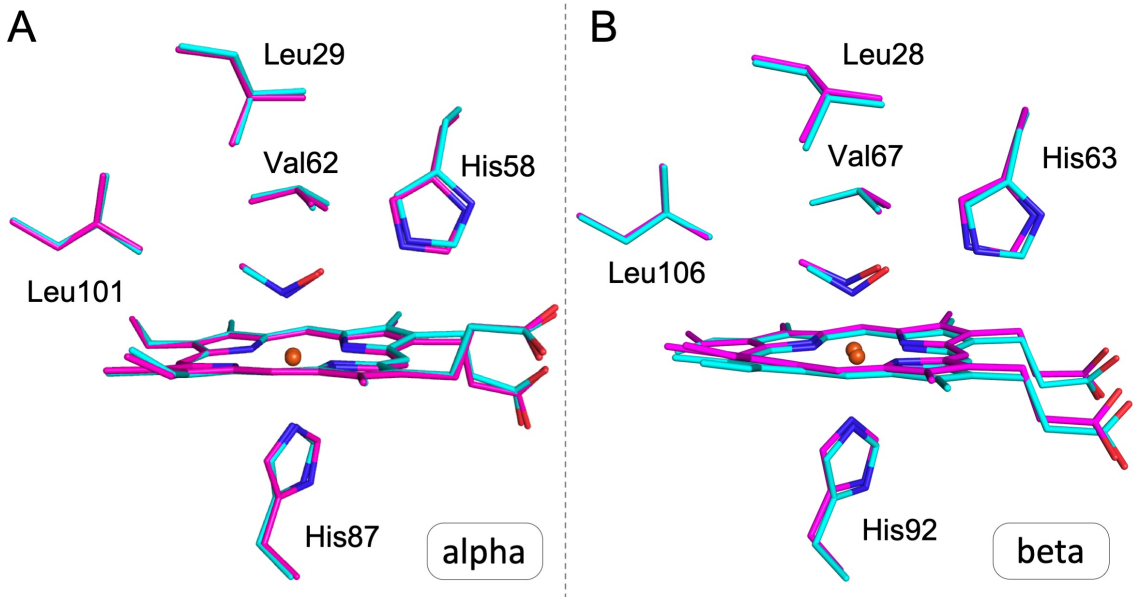

Figure 3.26 Superpositioning of the heme sites of the (A) α1 subunits and (B) β1 subunits of the Hb[α-Fe^{II}(MeNO)][β-Fe^{II}(MeNO)] structure from this work (cyan) and the previously published equivalent (magenta; PDB ID 4M4A).

3.4.2.2 Step 2, heme oxidation: Hb[α-Fe^{II}(MeNO)][β-Fe^{III}(H_2O)]

After solving this structure and determining the ligand bound Hb[α-Fe^{II}(MeNO)][β-Fe^{II}(MeNO)] models, I continued to monitor the integrity of the Hb structure by X-ray crystallography. I made sure to use crystals from the same (preparation) vial to minimize outside variables (i.e. differences in pH, buffer concentration, etc.). After chronologically screening crystals for several weeks (~3-4), the Hb[α-Fe^{II}(MeNO)][β-Fe^{III}(H_2O)] structure was solved. Comparing this structure to the Hb[α-Fe^{II}(MeNO)][β-Fe^{II}(MeNO)] derivative and the ferric Hb^{III}-H_2O model resulted in overall RMSD values of 0.270 and 0.250 Å (Figure 3.27). Analysis of the protein shows that the global structure of Hb and its R-state configuration remain intact even weeks after ligand binding (Figure 3.9, Table 3-3). Also, no significant differences were noted between structures in the α subunit. However, in the β subunit, MeNO was replaced by a water molecule, creating a ferric Fe^{III}-(H_2O) complex with an Fe-OH_2 bond of 2.4 Å. Superpositioning also showed that, after ligand dissociation, the distal His63 residue did not swing back into the position corresponding to the ferric Hb^{III}-H_2O model. This created a His63(N^{ε})-OH_2 distance of a 3.4 Å, which is too long to maintain H-bonding.

These "minor" differences are quite significant. Previous studies have determined that oxidation of Hb promotes tetramer dissociation and subsequent tertiary structural distortions [12, 16, 31]. Therefore, our Hb[α-Fe^{II}(MeNO)][β-Fe^{III}(H_2O)] model provides structural evidence supporting Fe oxidation as the next step in the overall mechanism leading to heme loss.

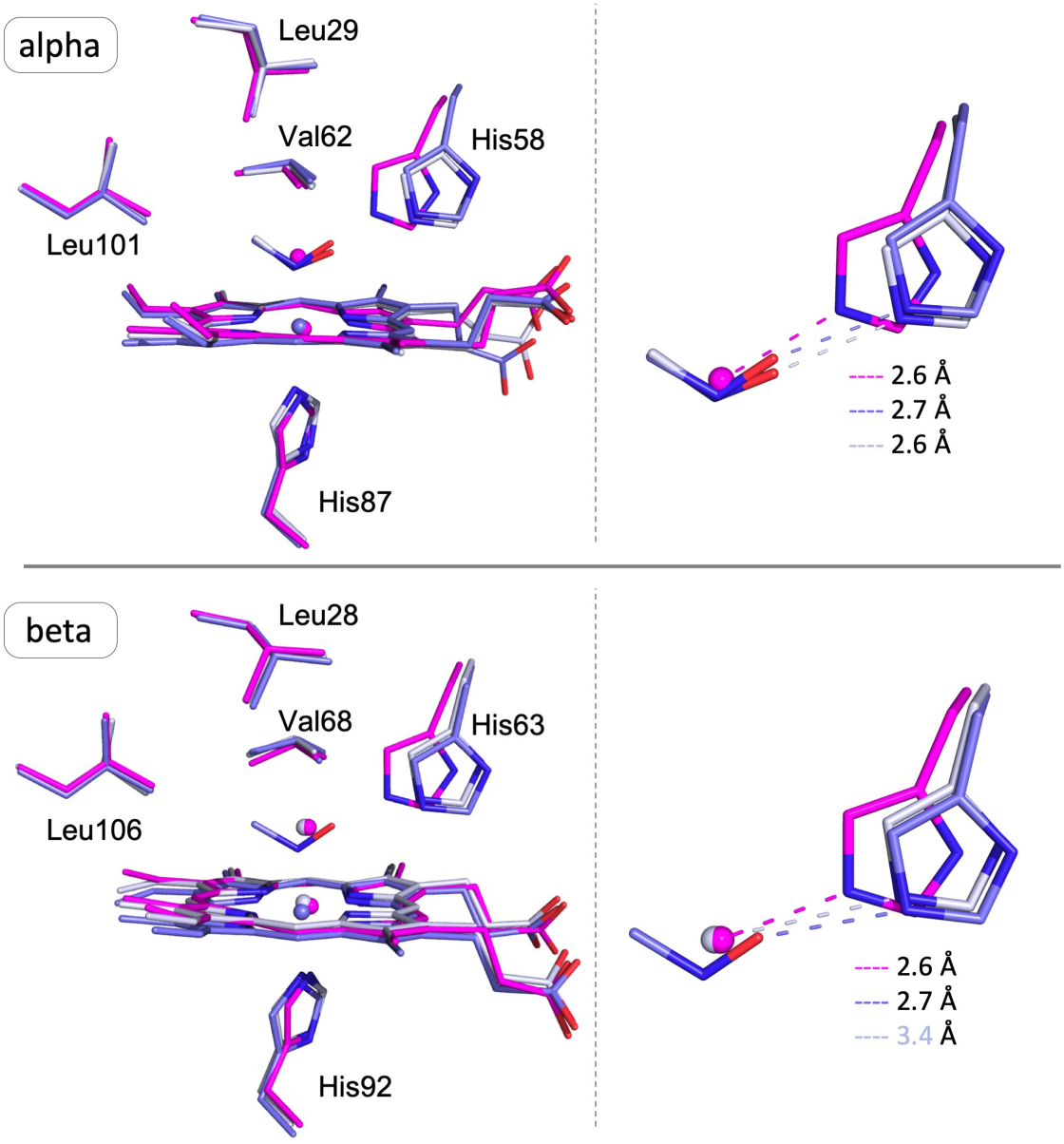

Figure 3.27 Superpositioning of the heme active sites of the α1 and β1 subunits of ferric Hb^{III}-H_2O (magenta; PDB ID 3P5Q), and the Hb[α-Fe^{II}(MeNO)][β-Fe^{III}(MeNO)] (slate) and Hb[α-Fe^{II}(MeNO)][β-Fe^{III}(H_2O)] (blue white) structures from this work.

3.4.3 Structural morphology resulting from Hb-EtNO binding

The Hb^{II}-EtNO crystals morphed at a different rate than the Hb^{II}-MeNO ones, which revealed additional steps in the structural mechanism of Hb degradation, hemichrome formation and heme slippage.

3.4.3.1 Step 1, EtNO binding: Hb[α-Fe^{II}(EtNO)][β-Fe^{II}(EtNO)]

The Hb[α-Fe^{II}(EtNO)][β-Fe^{II}(EtNO)] structure from this study is the first reported with both subunits in complex with EtNO. Global alignment of Hb[α-Fe^{II}(EtNO)][β-Fe^{II}(EtNO)] against ferric Hb^{III}-H_2O resulted in an RMSD value of 0.231 Å (Figures 3.25 and 3.26, cyan). Binding of EtNO did not affect the R-state conformation of the ferric Hb^{III}-H_2O protein used to prepare the crystals. Further analysis of the active sites disclosed slight differences in the position of the His58/63 residues. In both subunits, the distal His residue is shifted outwards by 1.1 (α) and 0.9 (β) Å (as calculated between His N^{ε} atoms), to accommodate EtNO binding. As with Hb[α-Fe^{II}(MeNO)][β-Fe^{II}(MeNO)], this structure confirmed that the first step in Hb degradation is ligand binding.

3.4.3.2 Step 2, heme oxidation: not observed

Despite continued monitoring of the Hb^{II}-EtNO crystals, a structure showing heme oxidation resulting in a ferric Fe^{III}-H_2O β subunit was not captured. However, this may be due to rapid transition from the ligand bound Hb[α-Fe^{II}(EtNO)][β-Fe^{II}(EtNO)] state to Hb[α-Fe^{II}(EtNO)][β-Fe(His)$_2$-SNO] hemichrome formation.

3.4.3.3 Step 3, hemichrome formation: Hb[α-Fe^{II}(EtNO)][β-Fe(His)$_2$-SNO]

Global alignment of Hb[α-Fe^{II}(EtNO)][β-Fe^{II}(EtNO)] against Hb[α-Fe^{II}(EtNO)][β-Fe(His)$_2$-SNO] and ferric Hb^{III}-H_2O yielded RMSD values of 0.265 and 0.200 Å (Figure 3.28 and Figure 3.29). These values indicate that the quaternary architectural integrity of the protein remains relatively intact. Comparison of the α subunits shows that the active site did not undergo spatial changes during the transition of the β subunit from the EtNO bound state to the hemichrome state (Figure 3.28, green).

However, significant changes were observed at the tertiary level for the β subunit as it evolved from one state to the next. In the Hb[α-Fe^{II}(EtNO)][β-Fe$(His)_2$-SNO] structure, the β F-helix (residues 82-100) unwinds and glides outwards (Figure 3.29D, green). This local unravelling propagates positional changes to the distal His92 residue, causing it to slide towards the exterior by 4.9 Å (measured from His92 N^{ε}-N^{ε} against Hb[α-Fe^{II}(EtNO)][β-Fe^{II}(EtNO)]) as shown in Figure 3.29B (green). In turn, this generates outward slippage of the heme to the solvent by 5.1 Å (measured from Fe-Fe against Hb[α-Fe^{II}(EtNO)][β-Fe^{II}(EtNO)]), which leads to bis heme coordination by distal amino acid residues His63 and proximal His92. Bis-His coordination of the heme is accompanied by a downward diagonal gliding of His63 by 1.0 Å (measured from His63 N^{ε}-N^{ε} against Hb[α-Fe^{II}(EtNO)][β-Fe^{II}(EtNO)]) to facilitate hemichrome formation (Figure 3.29B). Additionally, the lone Fe atom modeled behind the heme sits at position Fe^{1}, which corresponds to the location of the heme Fe atom in both Hb[α-Fe^{II}(EtNO)][β-Fe^{II}(EtNO)] and ferric Hb^{III}-H_2O structures. This provides evidence that the structure of Hb morphed from the heme-nitroso derivative into the hemichrome state, and that a minimal portion of the Hb population (within the crystal) remains in the ligand bound configuration.

These localized changes in the beta subunit have a significant impact on the function of the protein. The quaternary state of the protein adopts an altered R-state. Hb is reliant on fast and efficient allosteric transitions to achieve its role in oxygen storage and transport. Bis-coordination of the heme prevents Hb from functioning properly. For instance, hemichrome formation has been characterized as resulting in low-spin species that are followed by increased protein precipitation [14-16].

3.4.3.4 Step 4, Heme slippage: Hb[α-Fe^{II}(EtNO)][β-Fe(2 positions)]

After hemichrome formation, the structure of Hb continued to transform. Structural alignment of Hb[α-Fe^{II}(EtNO)][β-Fe(2 positions)] against ferric Hb^{III}-H_2O and Hb[α-Fe^{II}(EtNO)][β-Fe$(His)_2$-SNO] resulted in RMSD values of 0.209 and 0.190 Å respectively. The α subunit structure remained "static" through the transitions of the β subunit (Figure 3.28, green and yellow traces). After hemichrome formation, the F-helix of the β subunit recoiled back into the position observed at the initial ligand binding stage. This shifted the proximal His92 residue back towards the inside of the protein by 4.5 Å (measured from His92 N^{ε}-N^{ε} against Hb[α-Fe^{II}(EtNO)][β-Fe$(His)_2$-SNO]). This backwards movement of the His92 residue "dragged" 56% of the heme back to position Fe^1, leaving the rest behind at position Fe^2. Simultaneously, the distal His63 residue drifted back into the active site by 1.8 Å (measured from His63 N^{ε}-N^{ε} against Hb[α-Fe^{II}(EtNO)][β-Fe$(His)_2$-SNO]), distancing itself from Fe^2. As a result, the heme at position Fe^2 is no longer directly coordinated to the protein. Finally, the quaternary state of this derivative returns to the R-state configuration as observed at the EtNO binding stage. This heme-slippage phase represents a new step in the overall mechanism leading to Hb degradation. Moreover, due to the crystal packing environment, it is likely that a structure showing complete heme-loss will be very difficult to obtained (see 3.4.4.2 for further discussion).

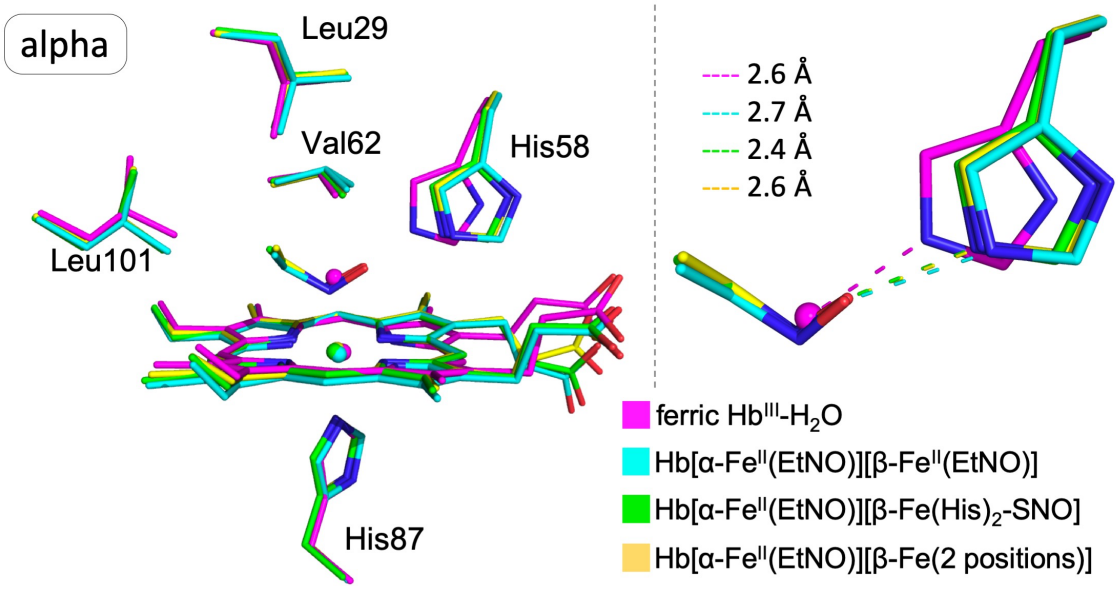

Figure 3.28 Heme active site models of the α1 subunits of ferric Hb^{III}-H_2O (magenta; PDB ID 3P5Q), and the Hb[α-Fe^{II}(EtNO)][β-Fe^{II}(EtNO)] (cyan), Hb[α-Fe^{II}(EtNO)][β-Fe(His)$_2$-SNO] (green) and Hb[α-Fe^{II}(EtNO)][β-Fe(2 positions)] (yellow) structures from this work, superimposed along Cα backbone.

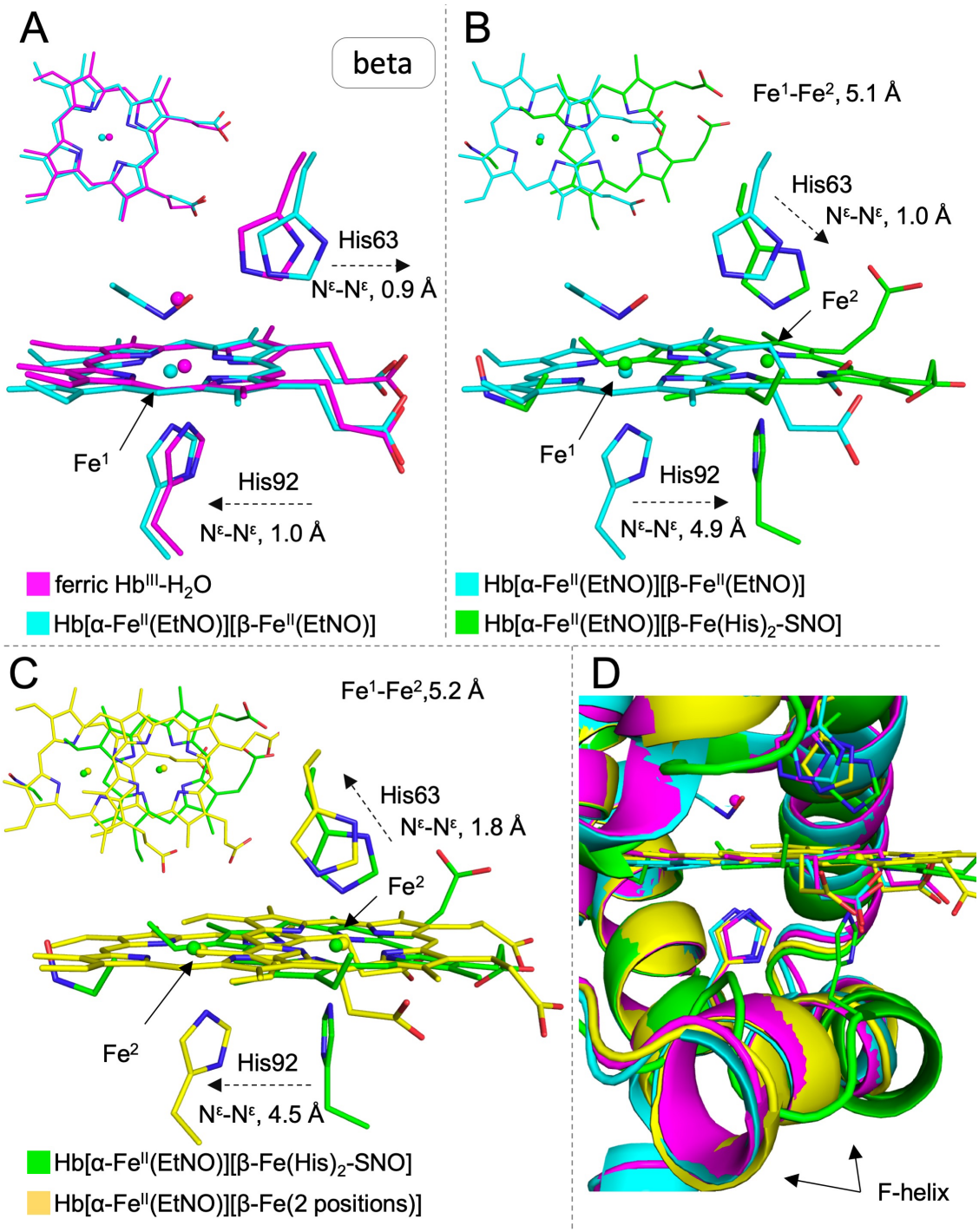

Figure 3.29 Superimposed structures of the heme sites of the β1 subunits of ferric Hb^{III}-H_2O (magenta; PDB ID 3P5Q), and the Hb[α-Fe^{II}(EtNO)][β-Fe^{II}(EtNO)] (cyan), Hb[α-Fe^{II}(EtNO)][β-Fe$(His)_2$-SNO (green) and Hb[α-Fe^{II}(EtNO)][β-Fe(2 positions)] (yellow) structures from this work, superimposed along the Cα backbones. Dashed arrows represent movements as the structure undergo A) ligand binding, B) hemichrome formation, and C) heme slippage. D) Accompanying changes to the F-Helix of the structures.

3.4.4 Structural morphology resulting from Hb-PrNO binding

The Hb^{II}-PrNO crystals morphed more rapidly than the Hb^{II}-MeNO and -EtNO counterparts. Monitoring of the crystals allowed me to obtain two distinct X-ray crystal structures at different stages of Hb degradation.

3.4.4.1 Step 1, PrNO binding: Hb[α-Fe^{II}(PrNO)][β-Fe^{II}(PrNO)]

As with my previously discussed ligand bound structures, the global structure of the Hb[α-Fe^{II}(PrNO)][β-Fe^{II}(PrNO)] is highly similar to the ferric Hb^{III}-H_2O model. Comparison of both structures resulted in an RMSD values of 0.268 Å (Figure 3.30, purple). The only difference detected between the active sites of α subunits of the ferric Hb^{III}-H_2O and the Hb[α-Fe^{II}(PrNO)][β-Fe^{II}(PrNO)] structures is the spatial arrangement of His58. In the nitroso ligand bound protein, His58 swings outwards by 1.4 Å (measured between His58 N^{ε} atoms) to accommodate RNO binding (Figure 3.30, purple). Similar fluctuations were observed in the distal His63 residue in the active site of the β subunit to facilitate PrNO binding (Figure 3.31, purple). However, nitroso binding did not change the quaternary state of the protein, which remains in the R-state.

3.4.4.2 Step 2, heme oxidation: not observed

Although several X-ray diffraction data was collected on Hb^{II}-PrNO crystals that had aged over several time periods, I was unable to capture a structure showing heme oxidation and β-Fe^{III}-H_2O formation. This could be due to the high instability of the heme-nitroso bound Hb^{II}-PrNO complex, which transformed quickly to the next stage. This argument is based on our UV-vis spectroscopy studies, which showed that the Hb^{II}-PrNO complex is shorter lived in solution (Figure 3.5), and yields larger amounts of aggregation (Figure 3.25) as compared to the other the Hb^{II}-RNO derivatives investigated.

3.4.4.3 Steps 3 and 4, simultaneous hemichrome formation and heme slippage: Hb[α-Fe^{II}(PrNO)][β-Fe(2 positions)]

After PrNO binding, the Hb structure continued to transform. Superpositioning of the Hb[α-Fe^{II}(PrNO)][β-Fe(2 positions)] structure over ferric Hb^{III}-H_2O and Hb[α-Fe^{II}(PrNO)][β-Fe^{II}(PrNO)] resulted in RMSD values of 0.268 and 0.248 respectively. This structure was solved in the hemichrome state and also in the heme-slippage state. Thus, the quaternary state of the protein was partly solved as an R-state and partly as an altered R-state configuration. Despite these changes to the structure, the active site of the α subunit had only minimal distortions. Specifically, His58 migrated towards the inside of the heme-pocket by 0.8 Å (as measured between His58 N^{ε} atoms) as compared to the nitroso ligand bound structure.

Not surprisingly, the major structural transitions were observed in the β subunit of Hb[α-Fe^{II}(PrNO)][β-Fe(2 positions)]. In the distal pocket, the His63 residue slides down and outwards by 1.3 Å (as measured between His58 N^{ε} atoms) to promote hemichrome formation (Figure 3.31B). However, the His63(N^{ε})-Fe distance was calculated as 2.9 Å, as compared to the much closer interaction (2.0 Å) observed in the Hb[α-Fe^{II}(EtNO)][β-Fe$(His)_2$-SNO] hemichrome derivative. Additionally, the F-helix of the β subunit was modeled in two distinct conformations. This created two positions for the proximal His92 residue, which are located 4.6 Å apart (as measured between His58 N^{ε} atoms). This movement propagated to the heme, causing part of the heme to slip towards the solvent exterior of the protein by 5.1 Å. Not only does the Hb[α-Fe^{II}(PrNO)][β-Fe(2 positions)] structure confirm two distinct steps in the overall mechanism leading to heme-loss, it also provides clear evidence that the Hb[α-Fe(ligand)][β-Fe(ligand)] structures obtained morphed from one stage to the next, instead of appearing randomly.

Finally, we expect heme-loss to be the final step in Hb degradation. However, capturing a Hb X-ray crystal structure in which the β subunit has undergone complete heme-loss is highly unlikely. As can be seen in Figure 3.32, the heme cannot move out of the active site any further, as it is blocked by residues in neighboring α subunits corresponding to symmetry related mates in the crystal packing.

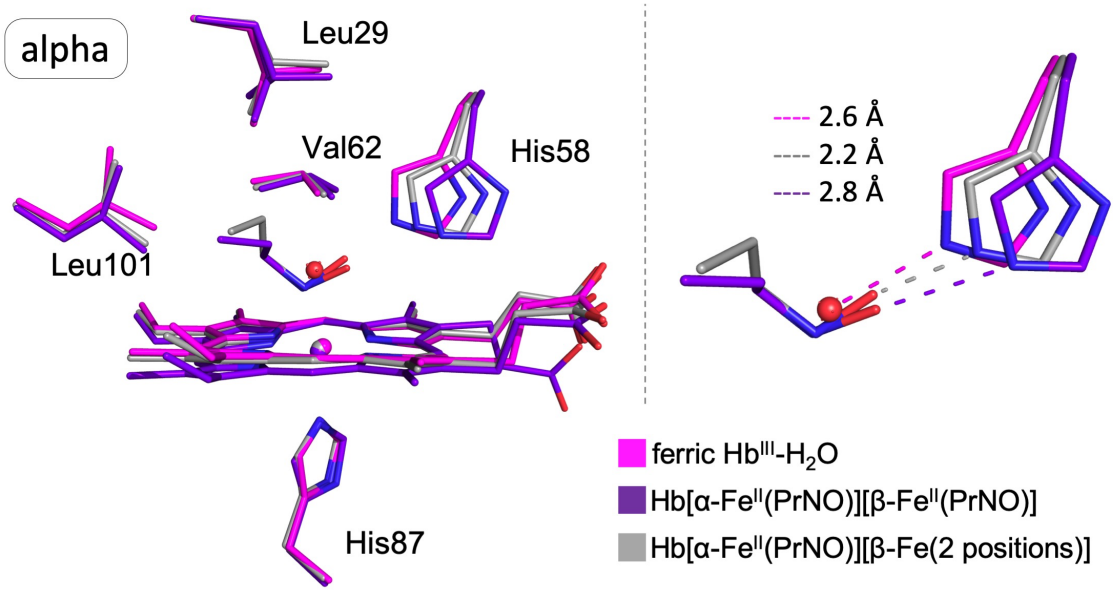

Figure 3.30 Heme active site models of the α1 subunits of ferric Hb^{III}-H$_2$O (magenta; PDB ID 3P5Q), and the Hb[α-Fe^{II}(PrNO)][β-Fe^{II}(PrNO)] (purple) and Hb[α-Fe^{II}(PrNO)][β-Fe(2 positions)] (gray) structures from this work, superimposed along Cα backbone.

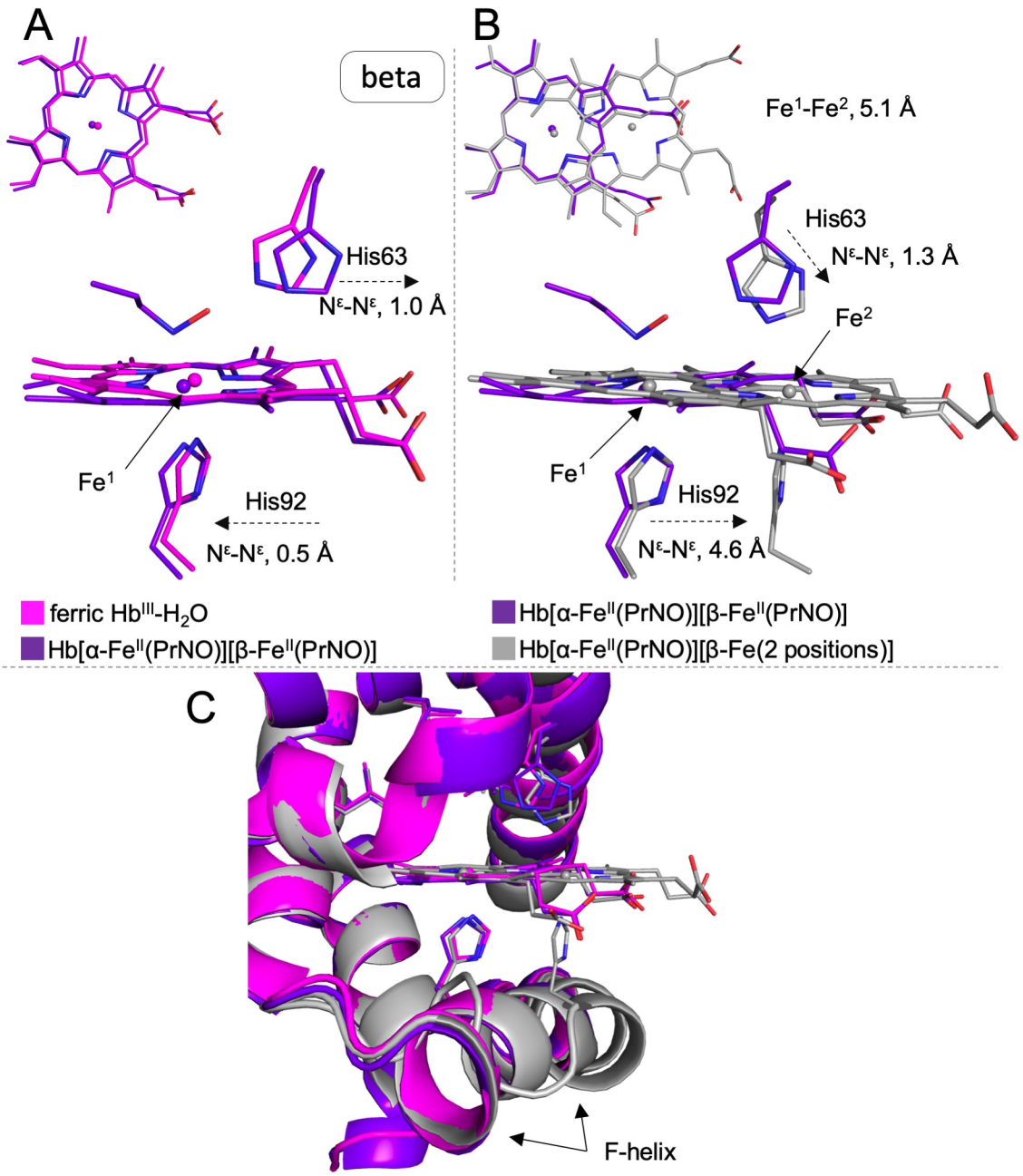

Figure 3.31 Superimposed structures of the heme sites of the β1 subunits of ferric Hb^{III}-H_2O (magenta; PDB ID 3P5Q), and the Hb[α-Fe^{II}(PrNO)][β-Fe^{II}(PrNO)] (purple) and Hb[α-Fe^{II}(PrNO)][β-Fe(2 positions)] (gray) structures from this work, superimposed along the Cα backbones. Dashed arrows represent morphological movements as the structures undergo A) ligand binding, B) hemichrome formation and heme slippage. The bottom panel shows the accompanying changes to the F-Helix of the structures.

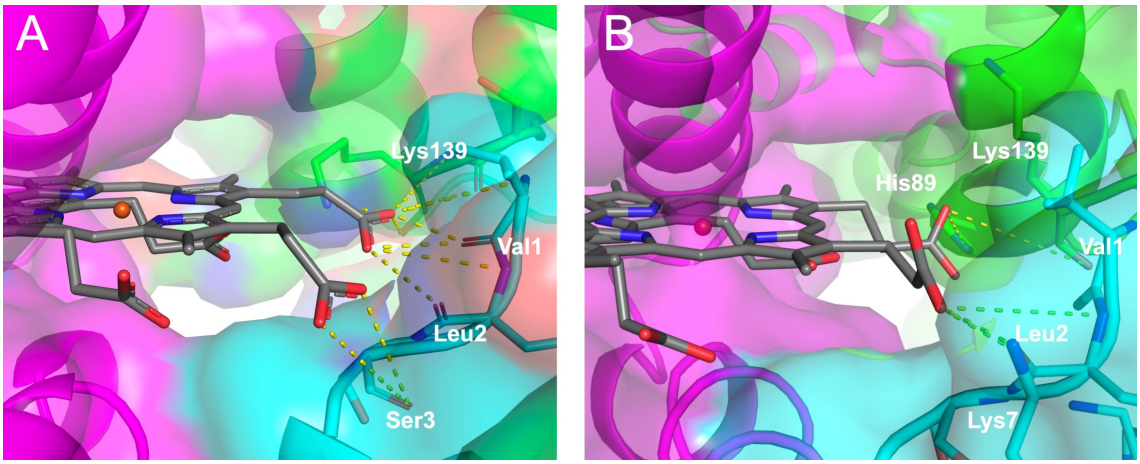

Figure 3.32 Environment surrounding the slipped hemes in the β subunits of A) Hb[α-Fe^{II}(EtNO)][β-Fe(2 positions)] and B) Hb[α-Fe^{II}(PrNO)][β-Fe(2 positions)]. Magenta: surface of the β subunit, cyan and green: surface of symmetry related α subunits. Distances shown are 2.5-5.0 Å.

3.4.5 Step-wise structural mechanism leading to heme-loss as a result of RNO binding to Hb

Binding of *C*-nitroso compounds to hemeproteins has been documented to lead to protein inhibition [32-34] and structural degradation [16, 18, 35]. Moreover, high levels of certain nitroso compounds in the blood have been linked to methemoglobinemia and hemolytic anemia. However, prior to this work, the step-by-step structural mechanism resulting in Hb degradation remained relatively unknown.

In separate works, designed to explain Heinz body formation associated with unstable Hb disease, and drug-induced hemolytic anemia, McDonald [12] and Sugawara [36], proposed similar pathways for Hb degradation. Generally speaking, they reported that Hb^{II}-O_2 undergoes oxidation into ferric Hb^{III}-H_2O, followed by hemichrome formation and ultimately protein precipitation, as shown in the scheme below. However, no structural evidence was available to support their proposal.

Hb^{II}-O_2 ⟶ ferric Hb^{III}-H_2O ⟶ hemichrome ⟶ precipitation

These new Hb structures (my work) provided distinct pieces of information that allowed me to propose a step-by-step structural mechanism leading to Hb degradation. In *C*-nitroso induced degradation, the initial stages are marked by substrate binding to ferrous Hb^{II} (Figure 3.33, steps s and i). These steps were confirmed both using UV-vis spectroscopy and X-ray crystallography.

Based on information gleaned from my X-ray crystal structures, after nitroso binding, the beta subunit of Hb undergoes oxidation, resulting in the formation of ferric Hb^{III}-H_2O. Autoxidation of Hb^{II}-O_2 has been studied in detail and is suggested to occur by nucleophilic displacement of O_2^- by either a water molecule, or a OH^- ion, that migrated from the solvent exterior into the heme-pocket. The Fe is converted to the ferric form with the water molecule bound at the sixth coordinate position.

Then, as proposed by McDonald [12] and Sugawara [36], the next step in my proposed mechanism is also hemichrome formation (Figure 3.33, step iii). Hemichromes are reported to give rise to "sticking points" in erythrocytes where Heinz body cells can become trapped and undergo cell lysis, which ultimately may lead to hemolytic anemia [14, 37, 38]. Two of the structures in this work provided a detailed structural understanding of the fluctuations that Hb undergoes in the very important process of hemichrome formation.

The fifth step proposed in the mechanism of Hb degradation is heme-slippage towards the exterior of the active site (Figure 3.33 iv). Similar structures have been reported by Dr. Yi (Richter-Addo lab). In both cases, there is a significant movement of the heme towards the solvent ~5 Å, and weak coordination to the active site. Finally, we propose that the last step in Hb degradation is complete heme loss (Figure 3.33 step v), something that I was unable to observe through X-ray

crystallography due to the packing of the crystals. However, I did confirm protein aggregation in solution.

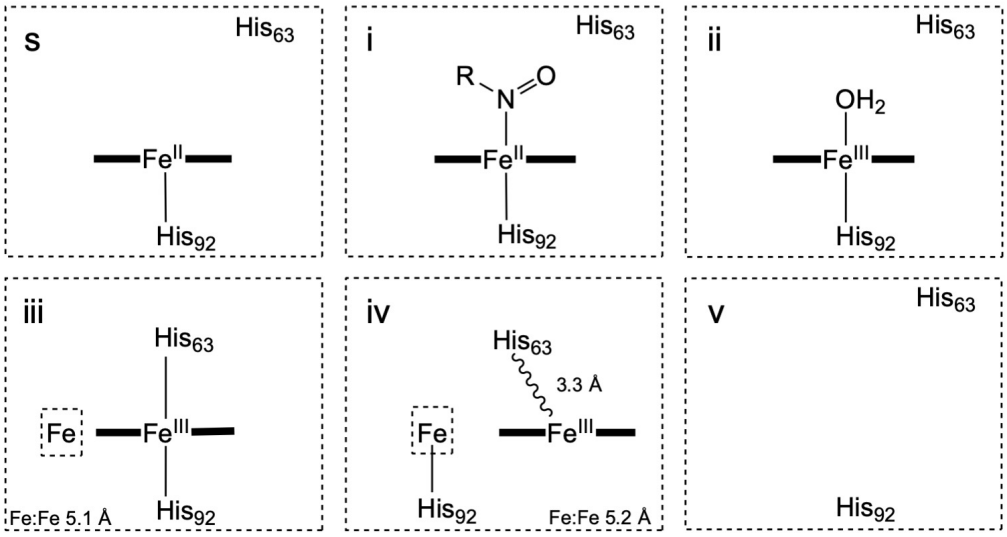

Figure 3.33 A. Steps of the mechanism of RNO-induced heme loss, followed by source of evidence. **s) Ferrous Hb^{II}**, UV-vis reactions in solution. **i) Nitroso binding**, Hb[α-Fe^{II}(RNO)][β-Fe^{II}(RNO)] R = Me, Et, Pr. **ii) Heme oxidation**, Hb[α-Fe^{II}(MeNO)][β-Fe^{III}(H_2O)]. **iii) Hemichrome formation**, Hb[α-Fe^{II}(EtNO)][β-Fe(His)2-SNO]. i**v) Heme slippage**, Hb[α-Fe^{II}(EtNO)][β-Fe(2 positions)], Hb[α-Fe^{II}(PrNO)][β-Fe(2 positions)] **v) Heme-loss and protein degradation**, aggregation studies in solution.

3.5 Conclusion

In this project, I set out to investigate the step-by-step structural mechanism leading to *C*-nitroso induced Hb degradation. Protein degradation can be drug-induced, occur naturally, or as a result of unstable Hb disease. Although the overall mechanisms of Hb degradation are considered to be similar (despite the cause), prior to this work, only a simplistic mechanistic proposal was available. In this work, I was able to propose a six-step process leading to nitroso-induced Hb degradation, based in large part on structural biology.

3.6 References

1. O'Brien, P.J., et al., *Toxicity of nitrobenzene compounds towards isolated hepatocytes: dependence on reduction potential.* Xenobiotica, 1990. **20**(9): pp 945-55.
2. Mahy, J.P. and D. Mansuy, *Formation of prostaglandin synthase-iron-nitrosoalkane inhibitory complexes upon in situ oxidation of N-substituted hydroxylamines.* Biochemistry, 1991. **30**(17): pp 4165-72.
3. Jonsson, K.H. and B. Lindeke, *Cytochrome P-455 nm complex formation in the metabolism of phenylalkylamines. XII. Enantioselectivity and temperature dependence in microsomes and reconstituted cytochrome P-450 systems from rat liver.* Chirality, 1992. **4**(8): pp 469-77.
4. Belisario, M.A., et al., *Erythrocyte enzymes catalyze 1-nitropyrene and 3-nitrofluoranthene nitroreduction.* Toxicology, 1996. **108**(1-2): pp 101-8.
5. Yi, J., et al., *Crystallographic trapping of heme loss intermediates during the nitrite-induced degradation of human hemoglobin.* Biochemistry, 2011. **50**(39): pp 8323-32.
6. Shetlar, M.D. and H.A. Hill, *Reactions of hemoglobin with phenylhydrazine: a review of selected aspects.* Environ Health Perspect, 1985. **64**: pp 265-81.
7. Schimelman, M.A., J.M. Soler, and H.A. Muller, *Methemoglobinemia: nitrobenzene ingestion.* JACEP, 1978. **7**(11): pp 406-8.
8. Lee, C.H., et al., *Two cases of methemoglobinemia induced by the exposure to nitrobenzene and aniline.* Ann Occup Environ Med, 2013. **25**(1): pp 31.
9. Martinez, M.A., et al., *Acute nitrobenzene poisoning with severe associated methemoglobinemia: identification in whole blood by GC-FID and GC-MS.* J Anal Toxicol, 2003. **27**(4): pp 221-5.
10. Khan, M.F., et al., *Phenylhydroxylamine: role in aniline-associated splenic oxidative stress and induction of subendocardial necrosis.* Toxicol Sci, 1998. **42**(1): pp 64-71.
11. Sugawara, Y., *New Mode (Molecular-Sensing) of Heinz Body Formation Mechanisms Inherent in Human Erythrocytes: Basis for Understanding of Clinical Aspects of Drug-Induced Hemolytic Anemia and the Like.* Journal of Bioanalysis & Biomedicine, 2013. **05**(02).
12. Macdonald, V.W., *Measuring relative rates of hemoglobin oxidation and denaturation.* Methods Enzymol, 1994. **231**: pp 480-90.
13. Peisach, J., et al., *The effects of protein conformation on the heme symmetry in high spin ferric heme proteins as studied by electron paramagnetic resonance.* J Biol Chem, 1971. **246**(10): pp 3342-55.
14. Winterbourn, C.C. and R.W. Carrell, *Studies of hemoglobin denaturation and Heinz body formation in the unstable hemoglobins.* J Clin Invest, 1974. **54**(3): pp 678-89.
15. Jacob, H.S., *Mechanisms of Heinz body formation and attachment to red cell membrane.* Semin Hematol, 1970. **7**(3): pp 341-54.
16. Ohno, H., M. Nomura, and K. Watanabe, *A possible mechanism of heinz body hemolytic anemia induced by DQ-2511, a new gastroprokinetic drug, in dogs.* Fundam Appl Toxicol, 1996. **32**(2): pp 269-77.
17. Beutler, E., et al., *Drug-induced haemolytic anaemias and the mechanism and significance of Heinz body formation in red blood cells.* Nature, 1962. **196**: pp 1095-7.
18. Yi, J., et al., *Degradation of human hemoglobin by organic C-nitroso compounds.* Chem Commun (Camb), 2013. **49**(95): pp 11179-81.

19. Antonini, E. and M. Brunori, *Hemoglobin and myoglobin in their reactions with ligands*. Frontiers of Biology (Amsterdam). 1971, Amsterdam,: North-Holland Pub.
20. Safo, M.K. and D.J. Abraham, *X-ray crystallography of hemoglobins.* Methods Mol Med, 2003. **82**: pp 1-19.
21. Meng, F. and A.I. Alayash, *Determination of extinction coefficients of human hemoglobin in various redox states.* Anal Biochem, 2017. **521**: pp 11-19.
22. Mansuy, D., J.C. Chottard, and G. Chottard, *Nitrosoalkanes as Fe(II) Ligands in Hemoglobin and Myoglobin Complexes Formed from Nitroalkanes in Reducing Conditions.* European Journal of Biochemistry, 1977. **76**(2): pp 617-623.
23. Otwinowski, Z. and W. Minor, *Processing of X-ray diffraction data collected in oscillation mode.* Methods Enzymol, 1997. **276**: pp 307-26.
24. Winn, M.D., et al., *Overview of the CCP4 suite and current developments.* Acta Crystallographica Section D-Biological Crystallography, 2011. **67**: pp 235-242.
25. Murshudov, G.N., A.A. Vagin, and E.J. Dodson, *Refinement of macromolecular structures by the maximum-likelihood method.* Acta Crystallographica Section D-Structural Biology, 1997. **53**: pp 240-255.
26. Emsley, P. and K. Cowtan, *Coot: model-building tools for molecular graphics.* Acta Crystallographica Section D-Biological Crystallography, 2004. **60**: pp 2126-2132.
27. Chen, V.B., et al., *MolProbity: all-atom structure validation for macromolecular crystallography.* Acta Crystallographica Section D-Structural Biology, 2010. **66**: pp 12-21.
28. Long, J.A., N.J. Harris, and K. Lammertsma, *Formaldehyde oxime <--> nitrosomethane tautomerism.* J Org Chem, 2001. **66**(20): pp 6762-7.
29. Beaudoin, D. and J.D. Wuest, *Dimerization of Aromatic C-Nitroso Compounds.* Chem Rev, 2016. **116**(1): pp 258-86.
30. Raczyńska, E.D., et al., *Tautomeric equilibria, H-bonding and π-electron delocalization ino-nitrosophenol. A B3LYP/6-311 + G(2df,2p) study.* Journal of Physical Organic Chemistry, 2005. **18**(8): pp 892-897.
31. Rifkind, J.M., et al., *Detection, formation, and relevance of hemichromes and hemochromes.* Methods Enzymol, 1994. **231**: pp 449-80.
32. Alston T.A, P.J.T.D., Bright H.J., *Enzyme Inhibition by Nitro and Nitroso Compounds* Acc. Chem. Res., 1983. **16**: pp 418-424.
33. Gill, H.J., M.D. Tingle, and B.K. Park, *N-Hydroxylation of dapsone by multiple enzymes of cytochrome P450: implications for inhibition of haemotoxicity.* Br J Clin Pharmacol, 1995. **40**(6): pp 531-8.
34. Mitra, A.K., et al., *Metabolism of dapsone to its hydroxylamine by CYP2E1 in vitro and in vivo.* Clin Pharmacol Ther, 1995. **58**(5): pp 556-66.
35. Murray, T. and A.A. Yunis, *The cellular uptake and covalent binding of nitroso-chloramphenicol.* J Lab Clin Med, 1981. **98**(3): pp 396-401.
36. Nakamura, N., et al., *Paroxysmal nocturnal hemoglobinuria in systemic lupus erythematosus: a case report.* J Med Case Rep, 2011. **5**: pp 550.
37. Rachmilewitz, E.A., et al., *Role of haemichromes in the formation of inclusion bodies in haemoglobin H disease.* Nature, 1969. **222**(5190): pp 248-50.
38. Rachmilewitz, E.A., *Denaturation of the normal and abnormal hemoglobin molecule.* Semin Hematol, 1974. **11**(4): pp 441-62.

Chapter 4. Interactions of nitrogenous compounds with Mb, in its natural ferric form, and cobalt- and chlorin-substituted species, and reactions of arylhydrazines with Hb

4.1 Introduction

Metalloproteins depend on several intrinsic factors to catalyze specific chemical reactions, some of which are i) the active site amino acid composition, ii) metal identity, and iii) type of macrocycle coordinating the metal (Figure 4.1). The functional activity of heme-proteins is also dependent on the size and type of substrate. In this chapter I probed the influence of each of these factors on metalloprotein heme-nitroso chemistry.

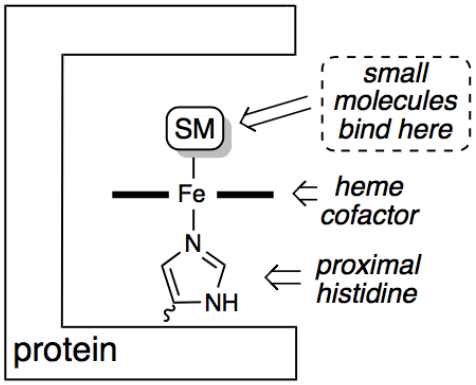

Figure 4.1 Prototypical heme-protein active site (histidine ligated) highlighting factors influencing the protein's chemical activity.

The active site composition of the protein can help guide reactions through specialized pathways. Amino acids in the active site can participate in redox chemistry by donating or accepting electrons, or they could simply be there to determine the spatial arrangement of a substrate [1]. Small changes in the composition of the active site can change the innate chemistry of the protein or disrupt its function altogether [1-3]. Other amino acids can dictate whether a substrate reaches the active site or not by acting as heme-pocket gatekeepers [4-6]. Furthermore,

the overall volume of the active site plays a crucial role in its chemistry. For example, larger active sites such as those of cytochrome P450 can accommodate larger ligands for binding than the active sites of the smaller heme proteins myoglobin (Mb) and hemoglobin (Hb).

As described in Chapter 2, Mb can react with small nitroalkanes (RNO_2) to form ferrous Mb^{II}-RNO complexes in presence of the reducing agent dithionite, creating an Fe-N bond between the heme cofactor and the nitroso product. However, due to Mb's restricted active site volume, it had been expected that larger RNOs would be unable to bind. In 2017, Bing and Powell provided crystallographic evidence to the contrary when they solved the structure of a distal pocket mutant of Mb bound to nitrosoamphetamine (AmphNO) [7]. Based on this knowledge, I decided to test the reactions of Mb with a series of nitrotoluenes with distinct steric hindrance (NTs). The NTs used in this study served as models for other nitrotoluenes (e.g., TNT) that are known to interact with and degrade Hb [8]. Furthermore, these ligands (Figure 4.2) are relatively larger in size than those studied in Chapter 2. Therefore, this set of nitrotoluenes helps probe further the influence of ligand sterics on RNO binding to Mb and the lifetime of the resulting complexes.

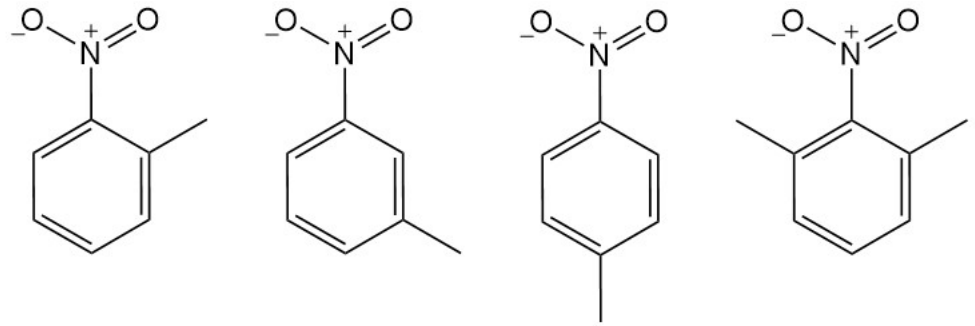

Figure 4.2 Series of nitrotoluenes used as precursors for RNOs in this study.

Mutation of the distal pocket residue His64 into Ala64 opens the active site entrance of Mb and slightly increases the volume of the heme-pocket. The H64A mutation also removes any fixed

H-bond donor capability of the active site residues to the ligand. In Chapter 2, I showed that this "small" active site change has a significant impact on the time it takes for each Mb^{II}-RNO complex to form and the extent to which they form. Furthermore, the Mb-AmphNO structure was obtained using the H64A Mb mutant, which suggests the slightly increased active site volume is necessary to accommodate larger ligands. Therefore, I probed the reactions of the H64A Mb mutant with the selected series of nitrotoluenes to determine the influence of distal pocket composition on Mb^{II}-RNO complex formation.

The second factor studied in this chapter, which impacts heme-protein chemistry, is metal identity [9]. Nature employs distinct metals to carry out the diverse functions of life, because different metals have different redox potentials and electrochemical behaviors. For instance the native ferrous Mb^{II} changes from high spin to low spin upon oxygen binding [10]. On the other hand, in CoMb (in which Mb's naturally occurring heme cofactor has been replaced with cobalt protoporphyrin IX) the cobalt atom is low spin in both oxy and deoxy forms [11]. Differences in electrochemical characteristics have been shown to influence substrate binding and reactivity trends [9, 11, 12]. To determine the influence of metal identity on heme-nitroso binding, the reactions of CoMb with alkyl nitroalkanes (R = Me, Et and Pr) were monitored via UV-vis spectroscopy. Then, the products of those reactions were compared against the analogous reactions performed with native Mb (see Chapter 2), to elucidate the differences in nitroso binding between Co and Fe-containing species.

The third factor studied in this chapter, which influences metalloprotein-substrate interactions, is the macrocycle. Previous research from our group has shown that the electrochemical characteristics of the macrocycle have a significance influence in dictating NO_x substrate binding modes (e.g., O- vs N-bound). For instance, cobalt (Co-PPIX) and manganese

(Mn-PPIX) substituted Mb, as well as native Fe containing Mb, were crystallized bound to nitrite (NO_2^-). In each case, the substrate was O-bound, regardless of the identity of the metal. However, for Mb reconstituted with chlorin (ChlMb), an Fe containing reduced macrocycle (Figure 4.4), the results were different. Independent X-ray crystal structures of ChlMb with nitrite revealed the ligand in both the N- and O-bound modes (Figure 4.3). To determine the influence of macrocycle on Mb^{II}-RNO binding, I probed the reactions of chlorin substituted Mb with alkyl nitroalkanes (R = Me, Et, Pr and *i*Pr). Then the results of those reactions were compared with the analogous reactions of native Mb.

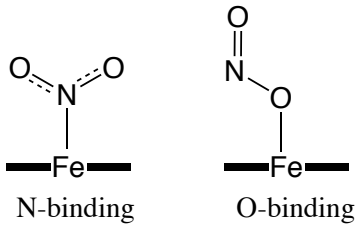

Figure 4.3 Nitrite binding modes in ChlMb.

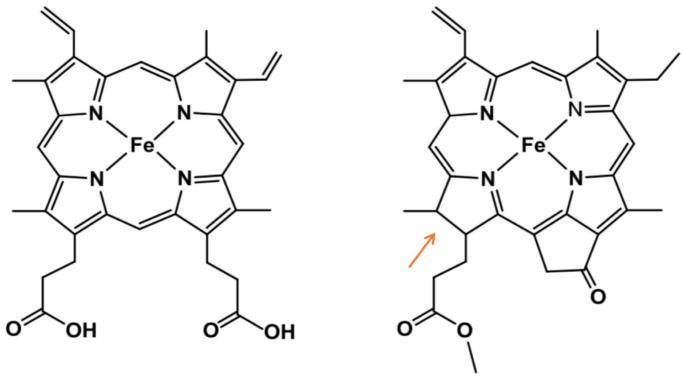

Figure 4.4 Structures of heme and chlorin. Arrow indicates reduced portion of macrocycle.

Finally, in the last portion of this chapter I discuss my work with Hb and a different class of ligands. As discussed in Chapter 3, Hb undergoes degradation upon binding to small RNOs (R

= Me, Et, Pr), in this chapter I probed the reactions of Hb with arylhydrazines, which are also known to cause Hb degradation [13, 14]. Unlike RNOs which bind hemoglobin through an Fe-N bond, arylhydrazines are known to form C-Fe bonds as illustrated in Figure 4.5 [13, 15, 16]. Dr. Bing Wang of our laboratory reported a related study with Mb [15]. In some cases, the phenyl group can shift from the Fe atom to the porphyrin N-atoms. My initial goal for this work was to solve the X-ray crystal structures of the products resulting from the reactions of ferric Hb^{III}-H_2O with a series of arylhydrazines. Three distinct arylhydrazines were chosen to determine which carbon atom of the aryl group is involved in the Fe-C bond (Figure 4.6).

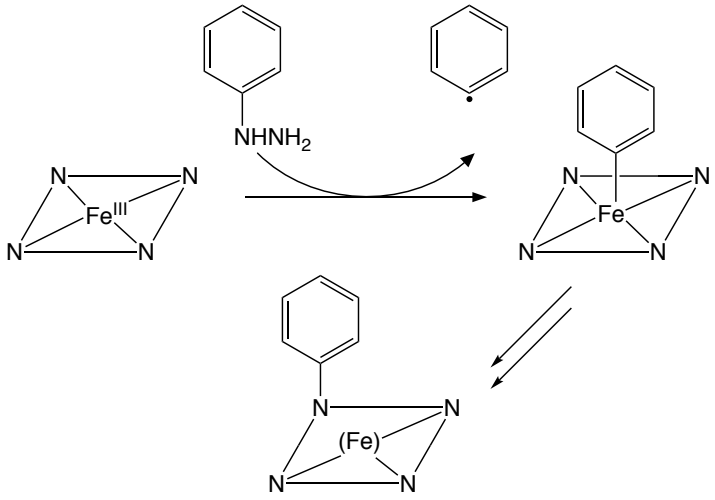

Figure 4.5 Reactivity of arylhydrazines with the heme of cytochrome P540.

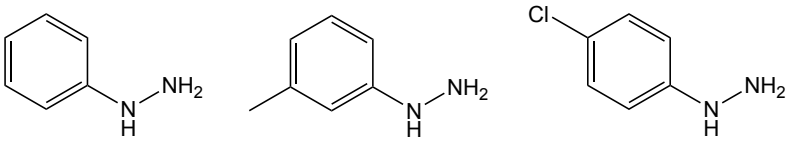

Figure 4.6 Arylhydrazines selected in this work.

4.2 Materials and Methods

4.2.4 Interactions of myoglobins with nitrotoluenes

4.2.4.1 Preparation of swMb proteins

For details regarding cloning of swMb H64A mutant, see reference section *2.2.1*. Details of expression and purification of swMb proteins can be found in section *2.2.2*.

4.2.4.2 UV-vis spectroscopy studies of the reactions of ferrous wt and H64A swMb^{II} with nitrotoluenes (2NT, 3NT, 4NT and 2,6DNT)

The reactions between ferrous swMb^{II} and the nitrotoluenes were monitored by UV-vis spectroscopy to determine Mb's ability to interact with larger RNOs as compared to those studied in Chapter 2. Ferric swMb^{III}-H_2O (wt or H64A mutant; 30 mg/mL) was added into a 3.5 mL quartz cuvette (Starna Cells) containing 3.0 mL of 0.1 M phosphate buffer (pH 7.4) to a final concentration of ~5-6 μM. The spectrum corresponding to ferric swMb^{III}-H_2O (wt or H64A mutant) was obtained, and then 2 M sodium dithionite was added as the reducing agent (to a final concentration of 20 mM). Once the spectrum of the resulting ferrous swMb^{II} (wt or H64A mutant) was recorded, 0.5 M nitrotoluene (2NT, 3NT, 4NT, 2,6DNT; dissolved in MeOH) was added to a final concentration of 3.0 mM. At this point, the reactions were monitored at regular time intervals aerobically using a Hewlett Packard 8453 diode array spectrophotometer.

4.2.2 Studies of chlorin substituted hhMb with nitrosoalkanes

4.2.2.1 Preparation of apoMb

Apo horse heart myoglobin (apoMb) was prepared using similar protocols as described by Yonetani [17] and Teale [18]. All steps were carried out at 4 °C, unless otherwise noted. In brief,

65 mg of hhMb (Sigma) were transferred into a small beaker and dissolved in 10 mL of distilled water. The protein was stirred for 30 min on ice. Then the pH was adjusted to ~2.0 by slowly adding ice-cold 1 M HCl to the protein mixture. Afterwards, the solution was transferred into a 125 mL separatory funnel. Two volumes of glass-distilled, ice-cold 2-butanone (20 mL) were added to the funnel and mixed by gentle inversion. The organic and aqueous layers were given enough time (~5 min) to separate and the top organic layer containing released heme was discarded. Two additional extractions with 2-butanone (10 mL each) were performed to remove any remaining heme from the aqueous layer containing the protein. After removing as much heme as possible, the apoprotein was dialyzed twice against 2 L of 10 mM $NaHCO_3$ solution and 1 mM EDTA for ~5 h each time. Then, a third dialysis in 2 L of 10 mM sodium phosphate pH 6.8 and 1 mM EDTA was performed (~5 h). The sample was centrifuged twice to remove any aggregated protein (5 krcf, 10 min). Then, the concentration of apoMb was calculated using the molar absorptivity coefficient of $\varepsilon = 15.2\ mM^{-1}\ cm^{-1}$ at λ 280 nm. For quality control, the concentration of heme-bound Mb remaining in solution was also calculated by using the molar absorptivity coefficient of $\varepsilon = 188\ mM^{-1}\ cm^{-1}$ at λ 409 nm. Samples were deemed desirable for reconstitution when less than 2% heme-bound Mb remained in the apoMb prep.

4.2.2.2 Reconstitution of apoMb with chlorin to form ferric ChlMb^{III}

ApoMb was reconstituted with chlorin (Fe(III) pyropheophorbide *a* methyl ester) to form ferric ChlMb^{III}. Reconstitution was performed by adding 1.2 molar excess chlorin (dissolved in a pyridine water mixture; 1:1 v/v ratio) to apoMb and stirring the solution overnight at 4 °C (~10 h). The following morning, the forest-green reconstituted ChlMb^{III} was centrifuged at 5 krcf for 15 min to remove any aggregated protein or uninserted chlorin from the mixture. The supernatant was loaded onto a Sephadex G25 gel filtration column (equilibrated with 10 mM sodium phosphate,

pH 6.8), and then fractions were collected and their purity was inspected by SDS-PAGE. The desired fractions were pooled together and concentrated to 30 mg/mL (as determined by UV-vis; $\varepsilon = 15.2\ mM^{-1}\ cm^{-1}$ at λ 280 nm) using a Millipore Amicon ultra filter with a cutoff of 10 kDa.

4.2.2.3 UV-vis spectroscopy studies of the reactions of dithionite reduced ferrous ChlMb^{II} with nitroalkanes ($MeNO_2$, $EtNO_2$, $PrNO_2$ and $iPrNO_2$)

To investigate the influence of electronic character of the macrocycle on ligand binding, as compared to Mb's natural cofactor heme PPIX (Chapter 2), UV-vis spectroscopy was used to monitor the reactions between dithionite reduced ferrous ChlMb^{II} and nitroalkanes ($MeNO_2$, $EtNO_2$, $PrNO_2$ and *i*$PrNO_2$). The spectrum of ferric ChlMb^{III} (in 3.0 mL of 0.1 M phosphate buffer (pH 7.4) was recorded, followed by the spectrum of dithionite reduced (20 mM final concentration) ferrous ChlMb^{II}. Immediately after, the nitroalkane ($MeNO_2$, $EtNO_2$, $PrNO_2$ or *i*$PrNO_2$ half diluted in MeOH) was added to a final concentration of 20 mM and the spectral changes were monitored for 1 h.

4.2.3 Studies of cobalt-PPIX substituted hhMb with nitroalkanes

4.2.3.1 Reconstitution of hhMb with cobalt-PPIX to form ferric Co^{III}Mb

ApoMb (prepared as described in section *4.2.3.1*) was reconstituted with cobalt protoporphyrin IX (CoPPIX; Frontier Scientific) to form Co^{III}Mb. Briefly, apoMb was stirred with 1.2 molar excess CoPPIX (dissolved in 0.1 M NaOH) overnight at 4 °C. Unbound CoPPIX and any aggregated proteins were removed by centrifugation (10 min, 5 krcf). The supernatant was loaded onto a CM-52 cellulose cation exchange column (equilibrated in 10 mM sodium phosphate buffer, pH 6.8). After washing the column with a two-fold volume equivalent of buffer, Co^{III}Mb was eluted using a salt gradient from 10 – 500 mM sodium phosphate buffer at pH 6.8. The

resulting fractions were inspected by SDS-PAGE and by UV-vis spectroscopy. Fractions with no evident impurities, and only those displaying a A_{Soret}/A_{280} (λ_{Soret} = 424 nm) ratio > 4.0 were pooled together. The final $Co^{III}Mb\text{-}H_2O$ samples were concentrated to 30 mg/mL using the extinction coefficient for this species (ε = 140 mM^{-1} cm^{-1} at λ_{max} 424 nm) [19].

4.2.3.2 UV-vis spectroscopy studies of reduced $Co^{II}Mb$ with nitroalkanes ($MeNO_2$, $EtNO_2$ and $PrNO_2$)

The reactions between reduced $Co^{II}Mb$ and nitroalkanes were monitored by UV-vis spectroscopy under reducing conditions to determine the influence of the electronic structure of the metal on ligand binding, as compared to Fe (Chapter 2). Briefly, the spectrum of $Co^{III}Mb\text{-}H_2O$ in 3.0 mL of 0.1 M phosphate buffer (pH 7.4) was obtained. Then, 2 M sodium dithionite was added (to a final concentration of 20 mM) to the cuvette and the spectrum of the resultant reduced $Co^{II}Mb$ was recorded. The reaction was then initiated by the addition of nitroalkane precursor ($MeNO_2$, $EtNO_2$ or $PrNO_2$ half diluted in MeOH; final concentration 20 mM) and monitored at regular time intervals for 3 h.

4.2.4 Interactions of human ferric $Hb^{III}\text{-}H_2O$ with arylhydrazines

4.2.4.1 Preparation of human hemoglobin

The extraction of human oxyHb from red blood cells (section *3.2.1.1*) and the preparation of ferric $Hb^{III}\text{-}H_2O$ (see section *3.2.1.2*) have been described in Chapter 3.

4.2.4.2 UV-vis spectroscopic studies of Hb with arylhydrazines

To expand our work into a different class of nitrogen-based ligands also involved in Hb degradation, as discussed in Chapter 3, the reactions between ferric $Hb^{III}\text{-}H_2O$ with arylhydrazines

were monitored via UV-vis spectroscopy. Similar reaction conditions as described by Wang for the reactions of Mb with arylhydrazines were used [15]. The reagents were mixed in 3.5 mL quartz cuvettes equipped with screw caps (Starna Cells) and monitored using a Hewlett Packard 8453 diode array spectrophotometer. Briefly, ferric Hb^{III}-H_2O was added (to a final concentration of ~3 μM) to a cuvette containing 3 mL of 0.1 M phosphate buffer at pH 7.4. The spectrum corresponding to ferric Hb^{III}-H_2O was recorded. Then, 0.5 M arylhydrazine (phenylhydrazine, 3-methylphenylhydrazine or 4-chlorophenylhydrazine, diluted in MeOH) was added to the solution to a final concentration of 1.5 mM and allowed to react. Each reaction was monitored up to 1 h by collecting spectrum readings at regular time intervals.

4.2.4.3 Time-course for the reactions and extents of formation

The time-course and extent of formation for the reactions of Hb with arylhydrazines were determined in a similar manner as described in section *3.2.2.3.* However, due to the differences in absorption spectra, the absorbance at λ 483 nm served as the apparent isosbestic point, while the Soret absorbance at λ_{max} ~430 nm was used as corresponding to the ligand-bound protein. The differences in absorbance at λ_{max} 430 nm and λ 483 nm were calculated and plotted as a function of time.

4.3 Results and Discussion

4.3.1 Reactions of ferrous wt and H64A swMb^{II} with nitrotoluenes (2NT, 3NT, 4NT and 2,6DNT)

4.3.1.1 Wild-type swMb

UV-vis spectroscopy was used to monitor the aerobic reactions of ferrous wt swMb^{II} with nitrotoluenes in the presence of dithionite, and the corresponding spectra are shown in Figure 4.7. Addition of excess dithionite as a reducing agent to ferric wt swMb^{III}-H_2O resulted in spectral changes in the Soret band from λ_{max} 409 to 433 nm, and changes in the Q-region of the visible spectrum from λ 505 to 559 nm. Addition of 2-nitrotoluene (2NT) to the ensuing ferrous wt swMb^{II} oxidized the protein back to the ferric state, as evidenced by the reappearance of absorbance at λ_{max} 409 nm in the Soret band and a shift in the Q-region back to λ 505 nm. Similar spectral changes were observed for the reactions of ferrous wt swMb^{II} with 3-nitrotoluene (3NT), 4-nitrotoluene (4NT) and 2,6-dinitrotoluene (2,6DNT). Furthermore, oxidation back to ferric wt swMb^{III}-H_2O occurred fast (within ~5 min), despite having excess dithionite (20 mM) in the reaction mixture.

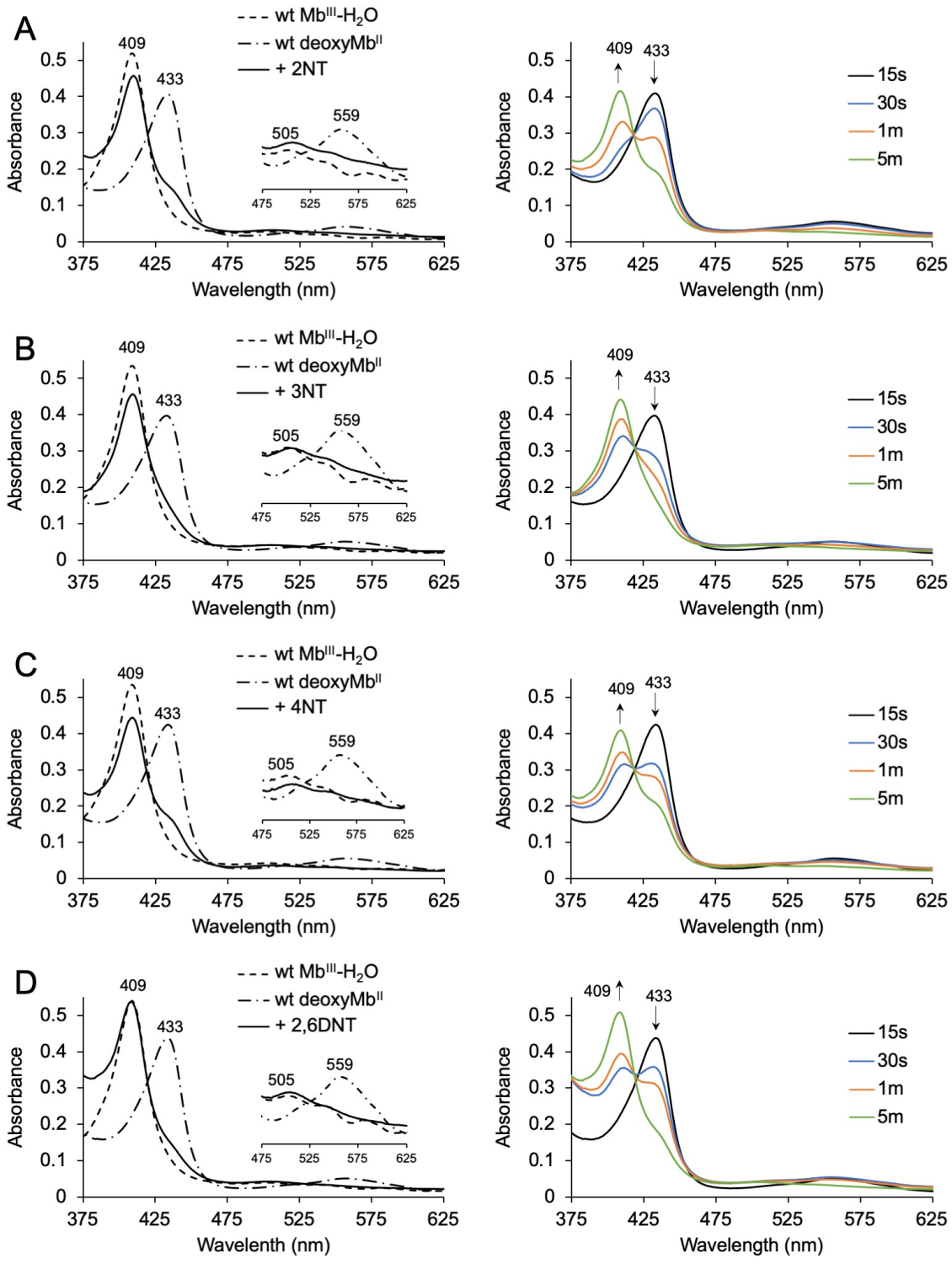

Figure 4.7 UV-vis spectral analyses of the reduction of ferric wt swMb^{III}-H$_2$O by dithionite, followed by the reaction of the resulting ferrous swMb^{II} with A) 2NT, B) 3NT, C) 4NT and D) 2,6DNT. Final reaction conditions: 0.1 M phosphate buffer (pH 7.4), 20 mM dithionite, 3 mM nitrotoluene.

4.3.1.2 The H64A swMb mutant

The UV-vis spectral changes corresponding to the reactions of ferrous H64A swMb^{II} with nitrotoluenes are shown in Figure 4.8. Reducing ferric H64A swMb^{III}-H_2O with excess dithionite resulted in the disappearance of the spectral peaks at λ_{max} 409 and λ 505 nm, and the appearance of new peaks at λ_{max} 433 and λ 559 nm representative of ferrous H64A swMb^{II}. Addition of 2-nitrotoluene to the solution mixture caused the Soret peak to shift to λ_{max} 424 nm and the Q-band to broaden with two peaks emerging at λ ~541 and 570 nm. These spectral changes occurred in <15 s and suggested N-binding of the nitroso product, 2-nitrosotoluene (2NOT), forming the ferrous H64A swMb^{II}-2NOT complex. However, under the conditions tested, the ferrous H64A swMb^{II}-2NOT complex is short-lived; spectral features characteristic of the ferric H64A swMb^{III}-H_2O species began to appear after 15 min (shoulder appearing at λ ~409 nm). Similar spectral aspects were observed for the reactions of ferrous H64A swMb^{II} with 3-nitrotoluene (3NT), 4-nitrotoluene (4NT) and 2,6-dinitrotoluene (2,6DNT). However, these resulted in shorter-lived N-bound protein-ligand complexes, presumably due to faster oxidation and consequential ligand dissociation. For instance, absorbance at λ_{max} 424 nm resulting from the reaction of ferrous H64A swMb^{II} with 2,6DNT almost completely shifted to λ_{max} 409 nm (indicative of the ferric wt swMb^{III}-H_2O species) within 15 min (Figure 4.8D right).

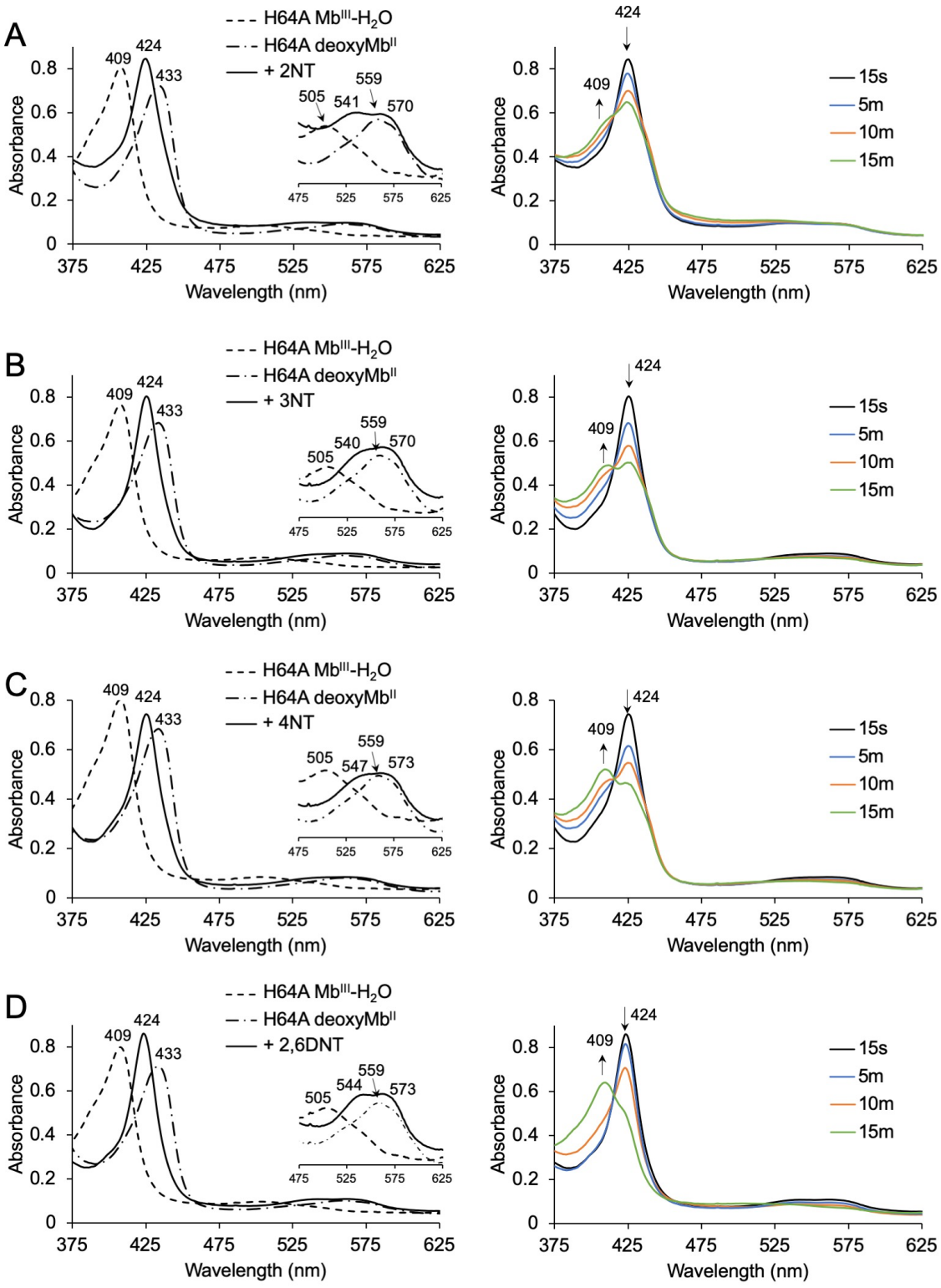

Figure 4.8 UV-vis spectral analyses of the reduction of ferric H64A swMb^{III}-H$_2$O by dithionite, followed by the reaction of the resulting ferrous H64A swMb^{II} with A) 2NT, B) 3NT, C) 4NT and D) 2,6DNT. Final reaction conditions: 0.1 M phosphate buffer (pH 7.4), 20 mM dithionite, 3 mM nitrotoluene.

4.3.1.3 Influence of distal pocket composition on Mb-nitrosotoluene complex formation

As described in Chapter 2, and by Mansuy [20], the analogous reactions of swMb with small alkyl nitroalkanes (R = Me, Et, Pr, *i*Pr) resulted in relatively long-lived intermediate peaks forming at λ_{max} ~424 nm, indicating N-bound Mb^{II}-RNO complex formation. Similar spectral changes were observed for both wt and the H64A swMb mutant. The binding mode of the complexes resulting from those reactions was further confirmed by me using X-ray crystallography (Chapter 2). However, despite not forming an intermediate peak for the analogous studies between dithionite reduced wt $swMb^{II}$ and NTs, it would be incorrect to state absolutely that there was no reaction to generate Fe^{II}-RNO derivatives. Instead, due to the conversion of ferrous $swMb^{II}$ to its ferric form, it is likely that these reactions formed very unstable $swMb^{II}$-RNO complexes that quickly dissociated their ligands resulting in the wt ferric $swMb^{III}$-H_2O species. This notion was confirmed after monitoring the reactions of dithionite reduced H64A $swMb^{II}$ with the same series of nitrotoluenes, which resulted in peaks appearing at λ_{max} ~424 nm. This indicates that H64A $swMb^{II}$-RNO derivatives formed and that the nitroso products were N-bound to the heme. However, the $swMb^{II}$-RNO complexes were short-lived. As such, co-crystallization attempts for these complexes resulted in the final ferric $swMb^{III}$-H_2O product.

Based on my results, it is difficult to tell whether lack of H-bonding, or the slight increased volume of the H64A swMb mutant is responsible for the formation of $swMb^{II}$-RNO complex. As such, it would be prudent to monitor the reactions of nitrotoluenes with the swMb H64Q and V68A/I107Y mutants, due to their differences in H-bonding and active site volumes. However, based on the increased size of the NTs, it is likely that the most influential factor in facilitating H64A $swMb^{II}$-RNO complex formation is active site volume.

4.3.2 Reactions of chlorin substituted hhMb with nitroalkanes ($MeNO_2$, $EtNO_2$, $PrNO_2$, $iPrNO_2$)

Reconstitution of hhMb with chlorin resulted in a forest-green ferric $ChlMb^{III}$ species with prominent absorbance in the Soret band of the UV-visible spectrum at λ_{max} 417 nm and a second peak at λ 653 nm in the Q-region (Figure 4.9). In the presence of the reducing agent sodium dithionite, the color changed to bright emerald-green with new peaks forming at λ_{max} 428 nm and λ 644 nm for the ferrous $ChlMb^{II}$ product. Addition of $MeNO_2$ to the reaction mixture caused the Soret band to decrease in absorbance and form a broad peak at λ_{max} ~418 nm. Simultaneously, the Q-band decreased and widened without shifting from its position at λ 644 nm. These spectral features are significantly different from those corresponding to the starting ferric $ChlMb^{III}$ species or the ferrous $ChlMb^{II}$ protein, thereby suggesting the likely formation of a ferrous $ChlMb^{II}$-MeNO derivative (Figure 4.9A). Similar spectral changes, albeit with less pronounced Soret peaks at λ_{max} ~420 nm, were observed for the reactions of dithionite reduced $ChlMb^{II}$ with $EtNO_2$ and $PrNO_2$ (Figure 4.9B, C). While similar changes were observed in the Soret band for the reaction of $ChlMb^{II}$ with *i*$PrNO_2$, this reaction generated a shift in the Q-band to λ 653 nm, unlike any of the other RNOs in this study (Figure 4.9D).

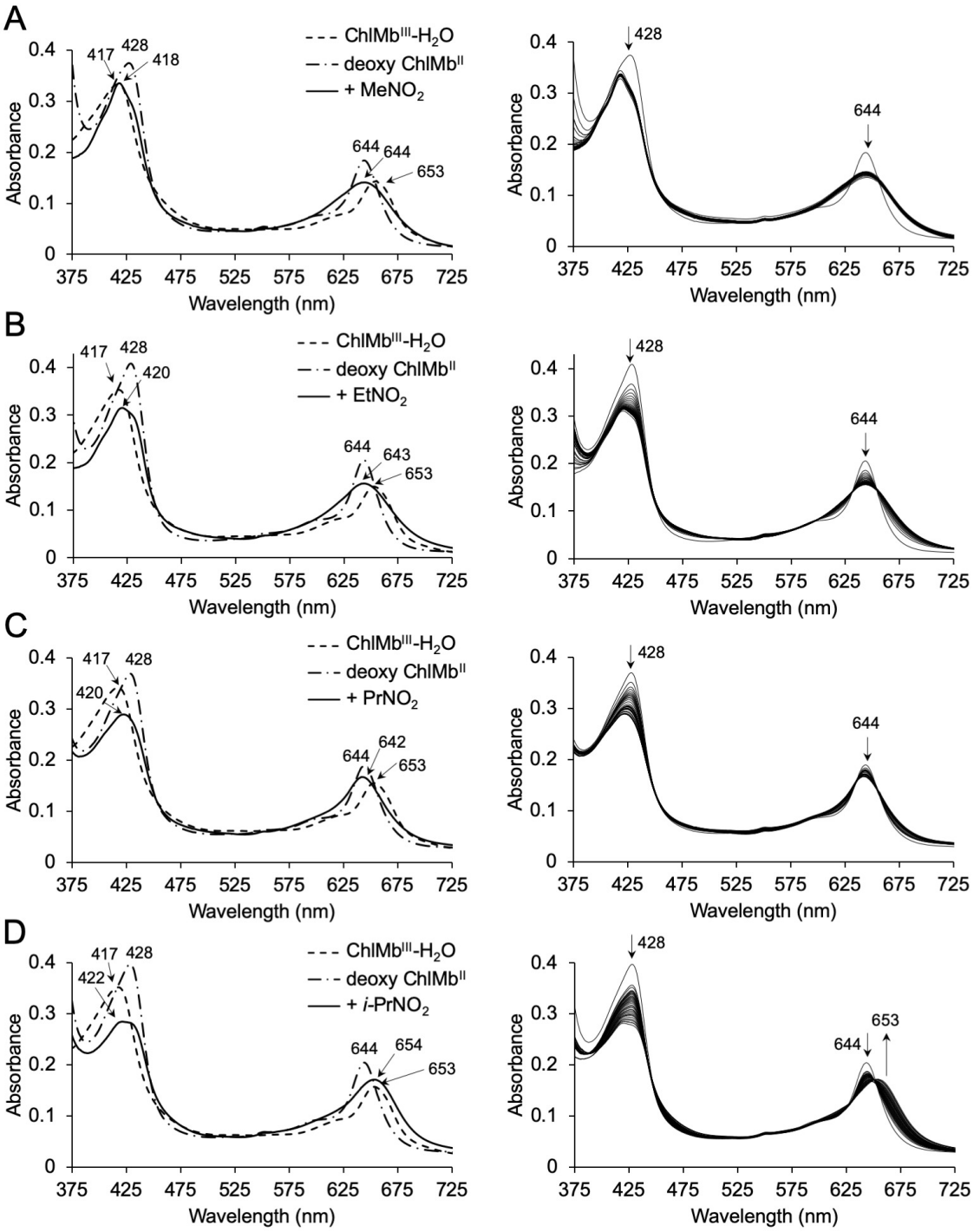

Figure 4.9 UV-vis spectral analyses of ferric ChlMb^{III} and dithionite reduced ferrous ChlMb^{II}, followed by the reaction of the ferrous ChlMb^{II} with A) $MeNO_2$ B) $EtNO_2$, C) $PrNO_2$ and D) *i*$PrNO_2$. Final reaction conditions: 0.1 M potassium phosphate buffer pH 7.4, 20 mM dithionite, 20 mM RNO_2.

4.3.2.1 Analysis of the reactions of ChlMb with alkyl nitroalkanes

X-ray crystallographic studies from our group have shown that nitrite can bind to ChlMb in both the N- and O-binding modes (Figure 4.10). The ChlMb-N_2O and ChlMb-ONO derivatives have distinct spectral features. The N-bound derivative resulted in peaks at λ 419 and 652 nm, whereas the O-bound compound had peaks at λ 422 and 662 nm. The UV-vis spectroscopy studies of ChlMb with nitroalkanes presented here resulted in peaks different than these. Therefore, while it can be concluded that a reaction occurred, the binding mode of the RNO ligand cannot be determine solely through UV-vis spectroscopy. Unfortunately, my crystallization attempts of the ChlMb-RNO derivatives resulted in twined crystals that diffracted X-rays poorly, which prevented me from further analyzing the heme-nitroso chemistry of these complexes.

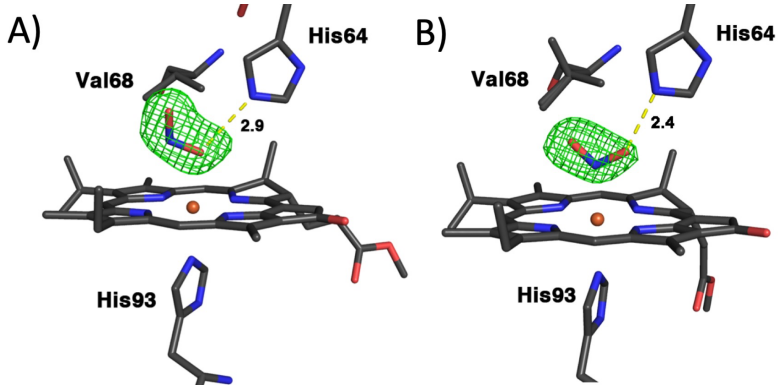

Figure 4.10 Nitrite binding modes in ChlMb. A) MbChl-ONO, PDB ID 3V2V. B) MbChl-NO_2, PDB ID 3V2Z.

4.3.3 Reactions of cobalt PPIX substituted hhMb with nitroalkanes ($MeNO_2$, $EtNO_2$ and $PrNO_2$)

Reconstitution of hhMb with CoPPIX resulted in Co^{III}Mb-H_2O, which has a Soret peak at λ_{max} 424 nm, and two peaks in the Q-region of the UV-vis spectrum at λ 534 and 570 nm (Figure 4.11) [19]. Addition of dithionite to the protein caused the peaks to shift, resulting in absorbance at λ_{max} 404 nm and 556 nm after reduction occurred. Addition of $MeNO_2$ to the resultant reduced Co^{II}Mb species resulted in oxidation of the protein; as evidenced by the reappearance of the

spectral traits typical of $Co^{III}Mb\text{-}H_2O$ (λ_{max} 424, and λ 534 and 570 nm). Similar results were observed for the reactions of dithionite reduced $Co^{II}Mb$ with $EtNO_2$ and $PrNO_2$. Furthermore, no additional changes were observed after prolonged monitoring of these reactions (up to 4h).

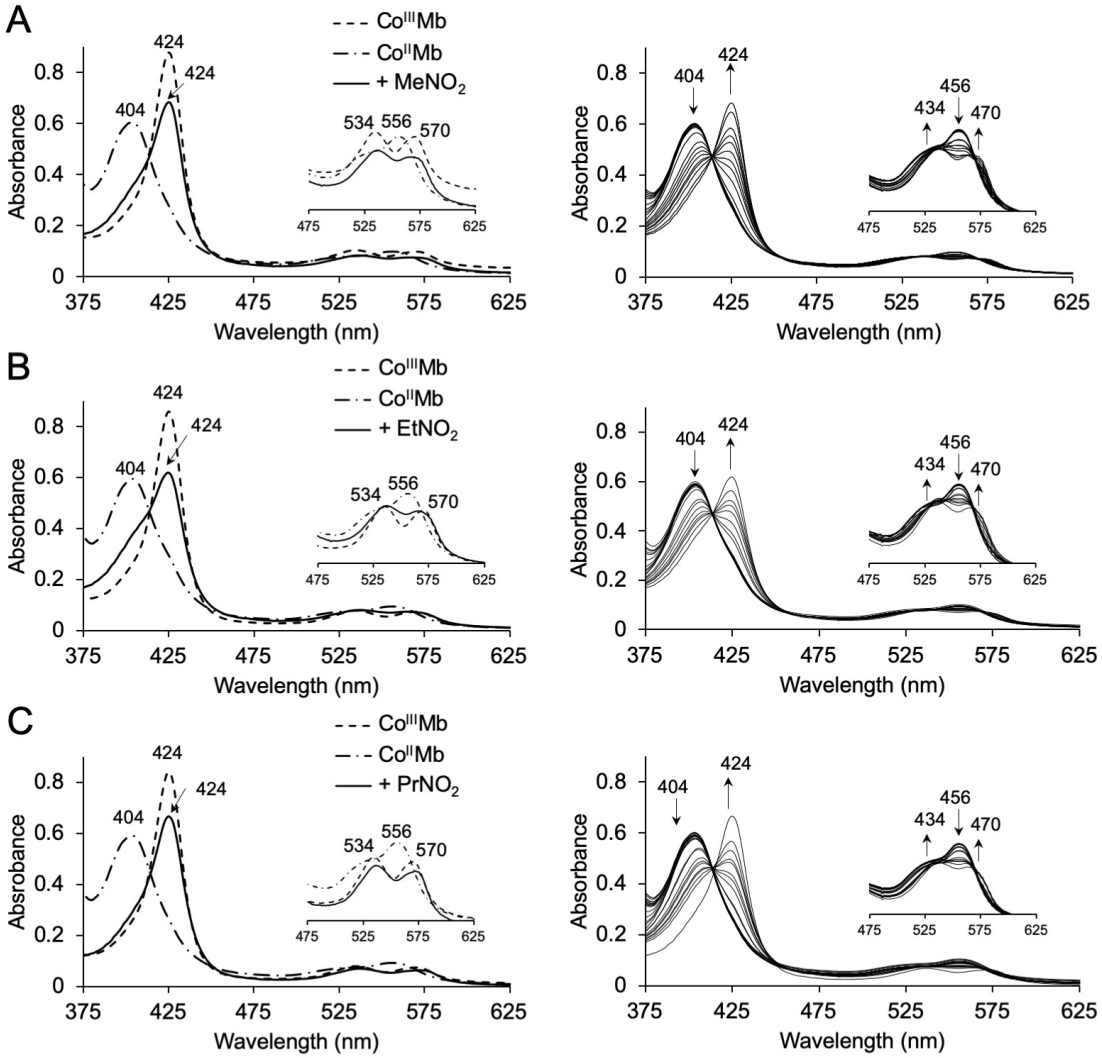

Figure 4.11 UV-vis spectral analysis of the reduction of $Co^{III}Mb\text{-}H_2O$ to the reduced $Co^{II}Mb$, followed by the addition of A) $MeNO_2$, B) $EtNO_2$ and C) $PrNO_2$. Final reaction conditions: 0.1 M potassium phosphate buffer pH 7.4, 20 mM dithionite, 20 mM RNO_2.

4.3.3.1 Analysis of the reactions of CoMb with nitroalkanes

The analogous reactions of ferrous Mb^{II} with alkyl RNOs (R = Me, Et, Pr, *i*PrNO) resulted in stable $swMb^{II}$-RNO adducts. The ferrous Mb^{II} protein and $Co^{III}Mb$ species share similar

electronic configuration (d^6), yet complex formation was not observed in either Co^{III}Mb or reduced Co^{II}Mb (d^7). Interestingly, metal oxidation by addition of RNO_2 was also observed for the reactions of wt swMb with nitrotoluenes. I postulated that oxidation of swMb occurred from the formation of unstable $swMb^{II}$-RNO complexes and quick ligand dissociation resulting in the ferric $swMb^{III}$-H_2O product. Perhaps, oxidation of Co^{II}Mb upon addition of RNO_2 into the reaction mixture resulted in a similar manner. Despite the lack of clear results, it can be concluded that the differences between Co and Fe metals have a significant influence in $swMb^{II}$-RNO complex formation and stability.

4.3.4 Reactions of ferric Hb^{III}-H_2O with arylhydrazines

Finally, the reactions of human ferric Hb^{III}-H_2O with arylhydrazines were monitored by UV-vis spectroscopy (Figure 4.12). The absorption spectrum of ferric Hb^{III}-H_2O revealed a Soret peak at λ_{max} 406 nm, and a second peak in the Q-region at λ 500 nm. Upon addition of phenylhydrazine, these spectral peaks gradually decreased and new peaks emerged at λ_{max} 430 nm and at λ 545 and 569 nm. Similar spectral changes were observed for the reactions of ferric Hb^{III}-H_2O with *m*-tolylhydrazine and *p*-chlorophenylhydrazine.

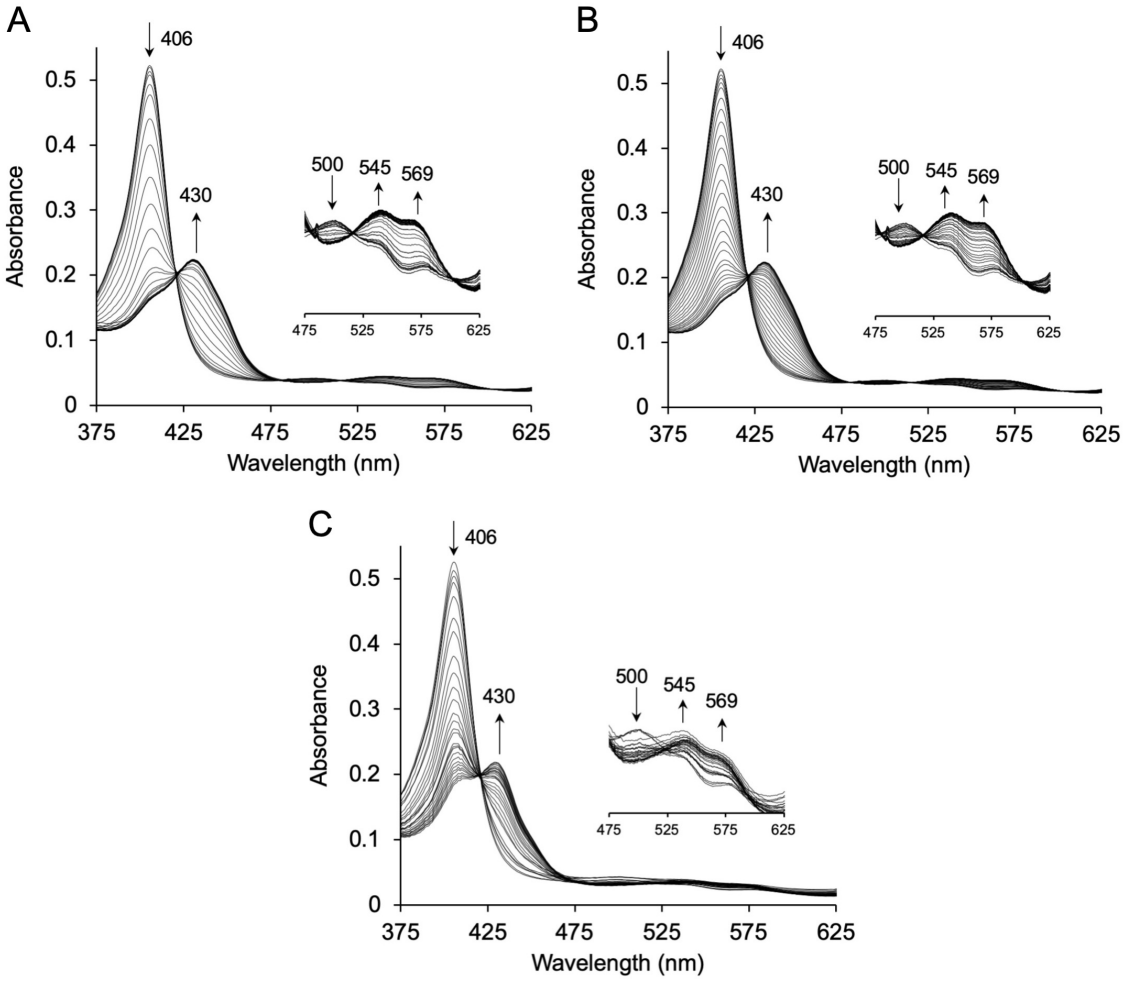

Figure 4.12 UV-vis spectral characterization of the reactions between ferric Hb^{III}-H_2O with arylhydrazines. A) phenylhydrazine, B) *m*-tolylhydrazine, C) *p*-chlorophenylhydrazine. Final reaction conditions: ~3 μM Hb, 0.1 M phosphate buffer (pH 7.4), 1.5 mM arylhydrazine.

4.3.4.1 Analysis of the reactions of Hb with arylhydrazines

Temporal tracking of the reactions of Hb with arylhydrazines indicated that the reactions ran to completion within ~15 min and remained stable throughout the 1 h time period of monitoring (Figure 4.13). Furthermore, both *m*-tolylhydrazine and *p*-chlorophenylhydrazine have similar extents of formation, which are slightly higher than the phenylhydrazine Hb products. Attempts to co-crystallize Hb with arylhydrazines resulted in high levels of precipitation but yielded no crystals. Similarly, ligand soaking into ferric Hb^{III}-H_2O crystals proved difficult. Ligand soaking

was performed several times using different condition (e.g. soaking time, ligand concentration, temperatures, buffer, etc.) and >50 crystals were screened. Each time, this process disrupted the packing of the crystal and as a result they lost their X-ray diffraction ability. However, given the high similarities in active site composition between Mb and Hb, it is likely that they share similar modes of binding. In the Mb analogues, the N-C(aryl) bond of the arylhydrazine breaks, creating a phenyl radical which binds directly to the Fe-center of the heme [15].

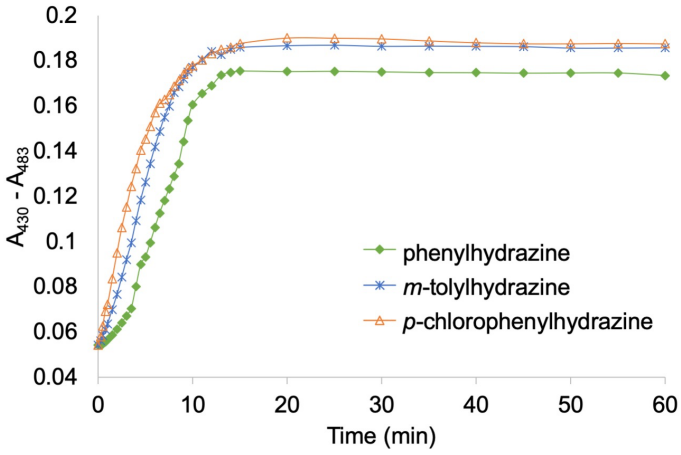

Figure 4.13 Temporal changes in UV-vis spectra after addition of arylhydrazine to ferric Hb^{III}-H_2O; determined by plotting the difference between the absorbance at λ 430 and 483 nm as a function of time.

4.4 Summary and Conclusion

The goal of this research was to determine the how different factors influence the heme-nitroso chemistry of Mb. First, ligand size and sterics proved to be significant. Unlike small alkyl RNOs, nitrotoluenes bound to dithionite reduced Mb^{II} and formed relatively short-lived Mb^{II}-RNO complexes that quickly dissociated resulting in the ferric Mb^{III}-H_2O forms. Second, the redox properties of the metal drastically changed the interactions of Mb with alkyl RNOs. In the native Fe-containing Mb, the Mb^{II}-RNO complexes are stable. In contrast, formation of the protein-ligand complexes was not detected with the CoMb species. Similarly, the role of the electron-richness of

the macrocycle on Mb-nitroso reactivity was also analyzed. For the reactions of ChlMb with nitroalkanes, the UV-vis results suggest formation of ChlMb-RNO complexes. However, without further crystallographic evidence, it is difficult to ascertain the binding mode of the RNO ligands.

Finally, the reactions of Hb with arylhydrazines were characterized with UV-vis spectroscopy. Comparably to the analogous reactions reported for Mb Dr, Wang, my results suggest an Fe-C(aryl) binding mode in the products, instead of heme(N)-C(aryl) interactions.

4.5 References

1. Poulos, T.L., *Heme enzyme structure and function.* Chem Rev, 2014. **114**(7): pp 3919-62.
2. Lu, Y., et al., *Design of functional metalloproteins.* Nature, 2009. **460**(7257): pp 855-62.
3. Liu, Y., et al., *Functional conversion of nickel-containing metalloproteins via molecular design: from a truncated acetyl-coenzyme A synthase to a nickel superoxide dismutase.* Chem Commun (Camb), 2013. **49**(14): pp 1452-4.
4. Johnson, K.A., J.S. Olson, and G.N. Phillips, Jr., *Structure of myoglobin-ethyl isocyanide. Histidine as a swinging door for ligand entry.* J Mol Biol, 1989. **207**(2): pp 459-63.
5. Ruscio, J.Z., et al., *Atomic level computational identification of ligand migration pathways between solvent and binding site in myoglobin.* Proc Natl Acad Sci U S A, 2008. **105**(27): pp 9204-9.
6. Scott, E.E., Q.H. Gibson, and J.S. Olson, *Mapping the pathways for O2 entry into and exit from myoglobin.* J Biol Chem, 2001. **276**(7): pp 5177-88.
7. Wang, B., et al., *Nitrosoamphetamine binding to myoglobin and hemoglobin: Crystal structure of the H64A myoglobin-nitrosoamphetamine adduct.* Nitric Oxide, 2017. **67**: pp 26-29.
8. Bakhtiar, R., et al., *Evidence for a novel heme adduct generated by the in vitro reaction of 2,4,6-trinitrotoluene with human hemoglobin using electrospray ionization mass spectrometry.* J Inorg Biochem, 1997. **68**(4): pp 273-8.
9. Bhagi-Damodaran, A., et al., *Why copper is preferred over iron for oxygen activation and reduction in haem-copper oxidases.* Nat Chem, 2017. **9**(3): pp 257-263.
10. Antonini, E. and M. Brunori, *Hemoglobin and myoglobin in their reactions with ligands*. Frontiers of Biology (Amsterdam). 1971, Amsterdam,: North-Holland Pub.
11. Brucker, E.A., et al., *High resolution crystal structures of the deoxy, oxy, and aquomet forms of cobalt myoglobin.* J Biol Chem, 1996. **271**(41): pp 25419-22.
12. Stone, K., J. Hua, and H. Choudhry, *Manganese-Substituted Myoglobin: Characterization and Reactivity of an Oxidizing Intermediate towards a Weak C-H Bond.* Inorganics, 2015. **3**(2): pp 219-229.
13. Shetlar, M.D. and H.A. Hill, *Reactions of hemoglobin with phenylhydrazine: a review of selected aspects.* Environ Health Perspect, 1985. **64**: pp 265-81.
14. Shukla, P. and R.K. Singh, *Toxicogenomics of Phenylhydrazine Induced Hematotoxicity and its Attenuation by Plumbagin from Plumbago zeylanica.* Pharmacogn Mag, 2015. **11**(Suppl 3): pp S380-7.
15. Wang, B., L.M. Thomas, and G.B. Richter-Addo, *Organometallic myoglobins: Formation of Fe-carbon bonds and distal pocket effects on aryl ligand conformations.* J Inorg Biochem, 2016. **164**: pp 1-4.
16. Ortiz de Montellano, P.R., et al., *Carbon radicals in the metabolism of alkyl hydrazines.* J Biol Chem, 1983. **258**(14): pp 8623-9.
17. Yonetani, T., *Studies on cytochrome c peroxidase. X. Crystalline apo-and reconstituted holoenzymes.* J Biol Chem, 1967. **242**(21): pp 5008-13.
18. Teale, F.W., *Cleavage of the haem-protein link by acid methylethylketone.* Biochim Biophys Acta, 1959. **35**: pp 543.
19. Heinecke, J.L., et al., *Nitrite reduction by Co(II) and Mn(II) substituted myoglobins: towards understanding necessary components of Mb nitrite reductase activity.* J Inorg Biochem, 2012. **107**(1): pp 47-53.

20. Mansuy, D., J.C. Chottard, and G. Chottard, *Nitrosoalkanes as Fe(II) Ligands in Hemoglobin and Myoglobin Complexes Formed from Nitroalkanes in Reducing Conditions.* European Journal of Biochemistry, 1977. **76**(2): pp 617-623.